University of Glasgow

Fabrication and Development of Nanomaterial-based Screen-Printed Electrochemical Sensing Technology for the Detection of Potentially Toxic Elements in Water

Deepan Kumar Neethipathi

A thesis submitted at the University of Glasgow in fulfilment of the requirements for the Degree of

Doctor of Philosophy

College of Science and Engineering

October 2024

Abstract

Electrochemical sensing technology is predominantly used to detect and monitor potentially toxic elements in water. Carbonous-based new screen-printed-based electrochemical sensors were built and further modified with interesting nanomaterials for the detection of heavy metal ions using various electrochemical techniques. As a vast amount of research work has been done in this research area, there are many practical issues in handling them for infield application. Even exhibiting a reasonable performance in the approach towards real field applications, A majority of electrochemical sensors reported have never left the laboratory conditions even while providing advantages over expensive conventional sensing system and their methods. The work focuses on guiding beginners approaching the research field of the printed electrochemical sensor and provides an in-depth understanding of a step-by-step approach to sensor fabrication, sensor characterisation, data collecting, data processing, and data analysis and further proceeds towards building the bridge between the technical gap between using the laboratory-based and field practicality application.

The work described in this thesis majorly includes 1) fabricating new printed electrochemical sensors for the detection of potentially toxic elements such as Ag, Au, Cd, Co, Cu, Fe, Mn, and Pb ions in water using multiple electrochemical techniques; 2) Discussion on the precondition, and Postconditioning stages for the reusability of the sensor; 3) An insight on pulsed anodic stripping voltammetry and the requirement of optimisation between the deposition and condition stages for the reproducibility of the printed sensor; and 4) Different nanomaterials such as molybdenum disulphide, graphitic carbonic nitride, Zinc oxide, and a mixture of Titanium dioxide and Magnesium oxide were infused with the screen-printed carbon electrode as a working sensing electrode for the detection of targeted analyte with excellent sensitivity and selectivity among interfering akin analyte ions.

A comparison of sensor performance between conventional and printed electrochemical sensors was executed to achieve improved sensing performance. Two Arduino-based readout equipments were developed as sensing technology for low-cost potentiostats, and they were further incorporated with the nanomaterial developed for field deployments with two unique electrochemical techniques, i.e., chronoamperometric and Voltammetric detection.

Author's Declaration

I certify that the thesis presented here for examination for a PhD degree of the University of Glasgow is solely my own work other than where I have clearly indicated that it is the work of others (in which case the extent of any work carried out jointly by me and any other person is clearly identified in it) and that the thesis has not been edited by a third party beyond what is permitted by the University's PGR Code of Practice.

I declare that the thesis does not include work forming part of a thesis presented successfully for another degree.

I declare that this thesis has been produced in accordance with the University of Glasgow's Code of Good Practice in Research.

I acknowledge that if any issues are raised regarding good research practice based on review of the thesis, the examination may be postponed pending the outcome of any investigation of the issues

Deepan Kumar Neethipathi

List of Abbreviations

AA	Ascorbic Acid
AAS	Atomic Absorption Spectroscopy
AdCSV	Adsorptive Cathodic Stripping Voltammetry
ASV	Anodic Stripping Voltammetry
CDC	Centre for Disease Control
CE	Counter-Electrode
CPE	Constant Phase Element
CRC	Current Reversal Chronopotentiometry
CSV	Cathodic Stripping Voltammetry
CV	Cyclic Voltammetry
DASA	1, 2-dihydroxyanthraquinone-3-sulphonic acid
DI	Deionised
DMF	Dimethylformamide
DPAdSV	Differential Pulse Adsorptive Stripping Voltammetry
DPCSV	Differential Pulsed Cathodic Stripping Voltammetry
DPSV	Differential Pulsed Stripping Voltammetry
DPV	Differential Pulsed Volatmmtery
EC	Electrochemical
EDTA	ethylenediaminetetraacetic acid
EEC	Electrical Equivalent Circuit
EIS	Electrochemical Impedance Spectroscopy
EM2C2	Electrochemical Measurement of Multivalent Cations Concentration
EPA	US Environmental Protection Agency
EU	European Union
FAO	Joint Food and Agricultural Organization
FIA	Flow Injection Analysis
FRA	Frequency Response Analyser
FSDPV	Fast Scan Differential Pulse Voltammetry
gC3N4	Graphitic Carbon Nitride
GCE	Glassy Carbon Electrode
HMI	Heavy Metal Ions
ICP-MS	Inductively Coupled Plasma Mass Spectrometry
IEV	Ion-Exchange Voltammetry
ISE	Ion Selective Electrode
LOD	Limit Of Detection
LOQ	Limit Of Quantification
LSV	Linear scan voltammetry
MoS2	Molybdenum disulfide
MSWV	Multiple Square-Wave Voltammetry
PCL	Polycaprolactone
PET	Polyethylene terephthalate
PTE	Potentially Toxic Elements
PVC	polyvinyl chloride
RDE	Rotating Disk Electrode
RE	Reference Electrode
SCE	Saturated Calomel Electrode
SCP	galvanostatic Stripping Chronopotentiometry
SEM	scanning electrode microscopy
SGAuNP	Sol-Gel-Au nanoparticle

SHE	Standard Hydrogen Electrode
SP	Screen printing
SPCE	Screen-Printed Silver Electrodes
SPSE	Screen-Printed Silver Electrodes
SWAdSV	Square-Wave Adsorptive Stripping Voltammetry
SWV	Squarewave Voltammetry
TGA	Thermogravimetric Analysis
UV-vis	Ultraviolet-Visible Spectrophotometry
WE	Working Electrode
WHO	World Health Organization
XRD	X-ray Diffraction
XRF	X-ray fluorescence spectroscopy
ZnO	Zinc oxide

List of Publications

(1) Neethipathi, D. K., Beniwal, A., Bass, A., Scott, M., & Dahiya, R. MoS2 modified Screen Printed Carbon Electrode based Flexible Electrochemical sensor for Detection of Copper ions in water. IEEE sensors journal (10.1109/JSEN.2023.3257188).

(2) Neethipathi, D. K., Mishra, S., Ganguly, P., A., Bass, A., Scott, M., & Dahiya, R. Flexible MoS2 modified Screen Printed Carbon Electrode based Electrochemical sensor for wine quality monitoring by detection of ascorbic acid. Advanced sensor research journal (Submitted)

(3) Neethipathi, D. K., Beniwal, A., Ganguly, P., Scott, M., Bass, A., & Dahiya, R. Electrochemical Detection of Fe2+ Ions in Water Using 2-Dimensional g-C3N4 Modified Glassy Carbon Electrode-Based Sensor. 2023 IEEE Applied Sensing Conference (APSCON)

(4) Neethipathi, D. K., Ganguly, P., Beniwal, A., Scott, M., Bass, A., & Dahiya, R. (2022, July). MoS2 modified screen printed carbon electrode based flexible sensor for detection of copper. In 2022 IEEE International Conference on Flexible and Printable Sensors and Systems (FLEPS)

(5) Ganguly, P., Neethipathi, D. K., Beniwal, A., & Dahiya, R. (2022, July). Influence of Thickness of Screen-Printed Carbon Electrodes on Electrochemical Sensing. In 2022 IEEE International Conference on Flexible and Printable Sensors and Systems (FLEPS)

(6) Beniwal, A., Neethipathi, D. K., & Dahiya, R. PEDOT: PSS modified Screen Printed Graphene-Carbon Ink based Humidity and Temperature Sensor. IEEE Journal on Flexible Electronics (doi: 10.1109/JFLEX.2022.3228970)

(7) Beniwal, A., Ganguly, P., Neethipathi, D. K., & Dahiya, R. (2022, July). PEDOT: PSS modified Screen Printed Graphene-Carbon Ink based Flexible Humidity Sensor. In 2022 IEEE International Conference on Flexible and Printable Sensors and Systems

Acknowledgements

I am truly thankful for the wonderful individuals who have joined me on this journey.

First and foremost, I would like to express my gratitude to my supervisors, Dr. Adrian Bass, Prof. Marian Scott, and Prof. Cindy Smith, who have been steadfast supporters throughout my PhD journey. Your unwavering presence has often provided me with the courage needed to pursue my thesis work steadily. Over the past four years of my doctoral studies, I have been continually impressed and grateful for your invaluable guidance and support, which have enabled me to make consistent progress each day.

I would like to express my sincere appreciation to the European Union's Horizon 2020 program for funding the AQUASENSE project and the University of Glasgow for providing me with further IAA funding for the AQUA-ELECTROSENSE project.

I appreciate my colleagues in the BEST Group at the University of Glasgow for their support and assistance in my research efforts. I would like to extend special thanks to my friends, Mr. Radu-Răzvan Chirilă and Dr. Dina Anna John, for bringing joy to our workplace and for their unwavering assistance.

Special thanks to Prof. Ravinder Dahiya, Dr. Alexey Ganin, Mr. Shashank Mishra, Dr. Priyanka Gangul and Dr. Saoirse Delvin from UoG for guiding me in my research goals.y

I am thankful to Dr. Cristian Urlea and Dr. Laura Voinea for their continuous motivation toward my doctoral goals. I also appreciate the expeditions we shared, filled with many moments of joy and laughter.

I would like to express my gratitude to my friends and my unwavering support system back home for always making me feel alive: Mr. M. Gowre Sankar, Mr. M. Vigneshwaran, and Mr. R. Ajay.

Finally, I dedicate this thesis to my mother, Mrs. P. Pushpa (My father), Mrs. P. Shivapriya (my wife), Mrs. N. Janani (My sister), and Mr. S. Neethipathi (my father), for their boundless love and faith in me. I would also like to extend special thanks to Dr. Sivaprakash Sengodan for guiding me along this joyful path.

Once again, I would like to express my heartfelt gratitude to Dr. Adrian Bass for his encouragement throughout my studies.

Table of Contents

Table of Figures

[1] 1.Introduction

1.1 Introduction

In Modern times, Electrochemical (EC) Sensing has become widely employed in detection and monitoring applications in various fields, including environmental monitoring, clinical diagnostics, food safety, and more. Among these applications, the detection and monitoring of heavy metals in water is a primary global concern that has impacted both human health and the ecosystem.[1] From the middle of the 20th century especially after the third Industrial revolution[2], due to the expanding population, the global demand for people has increased in many product-based industries such as pesticides, electronics, semiconductors, paints, etc.[3, 4] This results in an enormous amount of industrial wastewater being disposed into the water resources on a daily basis. Heavy metals are significant and potentially impactful outcomes of such industrial wastewater, and they have led to a sudden increase in heavy metals across natural resources in recent centuries.[5, 6] Often toxic in nature, the presence of such non-degradable heavy metals in both surface water and groundwater becomes one of the major global threats as main water pollutants, concerning all living organisms as well as the environment due to their huge adverse effects.[7, 8] Even though broad research on electrochemical sensors for detecting such heavy metal ions has been conducted vigorously for the last few decades for its advantageous easier commercialisation and mass production agenda, the execution of such electrochemical sensing technologies in field operations is still lacking in comparison to other common conventional sensing technologies.[9, 10] However, the recent utilisation of printed electrochemical sensors displays promising field operation possibilities for field deployment along with attractive benefits such as low-cost production and less manpower requirement. Therefore this leaves an exciting gap in their implementation towards practical application in field conditions, especially in the case of screen-printed electrochemical sensors, which can be studied and improved in each stage of sensor development and deployment (designing, fabrication, and characterisation of the sensors, laboratory-based testing and building appropriate readout equipment and further field deployment of the sensing system, to data transmission, data collection, and data analysis).[11, 12]

1.1. Research Motivation (Context and Background)

In addition to comprehensive research on electrochemical sensing techniques, traditional methods for detecting heavy metal ions in water quality monitoring are primarily divided into two main categories: spectroscopy techniques and optical methods. Most highly sensitive conventional spectroscopy methods such as atomic absorption spectroscopy, atomic emission spectroscopy, inductively coupled plasma mass spectrometry, and cold vapour atomic fluorescence spectrometry generally require a pretreatment laboratory condition, which lacks continuous operation in field conditions and is not easily transportable.[13-16] This sensing equipment is expensive and requires regular maintenance. Conventional Optical methods such as absorption, reflection, or luminescence spectrometry, or with the help of dye indicators, optical fibres, integrated optics, and capillary-type devices, also result in high maintenance and require expensive instrumentation.[17, 18] The precision hugely

demands laboratory conditions as it is challenging to operate in field conditions.[19] Unlike traditional methods, electrochemical sensors offer several advantages, including portability, real-time monitoring, rapid response times, high sensitivity and selectivity, low power consumption, and cost-effectiveness. These features make them an excellent option for applications requiring real-time monitoring.

A technical gap exists among most of the electrochemical sensors reported in literature and research articles, and they fail to adapt from laboratory-based testing to field deployment as they tackle interfering physical and physicochemical changes that occur in real-time field conditions.[20] Most reported sensors follow a typical electrochemical sensor setup that fails to adapt due to rigidity and eventually breaks in real time.[21, 22] While addressing field deployment of conventional rigid laboratory-based EC sensors, they were limited in their adaptability to phenomena of water properties, such as physical parameters like flowrate velocity, temperature, and pH, and chemical parameters, such as the influence of external chemical agents, which affect the sensor's performance in selectivity, non-repetitiveness, sensitivity, and damage towards such rigid sensors.[23-25] Therefore, flexible printed sensors were tested in laboratory conditions to detect potentially toxic heavy metal ions in water selectively and further investigated to check the feasibility of the sensor technology to reach the measurable range of such trace elements present in the water sources.[26, 27]

Such printed sensors were built using techniques such as Die coating, inkjet, stencil, screen-printing, printer, and 3D printing.[28-32] Among these techniques, Screen-printed electrochemical sensors were widely explored mainly due to their manufacturing benefits, such as high production rate and simpler equipment operations.[33, 34] Even though these printed sensors are more robust, deploying them presents a few common challenges, such as a high noise output signal, a lack of better coating leading to easier pealing of material layers, and the influence of interfering ions affecting the sensor's selectivity.[35] However, these limitations can be considerably avoided and improved at every stage of sensor development, from material selection, sample preparation, calibration, and validation to the readout equipment, environmental conditions, data logging and analysis, maintenance and cleaning, and safety considerations.[36, 37]

Apart from printing technologies, the usage of single or multiple nanomaterials as a receptor or sensing layer among electrochemical sensors has been extensively used for their prominent performance of the sensor. Having excellent material and electronic properties such as high surface area, selectivity, good electrochemical properties, and tuneable electric conductivity, printing technologies were built with the utilisation of nanomaterial.[38, 39]

Therefore, in this work, to escort the practical complexity of utilising nanomaterial-based screen-printed electrochemical sensors for the detection of HMIs in water samples, The source and further adaptability towards such limitations of EC sensors were discussed in detail by exploring new novel sensors for sensing towards various heavy metals detection in water in the case of Ag, Au, Cd, Cu, Fe, Mn, Ni, Pb, Zn and further conducting case studies for improved sensing performance in field operation were conducted.

1.2. Objectives and Key Findings:

Some of the optimisation processes for the development of new electrochemical sensors have not been explored in a way to address the practical difficulties of their integration towards field operation. This includes selecting materials and optimising the electrodes' ideal thickness, shape design, and texture regarding the conductive material. The robust nature of the coating layer in regard to the solvent usage at ink formulation can be improvised. The selectivity of certain nanomaterials can be explored towards akin interfering analyte ions in water samples. The Electrochemical Impedance Spectroscopy (EIS) technique can be explored for optimisation.

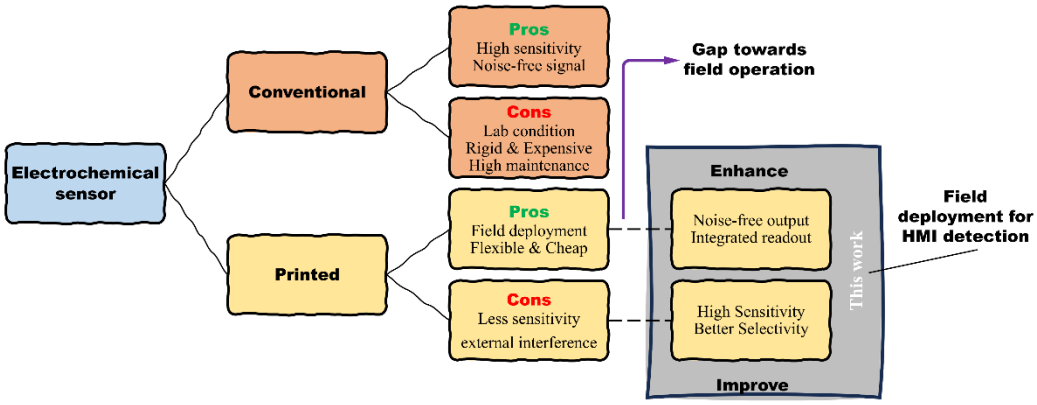

Figure 1-1: Schematic representation of the technical gaps that need to be overcome for field deployment while using a printed electrochemical sensor-based system.

In this thesis work, the research has the following objectives and key findings:

- The development of a two-dimensional Molybdenum disulfide (2D-MoS_2) nanoparticles-based flexible electrochemical sensor for the detection of copper ions in water and further used for the determination of copper ion concentration. This entails the comparison of rigid-based conventional electrochemical sensors and flexible printed sensors on the basis of fine-tuning operation with the help of an EIS study. This study also includes the selective detection of copper from other interfering heavy metal ions.

- The comparison study on utilising various electrochemical detection techniques on cobalt ions in water was demonstrated with the help of the newly developed 2D graphitic carbon nitride (2D-gC_3N_4) based electrochemical sensor. Different electrode materials, such as screen-printed carbon electrodes (SPCE) and screen-printed silver electrodes (SPSE), were investigated for detecting Fe^{2+} ions in water. The above sensor was also used to illustrate the detection of ferrous ions in water, which helps to understand the simultaneous detection between multiple analyte ions. The utilisation of g-C_3N_4 material for modifying SPCE was explored with various electrochemical techniques such as Cyclic Voltammetry (CV), Differential Pulsed Volatmmtery (DPV), and Squarewave Voltammetry (SWV) for the Co^{2+} ion detection to see how the response time and data acquisition impacted these methods.

- Mixed metal oxide nanoparticles, such as titanium dioxide and magnesium oxide, will be explored to detect the concentration of toxic heavy metal ions, such as Pb and Cd. Differential pulsed anodic stripping techniques will be compared with normal differential pulsed techniques to understand the selection of detection techniques in unique cases.

- The demonstration of a Zinc oxide (ZnO) nanoparticle-based electrochemical sensor for detecting multiple heavy metal ions concentrations such as Ag, Au, Co, and Mn. The integration of low-cost readout potentiostat will be optimised for the detection of Mn ions in water. A comparative study between the newly built readout and commercial workstation will be further explored for field deployment applications.

- A few of the field deployment complications such as repeatability, and interference ions will be studied using appropriate experiments, and their conclusions with common observations will be made. Also, the selection of materials will be discussed for various electrode materials and substrates in terms of their applications.

1.3. Structure and scope of this thesis

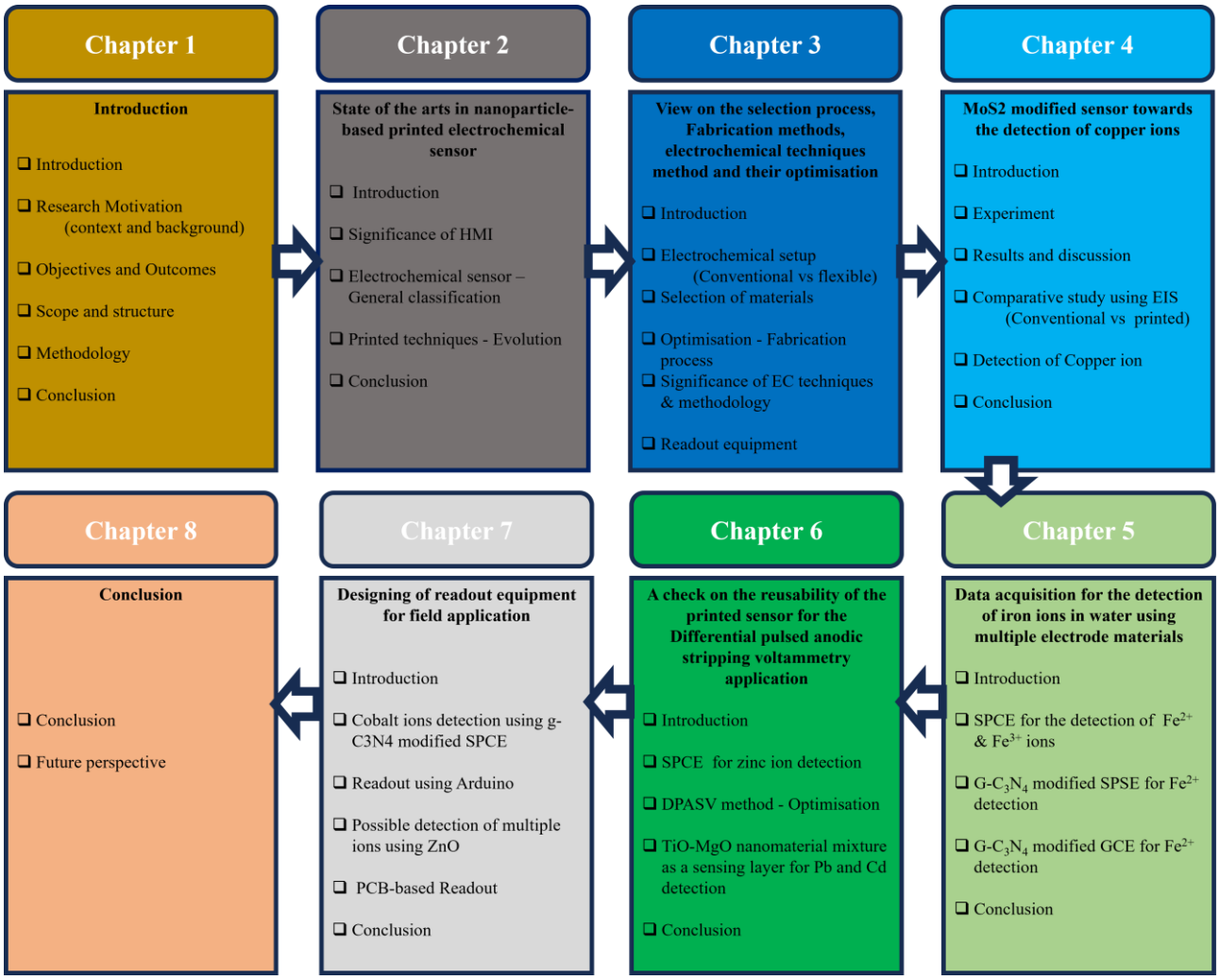

Figure 1-2 The organisation of the thesis chapters

This thesis work covers the views that were highlighted in the preceding section and was divided into seven chapters along with their reference and appendix. During the development of newly fabricated sensors for the detection and monitoring of heavy metal ions in water, several synthesis processes of nanomaterial such as MoS_2, gC_3N_4, ZnO, and TiO-MgO were included, and further, the ink formulation for each printing technique was discussed. A comparative study between several printing techniques was displayed for a brief understanding. This work also includes the development of a suitable low-cost potentiostat that was built accordingly to resonate similar laboratory-based electrochemical workstations. The selectivity and repeatability of the fabricated sensor were discussed in detail in regard to each unique sensor. It also includes a comparative study of various designs for three electrode systems where the mini portable sensor was characterised by both COMSOL simulation and EIS technique, in order to understand the sensing mechanism of the fabricated sensor. This Ph.D. work contains all the above aspects, and each chapter briefly describes its content at the beginning to give an overview of the topic covered.

The brief description of each chapter was organised in the following way.

Chapter 2 contains a detailed literature survey on the toxicity of heavy metal, which leads to the importance of the detection and monitoring purpose, a brief topic of common conventional detection methods, Various electrochemical sensor mechanisms, and the common electrochemical techniques that were commonly utilised. Here, a few sensing parameters for the characterisation methods were briefly described. The brief topic covers the already pre-existing printing methods, a detailed literature research study based on the materials available in the existing literature, and their adapted detection technique. A detailed discussion on reported readout types of equipment for field deployment was included.

The work in Chapter 3 describes my view on the selection and optimisation process that will be undertaken for the subsequent sensors. This chapter involves five portions i.e., 1) Description of the experimental setup, 2) fabrication methods, 3) Optimisation of printing parameters such as design and thickness, and 4) the methodology towards detection and characterisation, 5) Design and optimisation of integrated readout equipment printing technique. Optimisation of printing thickness for carbon-based electrodes was done for the detection of ascorbic acid in water using EIS results, which also showed affinity-based EC detection.

Chapter 4 covers the selection process of material for the development of MoS_2 nanoparticles-based flexible screen printed carbon-based electrochemical sensors, which were discussed, and a comparison study between the conventional electrochemical sensor and flexible printed sensors were explored using the EIS study. Initially, the material synthesis and characterisation technique for MoS_2 nanoparticles was mentioned. The work also includes several studies on the developed sensor such as concentration studies, accumulation studies, the effect of scan rate, interference studies, and repeatability studies.

Chapter 5 involves the detection of iron in different oxidation states, i.e., Fe^{2+} and Fe^{3+} ions in water. There are three sections: (1) The development and testing of SPCE for detecting Fe^{2+} and Fe^{3+} ions in water. (2) The development and testing of g-C_3N_4 modified SPSE and g-C_3N_4 modified Glassy Carbon Electrode (GCE), SPCE for detecting Fe^{2+} ions in water. Here, the material synthesis and their characterisation are involved. The EC-based characterisation and their testing results. This chapter includes a synthesis of g-C_3N_4 nanomaterial, and their material characterisation results, such as X-ray Diffraction (XRD), and scanning electrode microscopy (SEM). The fabricated sensor was used for the detection of iron ions in water. The Glassy carbon electrode (GCE) which is the typical conventional electrode was compared with SPCE-based electrodes. This work enables us to understand the lack of sensitivity between laboratory setup and printed electrodes for field conditions.

Chapter 6 consists of two sections: 1) mixed metal oxide-based nanomaterials assisted screen printed electrodes were used for the detection of Pb, Cd, and Zinc. Here, Differential pulse voltammetry is associated with the anodic stripping voltammetry (ASV) technique to detect the presence of such toxic analytes. Later, a comparative study between Differential pulsed anodic stripping voltammetry (DPASV) with DPV technique was executed. 2) To achieve good recovery of the used sensor, this chapter focuses on optimising the DPASV technique for several substages, such as preconditioning, deposition of ions, and post-conditioning of the sensor.

In Chapter 7, which consists of two sections, the ZnO-modified SPCE sensor was tested for the simultaneous detection of multiple heavy metal ion analytes (Ag, Au, Co, and Mn ions) in water. The designed readout is optimised for detecting Mn ions in water, and the results were further compared with those from the electrochemical workstation. This also involves the study of similar interfering heavy metal ions. The second section includes a g-C_3N_4 modified SPCE-based EC sensor for the detection of cobalt ions.

By Chapter 8, a conclusive discussion of the collective result and future aspects will be discussed for the worth investigating. To conclude, A final summary of all the above-printed sensors was presented in a brief way with insight suggestions, that were given for possible future directions.

1.4. Methodology

The methodological approach for the upcoming chapter includes

- Synthesis of desired nanoparticles and further material characterisation was done using XRD and SEM.
- Fabrication of newly printed sensors using a screen printing method.
- Characterisation of the printed sensor towards the detection of targeted analytes.
- Screen printing was done for different electrode materials, and further thickness optimisation was done using the EIS study.
- A comparative study on the designs of 3 electrode systems of a conventional setup and the printed-based sensor was done using the EIS technique.
- To find the electrochemical detection property of each sensor, an electrochemical technique such as Cyclic voltammetry (CV), DPV, and DPASV was used,
- For application purposes of monitoring, other techniques, such as Amperometry and open circuit potential (OCP), were used.
- For conducting the concentration study, the effect of scan rate, repeatability, and interference study, Both CV and DPV were used for the spiked water samples.
- For the calibration of readout equipment, results from the electrochemical workstation were used for similar detection procedures.
- Significance of preconditioning and postconditioning stages towards anodic stripping voltammetry-based detection.

[2] State of the Art in a nanoparticle-based Printed Electrochemical Sensors – A Literature Survey

Introduction

In this Chapter, the literature survey is divided into 4 sub-categories which are 1) Adverse effects of Heavy metal ions on living organisms and the environment, 2) literature studies on the electrochemical sensors that have been used for the sensing application towards heavy metal ions in water, 3) literature survey on the printed electrochemical sensors commonly used for the detection of heavy metal ions and 4) readout circuits for deploying sensors in water resources.

2.1 The significance of monitoring Heavy Metal Ions in the hydrosphere

Heavy metal element traces are fundamentally needed for the living organism as each element plays a crucial role in leading a healthy life.[40] Nowadays, heavy metal ions (HMI) are among the most serious pollutants found in water resources due to increased industrial activities.[41, 42] Because these substances are non-biodegradable, they can remain and accumulate in the air, water, and food for centuries, leading to severe health and environmental concerns.[43] As a result, identifying harmful and toxic heavy metals in drinking water has become essential and is regulated by multiple organisations. Various permissible limits for the concentration of each heavy metal have been set by both international and local government organisations including Several international organisations like the World Health Organization (WHO), the US Environmental Protection Agency (EPA), Centre for Disease Control (CDC), Joint Food and Agricultural Organization (FAO), and the European Union (EU). As lower concentrations for most of the heavy metal ions are necessary for living organisms to carry out their daily activities, there is a constant need to check their concentrations. Therefore, these permissible levels of such HMIs are in subparts per millions or billions (ppm or ppb).

2.1.1 Toxicity and human health adverse

HMIs naturally enter the food cycle chain and further reach human beings in the form of food, air, and water.[44] As shown in Figure 2-1, the impact of heavy metals can be outlined that both deficiency and overconsumption lead to several fatal health issues. The permissible levels were introduced to avoid the excess intake of such potentially toxic heavy metals daily. Unmonitored contaminated water is the major source of several health-based outbreaks in living beings, and regulatory organisations such as WHO, EPA, CDC, FAO, and the European Union have set a permissible limit for such HMI concentration. In this thesis, the detection of heavy metal ions which are focused are Cu^{2+}, Fe^{2+}, Pb^{2+}, Cd^{2+}, Co^{2+}, Au^{2+}, Ag^{2+}, and Mn^{2+}. Their negative impacts on health are discussed below.

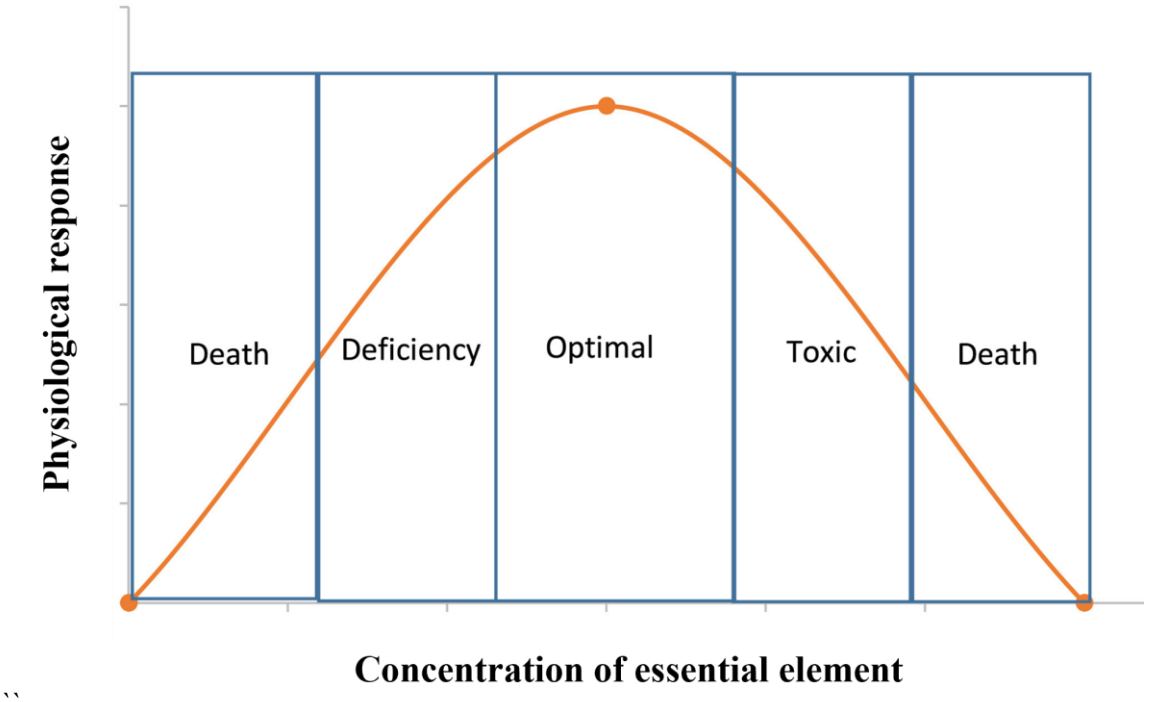

``

Figure 2-1 : Deficiency and overconsumption of heavy metal ions on Human health

Lead: The Environmental Protection Act (EPA) establishes the maximum allowable pollutant level at 15 µg/L, with oversight from the United States Environmental Protection Agency. High levels of lead consumption can damage several organs, such as the kidneys, liver, and reproductive system.[45] It can also adversely affect vital cellular functions, the central nervous system, and brain activity.[46, 47]

Zinc: Zinc is an essential and ubiquitous metal that plays a crucial role in various biological processes. The World Health Organization recommends a maximum zinc concentration of 3 mg/L in drinking water to ensure safe consumption.[48] The toxicity of zinc varies depending on how and how long of the metal one is exposed through water consumption.[49] Significant sources of zinc exposure include industrial activities such as smelting and mining. A substantial portion of zinc released into the environment comes from mineral processing activities, which can have a considerable impact on ecosystems and the organisms that inhabit them.[50] Zinc is involved in numerous enzymatic reactions by functioning as a cofactor, which is vital for the proper activity of many enzymes. Excessive zinc intake can lead to zinc toxicity, which may cause nausea, vomiting, diarrhoea, and abdominal pain in the short term. Long-term exposure to high levels of zinc can interfere with copper absorption, resulting in anaemia, immune dysfunction and neurological issues.

Iron: Iron is an essential nutrient for health, but ingestion of excessive amounts of iron in drinking water can be detrimental. The World Health Organization sets a 0.3 mg/L concentration of copper ions as a permissible limit in drinking water. Elevated concentrations of iron in drinking water can lead to gastrointestinal issues such as nausea, vomiting, and diarrhoea. Prolonged exposure to high iron levels may also result in more severe health problems, including liver damage and iron overload disorders.[44, 51] This is particularly worrisome for those with genetic disorders such as hemochromatosis, which makes them prone to iron buildup. Elevated iron

concentrations can negatively impact aquatic ecosystems by promoting the excessive growth of algae and other aquatic plants, disrupting the natural balance of these environments. When these plants die and decompose, the process consumes oxygen from the water, potentially leading to hypoxia (low oxygen levels) and harming fish and other aquatic organisms.[44, 52]

Copper: Copper is an essential micronutrient crucial for the health and functioning of living organisms. Here, WHO sets the permissible limit to 2 milligrams per liter. Copper is necessary for various physiological processes in plants, including chlorophyll synthesis, photosynthesis, and carbohydrate and protein metabolism. A lack of copper can interfere with these crucial metabolic functions, resulting in adverse effects. On the other hand, excessive copper exposure can cause toxicity, which can be detrimental to both plants and other organisms.[53-55]

Cadmium: Humans can be exposed to cadmium by consuming contaminated food, inhaling polluted air, or ingesting water containing high levels of the metal. WHO recommends a cadmium limit of 3 micrograms per Liter in drinking water. Cadmium can enter the atmosphere through both natural processes and human activities, leading to exposure for animals and humans in various ways. In aquatic ecosystems, cadmium pollution originates from sources like absorption, industrial discharges, and surface runoff, leading to its accumulation in soil and sediments. Cadmium is not advantageous for plant growth or metabolic functions and does not play a positive role in these processes.[56-58]

Cobalt: Cobalt is abundantly found in the environment, including plants, soils, rocks, and water, and is frequently utilised in alloy production. Although its discharge rate is relatively low, cobalt still poses considerable health risks. While small amounts of cobalt can be beneficial and generally do not cause harm, excessive releases into the environment can be extremely dangerous and potentially fatal, affecting the lungs, heart, and thyroid. The World Health Organization (WHO) has not set a specific cobalt limit for drinking water.[59, 60]

Gold: Gold is generally regarded as non-toxic and is commonly used in various medical applications and devices. However, gold ions, particularly at higher concentrations, can be harmful. Drinking water with elevated levels of gold ions may lead to gastrointestinal symptoms such as nausea, vomiting, and stomach pain. Extended exposure or high doses might cause more severe health issues, including kidney damage or systemic toxicity, though such instances are rare. Increased gold ion levels in aquatic environments can disrupt ecosystems. Gold ions can impair the health and growth of aquatic plants and animals, and in high concentrations, they can be toxic to fish and other wildlife, potentially causing developmental problems or death. Additionally, gold ions can interfere with natural biochemical processes, leading to imbalances in aquatic ecosystems. Gold ions in water can impact its visual quality. While gold generally does not significantly impact taste or colour, higher concentrations can lead to discolouration or reduced clarity, which may influence the water's suitability for drinking or recreational purposes. The World Health Organisation and other regulatory bodies have not specified an official permissible limit for gold in drinking water, as gold is not typically present at harmful levels in natural water sources. Gold is generally considered low toxicity, and

concerns about its safety mainly arise in industrial or medical contexts rather than environmental exposure through drinking water.[61, 62]

Silver: WHO has set the permissible limit as 0.1 mg/L for the silver content in drinking water. Silver in water can become toxic to humans, especially at higher concentrations. Although small amounts are generally harmless, prolonged exposure or high levels of silver can result in several health concerns. Here's an overview of how silver in water can affect human health. Health Effects of overdosage of Silver in Water include Gastrointestinal Issues, Kidney and Liver Damage, and Neurological effects, Skin and Eye Irritation.

Manganese: Manganese is an important trace element for human health, but when present in high concentrations in drinking water, it can become toxic and lead to various health issues, including neurological damage, cognitive and developmental impairments, and gastrointestinal problems. Elevated levels of manganese can adversely impact aquatic ecosystems. The World Health Organization (WHO) has established a guideline value of 0.4 mg/L for manganese in drinking water. High concentrations may disrupt the growth and reproduction of fish and other aquatic organisms, potentially resulting in population declines. While small amounts of manganese are beneficial, excessive levels in drinking water can result in serious health issues, particularly affecting neurological and cognitive functions. Monitoring manganese levels in water is crucial to avoid toxicity and safeguard public health.[63, 64]. The main drinking-water guideline or regulatory limits for the metal ions considered in this work are summarised in Table 2-1.

Table 2-1. Regulatory / guideline concentration limits for the metals studied in this thesis.

Analyte (ion)	**Typical limit in drinking water**	**Units**	**Main regulation / guideline and notes**
Copper (Cu^{2+})	2.0	mg L^{-1}	Health-based guideline value in WHO *Guidelines for Drinking-Water Quality*, 4th ed. (support.esdat.net) and parametric value in the EU Drinking Water Directive 98/83/EC. (lenntech.com)
Iron (Fe^{2+}/Fe^{3+})	0.2	mg L^{-1}	Indicator parameter in the EU Drinking Water Directive (aesthetic/operational limit rather than a health-based value). (lenntech.com)
Zinc (Zn^{2+})	≈3 (aesthetic threshold)	mg L^{-1}	WHO does not set a health-based guideline value for zinc; concentrations above ~3 mg L^{-1} may cause unacceptable taste and appearance. (World Health Organization)
Lead (Pb^{2+})	0.01 (10)	mg L^{-1} (µg L^{-1})	Health-based guideline value of 0.01 mg L^{-1} in WHO *Guidelines for Drinking-Water Quality* (support.esdat.net) and parametric value in the EU Drinking Water Directive. (lenntech.com)

Cadmium (Cd^{2+})	0.003 (3)	mg L^{-1} (µg L^{-1})	Health-based guideline value in WHO *Guidelines for Drinking-Water Quality*; (support.esdat.net) EU parametric value is slightly higher at 0.005 mg L^{-1}. (drinking-water-testing.co.uk)
Cobalt (Co^{2+})	–	–	No WHO guideline value and no parametric value in the EU Drinking Water Directive; cobalt is generally not regulated specifically in drinking-water at international level. (dwqr.scot)
Silver (Ag^{+})	0.1	mg L^{-1}	WHO has not set a general health-based guideline, but a provisional reference value of ~0.1 mg L^{-1} has been proposed in the context of silver–copper disinfection systems. (World Health Organization)
Gold (Au^{3+})	–	–	No specific guideline value is given for gold in the WHO *Guidelines for Drinking-Water Quality* or in the EU Drinking Water Directive, reflecting its very low expected concentrations in drinking water. (World Health Organization)
Manganese (Mn^{2+})	0.05	mg L^{-1}	Indicator parameter (0.05 mg L^{-1}) in the EU Drinking Water Directive. (lenntech.com) WHO previously proposed a health-based value of 0.4 mg L^{-1} for manganese but later discontinued a formal guideline because typical concentrations are much lower. (Europe PMC)

2.1.2 Sensing technologies for Detection and Monitoring Heavy metal ions in water:

Existing water quality monitoring sensing technologies:

Apart from recent fascinating research on electrochemical sensing methods, conventional sensing techniques for heavy metal ion detection in water quality monitoring applications were divided into two major categories: spectroscopy methods and optical methods.[65-67] Most highly sensitive conventional spectroscopy methods, such as atomic absorption spectroscopy, atomic emission spectroscopy, inductively coupled plasma mass spectrometry, and cold vapour atomic fluorescence spectrometry, generally require a pretreatment laboratory condition. This condition lacks continuous operation in field conditions and is not easily transportable. This sensing equipment is expensive (on average, the cost of laboratory-based techniques for analysing heavy metals per sample ranges from £16 to £80) and requires regular maintenance.[68] Conventional Optical methods such as absorption, reflection, or luminescence spectrometry, or with the help of dye indicators, optical fibres, integrated optics, and capillary-type devices, also result in high maintenance and require expensive

instrumentation. The precision hugely demands laboratory conditions as it is a bit challenging to operate in field conditions. In contrast to conventional techniques, electrochemical sensors are known for their advantages traits in terms of portability, real-time monitoring, quick responses, sensitivity and selectivity, low power consumption, and cost-effectiveness, making them a suitable alternative for real-time monitoring applications. Figure 2-2 shows the detection range of existing conventional analysing technologies and electrochemical-based techniques.

Currently, the accurate dosage level of heavy metal ions can be identified from several instrumental analysis methods, including X-ray fluorescence spectroscopy (XRF), ultraviolet-visible spectrophotometry (UV), atomic absorption spectroscopy (AAS) and inductively coupled plasma mass spectrometry (ICP-MS). It provides a lower detection limit in the range of femtomolar and can simultaneously detect multiple heavy metal ions in various complex matrices. Nevertheless, sophisticated treatment procedures by professional operators with high costs are required in the above methods. Also, the storage and handling of samples lead to changes in the sample's composition, which leads to risk. Moreover, multiple samples are required to perform these difficult analytical procedures.[69, 70] Most optical methods require high-precision fabrication methods, complex equipment such as lasers, etc., and high-power operations, and therefore, they are not suited for performing infield measurements.

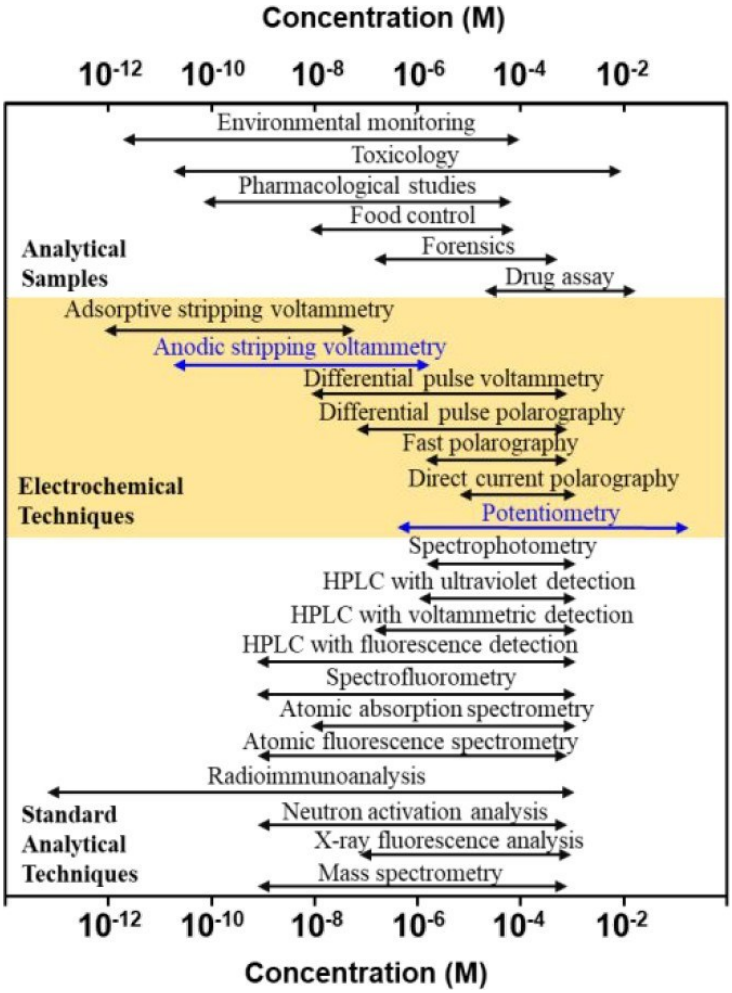

Figure 2-2 : Common detection range of various sensing technologies.

On the contrary, electrochemical techniques can be carried out in a more friendly and economical way and most importantly it is well suited to in-field applications as discussed in Table 2-1. They provide a considerably better detection range with the lower limit of detection in ppm and ppb concentration levels. The quicker response time and selective nature of the electrochemical sensor have provided impeccable opportunities for immediate in-field testing and measurement of individual HMI targets. It also helps in individually identifying various oxidation state natures of heavy metal ions. Compared to the other detection methods, simple fabrication procedures allow for the design or/and improvement of the sensing performance, which can also allow for a short analytical time in more reliable on-field testing. [66] The electrochemical detection toolkit is a quicker and more reliable determination method in infield conditions, and it can be easily integrated with Internet of Things (IoT)- based devices. It provides cost-effective equipment, simpler fabrication, and an analytical procedure.

Table 2-2: Instrumentation cost of sensing technologies available for the detection of heavy metal ions in water.

Conventional methods	**Various methods**	**Instrumentation approximate cost (Price range)**	**Field Deployable**
Spectroscopy methods	Atomic Absorption Spectroscopy (AAS)	3000-6500 USD	N
	Atomic Emission Spectroscopy (AES)	10000-50000 USD	N
	Inductively Coupled Plasma Mass Spectrometry (ICP-MS)	50000-500000 USD	N
	Cold Vapor Atomic Fluorescence Spectrometry	4500-35000 USD	N
Optical methods	Fluorescence Spectroscopy	3800-10000 USD	N
	Colorimetric Spectroscopy	Around 1500 USD	N
	Raman Spectroscopy	Around 12000 USD	Y
	Chemiluminescence Spectroscopy	20000-100000 USD	N
	Infrared Spectroscopy	15000-20000 USD	N
	Refractive Index Spectroscopy Sensing	Around 9500 USD	N
Electrochemical methods	Conventional electrochemical	10000-15000 USD (EC workstation)	N
	Mini-Portable potentiostat	Starts 1500 USD	Y (but requires a specialised sensor)
	Printed sensor with our readout potentiostat equipment	Less than 150 GBP	Y (our sensor)

2.2 Electrochemical sensors in the field of water quality monitoring

This section provides general content on the electrochemical sensing mechanism, various methods of detection used in this electrochemical sector, and collective literature studies on reported electrochemical-based research articles. Figure 2-3 shows the idea of the work, represented by the red line to show the aspects where this thesis focuses.

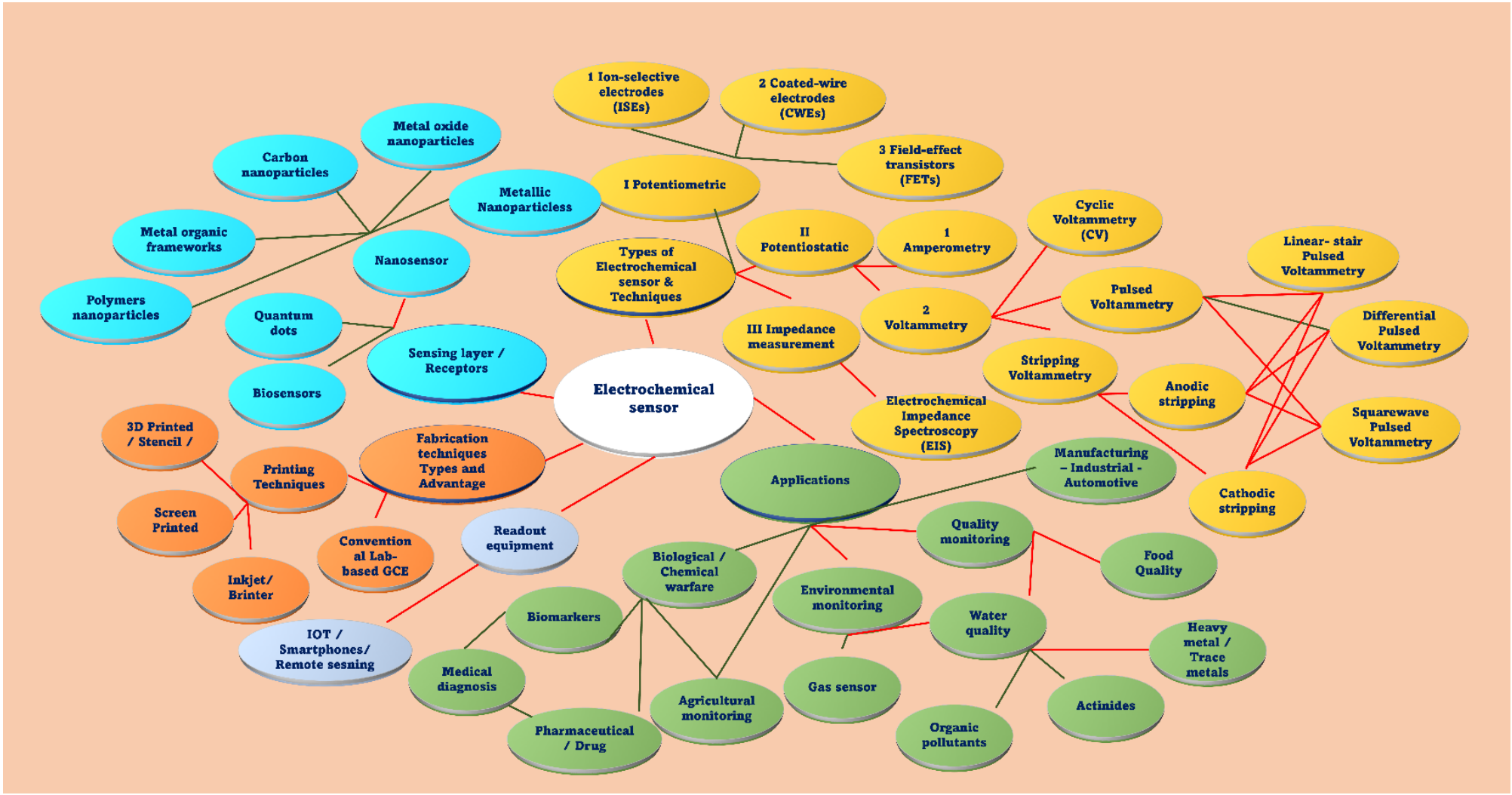

Figure 2-3 : Overview of various aspects of electrochemical sensing in this thesis.

2.2.1 General sensing mechanism of electrochemical sensor

Electrochemical sensing relies on the interaction between an analyte and an electrode within an electrochemical cell, where redox (oxidation-reduction) reactions produce a measurable signal. An electrochemical cell generally consists of a working electrode (WE), a reference electrode (RE), a counter electrode (CE), and an electrolyte. The working electrode is where the analyte undergoes electrochemical interaction, the reference electrode maintains a stable potential, and the counter electrode completes the circuit by allowing current to flow. The electrolyte is a conductive solution that facilitates ion movement between electrodes to support electrochemical reactions.[48, 71]

Electrochemical sensing can be based on faradaic or non-faradaic processes. In faradaic processes, the analyte participates in oxidation or reduction reactions that involve direct electron transfer between the analyte and the electrode. The current generated is proportional to the analyte concentration, enabling quantitative analysis. In contrast, non-faradaic processes do not involve electron transfer but rather involve changes in the electrical double layer, such as capacitive charging, where the analyte's presence influences the electrode's surface properties without undergoing redox reactions. In the current setup, an aqueous solution containing heavy metal ions (HMIs) serves as the electrolyte. The cell potential is measured at the interface between the electrode and the electrolyte solution. While multiple half-reactions may occur, the primary electrochemical event typically takes place at the working electrode.[72-75]

Here, the resulting interaction (change in current, potential or frequency) can be measured using various electrochemical techniques. Then, these data can be interpreted further for calibration and quantification to determine the concentrations of the targeted analytes. In the first stage, the sensor's response is typically calibrated with known concentrations of the analyte to establish a correlation between the measured signal and the analyte concentration. the collected signal data is analysed to determine the analyte concentration using the calibration curve or applying relevant mathematical models. For the second stage of using sensors in the field, The raw signal is refined to eliminate noise and improve accuracy. Advanced signal processing methods may extract significant information from the measurements. Finally, the processed data is presented or reported in an easily understandable format, offering details on the analyte concentration or other pertinent parameters.[76, 77]

2.2.2 Electrochemical Technique Methods

The general electrochemical cell comprises a delicate electrode, an electrolyte, and electronic circuitry that manages the current flow or the potential between the electrodes. In standard electrochemical techniques, a specific analyte is analysed by monitoring either the current or the potential within this setup. At the same time, the electronic circuitry regulates the other parameters. For instance, a galvanostat is employed to control the current flow in the electrochemical system, whereas a potentiostat is used to regulate the potential applied across the electrodes. Since it is impossible to maintain both current and potential simultaneously, this principle underpins two main measurement techniques: potentiostatic and galvanostatic. Additionally, some techniques do not involve control signals. Electrochemical techniques based on interfacial processes can be categorised into static and dynamic conditions. In static conditions, no current flows through the cell (i=0), and therefore,

only non-faradaic processes occur, as there is no alteration in the concentration of the chemical species within the cell. In potentiometry, a potentiometer measures the potential with zero current flow. In contrast, dynamic conditions involve varying current flow ($i \neq 0$), leading to faradaic processes where the concentration of species changes due to electrochemical reactions.[1] Figures 2-4 show the classification of electrochemical-based techniques that were widely used in detection applications.

2.2.2.1 Potentiometric sensor

Potentiometric ion sensor or Ion selective sensor (ISE) is known for its long-term online or onsite water quality monitoring application and its excellent selectivity as it tends to avoid the negative effect of other interfering analyte ions. Under the static condition of no current flow within the cell, the concentration of analyte species remains fixed, and here, the potentiometer is used to determine the concentration of the selective analyte by measuring the potential of the electrochemical cell. The working electrode is often modified with either inorganic, organic, or polymeric membrane, etc, for appropriate selectivity. Even under modification of electrodes, ISE doesn't exhibit much of a lower detection range. It also usually takes a long time (a slow response) to detect heavy metal ions.[78, 79]

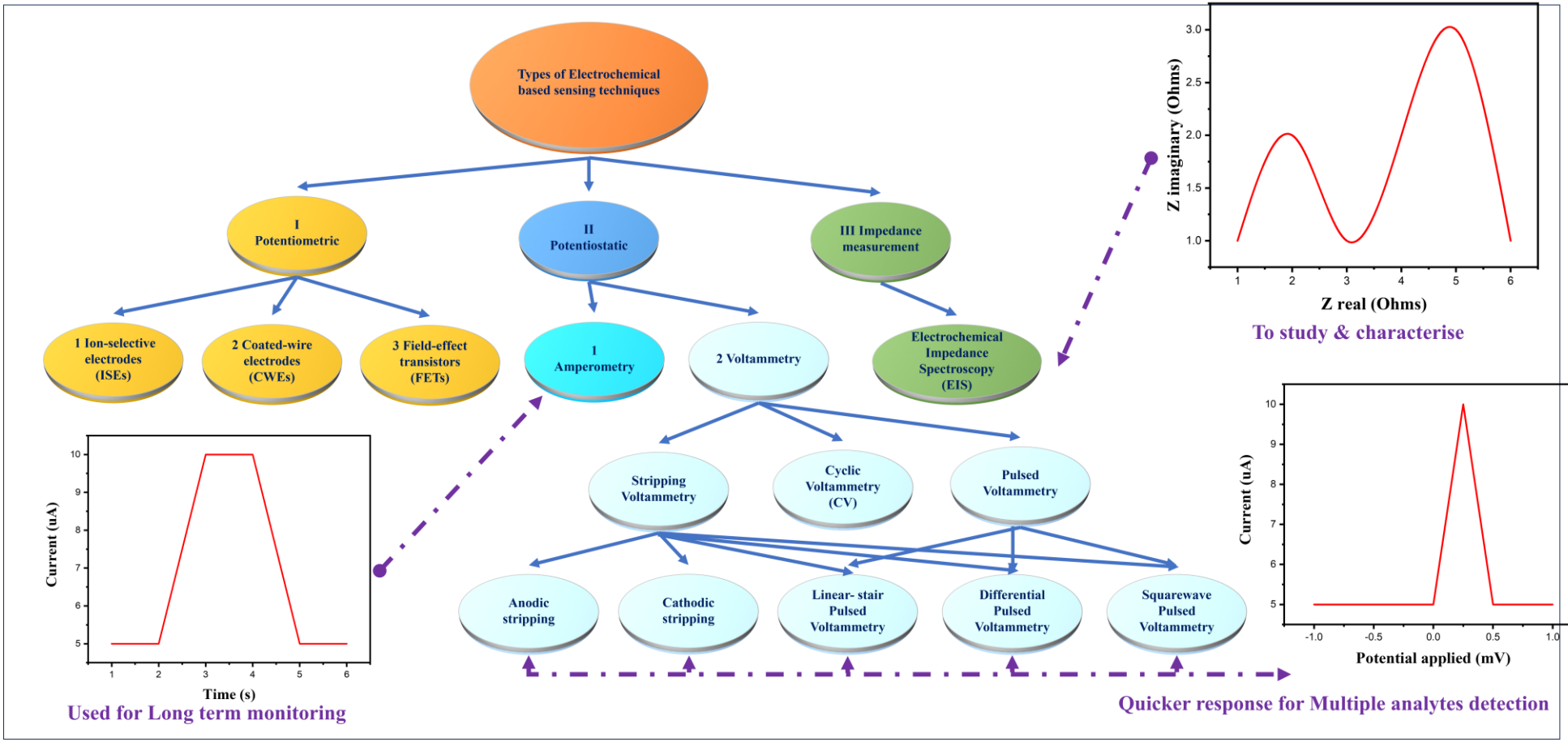

Figure 2-4 Various techniques involved in electrochemical detection

2.2.2.2 Potentiostatic sensor

The potentiostat instrument controls the potential difference between the working and the counter electrode by applying a potential between the counter and the reference electrode. The resultant flow of current within the electrochemical cell setup is recorded and further analysed to predict the concentration of the electroactive species. Based on the applied input voltage signal and recorded output current waveform, the potentiostatic technique can be further categorised into 1) Amperometric and 2)Voltammetric or polarographic.

AMPEROMETRY TECHNIQUE

In the amperometric technique, the potential difference between the electrodes is fixed constant voltage, and the current response of the resultant is measured as a function of time. Here, the polarity and the magnitude of the controlled applied potential, i.e., fixed voltage, are carefully chosen according to the particular oxidation or reduction potential of an electrochemical analyte species. However, due to the small surface area of the sensing electrode, only a fraction of analyte species undergo electrochemical oxidation or reduction over the electrode surface, leading to a very small change in current caused by the incomplete faradaic process. This leads to uncertainty and less reproducibility. The Chronoamperometry technique was one of the amperometry techniques where a step potential is applied to the working electrode, and the resultant current is measured as a function of a shorter time scale, usually in micro or milliseconds.[80, 81]

VOLTAMMETRY OR POLAROGRAPHY

Several forms of voltammetry differ in the type of varying potential applied to the indicator electrode. Polarography is voltammetry in which the indicator electrode is made of mercury or, rarely, another liquid metal. In classic polarography, mercury drops from a capillary tube. The surface of the mercury drop is the site of the electrochemical reaction with the analyte. How the direct-current (DC) potential of the indicator electrode varies with time is a potential (or voltage) ramp.

Voltammetry is the most used technique for applying the varying potential, and their current response is recorded in multiple waveforms.[82] In contrast to the amperometry technique, the varying potential points help determine multiple analytes, especially in the case of heavy metal ions. In addition to precise quantitative analyses, voltammetry shows qualitative knowledge, such as the reversibility of electrochemical reactions. In Linear sweep voltammetry, the potential difference applied between the reference electrode and the working electrode is linearly swept with time, and the generated current is measured as a function of both potential and time. Cyclic voltammetry is a double potential step where the potential scan is reversed, and the current response is recorded. CV provides excellent qualitative information such as redox potentials, reaction rate, and interactions of the electroactive species within the cell setup but has poor selectivity due to a non-faradaic background current. Pulsed voltammetry is a technique where a pulse of the applied voltage is given to the ramping voltage to obtain different recorded current waveforms while suppressing the background current caused by a non-faradaic process. Normal pulsed voltammetry applies a pulsed voltage to the linear swept with a fixed ramp voltage at regular intervals. Along with Square wave pulsed voltammetry, Differential pulsed voltammetry (DPV) is the widely used pulsed technique where sequential voltages with fixed amplitude are applied to the ramping potential and the differential between the measured current at two points, i.e.., before

and after the pulse is recorded and plotted against base potential. This subtraction method reduces the non-faradaic component by providing a delay after each pulse. Due to the reduction of non-faradic background current, the concentration of the electroactive analytes is directly related to the peak current observed from the response current waveform, which has a low response time due to the delay period. SWV is quite similar to the DPV technique, where a symmetrical square wave potential is applied to the ramping voltage swept, which leads to a staircase-type potential step. Here, the recorded current is formed at subtraction of the forward current to the reverse current and further plotted against the function of both potential and time. Compared to the DPV technique, the SQW technique is quite sensitive as the delay is caused by running a reverse cycle, which results in rapid response time.

Stripping voltammetry is a two-step process where the first step involves the electrodeposition of electroactive species onto the electrode surface by the interaction of either oxidised or reduced targeted heavy metal ions, and later, the second step involves the stripping process where the release of electroactive species. Here, parameters such as deposition time, electrode material and the deposition time are controlled as desired and fixed further for each determination process. Depending on the polarity of the potential scan for the electrodeposition process via electrolysis caused by potential voltage, they are classified as cathodic or anodic stripping voltammetry. Adsorptive Stripping Voltammetry (AdSV) is one form of commonly used stripping voltammetry where the physical absorption, i.e.., formation of the metal complex(es), causes the first step instead of electrolysis-based precondition over the electrode surface. In addition to the use of various waveforms, the stripping technique is further categorized into differential pulse anodic stripping voltammetry (DPASV), square wave anodic stripping voltammetry (SWASV), and linear sweep anodic stripping voltammetry (LSASV).

STRIPPING TECHNIQUE FOR METALS (M)

For heavy metals, the stripping mechanism that occurs at the electrode surface is deposition. When nanomaterials are used as sensing materials (both conductive and non-conductive), the stripping behaviours of heavy metal ions can be depicted using an adsorption-release model. In the first stage, heavy metal ions (M^{2+}) in water are first adsorbed onto the surfaces of the nanomaterials, and then M^{2+} ions desorb and diffuse to the electrode surface because of the concentration gradient. When deposition potential is applied, M^{2+} ions are reduced on the electrode surface ($M^{2+} + 2e \rightarrow M^{0}$). Subsequent scanning potential is applied, M^{0} is reoxidized to M^{2+} ($M^{0} - 2e \rightarrow M^{2+}$), and the stripping current signal is observed.[83]

2.2.2.3 Galvanostatic techniques

In Galvanostatic techniques, the current is controlled between the working and counter electrode using a simple galvanostat instrument, and the changing potential within the electrochemical cell setup is measured across the reference and working electrode to determine the quantitative number of electroactive species. Here, no feedback is needed from the reference electrode; thus, a simpler instrument is utilised compared to the potentiostat techniques. However, due to the charging effect caused by double-layer formation, this technique suffers from precision and lacks selectivity. This technique includes current reversal chronopotentiometry

(CRC) and Cyclic chronopotentiometry. Mainly applied technique for heavy metal ion detection is galvanostatic stripping chronopotentiometry (SCP)

2.2.2.4 Chronocoulometric technique (or controlled potential coulometric):

The Chronocoulometric technique is quite like the amperometric technique, where the larger surface area-based electrodes are used instead of the smaller electrodes, and the measured current response is a result of the quantitative reaction of the electroactive analyte species at the electrode caused due to exhaustive prolonged electrolysis. On Controlled potential coulometry, a fixed potential is applied at the working electrode and the current is measured until the analyte species' complete electrolysis (~ 100 %), i.e., either oxidation or reduction, occurs. As the electrolysis occurs, the analyte's current and concentration reduce, and this resultant current vs time profile gives the total amount of charge passes. It is most often used to understand the total extent of absorption of the analyte species at the electrode surface. Even though this technique has high accuracy and is even simpler to perform electrochemical analysis, it was not widely used due to the requirement of high current efficiency.[84]

2.2.2.5 Electrochemical Impedance Spectroscopy

EIS is one of the most powerful techniques for understanding the interaction between electrode-electrolyte interfaces, especially when multiple layers of films are involved. Here, a small sinusoidal voltage was applied to the working electrode, and the corresponding impedance was measured over an appropriate frequency range corresponding to the interaction between the electrode/electrolyte interface. To understand the interfacial properties between each interface, an electrical equivalent circuit (EEC) was used to represent the electrochemical reaction within the electrolytic cell. Here, an electrical equivalent circuit (EEC) is defined by the model of combined resistors and capacitors fitted to characterise the measured impedance spectrum. Here, the concentration of reactive HMI species can be predicted by determining the resistive-capacitive parameters of EEC through a frequency response analyser (FRA). Unlike other techniques, EIS can give insights regarding both faradaic and non-faradaic components as the current flow over electroactive species, caused by an electrochemical reaction that occurs with the electrolytic cell, generates charge transfer over the electrified interface. In addition, by obtaining the impedance spectrum over varying frequencies, phenomena such as ion exchange, charge transfer, adsorption, and diffusion of the electroactive species at the electrode-electrolyte interface can also be easily predicted.[85, 86]

2.2.3 Literature survey for HMI detection

In water, potentially toxic elements (PTEs) are widespread environmental contaminants with significant risks to health and the environment. Effective detection and monitoring of these elements are essential for safeguarding public health and environmental safety. Traditionally, detecting PTEs involves complex and time-consuming methods requiring sophisticated instrumentation and high operational skill, which can complicate field analysis. Printed electrochemical sensors have emerged as promising alternatives for the rapid, sensitive, and cost-effective detection of PTE ions. These sensors are notable for their high sensitivity, quick response times, low detection limits, and excellent reproducibility. The miniaturisation and integration

of these sensors with portable devices allow for on-site, real-time monitoring of PTE ions in various environmental samples, including water, soil, and biological fluids.

Over the last ten years, there has been a significant and growing interest in electrochemical sensors for detecting heavy metal ions, as clearly illustrated in the Figure 2-5. Here, the Publication trends over the past decade related to electrochemical detection of heavy metal ions, based on data from Scopus (keywords: electrochemical detection of heavy metal ion). [202]

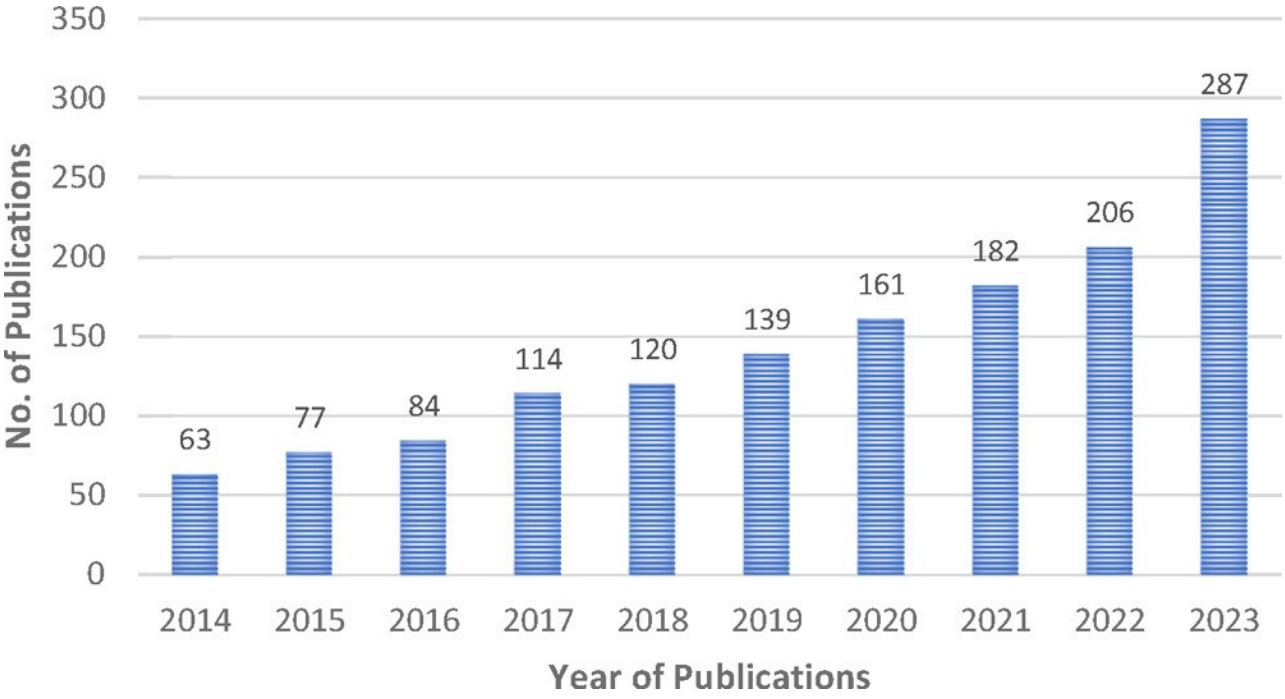

Figure 2-5 : Research articles in the field of heavy metal ion detection using electrochemical sensors that were published in years

Table 2-2. List of reported electrochemical sensors for the application of detection of Al3+ ions. *Here, the Abbreviation for the list of electrochemical techniques used as follows:* Ion selective electrode (ISE), Cathodic stripping voltammetry (CSV), Adsorptive cathodic stripping voltammetry (AdCSV), Differential pulsed stripping voltammetry (DPSV), Differential pulse adsorptive stripping voltammetry (DPAdSV), Fast scan differential pulse voltammetry (FSDPV), Linear scan voltammetry (LSV), Square-wave adsorptive stripping voltammetry (SWAdSV), flow injection analysis (FIA), anodic stripping voltammetry (ASV), Differential pulsed cathodic stripping voltammetry (DPCSV), Differential pulsed anodic stripping voltammetry (DPASV), Electrochemical Measurement of Multivalent Cations Concentration (EM2C2), Multiple Square-Wave Voltammetry (MSWV); . *Abbreviation for the list of chemicals used for the sensing layer*: Sol-Gel-Au nanoparticle (SGAuNP), 1,2-dihydroxyanthraquinone-3-sulphonic acid (DASA), Carbon paste electrode (CPE), ethylenediaminetetraacetic acid (EDTA), rotating disk electrode (RDE), carbon paste electrode (CPE), ion-exchange voltammetry (IEV)

Sensing layer (working electrode)	*Detection method*	*Targeted analyte/ Sample matrix / electrolyte*	*Performance (LOD/Detection range)*	*Reference (DOI)*
MDE	CSV	Fe(II)	$1*10^{-7}$ M	-
Bi/Fe_2O_3/G/GCE	CV, DPASV	Zn^{2+},	0.11 µg L^{-1}, 0.08 µg L^{-1}, 0.07 µg L^{-1}.	[87]
rGO@CNT@Fe_2O_3/polypyrrole nanocomposite	CV, SWASV	Cd^{2+},	0.1 nM	[88]
Fe_3O_4 nanoparticles	SWASV	Pb^{2+}.	0.119 µM	[89]
Fe_3O_4@Au	CV, DPV	Pb^{2+}	59 nmol/L	[90]
Fe_3O_4–RGO	CV,EIS, SWASV	Pb^{2+}	0.056 µM	[91]
spherical, rod and band Fe_3O_4/rGO nanocomposites	CV, EIS	Ag^{+}		[92]
amine-Fe_3O_4 modified glassy carbon	CV,EIS, SWASV	Cd^{2+}	0.15 µM	[93]
PDA@Fe_3O_4/magnetic GCE	SWASV	Pb(II)	0.0029	[94]
Terephthalic acid (TA)/ Iron oxide (Fe_3O_4)	Square wave anodic stripping voltammetry (SWASV)	Pb (II)	0.04, and 0.2 µM for Pb(II), and Cd(II), respectively	[95]
Glutathione-functionalized magnetic nanocomposite (GSH@Fe_3O_4)	AS	Pb^{2+} and Cd^{2+}	0.182 µg/L and 0.172 µg/L	[96]
monodisperse Fe_3O_4-chitosan nanoparticles	square wave anodic stripping voltammetry (SWASV)	Pb(II) and Cd(II)	0.0422 µM	[97]
Fe_3O_4@SDX G-150	LSV	Pb^{2+} and Cd^{2+}	0.52 µg/L	[98]
$MnFe_2O_4$/ GCE	SWASV	Pb^{2+}	0.054 µM	[99]
$MnFe_2O_4$/GO GCE	SWASV	Cr(VI)	0.0883	[100]
novel L-cysteine functionalized mesoporous $MnFe_2O_4$ hybrid nanospheres ($MnFe_2O_4$@Cys)	SWASV	Pb II	0.083	[101]
$CoFe_2O_4$/Bi nanocomposite	SWASV	Pb(II)	1.51 ppb	[102]
Co_3O_4 nanocubes/SPCE	DPV	Pb(II), Cu(II) and Cd(II)	0.92 ppb	[103]
Co_3O_4 nanoplates & nanocrystals	SWASV	Pb^{2+} and Cd^{2+}	0.12 nM and 0.16 nM	[104]
CoO – Exfoliated graphite	SWASV	Pb^{2+}, Cu^{2+}	94 µg/L	[105]
Co:ZnO/RGO/GCE	DPV EIS CV	Pb^{2+}	0.94 µg/L 0.83 µg/L	[106]
core-ring structured $NiCo_2O_4$ nanoplatelets	SWASV	Cu^{2+}	29.2 nM 40 nM 29.5 nM	[107]
Lance-shaped SnO_2/GCE	SWASV	Cd^{2+} Pb^{2+}	0.017 µM 0.023 µM	[108]
SnO_2 quantum dots	CV,EIS, AMPEROMETRY	Pb(II), Cd(II), Cu(II)	0.5 ppm	[109]

SnO_2/reduced graphene oxide nanocomposite modified GCE	CV, EIS, SWASV	Pb(II)	$1.015*10^{-10}$ M, $1.839*10^{10}$ M, $2.269*10^{10}$ M	[110]
F@SnO_2/T/RGO, Cl@SnO_2/T/RGO and I@SnO_2/T/RGO	CV	Cd(II)	0.3 nM	[111]
triton X-100 functionalized SnO_2 nanoparticles	DPV,CV	Cd+2	0.0084 nM	[112]
NH_2/SnO_2-RTIL nanocomposite modified GCE.	SWASV	Cd(II), Pb(II), Cu(II)	0.0054 µM	[113]
graphene/CeO2	DPASV	Cu (II)	0.1944,0.1057, 0.1636	[114]
CeO_2–MWNTs–$EMIMBF_4$ modified GCE	DPV	Cd^{+2}	5.0×10^{-9} M	[115]
CeO_2-MWCNT	DPV	Cd(II)	3.53 µg/L 1.10 µg/L	[116]
r-CeO_2/EG	DPV	Cd(II),Pb(II),Cu(II)	0.39 and 0.21 µg/L	[117]
Ce-CNFs modified glassy carbon electrode	CV,DPV	Pb^{2+}	0.6 ppb and 0.3 ppb	[118]
$CeFe_2O_5$/GCE	SWASV	Pb Cu	0.94 nM	[119]
Bi/CeO_2/rGO/FTO	DPASV	Cd^{2+} and Pb^{2+}	0.00045 uM	[120]
rGO/CeO_2/FTO nanoribbons	DPASV	Pb (II) and Cu (II)	0.35 µg/L 0.04 µg/L	[121]
Porous structured Cerium Oxide/Zinc Oxide fabricated on aluminium foil substrate	DPV	Cd(II)	14.7 nM	[122]
ZnO@G	SWASV	Pb^{2+}	0.6 and 0.8 µg/L	[123]
ZnO-RGO/GCE	SWASV	Cd^{2+}	4.8 × 10–10 M	[124]
Ag–ZnO Nps modified glassy carbon electrode	DPASV	Pb^{2+}	3.5 and 3.8 nM	[125]
CGE/ZnO_Lcys	SWASV	Pb	0.397 µg/L	[126]
ZnO QDs /Nafion/Au electrode	LSV and chronoamperometry	Cd^{2+} and Pb^{2+}	5 ppb	[127]
ZnO-NP/CPE	Cv,swv	Pb^{2+}	4.2 nM,	[128]
CA/ZnO NC/GCE	SWV	lead and cadmium	0.41 µM	[129]
ZnO@MWCNT/GCE)	CV,DPV	Pb2+	2.38 µM	[130]
ZnO/RGO/GCE	SWASV	Mercury	0.04 µM, 0.03 µM 0.03 µM,	[131]
Fe_2O_3NPs/ZnONRs/ITO	SWASV	Cd (II)	0.01 µM	[132]
ZnO/Nafion/Au electrode	chronoamperometry	Cd(II)	4 ppb	[133]
TiO_2 nanoparticle modified gold strip electrode	LSV	Pb(II)	10 µg/L	[134]
Au–TiO_2–FH	EIS	Cu(II), Cd(II), Pb(II)	4.29 pM	[135]
Fe_3O_4@TiO_2@NG@Au@ETBD/GCE	SWV	Pb	0.00075 nmol/L	

TiO_2/ZrO_2 carbon paste composite electrode	CV, SWASV	Cd	7.6×10−6 M 1.1×10−5 M	[136]
TiO_2NPs-APTE-CPE	DPV	As(iii)	2.0 × 10−9	[137]
HA−TiO_2 NP	DPV	Cu^{2+}	0.98 µM	[138]
PEDOT/B-TiO_2 PProDOT/B-TiO_2	DPV	Pb(II)	0.00087 µM, 0.00186 μM;	[139]
MgO nanoflowers	DPV	Pb and Cd	4.35 × 10−4; 7.21 × 10−3 ppb	[140]
aminotetrazole functionalized MgO–SiO_2 (MSNT) nanocomposites	square wave anodic stripping voltammetry (SWASV)	CdII	0.019 µM	[141]
MgO nanoflower-modified glassy carbon electrode	square wave anodic stripping voltammetry	$Pb^{2+,}$ Cd(II)	4.35 × 10−4 ppb 7.21 × 10−3 ppb	[140]
$MgSiO_3$/Nafion electrode	Square wave anodic stripping voltammetry (SWASV)	Cd^{2+},Pb^{2+}	0.186 nM, 0.247 nM, 0.169 nM	[142]
Zr/ZrO_2/GCE	DPV	Pb(ii); Cd(ii)	5 × 10−8, 4 × 10−8	[143]

From the summary in Table 2-2, various electrochemical techniques were explored for solid rigid electrode materials and flexible-based printed sensors, such as Glassy carbon and Pt wire. Flexible, robust printed materials, such as diamond paste, carbon paste, etc., are used. This provides various choices, and exploring nanomaterials will enhance sensor performance. These include glassy carbon, graphite, graphene, and carbon nanotubes. Known for their chemical stability and conductivity, carbon-based electrodes can be readily modified with nanoparticles, polymers, or biomolecules to enhance functionality. Common anodic stripping voltammetry (ASV) choices include gold, platinum, and mercury. Gold electrodes, in particular, show a strong affinity for binding heavy metals such as arsenic and mercury. To increase sensitivity and selectivity, electrodes are often modified with metal nanoparticles (such as gold, silver, and platinum), metal oxides, or conductive polymers like polyaniline and polypyrrole. For instance, gold nanoparticles boost the surface area and available binding sites for metal ions, enhancing sensitivity. Alloys like Au-Pd or Ag-Au elevate electrocatalytic efficiency and ensure stability. Nanomaterials like metal nanoparticles, carbon nanotubes, graphene, and metal-organic frameworks (MOFs) are frequently used in sensor development. Gold, silver, and platinum nanoparticles increase sensitivity by offering a high surface area and advantageous electronic characteristics. Carbon nanotubes and graphene are famous for their excellent conductivity, chemical stability, and large surface area. Metal-organic frameworks (MOFs) are known for their high porosity and customisable design; MOFs represent an emerging focus in heavy metal detection, often functioning as “molecular sieves” that selectively capture metal ions. The table notes a collective idea regarding the sensor’s performance: the limit of detection goes lower until nanomolar concentrations, i.e., in the range of Parts-per Trillion (ppt) to Parts-per Billion (ppb). The detection range can depend on the usage of the appropriate sensing layer, electrode material, and electrochemical scanning technique.

2.3 Evolution of printed electrochemical sensor toward detection of HMI

2.3.1 History of screen printing

Screen printing began in China during the Song Dynasty (960–1279 AD) to transfer designs onto fabrics.[144] Japan was among the first Asian nations to develop and refine distinctive screen printing forms.[145] In the early 1900s, squeegees were developed and used to push ink through the screen mesh. Roy Beck, Charles Peter, and Edward Owens are recognised for transforming the commercial screen-printing industry with their innovation of photo-imaged stencils.[146] Carbon-based materials have a well-established history in electroanalytical science. Over the past 55 years, they have seen significant advancements in their form, properties, and modifications, which can influence their electrochemical behaviour. This review examines recent progress in carbon materials, highlighting the versatility of graphitic carbon and its modifications. It provides a comprehensive overview of printing techniques to create electrodes and sensors with modified carbon inks.[147-149] The carbon paste electrode, developed by Adams in 1958, was introduced as a viable alternative to traditional solid electrodes.[150] In 1963, Perone advanced the field by utilising wax-impregnated graphite electrodes for linear sweep voltammetry after pre-deposition, enabling the analysis of silver through stripping methods.[151]

2.3.2 Types of Printing Technology

Thin film and thick film technologies are the primary methods used in the production of electrochemical sensors. Thin film technologies, including lithographic techniques, enable the creation of high-performance, reproducible devices but are often associated with high fabrication costs. In contrast, thick film technologies, such as various printing methods, significantly reduce production expenses and facilitate the mass production of sensors with consistent reproducibility. Over the years, printing techniques have gained considerable attention for sensor fabrication. These techniques can be categorised into two main types: (a) contact-based methods (e.g., screen printing, gravure printing, pad printing, stamp-assisted printing, flexographic printing), which involve direct physical contact between the printing medium and the target substrate, and (b) non-contact printing processes (e.g., inkjet printing, aerosol-jet printing).[152-154]

In the early days of electrochemical experiments, solid metallic electrodes were essential. However, as electrochemistry has evolved and become more prominent in technology, there has been a shift towards reducing manufacturing costs. This has led to the adoption of carbon-based materials, such as carbon paste electrodes, which are cost-effective but may lack consistency in reproducibility.[155]

Since the early 1990s, various printing methods—such as pad printing, roll-to-roll printing, and screen printing—have created electrode circuits for electrochemical applications. Each of these techniques comes with its own set of advantages and limitations. For instance, pad-printing allows for thin-film transfers suitable for electrochemical setups but is not ideal for mass production of electrode systems, making it less favoured than screen-printing. Screen printing, on the other hand, enables the large-scale production of highly reproducible electrodes, bridging the gap between laboratory experiments and practical field applications. Screen-printed electrodes have revolutionised this field due to their cost-efficiency, reproducibility, and ability

to produce sensors on a large scale. These electrodes offer improvements in sensitivity, signal-to-noise ratio, and reduced sample volumes, making them viable alternatives to traditional solid electrodes. Additionally, the simplicity of mass-producing screen-printed sensors allows them to be used as single-use devices, minimising contamination risks and eliminating the need for pre-treatment for solid electrodes.

Advantage of screen printing

Screen-printing technology for fabricating electrode materials has emerged as a dependable and cost-efficient method for creating electrochemical sensors and biosensors. Various prototype devices have been developed and utilised in diverse contexts of environmental and industrial analysis. This technology also facilitates miniaturization, allowing the production of durable, disposable screen-printed electrodes. Due to their lightweight design and user-friendly nature, these materials have gained considerable attention in electrochemical sensing. The absence of intricate pre-treatment processes makes them suitable for real-time, on-site monitoring and detection.[156, 157]

2.4 Conclusion:

Thus, this chapter provides a detailed description of the standard electrochemical techniques available, and the literature study on reported electrochemical sensors helps to select the appropriate and most extensively used methods for the thesis work. In spite of the general description mentioned in this chapter, the upcoming chapter is a continuation of the introduction chapter where a combination of technical description along with my personal perception of the pre-setup of the following experimental works undertaken.

[3] Fabrication methods, electrochemical techniques and their optimisation

The work adapted from:

(1) Neethipathi, D. K., Mishra, S., Ganguly, P., A., Bass, A., Scott, M., & Dahiya, R. Flexible MoS2 modified Screen Printed Carbon Electrode based Electrochemical sensor for wine quality monitoring by detection of ascorbic acid. Advanced sensor research journal (Submitted)

(2) Ganguly, P., Neethipathi, D. K., Beniwal, A., & Dahiya, R. (2022, July). Influence of Thickness of Screen-Printed Carbon Electrodes on Electrochemical Sensing. In 2022 IEEE International Conference on Flexible and Printable Sensors and Systems (FLEPS)
(Neethipathi, D. K conceptualized the study, conducted the experiments, analysed the data and written (equal))

Introduction

This chapter will discuss a brief methodology for fabricating and further optimising the printed sensors to develop new sensors. These individual electrochemical sensors will be further studied in detail in the upcoming chapters. The chapter contains the basic electrochemical setup for the two and three-electrode setup, and the function of each fabricated part will be considered. Then, the sensing materials are selected, the synthesis process is performed, and the coating procedure is performed. The overall setup for the screen-printing process, the overview of adapted electrochemical techniques, the printing process optimisation, and the development of low-cost readout will be shown.

3.1 Electrochemical setups:

In general, printed electrochemical sensors are based on the principles of electrochemistry, where chemical reactions are coupled with electron transfer at the interface between the electrode and the solution. The typical part of an electrochemical sensor consists of a conductive substrate (e.g., screen-printed carbon-based electrodes, silver or gold ink), which is usually functionalised with specific recognition elements (e.g., polymers, metal oxides, chelating agents, nanoparticles etc) for selective detection of analytes (such as PTE ion detection, enzymes, etc). The sensing mechanism measures electrochemical signals during redox reactions between the target analyte and the electrode surface. By effectively utilising electrochemical methods and techniques, these signals can be correlated with the targeted characteristics of the analytes.

3.2.1 Parts of the Conventional Electrochemical Sensor & fabricated Printed Sensor

Conventional electrochemical sensors are generally defined using rigid substrates and traditional electrode materials, as Figure 3-1 illustrates. On the other hand, flexible electrochemical sensors are designed to be adaptable and conformable on a flexible substrate, such as the printed electrochemical sensor shown in Figure 3-2. An electrochemical sensor can be either a two-electrode or 3-electrode based system. Unlike the 3-electrode system, where electrodes such as the working electrode, counter electrode, and reference electrode

were separate, the 2-electrode system just consisted of the counter and working electrode. The introduction of a reference electrode is to provide a stable and known reference potential. Therefore, Potential control is more accurate because the working electrode and counter electrode share the same reference potential, which can lead to more accurate measurement.[158]

Figure 3-1: Conventional electrochemical sensing setup.

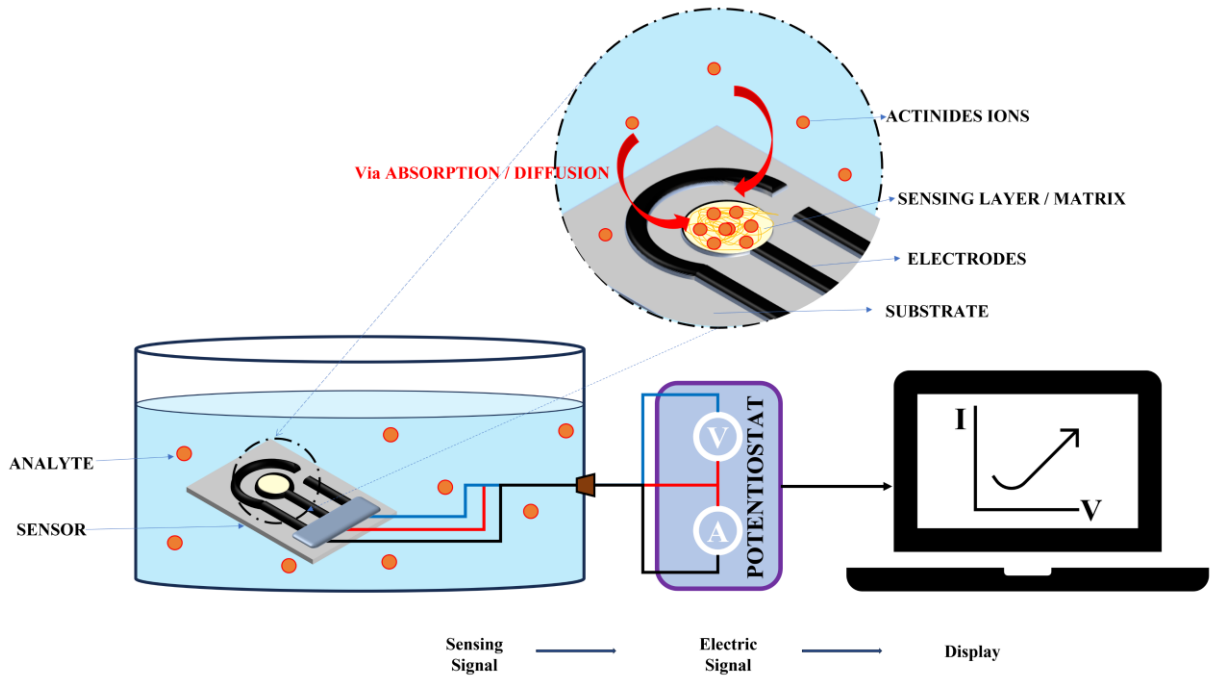

Figure 3-2: Printed electrochemical sensor-based sensing setup.

3.2.1 Substrate

Unlike the conventional electrochemical sensor setup with rigid electrodes, flexible electrochemical sensors can be built on various substrates using printing techniques on different materials, such as glass, metal, silicon, paper, textiles, and flexible polymers.[159-161] The substrate is essential in defining the sensor's mechanical properties, adaptability to various environments, and overall performance. Substrate materials offer numerous opportunities and advantages for practical applications, particularly in field-based settings where durability and lightweight properties are essential. Their versatility makes them well-suited for handling the demands of rigorous, real-world use. To enhance the applicability in real field applications, the substrate plays a significant role in the case of wearable devices, healthcare devices, and monitoring applications. Thus, considering the environmental aspects, substrate material properties such as flexibility, biodegradability, and disposability are crucial in the field of sensing applications. Unlike conventional detection methods, an Electrochemical sensor can be built on various substrates. Disposable plastic, paper, and textile electrodes are ideal for flexible and stretchable electrochemical sensors. These substrates offer flexibility, lightweight design, portability, and cost-effectiveness. Portable readers, wireless transmission modules, and data acquisition systems can also enhance flexible disposable electrodes for on-site heavy metal detection. However, the critical challenges in developing these electrodes lie in ensuring they are robust, mechanically stable, and deliver excellent electrochemical performance.

3.2.2 Reference electrode

The most important part of a 3-electrode system is the reference electrode. The reference electrode's potential must remain unaffected by electrolyte solution fluctuations and maintain a stable potential. As sensors are increasingly miniaturised to enhance speed, performance, and portability, this trend extends to the reference electrode. The miniaturisation of reference electrodes introduces several challenges that need careful consideration.[162] The reference electrode, made from precisely defined materials, has a stable and well-established potential against which all other electrode potentials are measured. For a conventional system, the common electrode types often appearing in this field are *Ag/AgCl Electrode, Calomel Electrode, and Hydrogen Electrode.* The silver/silver-chloride electrode is widely used in research and industry because of its straightforward construction. It typically consists of a silver wire coated with silver chloride, placed in a solution rich in chloride ions, such as potassium chloride (KCl). The Saturated Calomel Electrode (SCE) is composed of mercury coated with a mercury chloride paste (Hg_2Cl_2, known as calomel) and is immersed in a saturated potassium chloride (KCl) solution. This setup is housed in a glass tube, and a platinum wire is employed for making external electrical contact. The standard hydrogen electrode (SHE) is crucial because it is assigned a standard potential of 0 volts. All other electrodes' standard potentials are measured relative to this reference electrode. Integrating standardised reference electrodes is hard in the case of flexible sensors. Therefore, micro or microfabricated reference electrodes such as Solid-State Ag/AgCl, Ag/AgCl Electrodes in Capillaries, and *Ag/AgCl with Filling Solution* can be used. In most of my work, the printed carbon paste base electrode and the Ag electrode were used as a pseudo reference electrode material.[163]

3.2.3 Counter electrode

The counter electrode enables current to flow between the working electrode and the external circuit, thereby completing the circuit and ensuring that the necessary current passes through the electrochemical cell. Typically constructed from platinum, graphite, or carbon-based compounds, the counter electrode is generally larger in size than the working electrode. This design allows it to handle higher currents and reduce polarisation effects. It also serves other purposes, such as potential stability, and in some instances, it is used to avoid interfering with the measurement process; the counter electrode maintains a stable environment for the electrochemical reactions. Usually, the size of the counter electrode should be preferably bigger than the working electrode to provide sufficient current requirement for stable sensing. Despite most of my work involving the usage of barely bigger electrodes, the usage of the carbon electrode, which has a good surface area, helps in the even distribution of current without causing significant polarization.[164]

3.2.4 Working electrode

The working electrode is the electrode where the target electrochemical reactions are measured. The working electrode is where reduction or oxidation happens, depending on how the system interacts with the observed gas species. Every reaction on the surface of the working electrode will draw a response from the balancing pole, the counter electrode. As the system comes on, the counter electrode will try to balance the potential change due to the reaction between the detected analyte and the working electrode. This balancing current is dynamically monitored as the central reading of an amperometric electrochemical sensor. For the system to sustain, the potential on the working electrode must be inherently fixed using a reference electrode. Owing to these balancing mechanisms, the three-electrode design can maintain the sensor sensitivity and linearity for the better part of its lifetime.[165]

3.2.5 Sensing layer

The sensing layer in an electrochemical sensor is a crucial component that directly interacts with the target analyte, facilitating the detection process. This layer typically consists of materials that can promote specific reactions, such as oxidation or reduction, which generate a measurable electrical signal. The properties of the working electrode play a crucial role in determining the accuracy of measurement results. Proper surface modification of the electrode significantly impacts detection sensitivity and selectivity. Various materials or combinations of materials can be applied to the surface to enhance the electrode's performance, increasing sensitivity, lowering the detection limit, and improving overall detection capabilities.[71, 166]

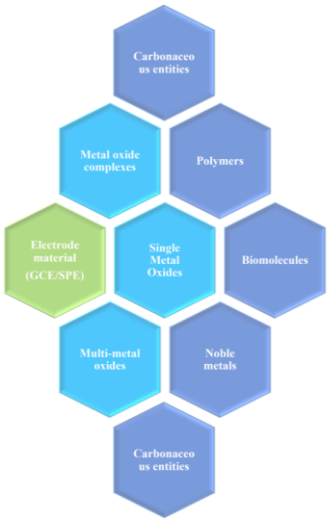

Figure 3-3: Sensing layer for the working electrode.

Extensive research is currently underway to develop chemically modified electrodes utilising a wide range of interface materials. These materials include electrochemical biosensors, nanomaterials, polymers, metal oxides, and carbon nanotubes. Usually, Electrodes modified with nanomaterials demonstrate several notable properties, including quantum effects, electron tunnelling, and surface catalytic effects. Additionally, these nanomaterials have proven highly effective in detecting heavy metal ions due to their excellent adsorption capacity, thermal stability, large surface area, and high catalytic efficiency. Some of the materials that are commonly used are Depending on the application, various materials can be used for the sensing layer, such as metal nanoparticles, conductive polymers, metal oxides, carbon-based materials, enzymes or biological molecules. [167, 168]

3.3 Selection of materials for the thesis work

The following paragraphs summarise a general overview of the various materials used for sensor preparation and briefly discuss the material selection for the fabricated sensors.

3.3.1 Substrate

For this thesis, paper-based, polyvinyl chloride (PVC)/ Polyethylene terephthalate (PET)- based substrates were used for their easier disposable nature (Photographs of these disposable PET/PVC substrates are displayed in Figure 3-4). It is observed that the prepared ink formulations for screen printing application tended to coat with the selected substrate material. During my work, Polycaprolactone (PCL) and textile-based substrates were also used for their environmentally friendly disposable nature. PCL is known for its degradable nature in water-based systems, and more work is planned for the future. The above-selected substrate materials were focused on their flexible nature. Images of such a sensor with various substrates are shown in Figures 4-5.

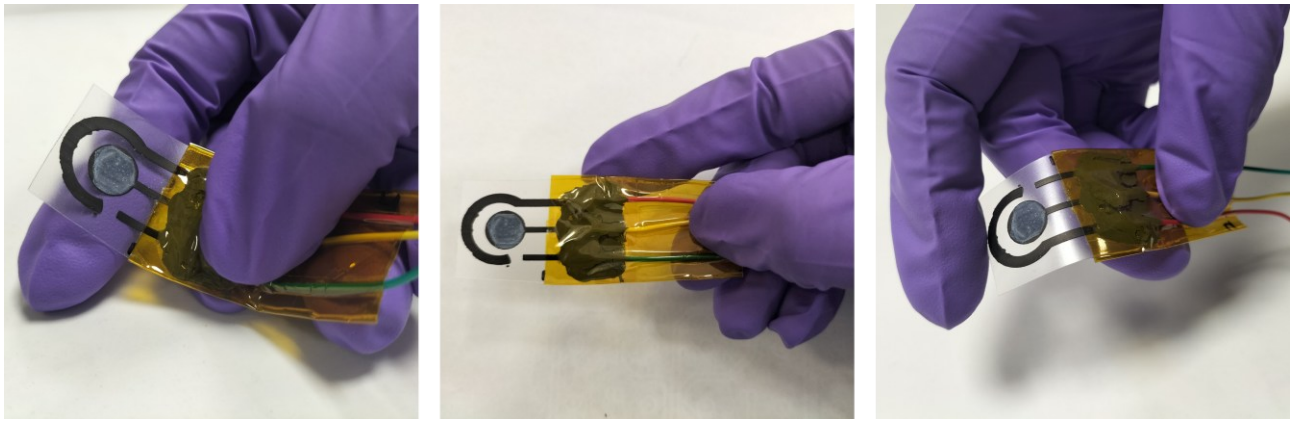

Figure 3-4: Flexibility of the fabricated sensor.

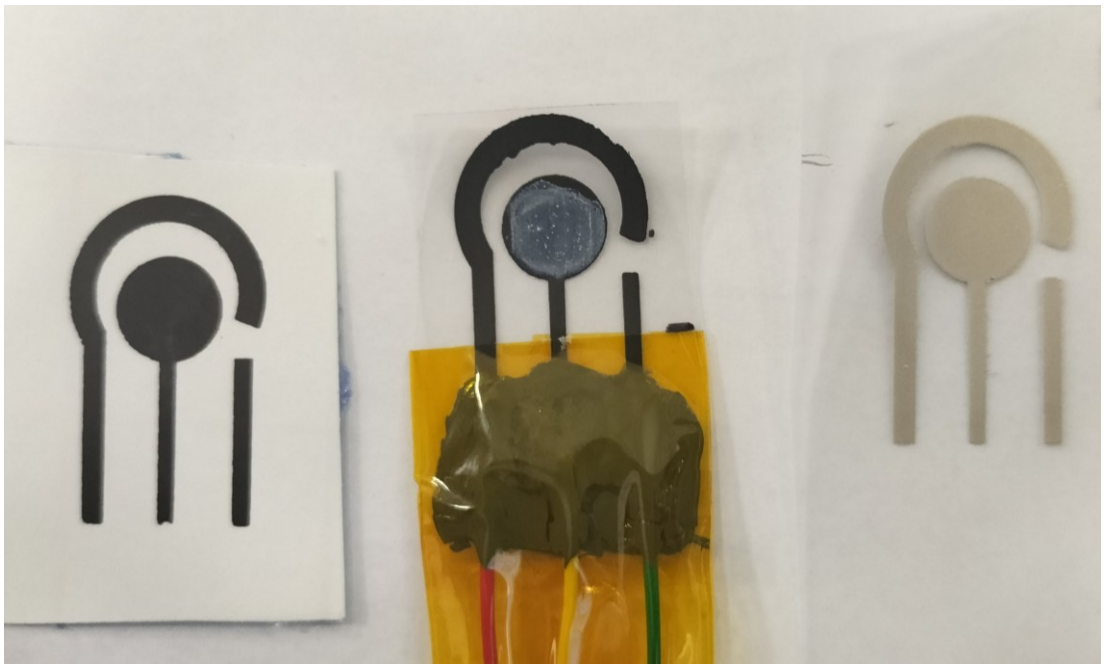

Figure 3-5: Various substrate and electrode materials printed (a - Carbon electrodes printed on paper substrate; b- Graphene carbon-based electrodes are printed over the PVC/PET substrate; c- Silver-based electrodes printed over PET sheet as substrate)

WHY IS FLEXIBILITY NEEDED FOR THE SUBSTRATE MATERIAL?

The flexibility of electrochemical sensors provides a range of significant benefits for water applications. Flexible sensors can conform to different surface shapes, including irregular or curved ones, ensuring stable contact and enhanced performance across various environments. Thanks to their flexibility, these sensors are more resistant to damage from mechanical stress, vibrations, or impacts, making them more reliable in dynamic conditions. Flexible sensors can be integrated into clothing or other wearable items, enabling continuous monitoring while maintaining comfort. Lightweight and adaptable sensors are more accessible to transport and install, especially in challenging or remote locations, which allows quicker and more efficient deployment in

the field. Flexible sensors can be designed for single-use or easy cleaning, which helps mitigate the effects of fouling from contaminants such as algae or sediment, thus ensuring more reliable long-term monitoring. Utilising flexible materials such as plastics, papers, or textiles typically results in lower production costs, making these sensors a cost-effective option for large-scale or disposable applications.[169, 170]

3.3.2 Reference electrode

The choice of a reference electrode depends on the application and the specific ionic species in the test solution. Typically, a single reference electrode cannot meet all the criteria of an ideal reference electrode. Consequently, an electrode that works well in one environment or application may not be suitable for another. For initial work, a known Ag/AgCl reference electrode is used to understand the appearance of the peak potential, as it is easier to study with the existing literature.[163, 171, 172] For the complete integration of printed sensors for flexible applications, pseudo-reference electrodes, such as carbon-based and silver-based electrodes, will be used for most of my work in the upcoming sessions. Few reported electrode potentials are available for the screen-printed carbon-based reference electrode. This somewhat helps in determining the closest value of the fabricated reference electrode. Unlike the conventional reference electrode, it is hard to decide on stable electrode potential as the conductivity and the electronic properties of the prepared ink formulation for printing such electrode vary from batch to batch. It may not be wise to use silver paste-based electrode material as the polarisation switch causes a sudden rise with the bad characteristics of a reference electrode material. Still, in the case of iron detection using all silver-based 3-electrode electrochemical sensors, it is used to collect data and the peak observed also gets amplified; therefore, it can also be used for the detection of iron ions in laboratory conditions.

3.3.3 Counter electrode

For the selection of counter electrodes, carbon-based material has been used in most of my work as it provides high surface area and excellent conductivity. Therefore, a better stencil design with a bigger counter electrode was purchased. However, to maintain uniformity in comparing data from older sensors with the new design, all the experiments were done with poor design for all the upcoming works in this thesis. A silver electrode was also used as a counter electrode, and it was found that, unlike the carbon electrode, the silver electrode has a poor surface area, which is significantly affected due to the polarisation risk. Both silver and carbon are quite resistant to the chemicals in the electrolyte solution and the by-products produced during electrochemical reactions, this ensures durability and reliable performance over an extended period.

3.3.4 Working electrode

For the selection of working electrodes, three-electrode materials, such as carbon, graphene carbon, and silver, were used. Among these, it was found that the silver electrode suffers from the risk of polarisation and, therefore, the accuracy of the sensor's measurement. Graphene carbon-based screen-printed electrodes were found to be easily breakable due to their 2D structure, and hence, this almost rigid sensor doesn't provide any flexibility. The carbon-based electrode showed promising characteristics with better flexibility and due to its better surface area, it reduces the risk of polarization. Therefore, most of my fabricated sensor was based on carbon paste-based screen-printed electrodes.

3.3.5 Sensing layer

While choosing the sensing layer, it is crucial to explore materials with high surface area and excellent conductivity, their flexibility, ability to immobilise, catalytic properties and strong interactions with analyte ions, and the ability to enhance sensitivity. For this stage, I have prepared nanomaterials that haven't been wholly explored during the beginning of the studies. I have included the preparation of nanomaterials and further formulation of the coating layer. Although various nanomaterials are listed below, only those that produced notable detection results are presented.

PREPARATION OF MOS_2 NANOMATERIAL

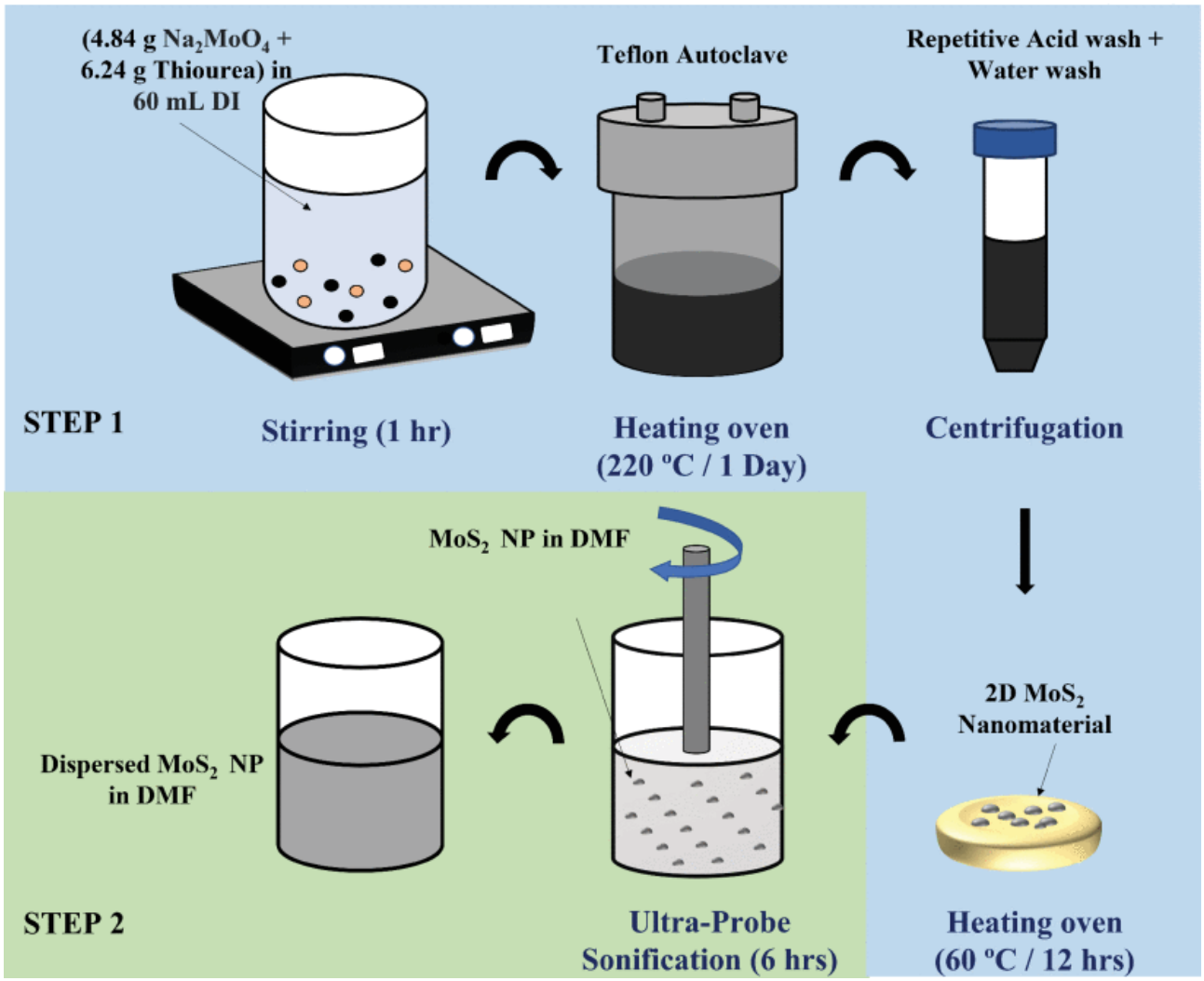

Figure 3-6: Synthesis of MoS_2 nanomaterial using hydrothermal process.

To synthesise molybdenum disulphide (MoS_2) by a hydrothermal method, a precursor mixture of thiourea and sodium molybdate was prepared. First, 6.24 g (0.080 moles) of thiourea was dissolved in 60 ml of deionised (di) water and 4.84 g (0.020 moles) of sodium molybdate was added. The solution was stirred for 1 h at room temperature and then transferred to a 100 ml teflon-lined stainless-steel autoclave (parr instruments). The autoclave was heated to 220 °C for 24 h and then allowed to cool naturally to room temperature. The resulting black precipitate was collected, washed several times with di water and isopropyl alcohol, and dried at 60 °c for 12 hr. The dried powder was dispersed in dimethylformamide (DMF) to obtain a mos_2 ink with a

concentration of 20 mg ml^{-1}, which was used to modify the working electrode (WE) of the screen-printed sensors.

The phase and morphology of the hydrothermally synthesised powder were characterised by x-ray diffraction and sem, as discussed in section 4.3.1 (fig. 4-2). The XRD pattern shows the characteristic reflections of hexagonal 2h-MoS_2 at $2\theta \approx 14.1°$, 33.5°, 39.5°, 49.2°, 58.8° and 69.4°, which can be indexed to the (002), (100), (103), (105), (110) and (201) planes, with no additional peaks from impurity phases. Sem images of the powder reveal agglomerates of platelet-like mos_2 nanosheets, while sem of the mos_2-modified spce shows a rough and cracked over-layer on top of the smooth carbon film observed for the bare spce. Together, these data confirm that the hydrothermal process yields phase-pure MoS_2 and that an additional mos_2 coating is formed on the surface of the printed working electrode.

MoS_2 ink formulation

For gce and spce modification, 20 µl of the dispersed mos_2 ink was drop-cast onto the circular working region using a micropipette. The sensor was dried in an oven at 65 °c for 45 min. To obtain a thicker sensing film, multiple mos_2 layers were built up by successive drop-casting of 5 µl aliquots, with intermediate drying between each step. The presence of this stacked mos_2 layer is evident from the change in surface morphology seen in the sem images of the modified spce (section 4.3.1), which show an additional granular over-layer that is absent on the unmodified carbon electrode. The counter and reference electrodes were left unmodified.

gC_3N_4 ink formulation

Pristine g-C_3N_4 powder was synthesised by the thermal condensation and evaporation of a melamine precursor. During the first stage, melamine, a nitrogen-rich molecular solid, was heated to promote polymerisation and formation of the graphitic carbon nitride framework. The condensed material was then subjected to a controlled evaporation step to remove volatile by-products and residual solvent. The resulting powder was used as the starting material for all g-C_3N_4-based inks in this work.

The structural identity and purity of the synthesised g-C_3N_4 were examined by X-ray diffraction and SEM (Section 5.2.3, Fig. 5-1). The XRD pattern exhibits two main reflections at $2\theta \approx 12.96°$ and 27.46°, corresponding to the (100) and (002) planes of graphitic carbon nitride, in good agreement with the reference ICDD card 00-066-0813 and with no extra peaks from secondary phases. SEM images of the g-C_3N_4-coated carbon substrate show a continuous, crack-free film composed of stacked 2D platelets, indicating a homogeneous coating. These results support the claim that the synthesised g-C_3N_4 is of high purity and possesses a well-defined layered structure suitable for electrochemical sensing.

For ink preparation, 20 mg of g-C_3N_4 powder was dispersed in 1 mL of DMF using probe ultrasonication to obtain a uniform 2D nanomaterial suspension. To modify the GCE, 5 µL of this dispersion was drop-cast four times onto the polished electrode surface, with intermediate drying in an oven at 60 °C for 15 min after each deposition step.

ZnO coating layer

20 mg of commercial ZnO nanomaterial is dispersed in 1 ml of DMF solvent and mixed well using magnetic stripping for 120 mins. It is then kept for bath sonication for 30 mins.

Preparation of TiO – MgO nanoparticle mixtures

10 milligrams of commercial TiO nanomaterial and 10 milligrams of MgO are mixed in 1 millilitre DMF solvent. The mixture is thoroughly agitated using magnetic stirring for 120 minutes and then subjected to bath sonication for 30 minutes.

3.3.6 Wiring and Insulation

Wiring and insulation play a vital role in electrochemical sensors, as they ensure accurate signal transmission and protect against interference or damage caused by factors like moisture, temperature, or chemical exposure. Dielectric paste and polyamide tape were used as insulation for the printed sensor. This encapsulation should be made even for all the sensors for reproducibility, ensuring the printed exposed electrode surface is common throughout the batch-produced sensors.

3.4 Fabrication Method

In this thesis, several complementary fabrication methods were explored to realise flexible three-electrode platforms and to integrate different sensing layers. The main route used throughout the work is screen printing of commercial carbon and silver pastes on flexible substrates to form robust SPCE-based sensors (Chapters 3–7). In addition, stencil printing was investigated as a rapid prototyping approach for testing alternative electrode geometries, and a Brinter-based inkjet printing setup was used to evaluate the feasibility of depositing our own, higher-viscosity nanomaterial inks without the mesh constraints of conventional screens. The following subsections briefly describe how each printing method was implemented and adapted for this work—covering the choice of substrates and pastes, curing conditions, and the practical limitations that led to screen printing being selected as the primary fabrication technique.

3.4.1 Printing Methods

3.4.1.1 Screen printing

Figure 3-7: Screen printer C920 from Aurel automation.

The setup for screen printing involves several components, including a screen, a squeegee, and a substrate. A frame holds a tightly stretched mesh made from materials like polyester, stainless steel, or nylon, which is designed with specific openings to create the desired pattern. The squeegee, applying a certain amount of pressure and moving at a controlled speed, forces the paste through the screen's openings onto the substrate below. This method supports the creation of various electrode geometries on a wide range of substrates, such as paper, plastic, ceramics, glass, and metal. Additionally, it allows for the application of thick layers, ranging from less than 1 μm to several hundred micrometres, in a single pass—something that is often difficult to achieve with other techniques. Screen printing benefits from the availability of diverse pastes, including conductive, semiconductive, and dielectric types. The required viscosity of these pastes depends on the width of the mesh apertures and the pressure applied. This factor also impacts the printing speed, which is a notable drawback of the technique, alongside the need to adjust various parameters to achieve precise results carefully. Figures 3-7 and 3-8 show the photograph of the screen printing instrument from the aurel automation, including the parts like a stencil and squeegee. Figure 3-9 shows the fabrication process of screen printing thick film electrodes.

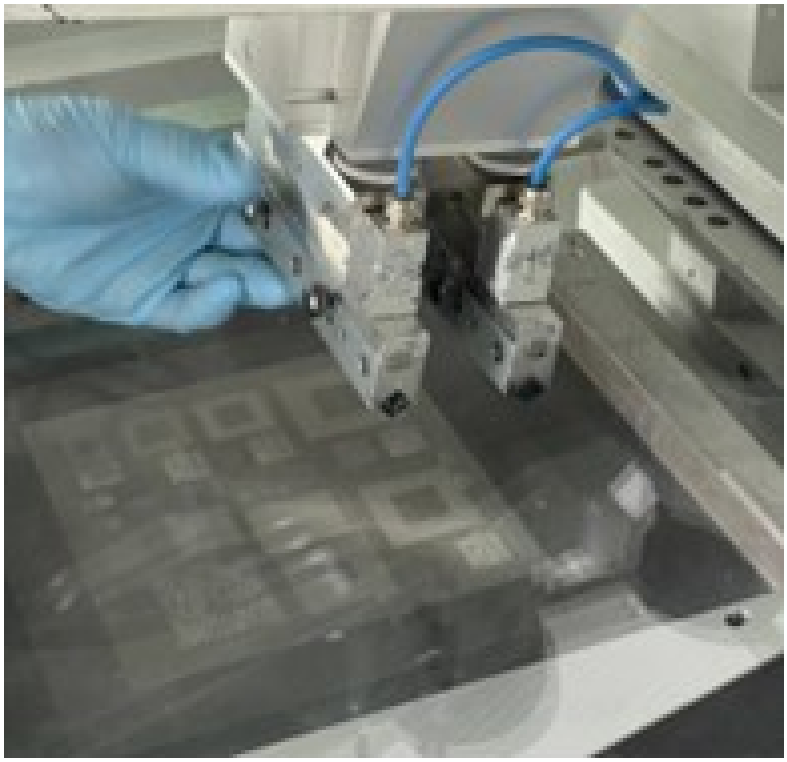

Figure 3-8: A picture of the metallic mesh-based stencil and squeegee.

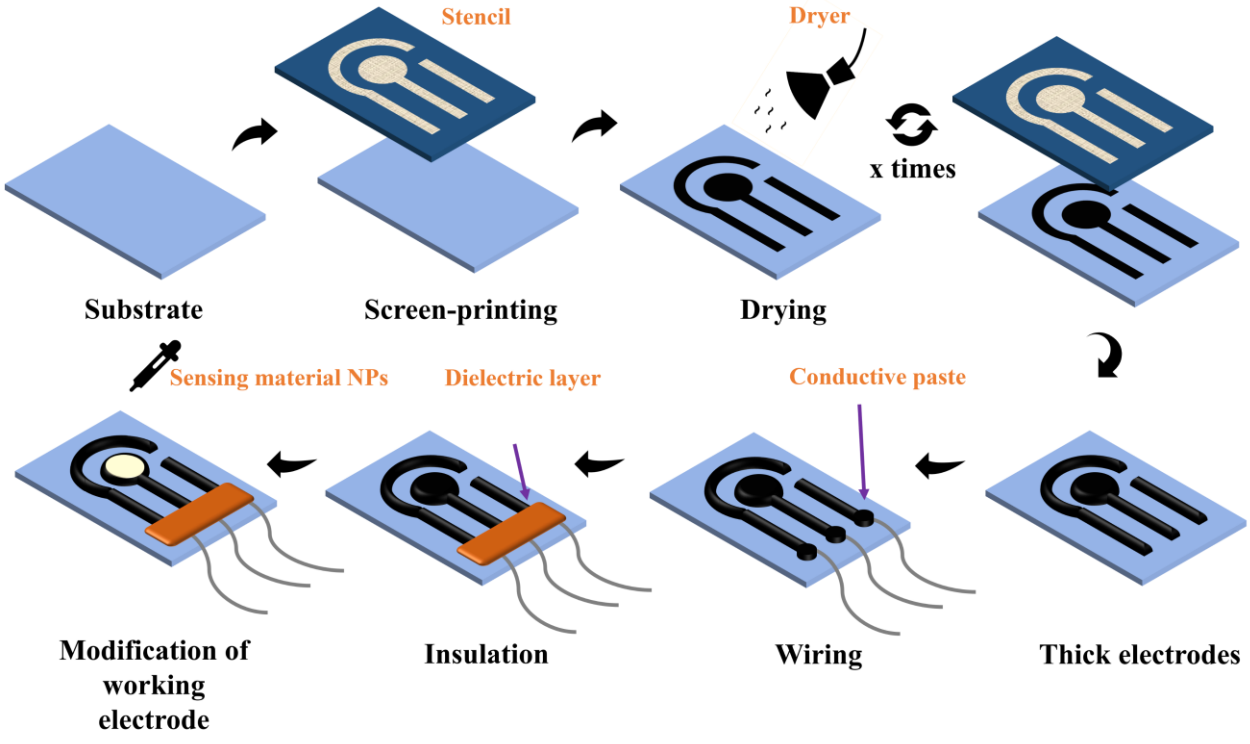

Figure 3-9: Fabrication process of an electrochemical sensor.

3.4.1.2 Stencil printing

A stencil can be produced through various techniques, including cutting paper, plastic, or metal designs. Stencil printing is typically ideal for simpler designs, smaller production runs, or scenarios where rapid and cost-

efficient production is necessary. While the setup is straightforward and affordable, it may not deliver the same detail or durability as screen printing. For stencil printing, either a laser cutter or a 3D printer was used for quicker sensor production. Unlike predefined stencils with definite designs such as a screen printer to print electrodes, the 3D printer can be used to make stencils with 3D modelled designs (such as SolidWorks, Fusion 360). Further, these stencils can be easily used for printing electrodes with the manual sweeping of prepared ink in similar to the screen-printing procedures. Here, it is observed that the printed electrodes aren't fine-shaped, and it is hard to remove the stencil without smudging the freshly pasted ink from the substrate. A Screen printer is preferred over the stencil technique to maintain uniformity with fabricated sensors. Screen printing is generally preferred for producing high-detail, long-lasting, and vibrant prints, particularly for larger quantities. Although it involves a more complex and costly setup, it is capable of handling diverse substrates and large-scale production, effective

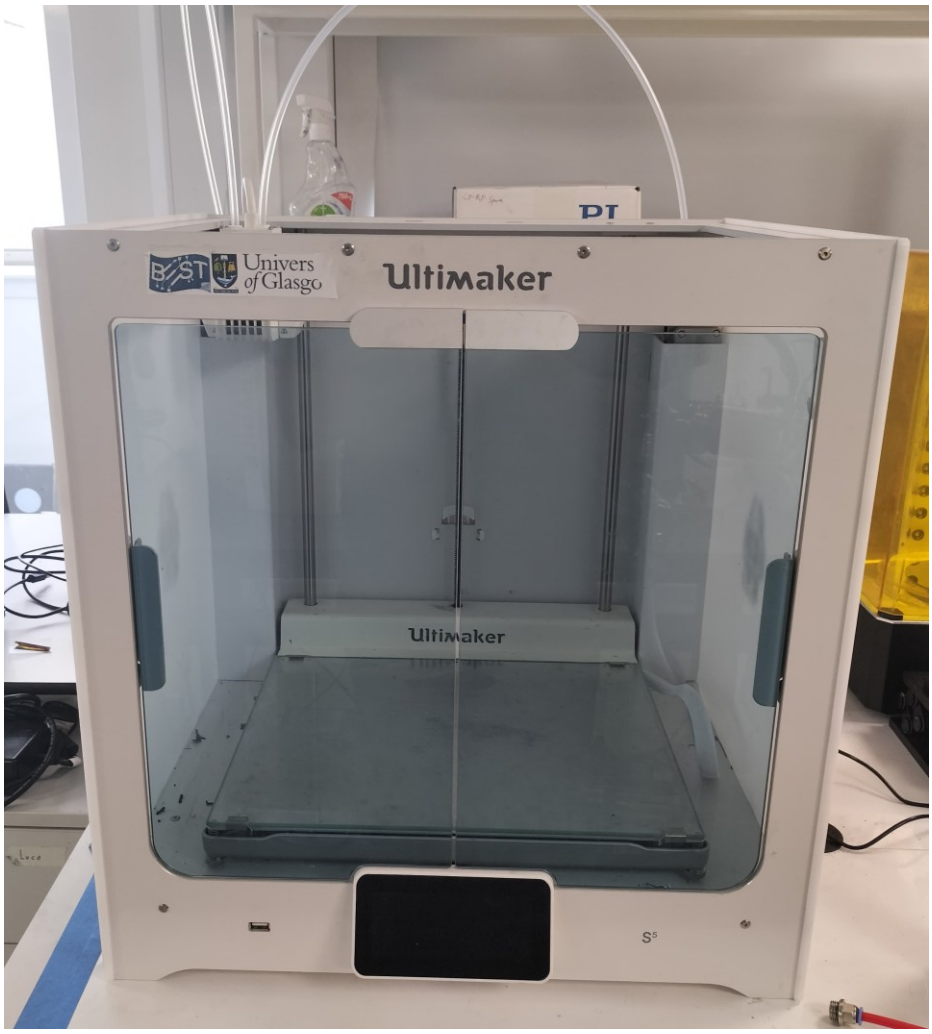

Figure 3-10: A photograph of a 3D printer from Ultimaker.

3.4.1.3 Printing

Another printing technique used for the production of electrodes was a Brinter.To use the screen printer effectively, commercial inks were required because the metallic mesh contains small pores that thicker ink formulations could obstruct. However, the Brinter allows using our prepared ink pastes as it acts similar to an

inkjet printer, where pressure is used to control the emission of coating ink. One of the disadvantages of using the brinter is to generate one's own G-Code Commands for printing separate designs on a single run, or else the needle often runs over the already printed designs, which results in difficulty in printing and designing complex structures.

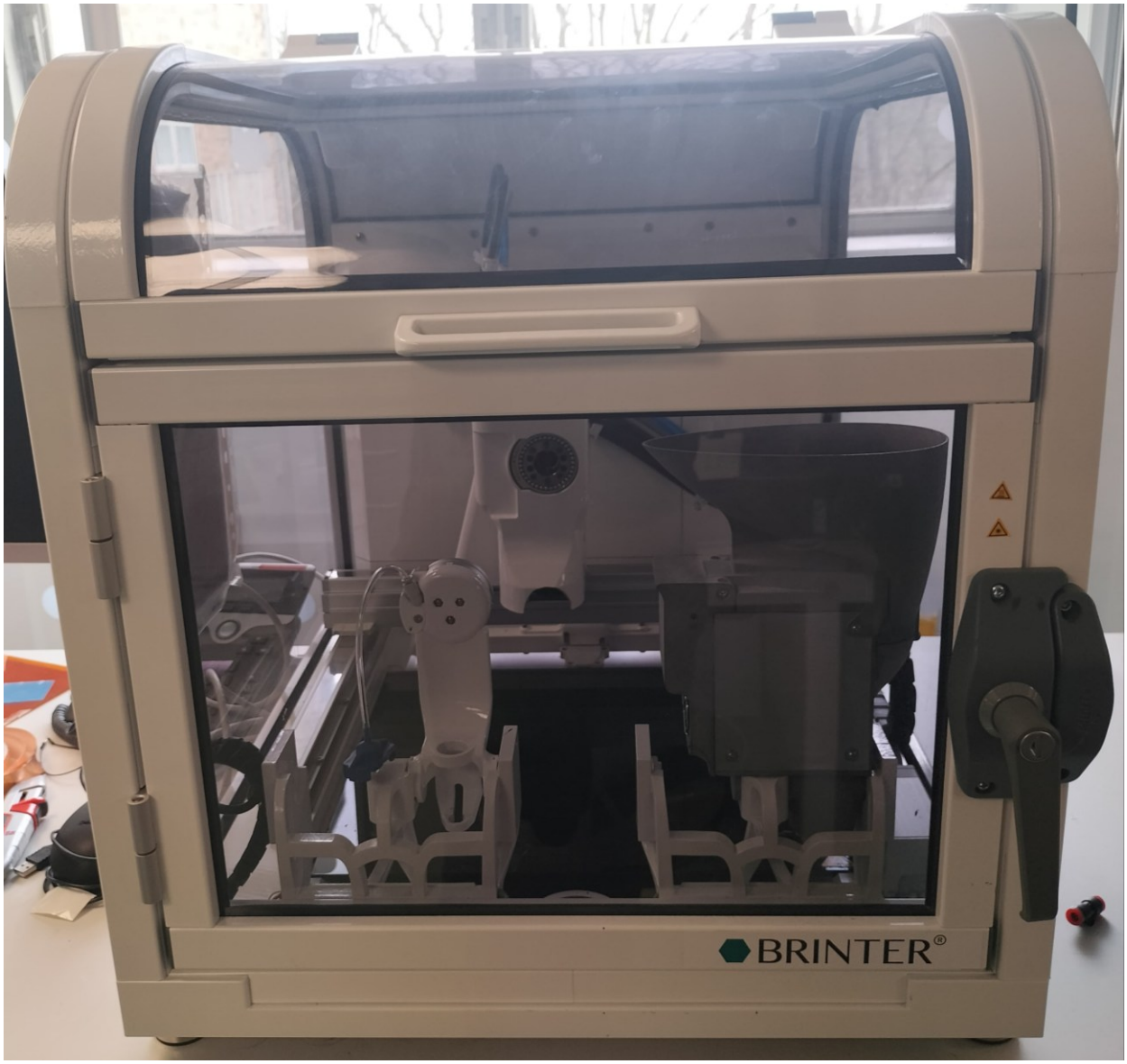

Figure 3-11: A photograph of an Inkjet printer from a Brinter.

3.4.2 Optimization

3.4.2.1 Solvent

The selection of solvents for the sensing layer is essential when creating printed sensors, as they can significantly affect the sensor's performance, stability, and overall efficiency. Some critical parameters while choosing a solvent are viscosity, evaporation rate, compatibility, toxicity and robustness it can provide. For most of the work, DMF solvent is mixed with IPA and acetone to develop the coating layer as they tend to be extremely robust in nature.

3.4.2.2 Thickness

Screen printing (SP) methods are widely utilised in producing flexible electronics, including gas, physical, and chemical sensors, due to their cost-effectiveness and suitability for mass production. According to existing literature, the characteristics of printed sensors—such as mechanical, electrical, photoluminescent, and optical properties—are significantly influenced by electrode parameters, including the design, roughness, and thickness of the electrodes. Specifically, the thickness of the printed electrode plays a crucial role in determining flexibility, photoluminescence, and other attributes.

For thin-layered physical sensors, screen-printed sensors can closely replicate the performance of their traditional, larger counterparts. However, in chemical sensing, particularly with electrochemical sensors, a thicker film is needed to match the performance of macro-sized sensors. This is due to the need for a stable reference potential and effective electrode-electrolyte interaction. Thin-film electrodes are prone to issues such as material degradation, fouling, or corrosion and typically exhibit lower signal-to-noise ratios compared to thicker screen-printed electrodes. Consequently, multi-layered or thicker screen-printed sensors are often necessary for reliable operation

The thickness of screen-printed sensors can be adjusted by varying parameters such as ink viscosity and adhesion, squeegee pressure, the distance between the substrate and stencil, and stencil properties like mesh size and number. This study explores the electrochemical performance of screen-printed carbon electrodes using graphene carbon, focusing on how varying the thickness of the SP layer by increasing the number of printed layers affects sensor performance. The thickness was optimised through impedance and capacitance studies to understand the electrode-electrolyte interaction better and achieve a higher signal-to-noise ratio.

TO STUDY THE THICKNESS ISSUE FOR THE SCREEN-PRINTED ELECTRODES:

A self-made MoS_2-based SPCE electrochemical sensor was studied for the detection of ascorbic acid ions in water as below. The fabrication and characterisation of such a sensor towards the detection of AA is shown in the appendix document.

The printed sensors, with varying layers (n = 1, 5, 10, and 20), were characterised using Scanning Electron Microscopy (SEM) to assess the electrode thickness. Figures 3-12 (a-d) show SEM images of the printed electrodes at different magnifications, with measured thicknesses ranging from approximately 4 µm to 120 µm. A graph comparing thickness to the number of printed layers reveals a nearly linear relationship (Figure 3-12(e)). The maximum number of printed layers is twenty; beyond this point, the spacing between electrodes and track width decreases, affecting the electrode geometry. The electrodes with different thicknesses were then modified with MoS_2 to examine the impact of thickness on electrochemical sensing. The diffractogram of the carbon electrode and the MoS2-modified electrode (n=20) is shown in Figure 3-12(f). The carbon electrode peaks around ~27.3° corresponding to the (002) plane. In contrast, the modified electrode shows peaks for both MoS_2 and carbon. The inset provides detailed information on the identifiable peaks, with MoS_2 peaks corresponding to the hexagonal (2H) structure and showing no additional impurities.[173]

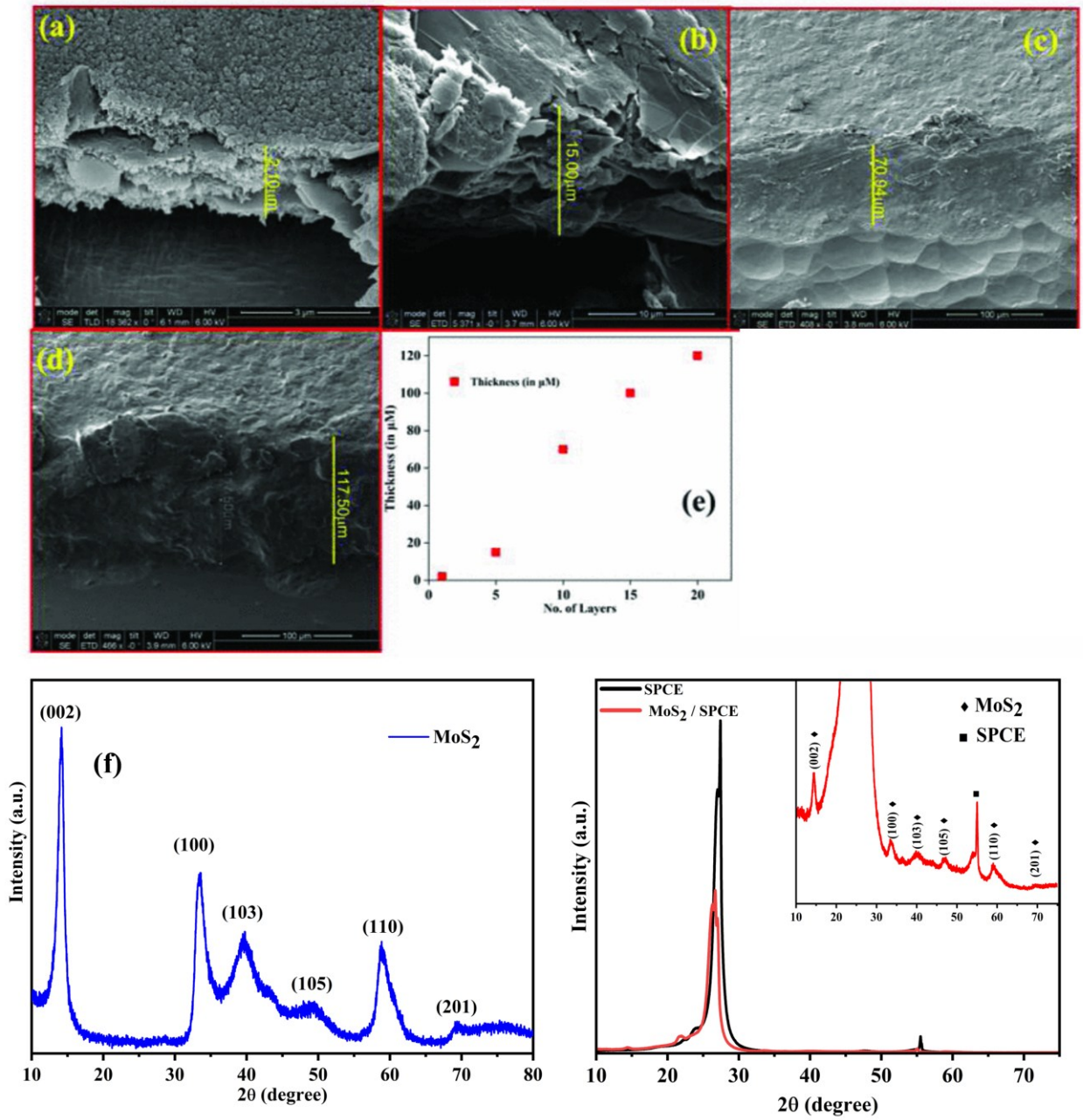

Figure 3-12: SEM images of screen-printed carbon electrode (a) layer 1; (b) layer 5; (c) layer 10; (d) layer 20, and (e) Plot of the number of layers vs thickness and (f) XRD of carbon electrode and modified electrode.

The printed sensors with varying layers (n = 1, 5, 10, and 20), both modified and unmodified, were used for comparative analysis. Ascorbic acid was selected as the analyte for detection using these sensors. Cyclic voltammograms for the unmodified and modified sensors, with and without 100 µM ascorbic acid (AA), were recorded at a scan rate of 50 mV/s over a potential range of -0.3 V to 0.8 V, as shown in Figure 3-13. The single-layer sensor exhibited a shallow current in the micron range, and modification with MoS_2 did not enhance sensing or sensitivity (Figure 3-13(a)). Notable changes in the cyclic voltammetry (CV) pattern were observed with MoS_2 modification, where the previously rectangular profile of the unmodified electrode

transformed into a pseudo-rectangular shape. With an increase to five layers, both modified and unmodified electrodes showed improved currents, though AA was still not distinctly detected in the peak potentials (Figure 3-13(b)). Further increasing the layer thickness to ten and twenty layers resulted in a significant increase in current, nearly up to six times (Figures 3-13(c) and 3-13(d)). The oxidation peak for AA appeared at 0.044 V, with a corresponding reduction peak around -0.1 V.[174]

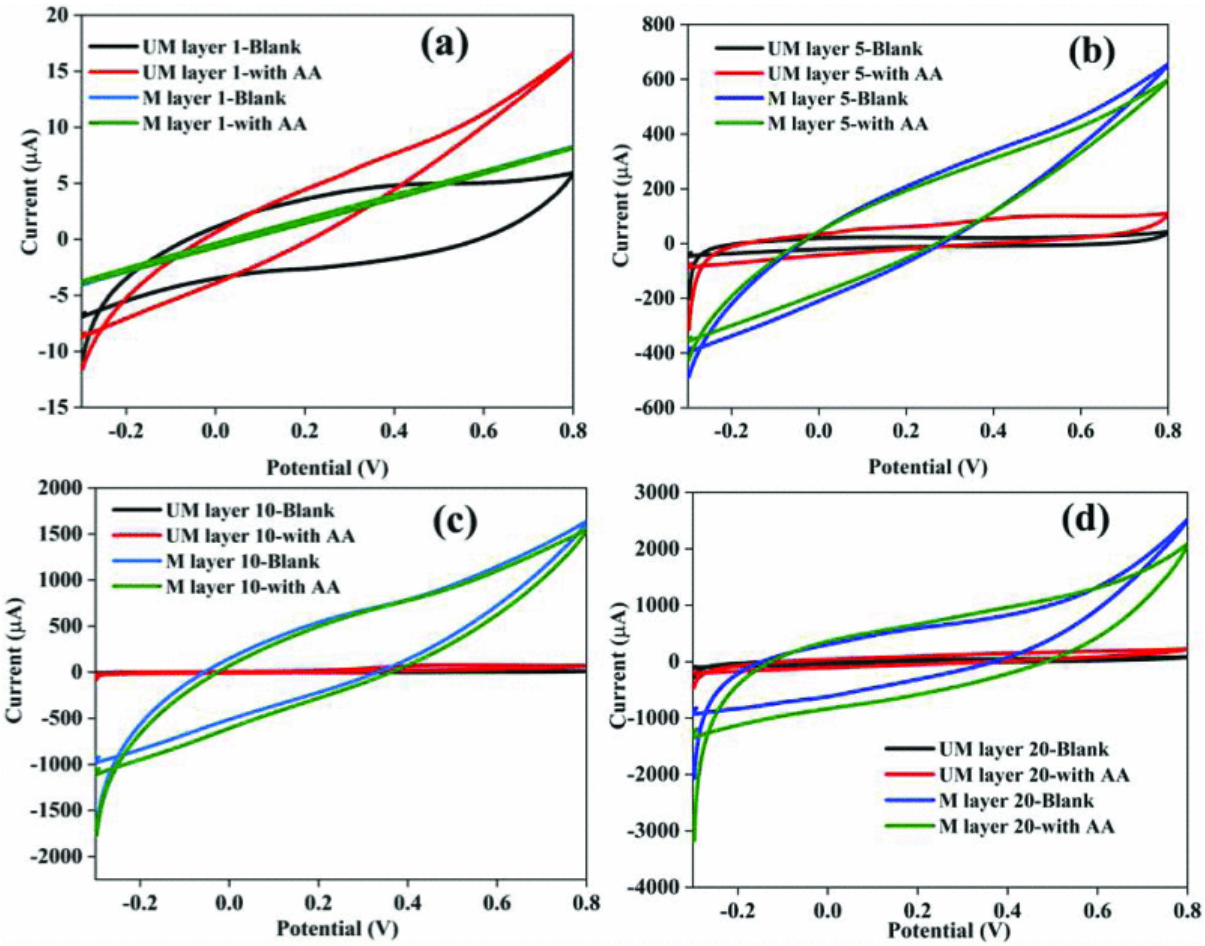

Figure 3-13: CV profile of unmodified and modified sensors in the presence and absence of 100 µM AA at a scan rate of 50 mV/s. (a) layer 1; (b) layer 5; (c) layer 10; and (d) layer 20.

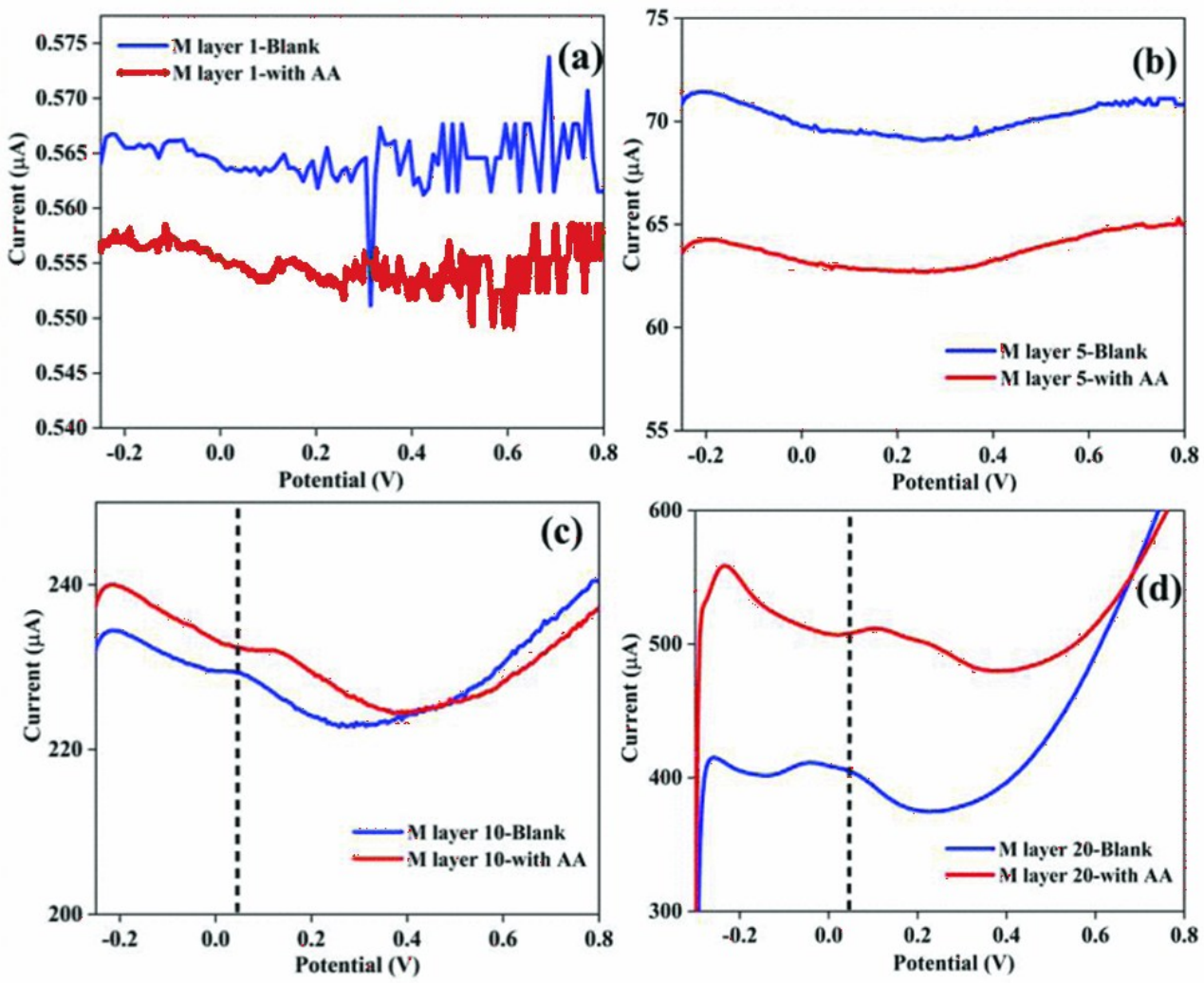

Figure 3-14: DPV profiles of modified sensors in the presence and absence of 100 µM AA at a scan rate of 50 mV/s. (a) layer 1; (b) layer 5; (c) layer 10; and (d) layer 20.

- Differential Pulse Voltammetry (DPV) profiles for various layers of modified sensors in the presence and absence of 100 µM AA are shown in Figure 3-14. The single-layer modified sensor exhibited noisy DPV curves (Figure 3-14(a)). In Figure 3-14(a), the voltammogram corresponding to the thinnest printed electrode shows a visibly noisier baseline. This electrode has the highest series resistance and the smallest faradaic current, so the recorded signal is closer to the instrumental noise floor and more sensitive to small fluctuations in double-layer charging current. As the number of printed layers increases (Figure 3-14(b–d)), the series resistance decreases and the faradaic current increases, which improves the signal-to-noise ratio and results in smoother baselines. As the thickness increased to five layers, the current values improved, though sensitivity to AA was not observed (Figure 3-14(b)), reflecting the CV results. In contrast, the DPV profiles for thicker sensors (n = 10, 20) showed improved characteristics similar to the CV results. These thicker sensors demonstrated increased peak currents and a slight shift in peak position upon AA addition, confirming the detection process (Figures 3-14(c) and 3-14(d)). Electrochemical impedance spectroscopy (EIS) measurements

were conducted over a frequency range from 1 MHz to 0.01 Hz to investigate the charge transfer characteristics of the printed sensors with varying thicknesses. The impedance responses, displayed as Nyquist plots, are shown in Figure 3-15(a) for both modified sensors in the presence and absence of 100 µM ascorbic acid (AA). In these plots, the real part of the impedance is represented on the X-axis, and the imaginary part is on the Y-axis.

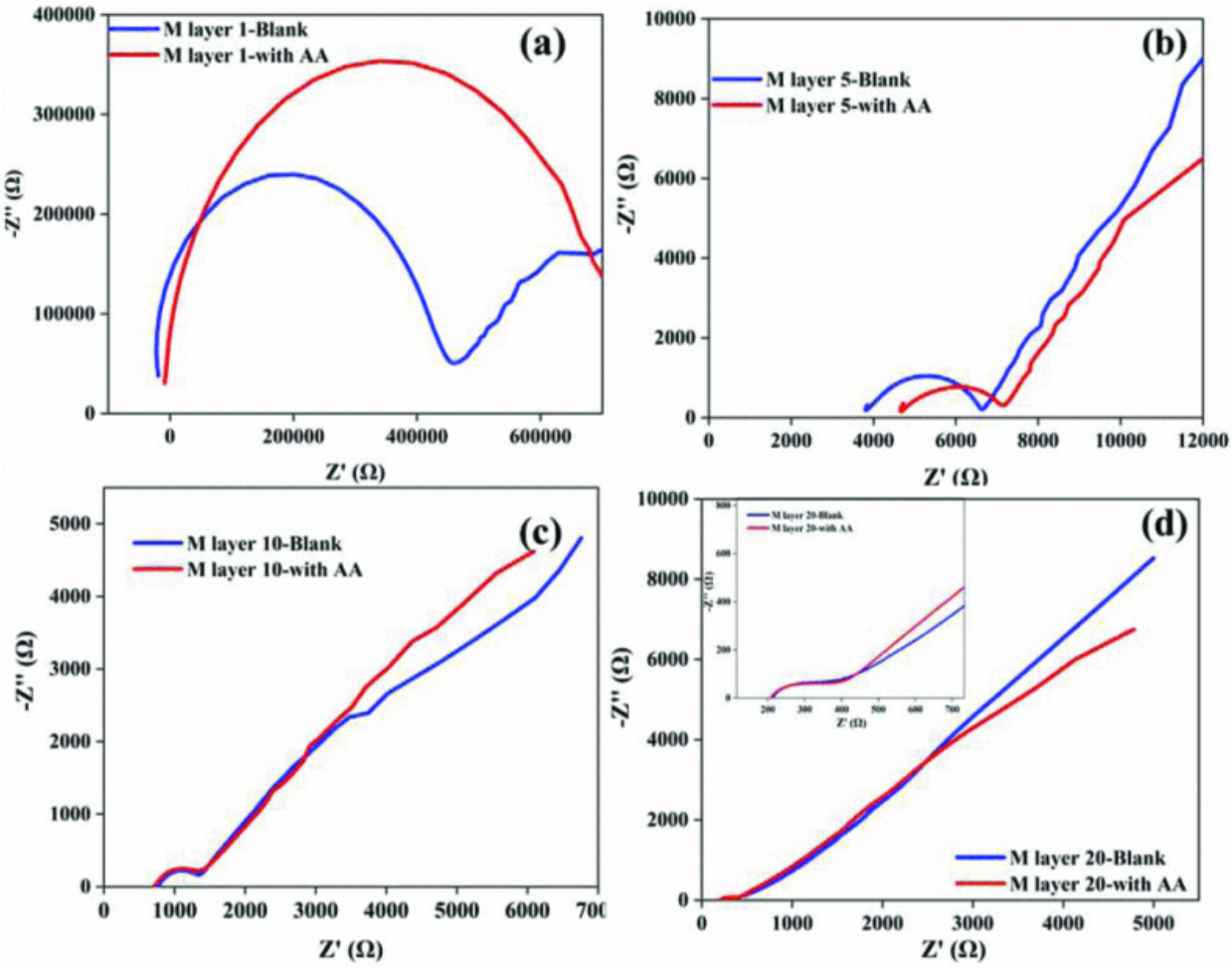

Figure 3-15: Nyquist plot of modified sensors in presence and absence of 100 µM AA (a) layer 1; (b) layer 5; (c) layer 10; and (d) layer 20.

For the single-layer printed electrode (Figure 3-15(a)), a prominent semicircle is observed at higher frequencies, with a smaller semicircle at lower frequencies. The larger semicircle at higher frequencies is attributed to the bulk electrolyte resistance, while the smaller semicircle at lower frequencies corresponds to the electrode resistance.[175] When AA is introduced, the diameter of the high-frequency semicircle increases, indicating a change in the electrolyte resistance, while the electrode resistance becomes less prominent.[176]

Increasing the number of printed layers reduces the overall equivalent series resistance of the sensors. For the thicker sensors (n = 5, 10, and 20), the impedance plots are divided into three distinct regions: (1) the high-frequency zone where semicircles appear, reflecting the charge transfer resistance; (2) the medium-frequency zone which provides insights into charge transport and ion diffusion; and (3) the low-frequency zone where a linear line parallel to the Y-axis indicates the internal capacitance of the electrodes (Figure 3-15(b-d)). The

semicircle observed at high frequencies for these modified electrodes can be attributed to the electric double-layer formation due to MoS_2 modification on the working electrode. Additionally, a Warburg impedance is evident in the low-frequency region, indicative of the diffusion process.[177] All plots show a slight change in series resistance (Rs) upon the addition of AA. Table 3-1 summarises the series resistance values for the sensors with and without AA.

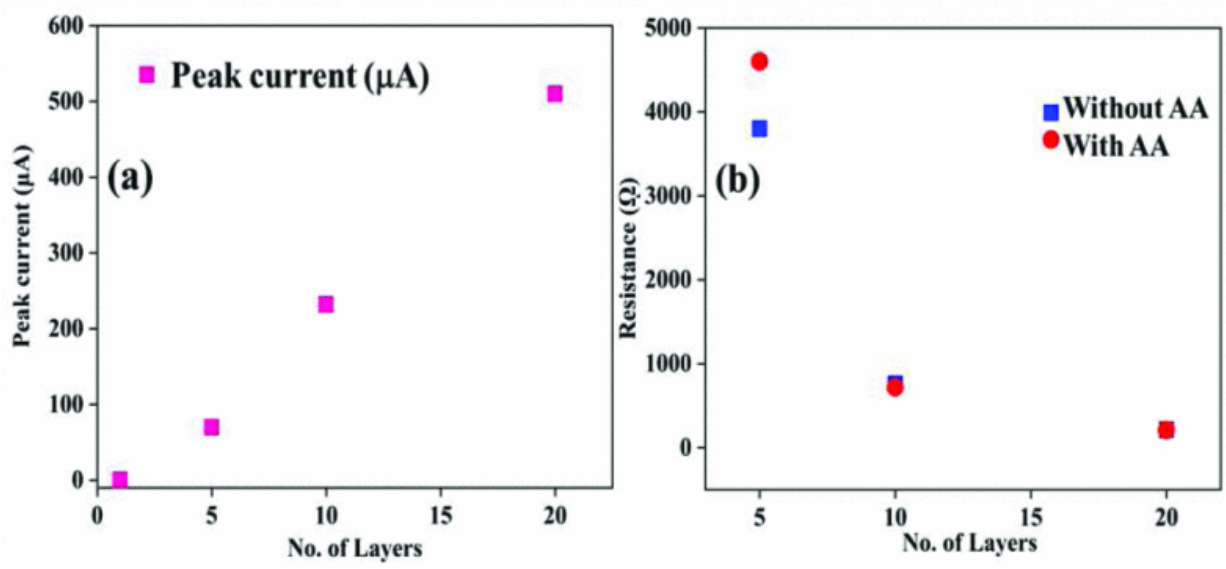

Figure 3-16: (a) Peak current vs number of layers and (b) Series resistance measured for modified sensors in presence and absence of 100 μM AA.

The electrochemical analysis reveals a clear relationship between layer thickness and sensing performance. Figure 3-16 illustrates the peak current and series resistance (Rs) for the detection of 100 μM ascorbic acid (AA) at 0.044 V across various printed layer configurations. A single-layer printed sensor exhibited very noisy and low current readings, accompanied by high electrode and electrolyte resistance. As the number of printed layers increased, both the current measured and the resistance values improved, as shown in Figure 3-16(b). The low current observed with fewer layers made these sensors unsuitable for remote monitoring due to their weak signal strength. Therefore, the optimal range for the number of printed layers is between 10 and 20 for enhanced performance.

Table 3-1: Summarised Value of Series Resistance (Rs) measured for modified different sensors

Printed Layer (n)	Series resistance (R_s) in Ω	
	Without Analyte	*With Analyte*
5	3811	4665
10	746	713
20	214	210

In summary, this study highlights the impact of layer thickness on electrochemical sensing performance. SEM images revealed that the printed layers exhibited a range of thicknesses. Modifying the working electrode with MoS_2 helped to assess how thickness affects sensing capabilities. Lower-thickness sensors showed low current values and high resistance, illustrating the importance of electrode thickness in the detection process. Conversely, sensors with 15 and 20 layers demonstrated higher current values, making them suitable for integration with commercial readout electronics that require low power. The findings suggest that the number of printed layers is a significant factor in optimising the performance of printed electrochemical sensors, offering new opportunities for design flexibility.

3.4.2.3 Design

In reference to a literature work [178]The working electrode design in an electrochemical sensor with the same surface area was compared with varying perimeters (different shapes) using a COMSOL-based simulation for a diffusion-controlled system (Appendix 2). However, other parameters, such as convection and migration, influence the transport of electroactive species in a bulk solution. Moreover, based on the position and size of the counter electrode, it has not been considered, and there is a high chance of influencing non-faradaic current, in this case, during the detection of the peak current of the ions. To investigate the influences of design and proximity of the fabricated sensor, a screen printable stencil was purchased from Aurel automation, and the work on this fabricated sensor in actual laboratory conditions is still ongoing for future work. Figures 3-17 and 3-18 display the CAD-based designs and photographs of the screen printable stencil.

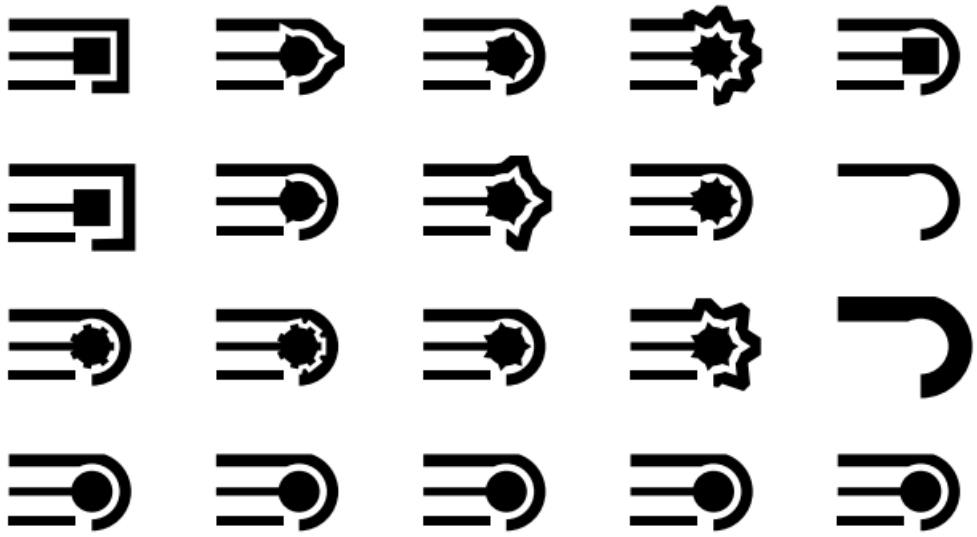

Figure 3-17: Various designs for the stencil for screen printing .

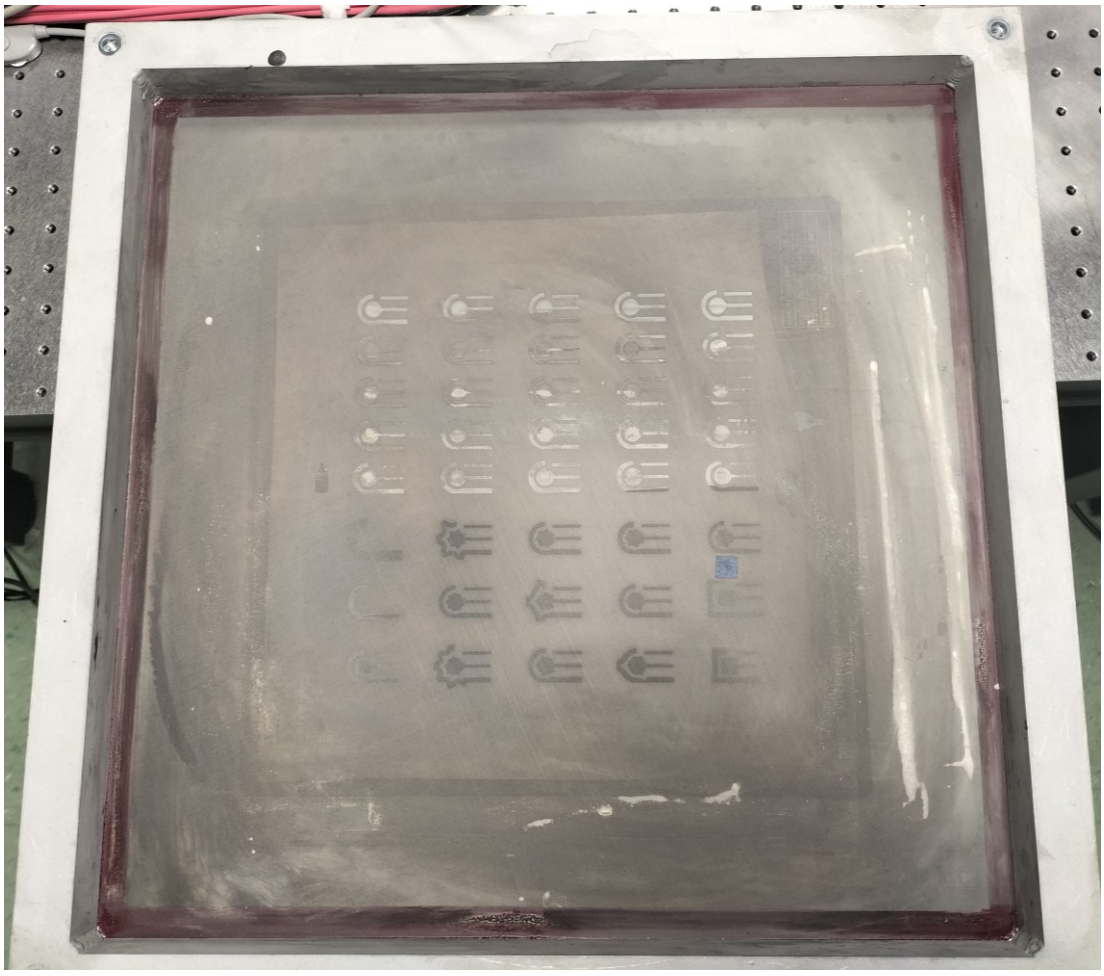

Figure 3-18: photographs of the screen printable stencil

3.5 Electrochemical-based detection methods

In this section, the standard electrochemical sensing techniques and their simple mechanisms are briefly mentioned, along with a unique example of particular affinity-based sensing.

3.5.1 Electrochemical methods

(a) **Cyclic voltammetry:** Cyclic voltammetry (CV) is a widely used electroanalytical method for evaluating electrochemical reactions and their kinetics. Typically, CV provides insights into the redox properties of electroactive materials, the kinetics of heterogeneous electron transfer, coupled chemical and electrochemical reactions, and adsorption processes. A linear potential is applied to a stationary working electrode in an unstirred solution at a constant scan rate during a CV measurement. The resulting current from electron transfer at active sites, corresponding to the applied potential, is plotted to generate a cyclic voltammogram. CV is beneficial for obtaining qualitative data on electrochemical reactivity. For the thesis work, The CV is used for multiple purposes, such as the detection of the redox reaction of heavy metal ions at higher concentrations, Preconditioning of newly printed sensor, postconditioning of the used sensor for reusability, and determining the stability and repeatability of the sensor.

Figure 3-19 illustrates the typical input and output signals for cyclic voltammetry. The upper trace shows the

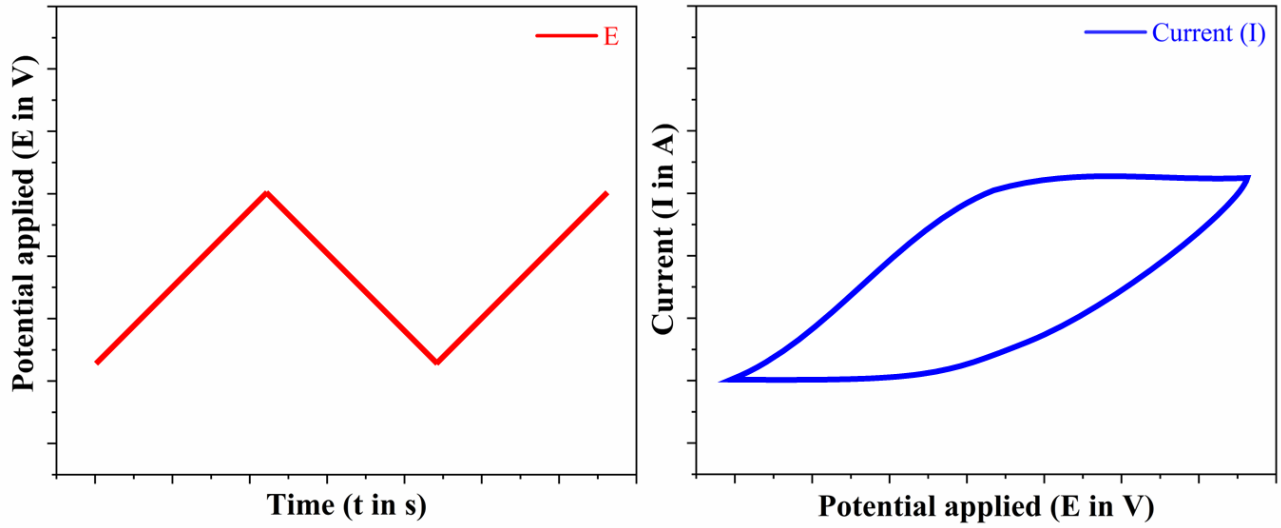

Figure 3-19: Input and output signal form of a typical CV

potential applied to the working electrode, which is swept linearly from the initial potential to a switching potential and then reversed to form a triangular waveform as a function of time. The lower trace represents the corresponding current response plotted versus potential, where anodic and cathodic peaks appear at the redox potentials of the analyte. These peak positions and shapes are used throughout the thesis to identify and analyse the redox behaviour of heavy-metal ions.

(b) **Pulsed technique**: Pulse voltammetry (DPV) is a highly sensitive technique that enhances the signal-to-noise ratio of the voltammogram. As indicated by its name, the potential waveform is delivered in pulses, with each pulse set at small amplitudes (typically ranging from 10 to 100 mV) superimposed on a staircase potential ramp. By measuring the current at the beginning and the end of each pulse, the technique effectively minimises capacitive or background current by allowing enough time for the nonfaradaic current to decay. In normal pulse voltammetry, rectangular potential pulses of increasing amplitude (Ep) and constant pulse duration (10–100 ms) are superimposed on a steady DC offset (Eb). The value of Eb is set to a potential lower than the threshold at which the oxidation or reduction of the analyte begins to take place. The DPV's current output

reflects the difference between these two sampled current values and is plotted against the base potential. DPV can accurately detect micromolar concentrations, whereas cyclic voltammetry (CV) is more suitable for analysing higher concentrations. In square-wave voltammetry, a symmetrical square-wave pulse is superimposed onto a staircase wave, forming the square wave. For the thesis work, DPV detects electroactive species at lower concentrations, which are usually hard to differentiate in the CV output signals. The SWV technique produces quicker response and much-amplified output signals, which are more suited for field-based detection. The pulsed techniques are combined with the stripping voltammetry technique for identifying lower concentrations in ppb or ppt range.

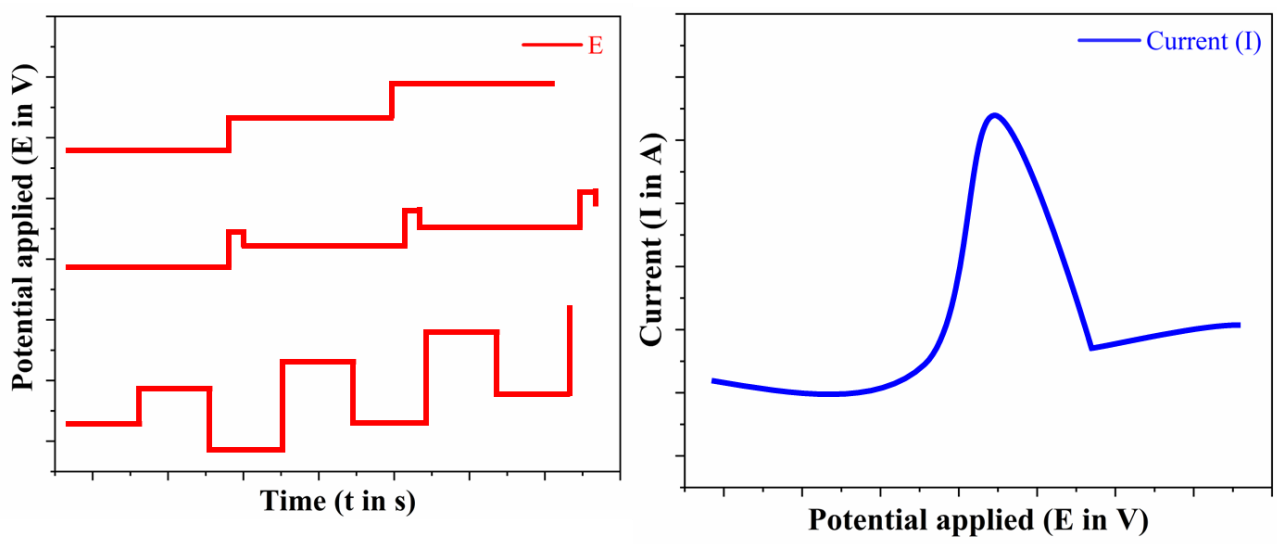

Figure 3-20: Input and output signal form of a typical Pulsed method (LSV, DPV, SWV)

Figure 3-20 compares the input potential waveforms and corresponding current outputs for linear sweep voltammetry (LSV), differential pulse voltammetry (DPV) and square-wave voltammetry (SWV). In LSV, the input is a simple linear potential ramp and the output is a smooth current–potential curve. In DPV and SWV, small pulses are superimposed on a staircase ramp; the current is sampled at defined times within each pulse, and the difference between these sampled values is plotted versus the base potential. This differential sampling suppresses the capacitive (non-faradaic) current and produces sharp peaks at the analyte redox potentials, which is why DPV and SWV are used in this thesis for low-concentration measurements.

(c) **Impedance spectroscopy**: Electrochemical impedance spectroscopy (EIS) is one of the more intricate methods in electrochemistry. It is utilised to investigate the kinetics of charge movements in bulk or interfacial regions, corrosion mechanisms, charge transfer resistance, and the overall electrochemical characterisation of materials and electrolytes. This technique assesses the system's impedance by applying a small sinusoidal alternating current (AC) potential and measuring the resulting current. For the thesis work, EIS study was used to understand both sensor development and characterisation purposes.

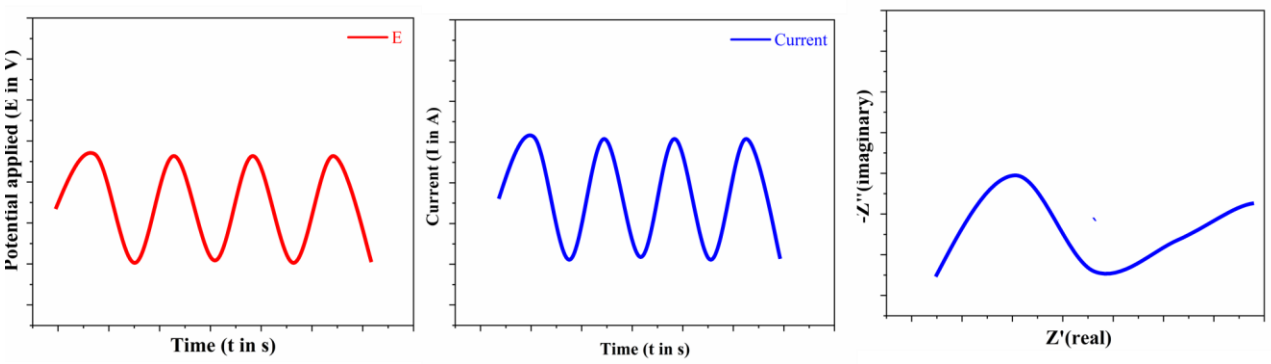

Figure 3-21: Input and output signal form of a typical EIS measuements.

Figure 3-21 schematically shows the input and output signals used in electrochemical impedance spectroscopy. A small-amplitude sinusoidal potential perturbation is superimposed on a DC bias and applied to the cell. The resulting current is also sinusoidal but exhibits a phase shift and different amplitude, reflecting the impedance of the electrode–electrolyte interface. These time-domain signals are transformed into the frequency domain and represented as Nyquist and Bode plots, which are used later in the thesis to extract parameters such as solution resistance and charge-transfer resistance.

(d) **Chronoamperometry**: Chronoamperometry examines how the current response changes over time under potentiostatic control. Typically, the working electrode is switched from a potential where no electrode

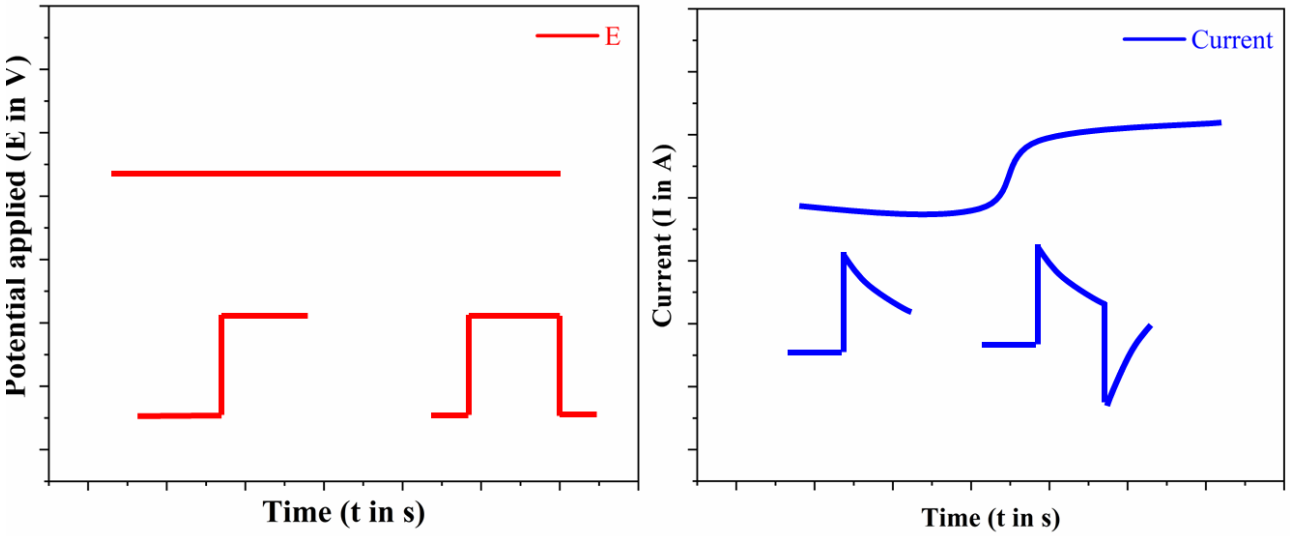

Figure 3-20: Input and output signal form of a typical amperometric and chronoamperometric techniques.

reaction occurs to one corresponding to the mass-transport-limited current, and the resulting current–time transient is documented. In double-step chronoamperometry, a second potential step reverses the electrode reaction, making this technique valuable for analysing situations where the product of the initial electrode reaction is subsequently consumed in solution through a coupled homogeneous chemical reaction.

Figure 3-22 presents the typical signals for amperometric and chronoamperometric measurements. The input is a potential step from a value where no reaction occurs to a value where the target redox process is mass-transport-limited. The output is the current recorded as a function of time: in chronoamperometry, the

current decays following a Cottrell-type behaviour as the diffusion layer grows, whereas in amperometric sensing the steady-state (or near-steady-state) current level is used as the analytical signal. These time-dependent currents are later exploited for real-time monitoring experiments in Chapters 6 and 7.

(e) **Stripping voltammetry**: Stripping voltammetry is an electroanalytical method that begins with the preconcentration of an analyte on an electrode, followed by a potential sweep that selectively oxidises or reduces the analyte. The resulting current is directly proportional to the amount of analyte on the electrode. This technique is primarily used for quantifying trace metals, and due to the broad electrochemical window and excellent solvation properties of ionic liquids (ILs), it can effectively quantify metals with reduction potentials that are more negative than those of water. The preconcentration step, or electrodeposition in the case of metal analytes, enhances the sensitivity of this method, allowing for detection limits in the sub-nanogram range. For the thesis work, The stripping voltammetry method is combined with the pulsed technique such as DPASV, SWASV methods for depositing and stripping HMIs such as Pb, Cd, Zn in the following chapters. Figure 3-23 illustrates the two-step input–output sequence used in stripping voltammetry. In the first (pre-concentration) step, a constant deposition potential is applied for a fixed time, causing the metal ions to be reduced and accumulated on the working electrode. In the second (stripping) step, the potential is scanned in the opposite direction using a DPV or SWV waveform. The corresponding output is a stripping voltammogram with one or more sharp peaks; the peak current is proportional to the amount of metal deposited and therefore to its concentration in solution. This principle underpins the DPASV measurements used later in Chapter 6 for trace-level detection of Zn, Cd and Pb ions.

3.5.2 Selective detection using the sensing layer (EC mechanism)

Types of interaction between sensing layer and targeted analytes: Usually for an electrochemical interaction, it happens due to: Adsorption: The attachment of metal ions to a surface, either through physical or chemical processes; Redox Reactions: Involves electron transfer where metal ions undergo oxidation or reduction; Complexation: The creation of coordination bonds between metal ions and ligands; Ionic Exchange: Selective

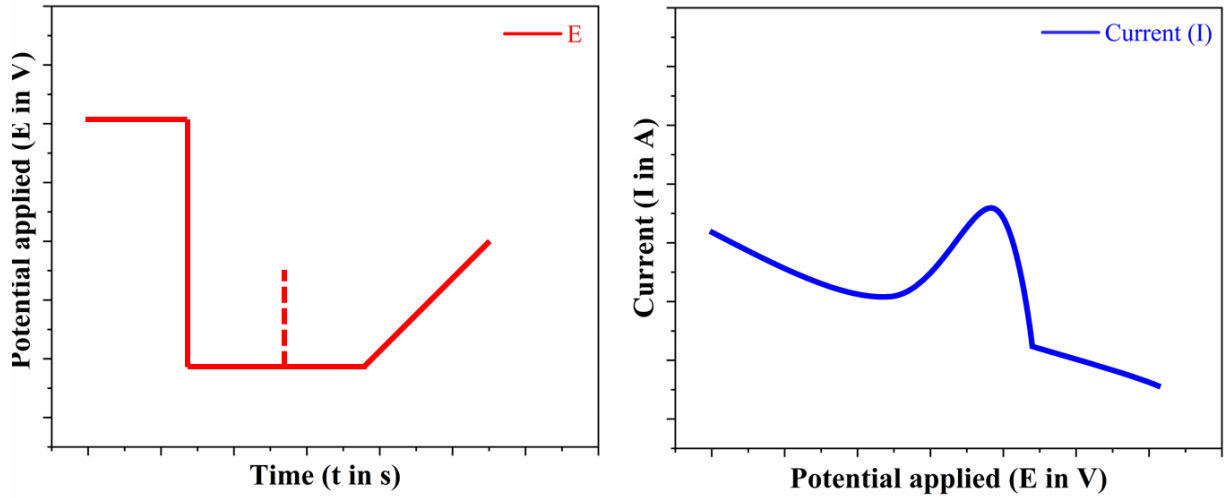

Figure 3-21: Input and output signal form of a typical stripping based voltammetry

interactions with metal ions facilitated through ion-exchange mechanisms; Catalytic Interaction: Involves catalytic materials that assist in accelerating redox reactions; Surface Affinity: Specific binding at the surface

that allows for selective interaction with metal ions; Electrostatic Interaction: Attraction or repulsion between ions and the surface, depending on their charges; Precipitation/Deposition: The process where metals settle or are deposited on the electrode surface during detection; Hydrophobic/Hydrophilic: How surface properties influence the interaction with metal ions; Nanoparticle-Based: Improved interactions due to the high surface area and active sites provided by nanoparticles.

The thesis predominantly observed diffusion, catalytic interaction, adsorption, and affinity-based interactions. Below is an example of affinity-based sensing, where a simulation using MoS_2 nanomaterial-modified SPCE to detect AA ions in water. It shows the affinity between the analyte and the sensing layer in water. Even though diffusion and adsorption-based phenomena can be identified using Cottrell's equation, observing other mechanisms is a bit difficult.

Free energy calculations

The free energy calculations for the adsorption of AA on MoS_2 were carried out using well-tempered metadynamics simulations [19]. The molecular dynamic study aids in computationally understanding the feasibility of the amino acid structure to be adsorbed on the surface of the MoS_2 nanosheets. The free energy as a function of the distance of the centre of mass of the AA molecule from the surface of the MoS_2 is shown in Figure 3-24(a). This free energy profile shows that the AA has good adsorption binding near the surface of MoS_2 with the global minima at a distance of around 3.35 Å. The alignment of the AA molecule at the minima of the free energy profile is nearly horizontal and parallel to the MoS_2 surface, as seen in Figure 3-24(b), (c), and (d). This shows that the MoS_2 molecule used in our sensors attracts the AA molecule toward its surface.

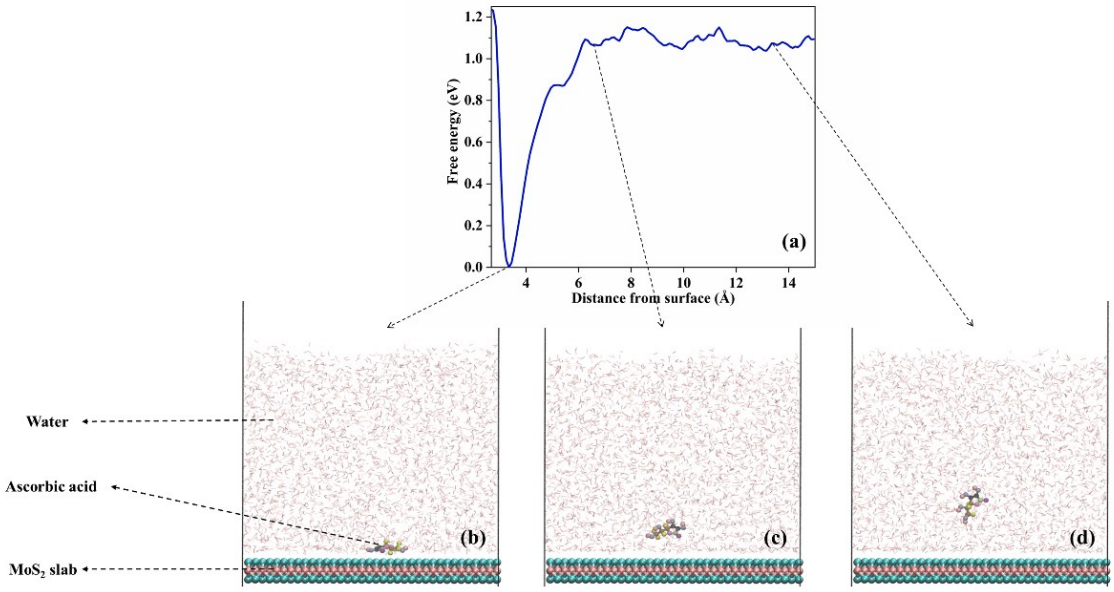

Figure 3-22. (a) Free-energy profile as a function of the distance of the centre of mass of AA from the surface of MoS2, (b),(c) and (d) show the position and orientation of AA molecule at a distance of 3.35 Å, 7.5 Å and 13.5 Å respectively.

It was found that the AA tends to naturally move towards the surface of the MoS_2 layer without any external force. These binding tendencies of AA over the surface make MoS_2 an excellent material for electrochemical detection in the aquatic environment through a feasible mechanism for both surface adsorption and diffusion-controlled processes. Based on these results, MoS_2 has been used to modify the SPCE-based sensing layer.

3.6 Conclusion

The chapter combines general oversights and my view on handling the experiment for the upcoming chapters. This study highlights the effect of printing thickness on electrochemical sensing performance. SEM images revealed a range of thicknesses in the printed layers. Modifying the working electrode with MoS_2 enabled the examination of how thickness impacts sensing capability. Sensors with thinner layers showed lower current values and higher resistance, indicating the role of thickness in the detection process. Conversely, thicker layers, precisely 15 and 20, exhibited higher current values, making them more suitable for integration with commercial readout electronics that operate with low power.

[4] Comparison of typical and printed electrochemical sensor-based setup using MoS_2 modified screen printed sensor for the detection of copper ions in water

The work adapted from:

(1) Neethipathi, D. K., Beniwal, A., Bass, A., Scott, M., & Dahiya, R. MoS2 modified Screen Printed Carbon Electrode based Flexible Electrochemical sensor for Detection of Copper ions in water. IEEE sensors journal (10.1109/JSEN.2023.3257188).

(2) Neethipathi, D. K., Ganguly, P., Beniwal, A., Scott, M., Bass, A., & Dahiya, R. (2022, July). MoS2 modified screen-printed carbon electrode-based flexible sensor for detection of copper. In 2022 IEEE International Conference on Flexible and Printable Sensors and Systems (FLEPS)

Traditionally, monitoring trace levels of heavy metals involves collecting discrete water or soil samples for weeks or months and analysing them in a laboratory setting. However, this approach is problematic for dynamic environments such as rivers and ample water supplies, where conditions can vary significantly over time and space. The infrequent sampling often makes establishing cause-and-effect relationships and developing timely management strategies challenging. Moreover, discrepancies can arise between sampling and analysis due to the time lag. Various sensors, including ion-sensitive field-effect transistors, have been investigated to overcome these issues.[179-181] Cost-effective sensors that can autonomously detect heavy metals are essential for large-scale applications. These sensors must be flexible, responsive, susceptible, and constructed using eco-friendly materials.[182] In this context, screen-printed electrochemical sensors on flexible substrates are particularly promising.[153, 183] They are low-cost and can be deployed for field testing under diverse conditions, including flowing and turbid water at various depths. Additionally, their affordability makes them suitable for frequent replacement or cleaning due to fouling from algae and bacteria in aquatic environments. We present a simple, disposable, and replaceable screen-printed carbon electrode (SPCE) sensor for detecting copper in response to these needs. The sensor utilises molybdenum disulfide (MoS_2) nanomaterials as the sensing layer, leveraging their high electrocatalytic properties and catalytic edge sites to achieve sensitivity in copper ion detection.[71] The sensor demonstrates excellent performance with a linear detection range from 5 µM to 1000 µM, a low detection limit (LOD) of 0.3125 µM, and high repeatability with a standard deviation of less than 0.5%.

4.1 Why is detecting copper ions in water important as an environmental aspect?

Heavy metals in water have emerged as a critical environmental and health issue. Effective monitoring practices are essential to guide policies that prevent the placement of chemical and ore mining operations near sensitive water resources or to mitigate harmful effluents from these operations.[184, 185] Due to its potential toxicity, it is crucial to monitor trace concentrations of heavy metals, particularly copper (Cu).[186] Excessive

copper intake can lead to severe health conditions, including Alzheimer's and Wilson's diseases.[187, 188] The Environmental Protection Agency (EPA) advises that the maximum allowable concentration of copper in drinking water should be 1.3 ppm (20.5 µM). In contrast, the recommended daily intake of copper for maintaining health is approximately 1.5 to 3 mg/day.

4.2 Experimental section

This section gathers all materials, fabrication steps and electrochemical procedures used in this chapter so that the MoS_2-modified SPCE and GCE measurements can be reproduced and compared.

4.2.1 Fabrication of sensor

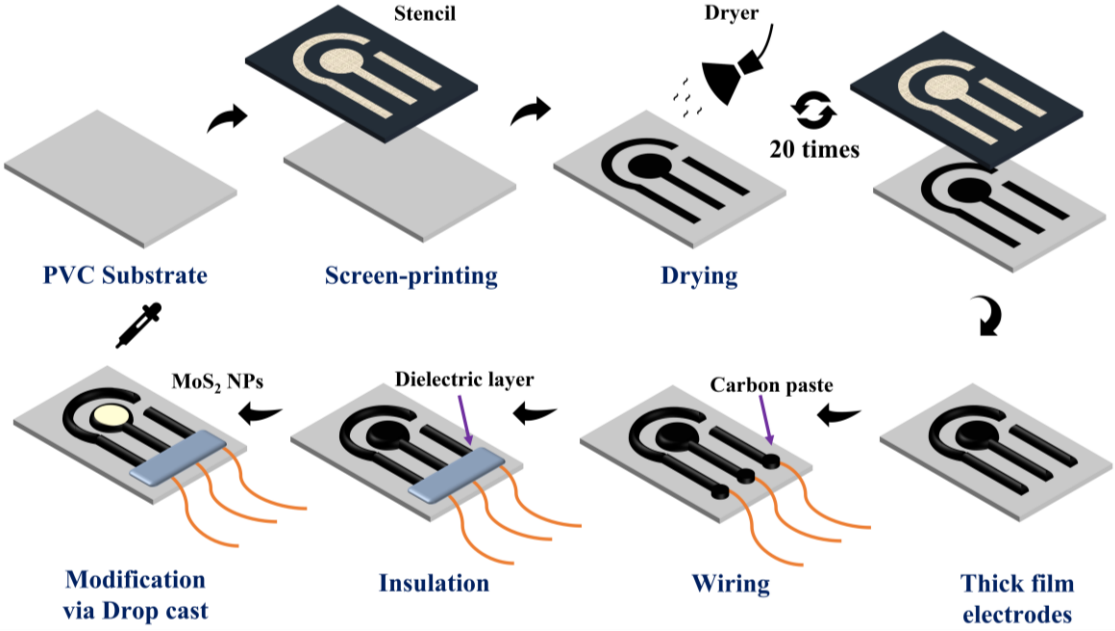

Figure 4-1: The manufacturing procedure of bulk electrodes for MoS_2 modified screen-printed sensor.

Figure 4-1 illustrates a schematic representation of the screen-printing process for thick film electrodes. The screen printing was carried out using the Screen Stencil Printer C920 from AUREL Automation. Prior to the screen-printing step, the commercially available carbon paste was thoroughly mixed with IPA and terpineol to achieve a paste with an appropriate viscosity for printing. In the case of the three-electrode system, comprising the working electrode (WE), counter electrode (CE), and reference electrode (RE), all electrodes were screen printed onto a flexible PVC substrate using the blended carbon paste ink. The working electrode, with a circular diameter of 0.5 cm, underwent the printing of multiple layers (20) to create a thick electrode layer.[189] To prevent the spreading or smudging of previously printed electrodes, each layer was dried individually by placing the sample in an oven at 70 ºC. The wire connections were established using the same conductive carbon paste, and the dried interconnections were covered with a thick layer of grey dielectric paste to prevent short-circuiting between the electrodes.

4.2.2 Modification of bare sensor with sensing coating layer

To modify the GCE and SPCE, 20 µl of the dispersed MoS_2 nanoparticle in DMF solution was dropped over the circular working region using a micropipette and kept in the oven at 65ºC for 45 mins. While drop casting the dispersed solution, multiple layers of MoS_2 were stacked on top of each other by successive drop casting method, where 5 µl quantity of the prepared solution was used to drop cast over the working electrode with intermediate drying at the oven. Here, the other electrodes (Counter, Reference) are unmodified, as it was intended to keep the analogous setup between screen-printed carbon-based and conventional setup as possible.

4.2.3 Characterization technique

XRD and SEM were used to characterise the material, which helped to understand the coating layer.

4.2.4 Electrochemical technique

Cyclic voltammetry (CV), differential pulse voltammetry (DPV), and electrochemical impedance spectroscopy (EIS) were conducted using an electrochemical workstation (Metrohm Autolab (PGSTAT302N)) to investigate the electrochemical behaviour of the developed sensor. For these studies, a neutral ionic solution with a constant pH of 7 was prepared by dissolving 1 PBS tablet in 500 mL of deionised (DI) water. The resulting PBS solution, with a concentration of 0.1 M, served as the electrolyte in electrochemical experiments. Analyte stock and interference solutions were prepared with 1 mM and 100 mM concentrations, respectively, by adding deionised water to copper, iron, cobalt, zinc, and nickel. For voltammetric techniques, these solutions were diluted and combined with 9 mL of PBS solution to achieve various concentrations of analyte solutions (ranging from 1 µM to 1 mM).

4.3 Results and Discussion

4.3.1 Material characterization of MoS_2 printed sensors

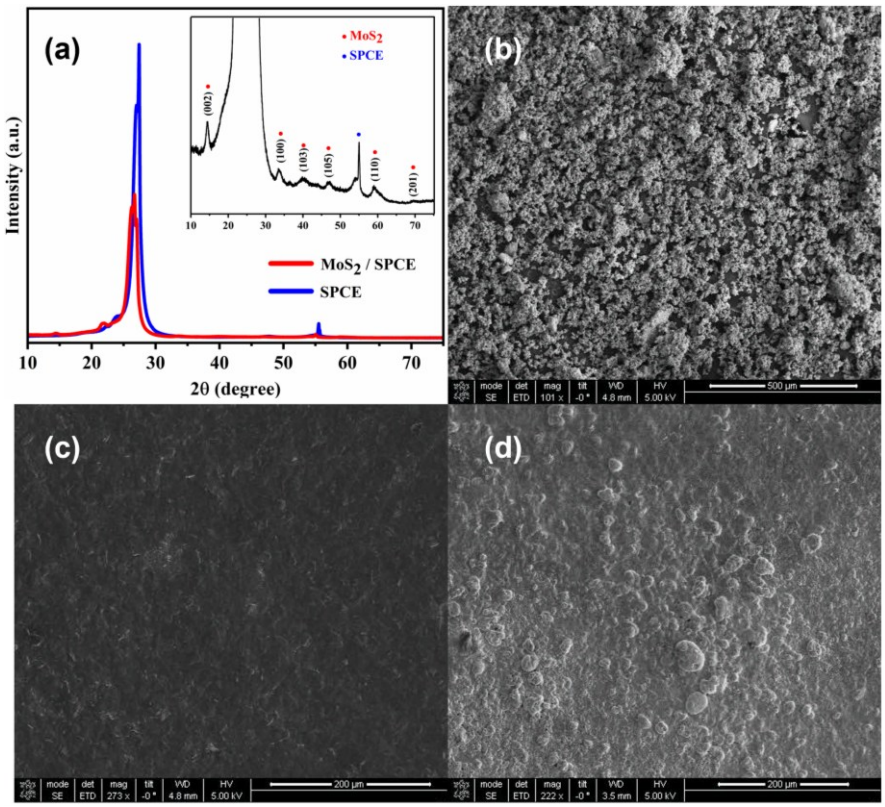

Figure 4-2: (a) shows the XRD Pattern for MoS2 powder and MoS2 coated SPCE layer; SEM images of (b) MoS_2 powder (c) SPCE, (d) MoS_2 modified SPCE.

.X-ray diffraction (XRD) analysis was conducted using XRD P'Analytical X'Pert with Cu Kα (λ = 1.541 Å), and scanning electron microscopy (SEM) analysis was performed using FEI Nova. The XRD patterns (Figure 4-2(a)) revealed peaks at 14.17º, 33.45º, 39.5º, 49.17º, 58.843º, and 69.434º (of the red line), confirming the lattice planes of the hexagonal phase of 2-H MoS_2 (i.e., (002), (100), (103), (105), (110), (201), respectively) based on ICDD card no: 37-1492.[189] The blue line represents the XRD pattern for SPCE. SEM images (Figure 4-2(b, c, d)) were captured to examine the surface morphology of MoS_2-modified SPCE, unmodified SPCE, and drop-casted MoS_2 over SPCE. The synthesized MoS_2 nanoparticle powder appeared as a cluster of agglomerated spherical nanoparticles. The SPCE exhibited a smooth layer of well-homogeneous carbon ink surface. In contrast, the modified SPCE displayed a surface with high roughness and a few cracks, confirming the presence of MoS_2 nanoparticles after modification.

4.3.2 Electrochemical detection results

Figure 4-3(a) exhibits the fabricated sensor based on SPCE after MoS_2 modification, while Figure 4-3(b) illustrates the electrochemical detection of copper ions using the MoS_2-modified SPCE-based sensor. The black and red lines in the figure represent the CV curve for bare SPCE and MoS_2-modified SPCE in a blank 0.1 M PBS solution. The blue line depicts the CV curve in the presence of 100 µM copper ions in PBS solution, showcasing oxidation and reduction peaks at 0.2 V and -0.01 V, respectively. This insight aids in understanding

the redox reaction of copper, detectable by the MoS_2-coated SPCE layer. Subsequently, the DPV curve in Figure 4-3(c) reveals the peak anodic current resulting from MoS_2 modification, providing a means to detect analyte concentration. The red line in the same range from -0.3 V to 0.8 V, at a step potential of 5 mV/pulse, confirms the increase in the peak anodic current. Additionally, a slight shift in the peak voltage from 0.2 V to -0.01 V is observed upon adding 100 µM Cu analyte ions to the blank solution, indicating the oxidation of Cu ions.

CONCENTRATION STUDY

For the concentration studies, cyclic voltammetry responses were obtained from -0.3 V to 0.8 V at a scan speed of 50 mV/s. Varying concentrations of copper ions from 1 µM to 1000 µM in 0.1 M PBS were investigated, as depicted in Figure 4-3(d). The oxidation peaks for these concentrations, ranging from 1 µM to 1000 µM, were observed at 0.16 V to 0.19 V, while their corresponding reduction peaks occurred at 0.01 V to -0.03 V. The differential curve in Figure 4-3(e) illustrates anodic current peaks shiting in the range of 0.04 V to 0.06 V with varied analyte concentrations in the 0.1 M PBS solution. The difference in peak current value between concentrations of 100 µM and 500 µM was found to be 0.00904 mA, which is four times higher than the change observed in the modified GCE.

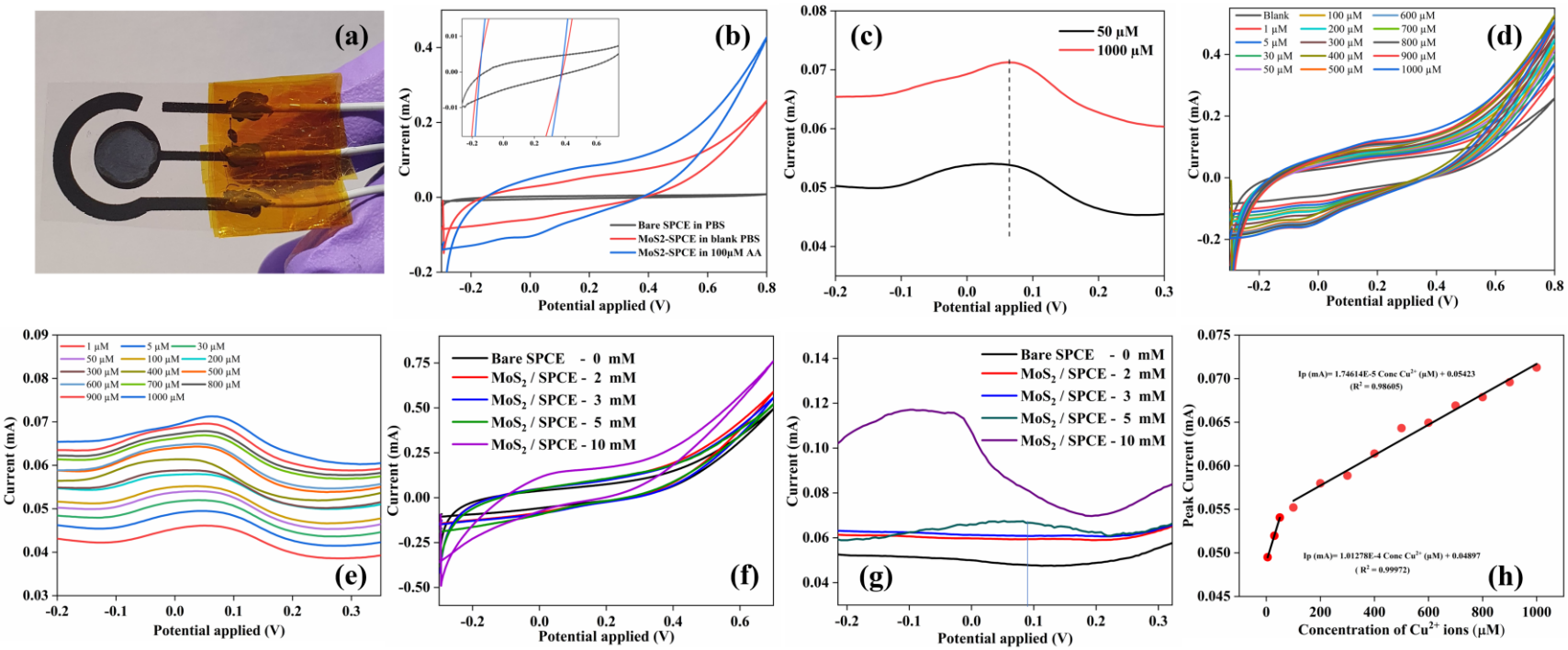

Figure 4-3: (a) A photograph of the fabricated sensor. (b) CV curves of bare SPCE, MoS_2/SPCE in PBS solution & MoS_2/SPCE in 100 µM of copper ions in PBS solution. (c) DPV response curve for MoS_2/SPCE in the presence of 100 µM to 1000 µM of copper ions in PBS. (d, e) CV and DPV responses for 1 µM to 1000 µM of copper analyte in PBS solution. (f, g) CV and DPV responses for 2 mM to 10 mM of copper analyte in PBS solution. (h) Peak current (Ip) vs copper concentration between 1 µM to 1000 µM

To comprehend the electrochemical behavior of the fabricated sensor at higher concentrations (2 mM to 10 mM), CV and DPV responses were obtained and presented in Figure 4-3(f, g). Based on the DPV curve response, the anodic peak current rose to 5 mM at 0.07 V. The DPV peak curve for 10 mM expanded significantly over the -0.3 V to 0.1 V region with a negative peak shift at -0.05 V, rendering it undetectable and outside the detection range. Linearity was assessed by plotting Cu concentrations between 5 µM to 1 mM against their respective DPV peak current values, as shown in Figure 4-3(h). Two linear regions were identified within the concentration range of 5 µM to 1000 µM.

$$Ip = 1.01278E - 4 * (Conc.Cu2+) + 0.04897 \quad (1)$$

A sharp initial rise was observed within the first linear range (5 to 50 µM) with high linearity (R^2 value of 0.99972). The linear regression equation for this range is expressed as follows:

$$Ip = 1.74614E - 5 \times (Conc.Cu2+) + 0.05423 \quad (2)$$

This sharp rise in peak current between 5 µM to 50 µM suggests that the diffusion of loosened valence electrons resulting from the oxidation of copper benefits from numerous electrocatalytic edge sites available on the surface of 2D MoS_2. The second linear range observed at higher concentrations (100 µM to 1000 µM) exhibits linearity with an R^2 value of 0.98605, expressed by the linear regression expression:

The second linear rise in peak current within the region of 100 µM to 1000 µM can be explained by the partial blockage of active sites by electrocatalytic edge sites after reaching a certain threshold concentration (100 µM in this case). The deposition of oxidized copper ions (cupric ions) over the electrocatalytic edge sites of the MoS_2 sensing layer during oxidation reduces the diffusion of loosened valence electrons due to fewer available active sites for further diffusion.[71] During the reduction phase, these deposited Cu^{2+} ions reduce to Cu ions, reversing the deposition onto the sensing layer. The slope in both linear ranges is close to 0.05, indicating that the increase in the concentration of Cu ions is directly proportional to the increase in peak current. The limit of detection (LOD) was found to be 5.43 µM, and the limit of quantification (LOQ) was 16.46 µM.

BASELINE CALIBRATION

Table 4-1: Baseline calibration and the percentage current increase for varying copper concentraions.

Increase in concentration of copper ions	% avg. peak current change observed (% change * base current)
	Here, + or – 1.5% variation
5 uM	~ 8%
100 uM	~ 22%
200 uM	~ 28%
500 uM	~ 36%
1000 uM	~ 58%

The average percentage of increase in baseline current with respect to the increasing current caused by the varying concentration is tabulated in Table 4-1.

ACCUMULATION STUDY

An investigation involving varying scan speeds was conducted to gain insights into the sensing mechanism, as illustrated in Figure 4-4(a). CV scans were acquired at different scan speeds ranging from 10 to 700 mV/s in the presence of 100 µM copper ions in a 0.1 M PBS solution. By analysing the scan speed and identifying the presence of recognisable peaks, the optimised scan rate for detecting the analyte solution was determined to be between 10 mV/s and 200 mV/s.

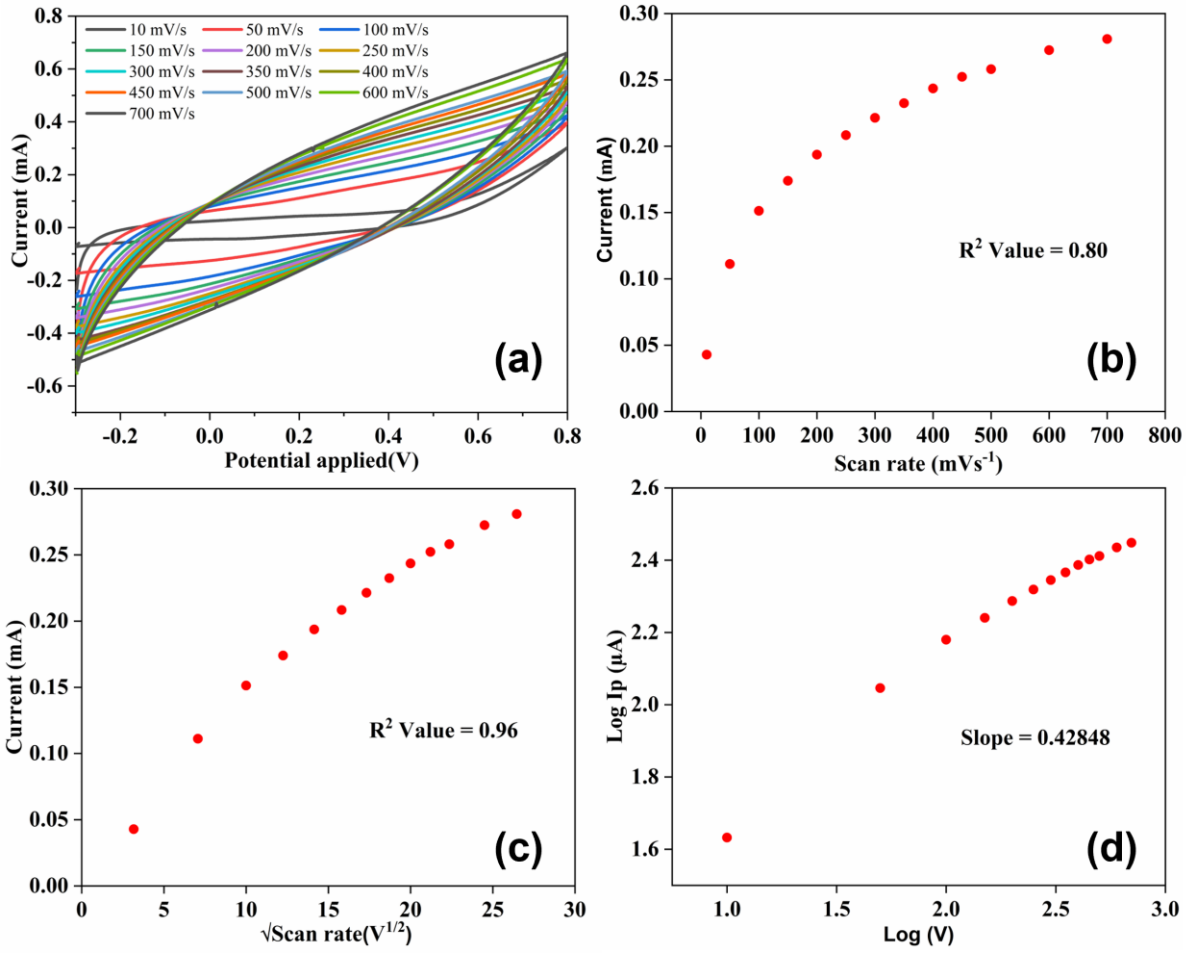

Figure 4-4: (a) CV response curves for detecting 100 µM of Cu2+ ions in PBS with a different scan rate of 10 to 700 mV/s; (b) IP versus scan rate; (c) IP versus √scan rate; (d) Log of IP versus Log of scan rate.

The oxidation peak current values for each CV scan were plotted against their corresponding scan rates in Figure 4-4(b), yielding an R^2 value of 0.8. Subsequently, the varying scan rate was plotted in Figure 4-4(c) against the square root of the oxidation peak value (Ip), resulting in an R^2 value for their regression line of 0.96. The regression line obtained from the square root of the scan rate vs. peak current value (Ip) plot was more linear than the line obtained from the scan rate vs. peak current value (Ip) plot. These findings indicate

that the sensing of analyte species is more likely a diffusion-controlled process than an absorption-controlled one.

In Figure 4-4(d), the logarithm of the oxidation peak current value is plotted against the logarithm of the scan rate, revealing a slope of the regression line close to 0.42848. This proximity to the ideal diffusion-controlled process value of 0.5 suggests that the sensing mechanism follows a diffusion-controlled pathway.[190]

REPEATABILITY STUDY

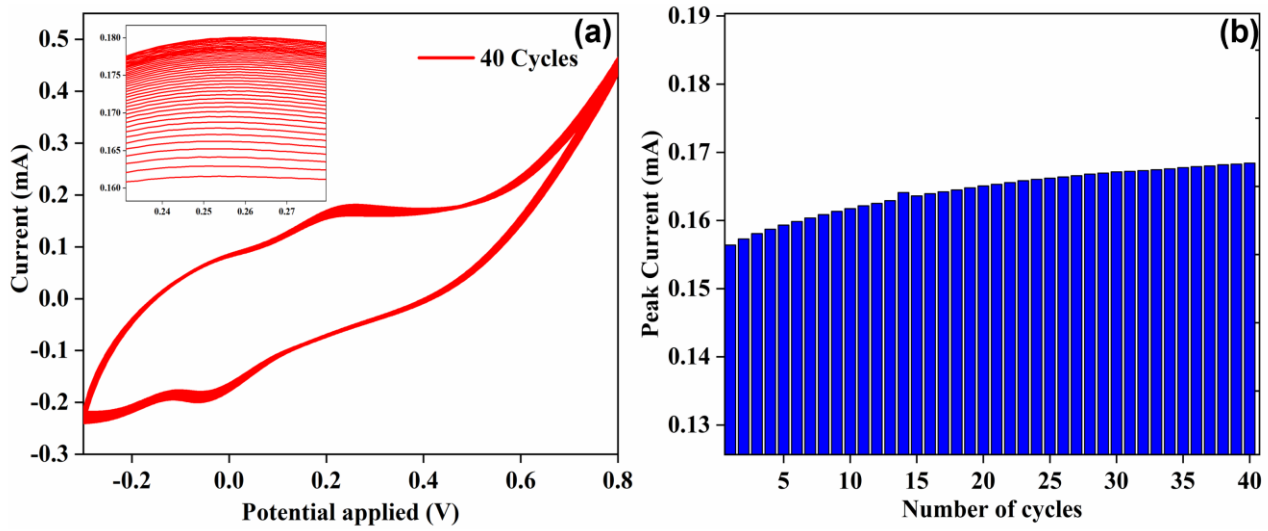

Figure 4-5: (a) CV response of MoS_2/SPCE in 100M of Cu^{2+} ions in PBS for 40 cycles at 50mV/s; (b)Bar graph for 40 CV cycles with their oxidation peak current response.

To investigate repeatability, a continuous cyclic voltammogram comprising 40 cycles was conducted for a 100 µM Cu ions concentration in a PBS electrolyte solution at a scan speed of 50 mV/s, as depicted in Figure 4-5(a). As a result of the preconditioning for the modified SPCE, both oxidation and reduction peak currents exhibited a gradual initial increase followed by saturation. In Figure 4-5(b), a bar graph illustrates the oxidation peak current for each cycle, with a standard deviation of 0.00334 mA observed over the collective 40 cycles.

INTERFERENCE STUDIES

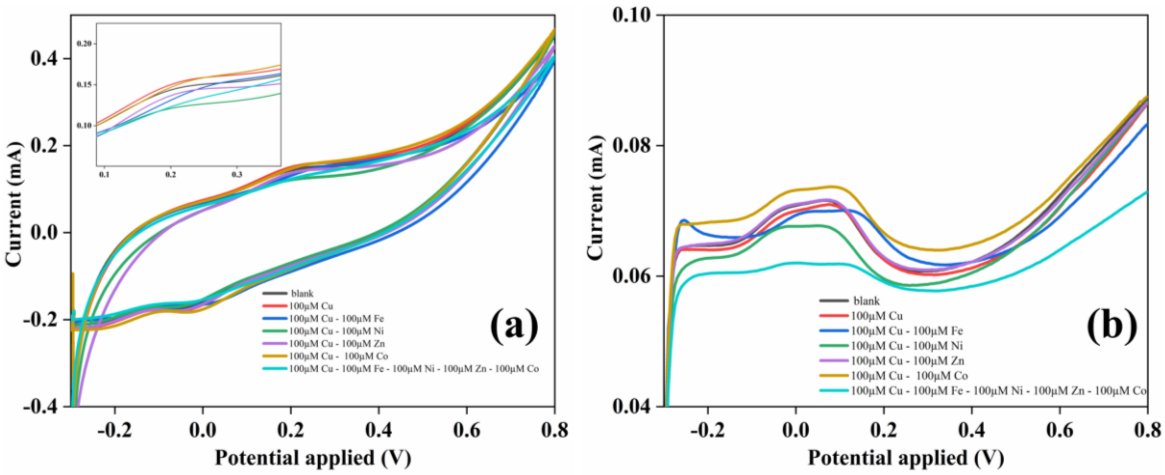

Figure 4-6: (a) CV responses for the detection of 100 µM Cu ions, along with other heavy metal ions; (b) DPV responses for the detection of 100 µM Cu ions, along with other heavy metal ions.

Interference studies were conducted to assess the electrochemical detection of the target analyte species, namely 100 µM Cu^{2+} ions, in the presence of other similar heavy metal ions, including nickel, zinc, cobalt, and iron. The CV and DPV responses for these interactions are presented in Figure 4-6(a, b). Additional CV and DPV responses illustrating the interaction with the mentioned analyte species can be found in Figures 4-7,4-8,4-9,4-10. These responses were obtained by introducing various heavy metal ions (HMIs) with 50 µM and 100 µM concentrations to a solution containing 100 µM Cu analyte ions in a 0.1 M PBS solution. Notably, the interference study observed that the addition of Fe^{2+} significantly impacted the response for copper ions, which was evident from the observed peak shift in anodic DPV current when Fe^{2+} ions were introduced.

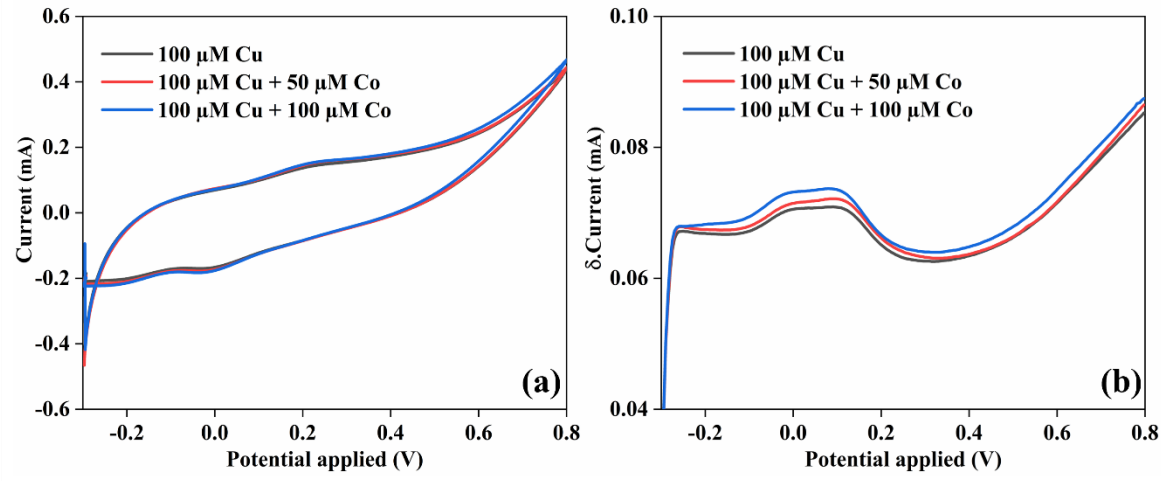

Figure 4-7: (a, b) CV and DPV responses for MoS2 coated GCE layer for the detection of copper ions in the presence of 0, 100, 500 µM Co2+ ions in 0.1M PBS respectively

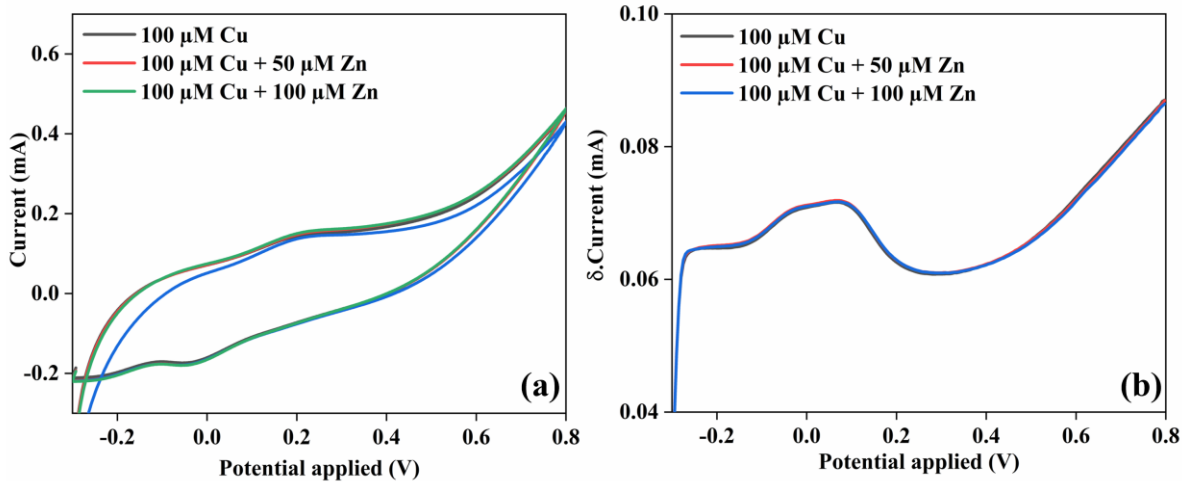

Figure 4-8: (a, b) CV & DPV responses for the detection of 100 µM Cu ions, along with Zn ions of 50 µM, and 100 µM.

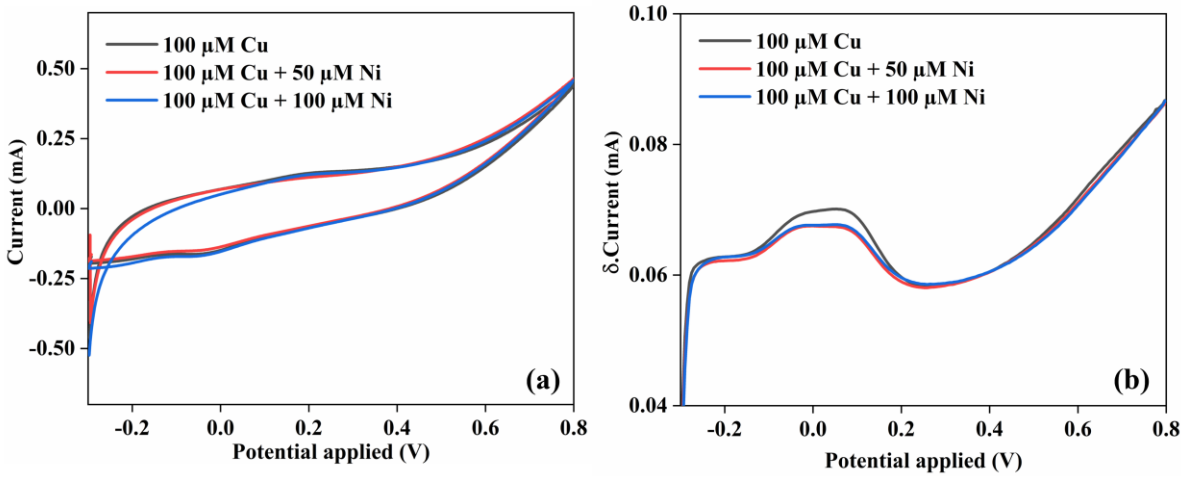

Figure 4-9: (a, b) CV & DPV responses for the detection of 100 µM Cu ions, along with Ni ions of 50 µM, and 100 µM.

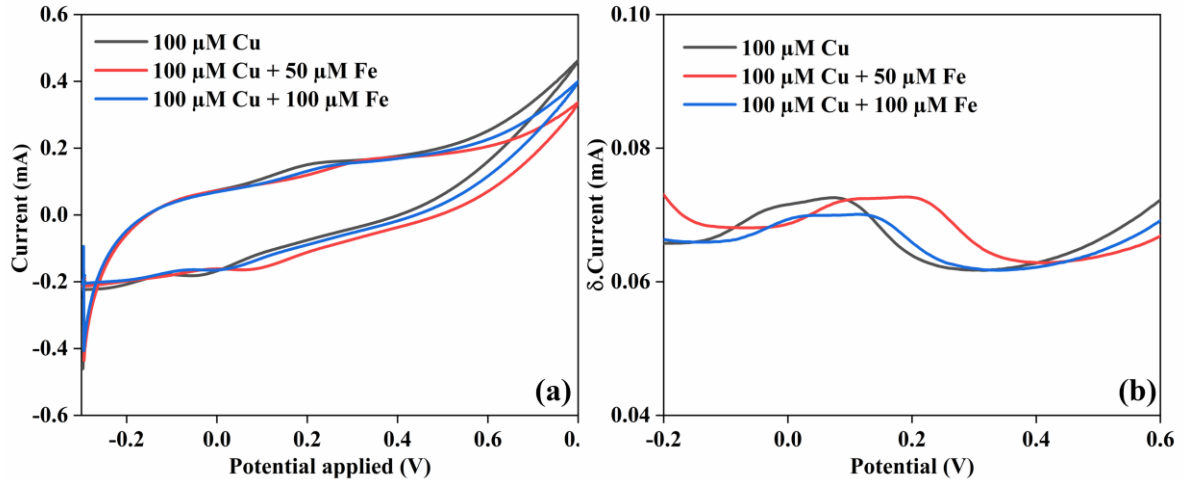

Figure 4-10: (a, b) CV & DPV responses for detecting 100 µM Cu ions, along with Fe ions of 50 µM, and 100 µM.

4.3.2.2 Detection of Copper Ions by MoS_2-Coated Glassy Carbon Electrode

In the employed 3-electrode system, the MoS_2-modified GCE served as the working electrode, a platinum coil functioned as the counter electrode, and an Ag/AgCl electrode was used as the reference electrode. In Figure 4-11(a, b), both CV and DPV responses are presented for the bare GCE and MoS_2-modified GCE in the absence and presence of 100 µM and 500 µM Cu^{2+} ions. The difference in peak current values for Cu^{2+} ion detection between 100 µM and 500 µM concentrations is 0.00228 mA.

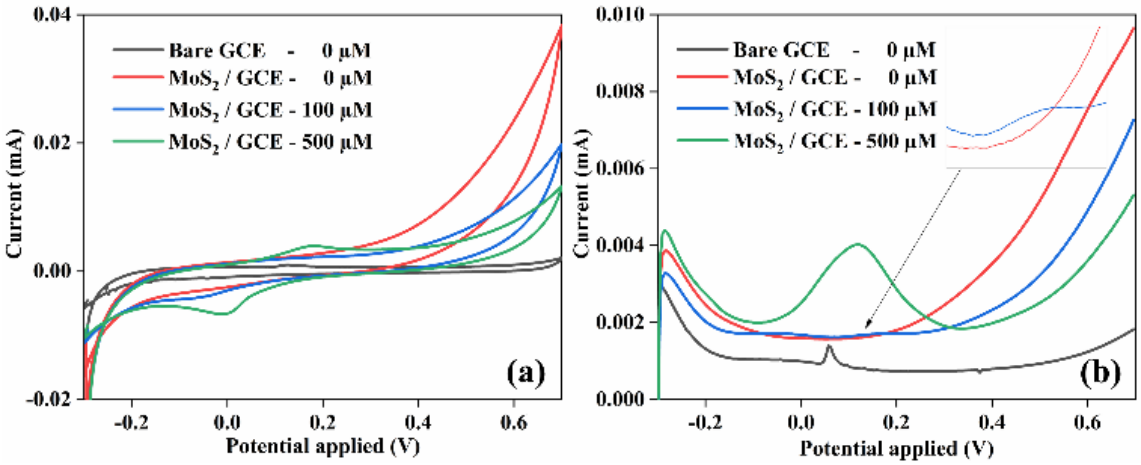

Figure 4-11: (a, b) CV and DPV responses for MoS_2 coated GCE layer in the presence of 0, 100, 500 µM Cu^{2+} ions in 0.1M PBS, respectively

4.3.2.3 Comparison of GCE and SPCE using EIS technique

To compare the response of SPCE with GCEs, Nyquist plots were obtained in the absence and presence of 100 µM copper ions, as depicted in Figure 4-12(a). For this study, bare GCE with Ag/AgCl and platinum coil was used for EIS measurements in the absence and presence of 100 µM Cu ions in a 0.1 M PBS solution. In both cases, the absence of a semicircle at the high-frequency zone indicates the absence of a double-layer region, resembling characteristics typical of a supercapacitor.[191] This is attributed to the high conductivity and low charge transfer resistance of glassy carbon. However, at the lower frequency zone, the bare electrode exhibits the behavior of a constant phase element (CPE) with a constant phase difference angle (θ) of 62º without copper ions and 84º with copper ions (n = 0.688 & 0.933). The bare GCE displays imperfect capacitive behavior with the addition of copper ions, as the deviating angle remains closer to the ideal capacitor behavior (θ = 90º).[192] Nevertheless, the series resistance of this bare electrode remains almost constant at around 108 ohms in the presence and absence of Cu ions, suggesting no significant change in the interaction between the electrode and the electrolyte in both cases. Figure 4-12(b) presents the Nyquist plot via EIS measurements for the MoS2 modified GCE, both in the absence and presence of Cu ions. In the absence of Cu ions, a semicircle is not observed in the high-frequency region, and the plot resembles a CPE at a lower frequency, possibly due to the surface roughness of the electrode (θ = 41º). However, the presence of a partial semicircle in the higher frequency region could be attributed to a combination of electrode resistance and charge transfer resistance at the surface interface (double-layer formation), acting as a CPE followed by Warburg impedance (θ = 44º).

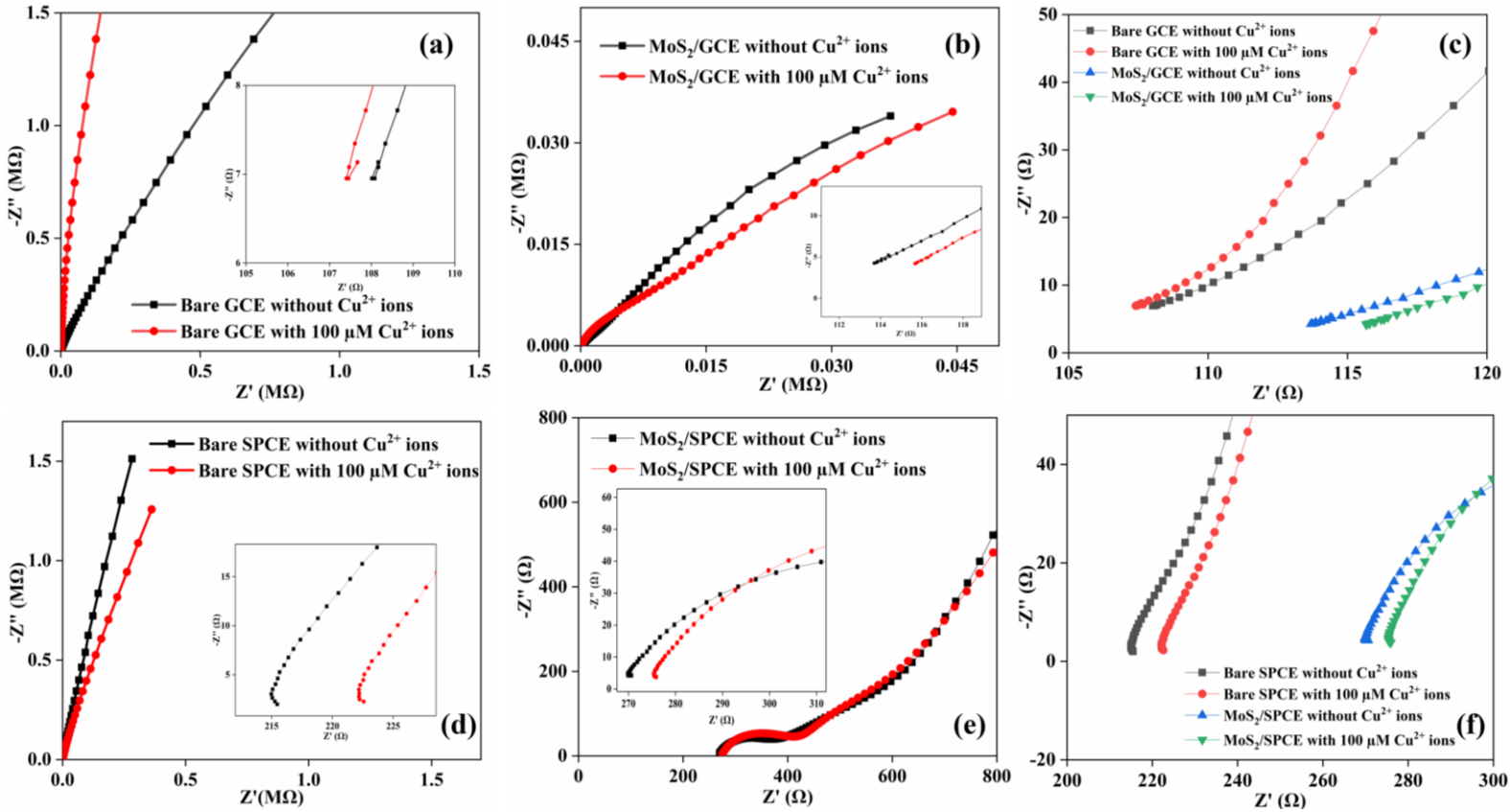

Figure 4-12: (a, b) Nyquist plot for the bare GCE and bare SPCE electrodes in the absence and presence of 100 µM copper ions respectively; (c) Nyquist plot for both bare GCE and bare SPCE in the high-frequency region; (d, e) Nyquist plot for the MoS_2 modified GCE and MoS_2 modified SPCE electrodes in the absence and presence of 100 µM copper ions respectively; (f) Nyquist plot for both the MoS_2 modified GCE and MoS_2 modified SPCE in the high-frequency region.

As shown in Figure 4-12(c), the initial electrode resistance for both bare and modified GCE is calculated to be around 111.47 ohms to 113.5 ohms in the absence and presence of copper ions, respectively. Figure 4-12(d) illustrates the Nyquist plot for the bare SPCE electrode obtained from the EIS measurements in the absence and presence of the analyte solution, i.e., 100 µM Copper ions. The bare SPCE exhibits similar CPE behaviour at lower frequencies and no formation of a double-layer region (charge transfer resistance) due to its high conductivity. The constant phase (n) value was found to be 0.877 and 0.811 with the phase difference angle of 79º & 73º in the absence and presence of Cu ions, respectively. Comparing the constant phase of these bare electrodes, it is noted that the capacitive impedance builds in MoS_2-modified GCE in the presence of the analyte solution, while the capacitive impedance drops in the case of SPCE. Figure 4-12(e) shows the Nyquist plot for the MoS_2 modified SPCE. In the absence and presence of the analyte solution, a semicircle is formed at a higher frequency due to the double-layer region, and CPE (n = 0.633 & 0.688, respectively) is seen at lower frequencies. The Nyquist plot for all electrodes in both the absence and presence of 100 µM Copper ions for a comparative study i.e The electrode and electrolyte resistances for both bare and modified SPCEs are shown in Figure 4-12(f). The internal resistance due to both electrode and electrolyte for MoS_2-modified GCE and SPCE is around 328.28 ohms and 370.27 ohms, respectively. In contrast, their respective electrode resistance is measured as 279.57 ohms and 280.12 ohms from the fitted graphs. Figure 4-14 includes the Bodes plot, and Figure 4-13 contains the Frequency vs. Impedance plots for all the above cases. From the above, it can be concluded that the modified GCE exhibits Warburg impedance, which is characteristic of an excellent diffusion-controlled process. In the case of modified SPCEs, even if there is a slight tendency towards CPE characteristics (n = 0.633 & 0.688), this could result from both the capacitive nature of SPCE and ion diffusion. Further, the response current results from both surface-controlled and diffusion-controlled currents.[193]

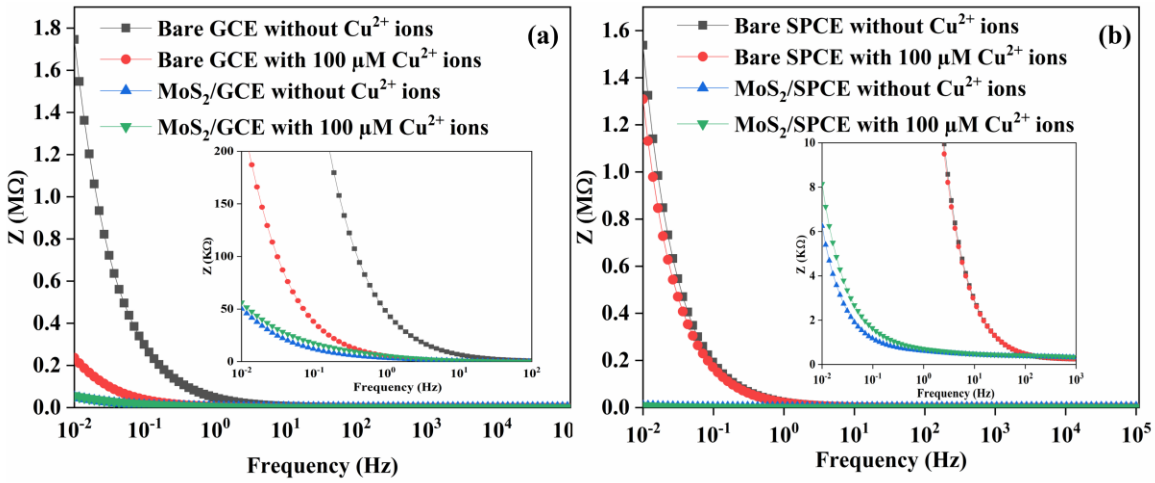

Figure 4-13: (a, b) Frequency vs. Impedance plots for both unmodified & modified GCE, and SPCE in the absence and presence of 100 µM copper ions.

The overall peak current change observed in the modified SPCE at different concentrations is higher than that observed for the modified GCE. The high charge transfer resistance and the internal capacitance behavior of MoS_2 modified SPCE aid in differentiating peak current changes between smaller concentrations. This

indicates that the SPCE exhibits better diffusion phenomena. The capacitive behavior for charge transfers due to the formation of a double-layer region helps in the better detection of diffusing Cu ion species.

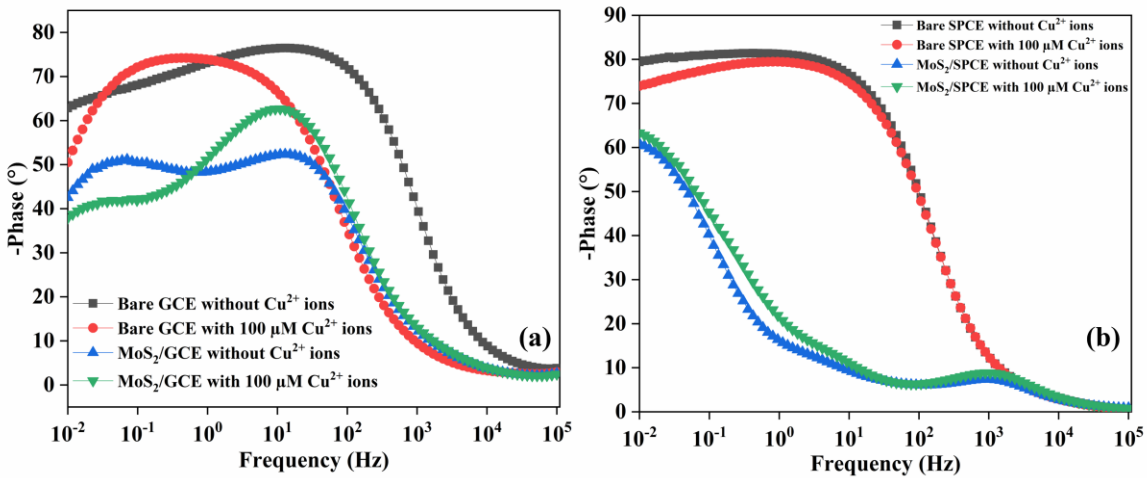

Figure 4-14: (a, b) Bode plots for both unmodified & modified GCE, and SPCE in the absence and presence of 100 µM copper ions.

4.4 Conclusion

Heavy metal ions (HMIs), such as Cu^{2+}, pose significant risks to both the environment and human health. Traditionally, these ions are detected using electrochemical sensors based on glassy carbon electrodes (GCE) mounted on rigid substrates. However, many modern applications demand flexible and even disposable sensors. In this study, we present a flexible electrochemical sensor based on molybdenum disulfide (MoS_2)-modified screen-printed carbon electrodes (SPCE) for detecting copper ions in water. The sensor demonstrates high sensitivity with a limit of detection (LOD) of 5.43 µM for Cu^{2+} ions within the range of 5 µM to 5 mM. Compared to MoS_2-modified GCE, electrochemical impedance spectroscopy (EIS) results show that the SPCE-based sensor has better linearity ($R^2 \approx 0.99$) and effectively detects copper ions. Additionally, interference studies, which tested the detection of copper in the presence of other HMIs, confirm the sensor's robust performance, making it suitable for practical copper ion detection in water.

[5] Electrochemical detection of Iron content in water using multiple electrode materials

The work adapted from:

(1) Neethipathi, D. K., Beniwal, A., Ganguly, P., Scott, M., Bass, A., & Dahiya, R. Electrochemical Detection of Fe2+ Ions in Water Using 2-Dimensional g-C3N4 Modified Glassy Carbon Electrode-Based Sensor. 2023 IEEE Applied Sensing Conference (APSCON); The first author, who led the experimental design, data acquisition, analysis, and manuscript preparation.

In this Chapter, the introduction of a 2-dimensional (2D) Graphitic Carbon Nitride (g-C_3N_4) modified glassy carbon electrode (GCE) as an electrochemical sensor for detecting Fe^{2+} ions in water is presented. The 2D g-C_3N_4 nanosheet used as the sensing layer is environmentally friendly, and the sensor demonstrates excellent performance within the range of 0.9 mM to 5 mM iron in water. Furthermore, Both Carbon-based electrodes and the silver-based electrode were used to illustrate the detection of fe^{2+} and fe^{3+} ions with different data collection approach, and they successfully achieved similar results with the ICP-OES results for the sample spiked water samples with less than 15% accuracy variation and thus providing an easily disposable, cheaper sensor for detection in the field.

5.1 Why should iron be monitored in water?

Iron is a critical element in both biological and environmental systems. It is found in water, as well as in various minerals within the Earth's crust. The human body needs an average of 8 to 12 mg of iron daily for essential functions, such as oxygen transport in the blood. Iron deficiency can lead to issues like fatigue and anemia. In aquatic ecosystems, iron traces are also crucial for sustaining life. However, excessive iron concentrations in water can be harmful, as high levels of heavy metal ions are toxic and non-biodegradable[194]. Therefore, regular monitoring of iron levels in water bodies, such as lakes, rivers, and ponds, is essential[185].

Traditional methods for assessing water quality include spectrophotometric and colorimetric analyses, which often require laboratory settings and are challenging to perform in the field. Given the variability in water quality due to environmental factors like rainfall or human activities such as chemical waste disposal, there is a need for compact and cost-effective on-site sensors.[195, 196] Electrochemical sensors are particularly valued for their rapid response, high sensitivity, and selectivity.[197, 198]

5.2 Experimental section

All experimental details for the g-C_3N_4-modified electrodes and Fe^{2+}/Fe^{3+} measurements are compiled in this section, including material preparation, sensor fabrication and electrochemical protocols, to enable reproducibility of the results presented in this chapter.

5.2.1 Synthesis of Pristine g-C3N4

The production of pure graphitic carbon nitride (g-C3N4) powder was achieved through the thermal condensation and evaporation of a melamine precursor. In this procedure, melamine—a nitrogen-dense organic compound—undergoes high-temperature polymerization. This thermal treatment facilitates the transition of melamine molecules into a stable, polymeric g-C_3N_4 network.To ensure the chemical integrity of the final product, an evaporation phase was conducted under regulated parameters. This crucial step eliminates secondary byproducts and leftover solvents, yielding a refined powder with the structural precision required for high-performance applications, such as electrochemical sensing.

5.2.2 Ink Preparation and Electrode Modification

2D nanomaterial suspension was prepared by integrating 20 mg of the synthesized g-C_3N_4 into 1 mL of dimethylformamide (DMF). To ensure a uniform dispersion, the mixture was treated via probe ultrasonication. For the modification of the Glassy Carbon Electrode (GCE), a multi-step drop-casting technique was employed:Volume: 5 µL of the g-C_3N_4 ink was applied per layer.Frequency: The casting process was repeated four times.Drying: Between each application, the electrode was dried in an oven at 60°C for 15 minutes to ensure a stable and consistent film.

5.2.3 Material Characterisation

The prepared g-C_3N_4 salts were characterized by X-ray diffraction patterns. Fig. 5-1(a) shows the peak obtained from the XRD for the prepared salt. The peaks at 12.96 and 27.46 indicate the lattice planes of (100) and (002) of g-C_3N_4 respectively. This is also confirmed using the ICDD card 00-066-0813. The SEM image for the coated g-C_3N_4 layers over the screen-printed carbon paste substrate (similar to the glassy carbon surface) is shown in Fig. 5-1(b). This indicates multiple coated layers having a homogenous surface over the substrate without any cracks or nanopores. These results also signify the well spread of 2D nanomaterial with uniformity.

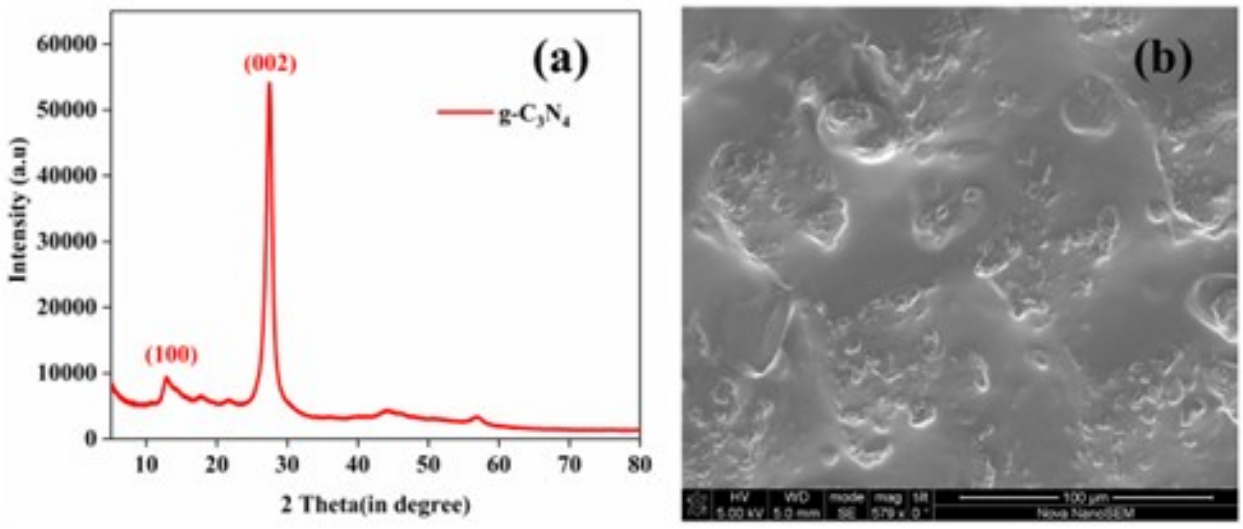

Figure 5-1: a) XRD pattern for g-C_3N_4 powder. (b) SEM images of g-C_3N_4 coated carbon layer.

5.2.4 Determination using a silver electrode

A printed sensor version was developed by modifying all silver electrodes of a screen-printed electrochemical sensor with g-C_3N_4 nanoparticles. The stock solution of fe^{2+} and fe^{3+} ions was prepared for the concentration study from Iron (II) chloride tetrahydrate. The plots of cyclic voltammetry and Differential pulsed voltammetry graphs are obtained between similar testing ranges from the referred paper, which is 0.5 mM to 5.01 mM (i.e., 28 mg/L to 280 mg/L).

Figure 5-2 shows the cyclic voltammetry and DPV results for detecting various Fe^{2+} concentrations. Figure 5-2(a) shows a clear reduction peak of Fe^{2+} ions to Fe ions, suggesting a redox reaction between Fe and Fe^{2+} ions. In DPV results, the modified silver electrode helps clearly distinguish the oxidation peak current from around -0.17 V to 0.4 V.

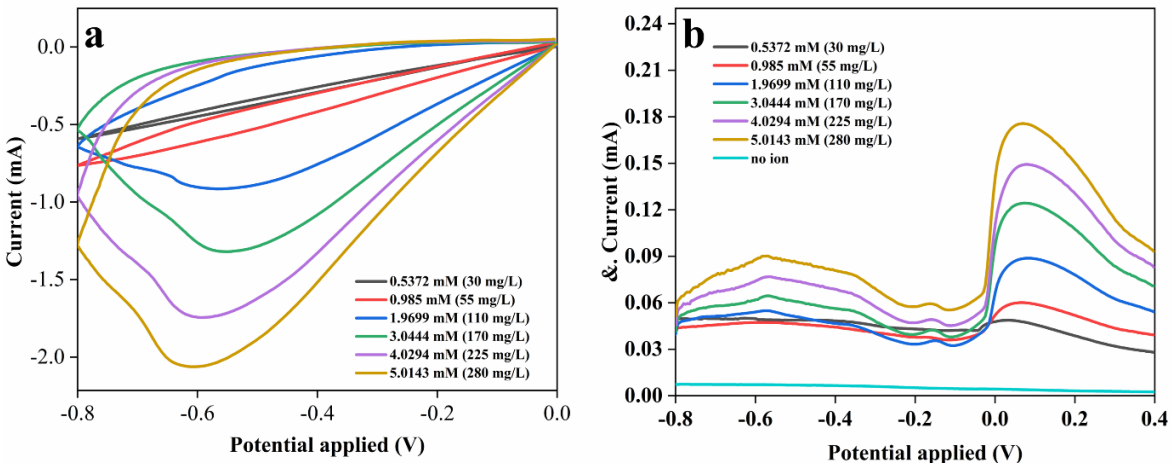

Figure 5-2: Cyclic voltammetry and Differential pulsed voltammetry response curve for varying fe^{2+} concentration.

From Figure 5-3, the peak currents were plotted against the concentrations of Fe^{2+} ions between 30 mg/L and 130 mg/L. The R-square value of 0.99615 shows a highly linear detection range between 30 and 130 mg/L.

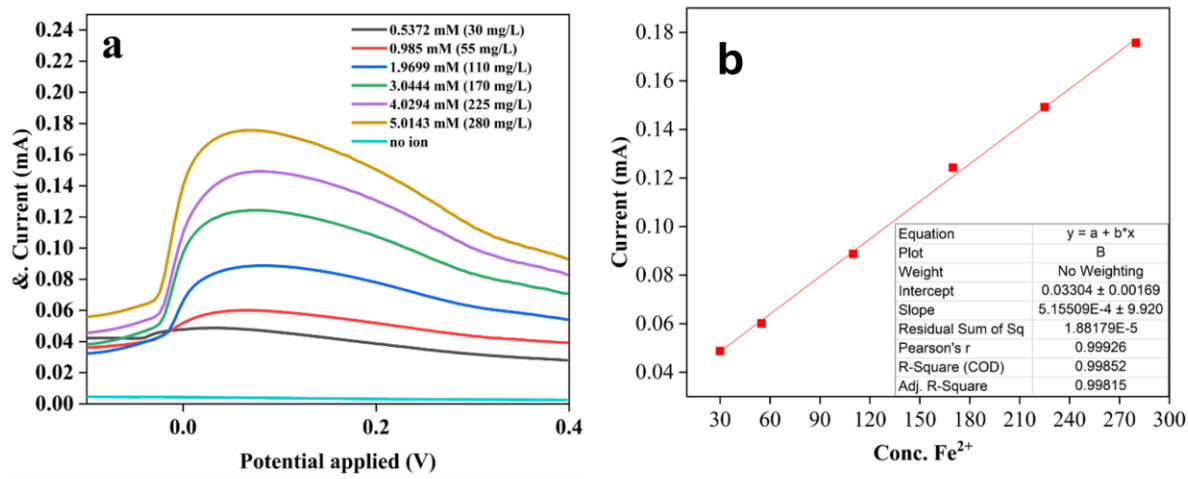

Figure 5-3: Peak current observed against the concentration of fe^{2+} ions – plot.

For this test, four Fe^{2+} ion solutions at different concentrations were prepared, and ICP-OES measurements were performed to verify the prepared concentrations and support the electrochemical results. These solutions were blind-tested with the same sensor. CV and DPV were obtained by directly dipping the fabricated sensor into the water samples. Among the given solutions, CV and DPV response results were obtained clearly for two of the given samples, which were further considered for testing (later found to be concentrations of 10 mg/L and 100 mg/L), as shown in Figure 5-4.

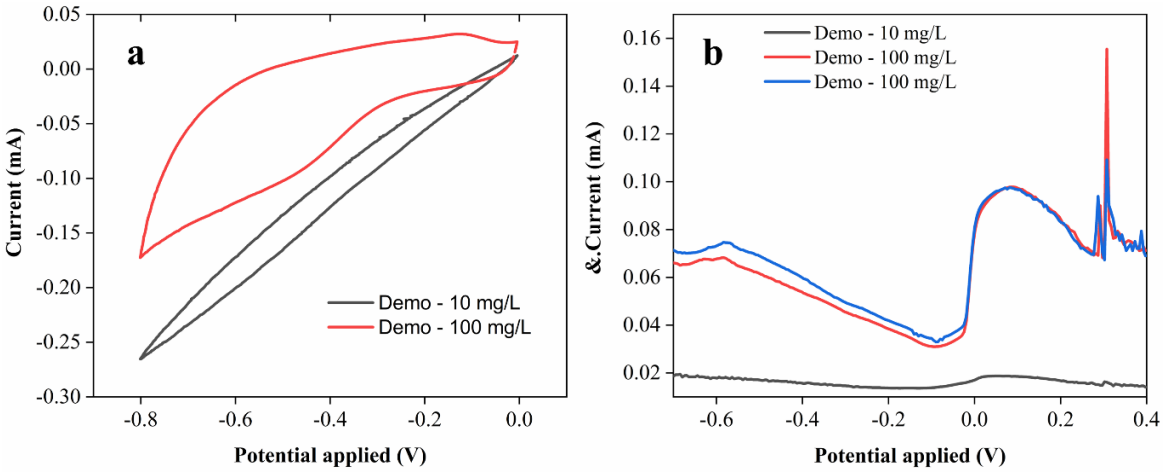

Figure 5-4: Cyclic voltammetry and DPV response of Fe^{2+} ions in water.

When these results overlapped with the existing data in Figure 5-5, in Figure 5-5(b), the measured peak current was correlated with the linear fit line between the peak current and the concentration graph. Here, the measured concentration was 126.48 mg/L. Based on the ICP-OES results, the tested solution has a concentration of 135.71 ppm (135.71 mg/L). Therefore, the accuracy error percentage is roughly 6.8 %.

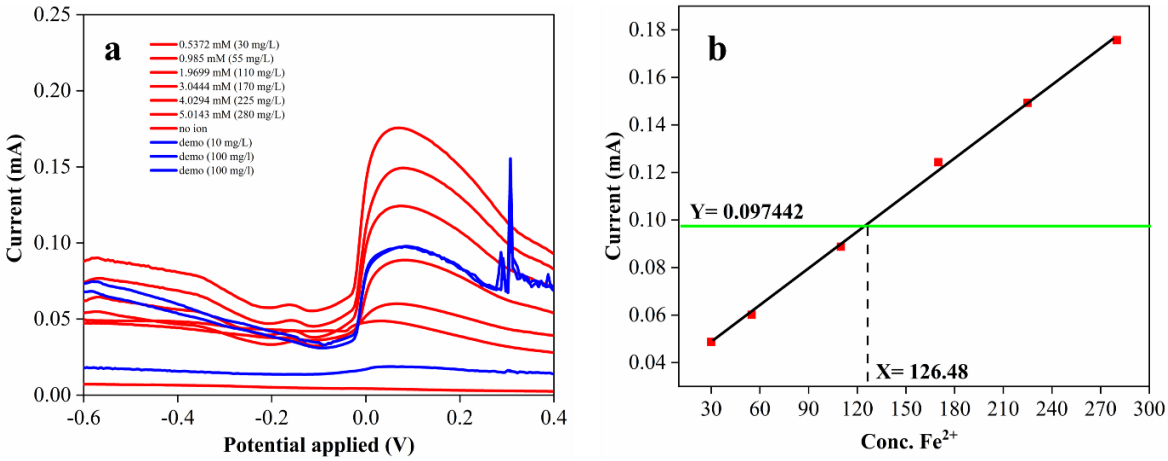

Figure 5-5: Overlap of demo solution on the sensor response.

5.2.5 Determination using Carbon paste based electrode

To demonstrate the detection of Fe^{2+} and Fe^{3+} ions, sensors were made using commercial carbon-based and silver paste inks. The sensors are fabricated using a screen printer, with the size and thickness of the sensors controlled by custom-designed stencils. Ag-based sensors were also prepared and tested. Attempts to use Ag-based sensors were also undertaken, but the Ag-based sensors were found unstable and prone to crumbling; therefore, they were found inadequate. The study's results on Ag-sensors are available on request as a summarised report.

This feasibility study aims to demonstrate the suitability of carbon graphene-based printed sensors for detecting Fe^{2+} and Fe^{3+} ions. The results were benchmarked against the samples analyzed by Inductively Coupled Plasma–Optical Emission Spectrometry (ICP-OES). The main aim was to ensure the studies' reproducibility and demonstrate the applicability of EC sensors in detection using commercially available inks as the sensors' active materials. Therefore, this stage did not explore the ability to use “bespoke” materials (for example, to withstand highly acidic conditions).

Carbon-based sensors: design

As mentioned above, the initial attempts were on a silver electrode-based sensor. Although the results were encouraging, with Fe^{2+} successfully detected and quantified, the Ag-based sensor was found to crumble when bent. Therefore, an alternative sensor was explored using the screen-printed approach with the help of carbon-based ink. A typical sensor is fabricated by applying the ink to a stencil, followed by screen printing (Figure 5-6). Mylar was used as a substrate. At this stage, no attempts were made to investigate the durability of the sensor in a corrosive chemical environment. The critical metrics for progressing with the sensor as suitable for applications were its mechanical and chemical stability in the iron-containing solution at a minimum tested pH = 2.5. The sensor is displayed in Figure 5-5, which showcases the ability to bend. The wired electrodes were not immersed into the solution and, therefore, were attached to the active coating using carbon paste and fixed with the Kapton tape.

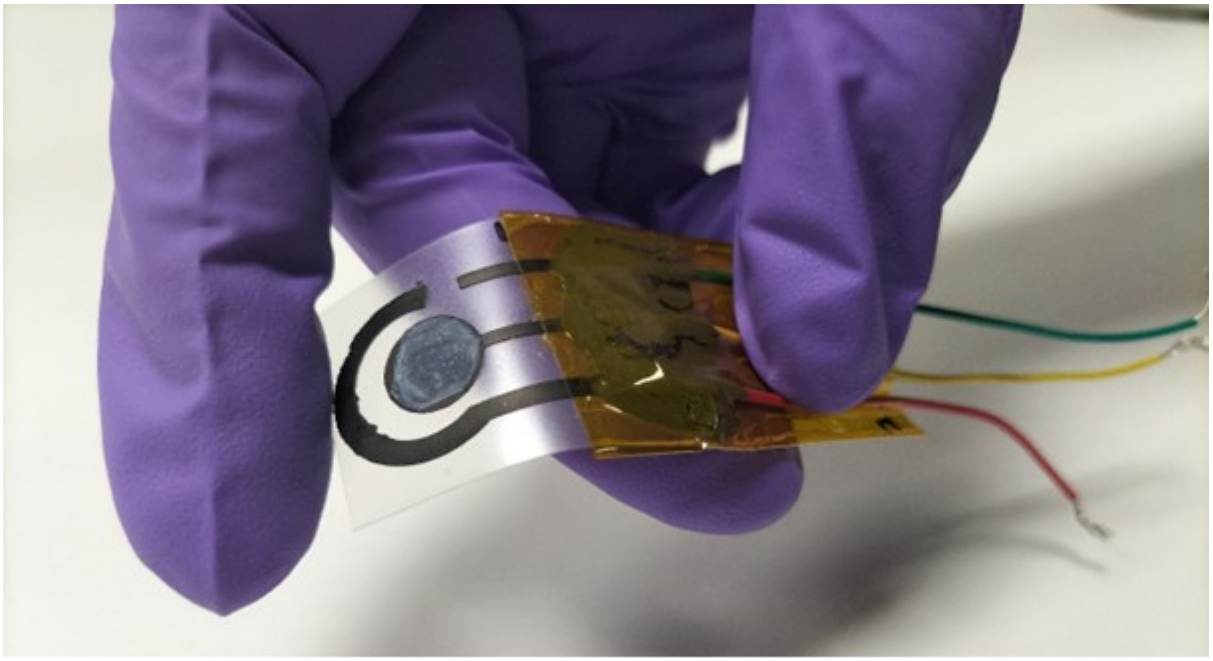

Figure 5-6: The screen-printing carbon based-based electrochemical sensor with gC_3N_4 nanoparticles.

With simplicity in mind, the general applicability of the sensors was tested using the cyclic voltammetry approach, which is the most suitable for applications both in a lab and in the field. Generally, a small voltage is applied when a current is detected. The specific voltage for the peak position determines the nature of the species, and the height (or area) of the peak quantifies the concentration. The initial work was focused on creating calibration curves using a $FeCl_2$ solution with Fe^{2+} concentrations ranging from ~5 - 560 ppm using cyclic voltammetry (CV). Figure 5-7 shows the CV curves for solutions within the ~35 – 550 ppm range recorded at the scan rate of 100 mV/s.

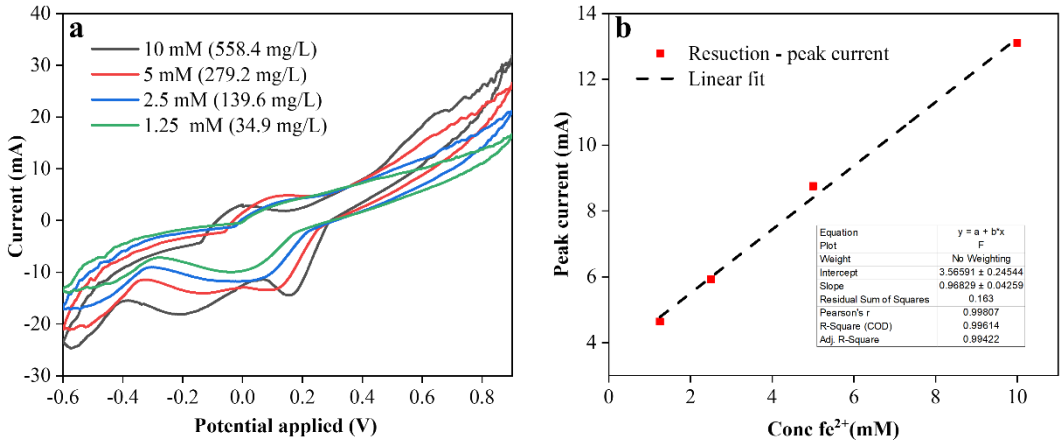

Figure 5-7:(a) Cyclic voltammograms of Fe^{2+} solutions with concentrations of 35 ppm to 560 ppm. (b) The current vs. concentration of Fe^{2+} solutions was measured at the key current peak height.

Showcase 1: Detection of concentration of Fe^{2+} ions by carbon-based sensors

Typically, recording each curve took 30 seconds, suggesting a quick response from the sensor is possible. The respective reduction peak current *vs* concentration graph of the tested solutions is plotted (Figure 5-7),

and data points fit linearly, suggesting that the intensity of the peak represents the concentration reliably. The position of the peaks was consistent and only influenced by variations in pH as the concentration of Fe^{2+} changes within the solutions.

Figure 5-8(a) displays the CV curves collected in the lower concentration range between ~ 9 – 35 ppm, while Figure 5-8(b) shows the relevant calibration graph with the data points fitted linearly. The sensor displays high linearity of R^2 values of 0.994 and 0.993, respectively.

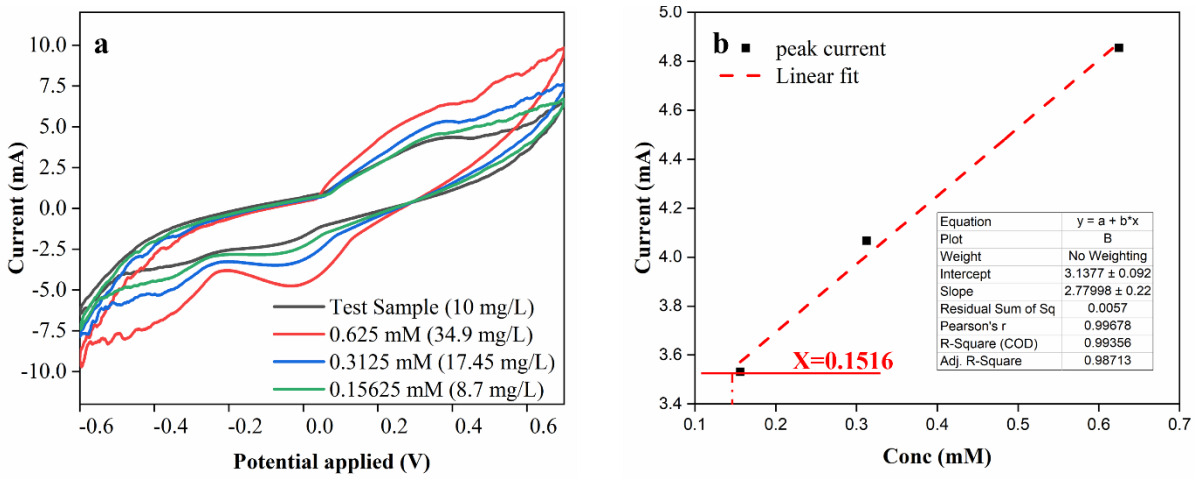

Figure 5-8: (a) Cyclic voltammograms of Fe^{2+} solutions with ~9 - 35 ppm concentrations. (b) The current vs concentration of Fe^{2+} solutions was measured at the key peak.

A blind sample provided by Scottish Universities Environmental Research Centre, SUERC (and later revealed as a 10 ppm of Fe^{2+}) was put to the test (Figure 5-8(a), Black curve). The peak oxidation current value for the tested sample was plotted on the linear fit. The tested sample's peak oxidation current intercepts the linear line at 0.1516 mM (corresponding to 8.5 ppm), suggesting roughly a 10 - 15 % error in the measurement. However, the accuracy of detecting lower concentrations can be further enhanced using more sophisticated electrochemical techniques such as pulsed voltammetry. The detection at high concentrations is much more efficient as the peak shape is more reliable. Increasing the surface area of the sensor's active layer is another way to increase sensitivity. As mentioned before, the goal was to demonstrate the detection of Fe^{2+} in principle at low concentrations rather than optimize the sensor performance for a targeted application.

Notably, the carbon electrode demonstrated a good lifespan, as evidenced by hundreds of CV scans, without impairing its performance or any evidence of crumbling or delamination. A high linearity was found in the range of 1.25 ppm to 560 ppm, but the optimal detection range for Fe^{2+} is probably > 20 ppm.

Showcase 2: Detection of concentration of Fe^{3+} ions by carbon-based sensors

A carbon-based electrode, as shown in Figure 5-9, was used to determine Fe^{3+} ions in solution. At first, simple calibration curves using the cyclic voltammetry method were obtained for a varying concentration from 6.5 ppm to 100 ppm of Fe^{3+} ions, prepared from the $Fe(NO_3)_3$ $9H_2O$. It should be mentioned that no investigation for water content was carried out by Thermogravimetric analysis (TGA), and the commercially purchased salt was used as supplied. Figure 5-8(a) shows the CV curves recorded for the solutions with the targeted Fe^{3+} concentration of 6.25 – 100 ppm at the scan rate of 100 mV/s. In the case of CV response towards

Fe^{3+} ions detection, recording each curve took 30 seconds, indicating that the sensor is capable of a quick response.

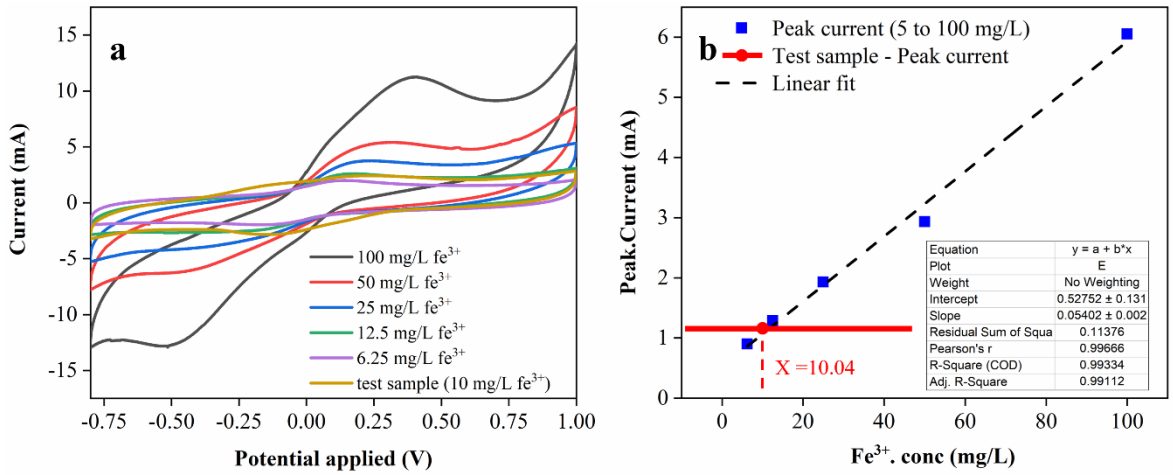

figure 5-9: (a) cyclic voltammograms of fe^{3+} solutions with concentrations ranging from 6.25 - 100 ppm. (b) the current vs concentration of fe^{3+} solutions was measured at the key oxidation peak.

The intensity of the oxidation peak currents was plotted on a graph (Figure 5-9(b)) against the respective concentrations of the solutions. These data points were fitted linearly, indicating that the intensity of these peaks reliably represents the concentration. Here, the intensity of the peaks was consistent while there was a slight variation in the position of the peak as influenced by the varying pH as lower concentration of Fe^{3+} required more dilution. It is observed that the sensor exhibits high linearity, as indicated by the R^2 value of 0.993. A blind sample provided by SUERC for the Fe^{3+} solution (which was later revealed as 10 ppm) was put to the test, and its CV curve was plotted along the yellow curve in Figure 5-9(a)**.** Its respective oxidation peak is intercepted on the linear calibration line, resulting in a concentration of 10.04 ppm, as shown in Figure 5-9(b). In this regard, Fe^{3+} detection showed a very high reliability compared with Fe^{2+}. A possible explanation for the improved detection could be either a weaker sensor response of the Fe^{2+} solution compared with Fe^{3+} as well as the uncertainty in the water content within salts supplied by manufacturers to UofG and SUERC. However, due to the budgetary constraints and timeline of this feasibility study, the primary cause for the higher error of the measurement for Fe^{2+} in comparison with Fe^{3+} was not established.

5.2.6 Determination using g-C_3N_4 modified Glassy carbon electrode

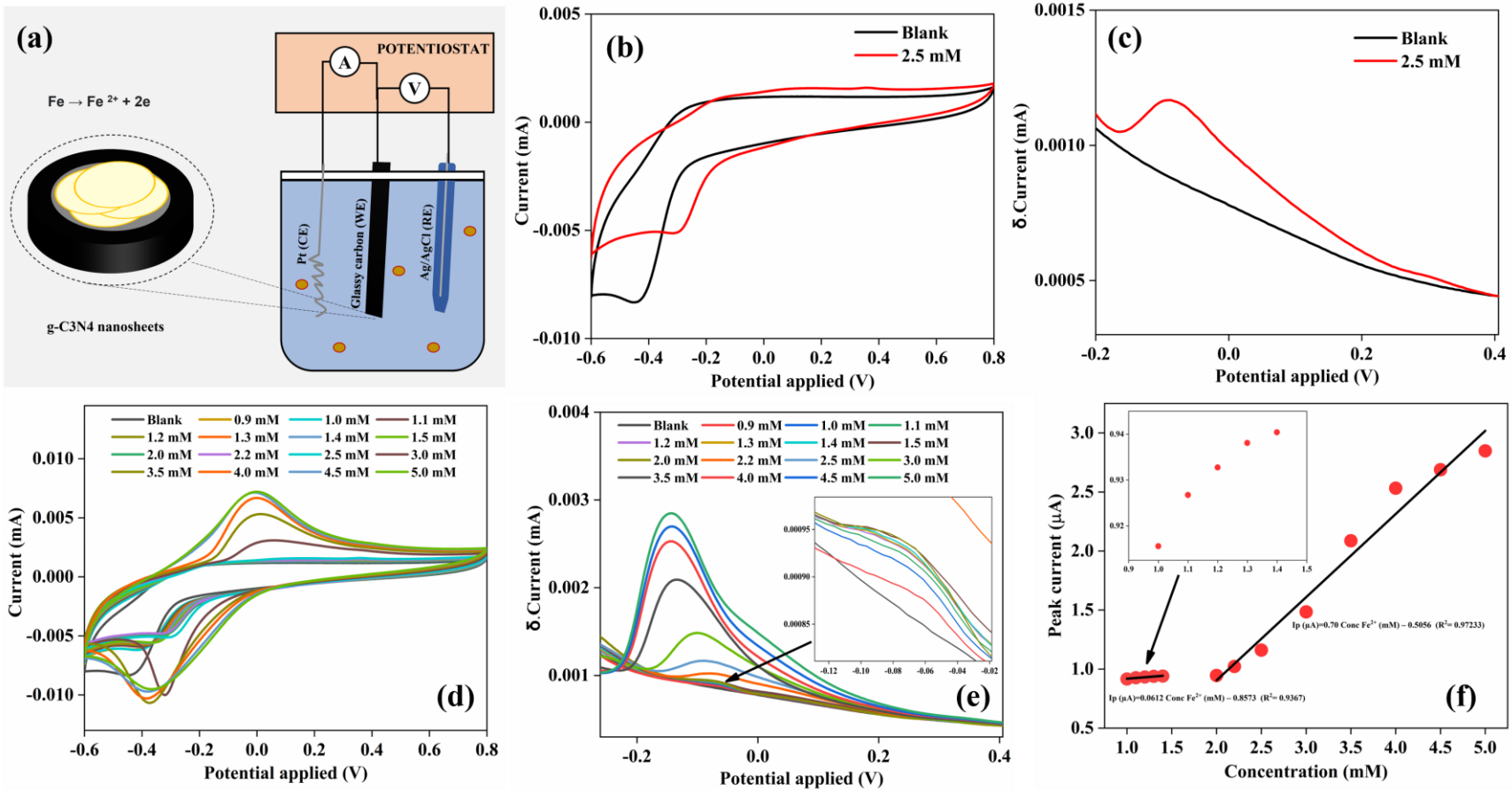

Figure 5-10: (a) Experimental setup. (b, c) CV and DPV curve responses of g-C_3N_4 coated GCE in absence and presence of 2.5 mM of iron (Fe^{2+}) ions in PBS solution. (d, e) CV and DPV curve responses for detecting 0.9 mM to 5 mM iron ions in 0.1 M PBS. (f) Concentration of iron analyte vs oxidation peak current (IP).

Figure 5-10(a) represents the system diagram of the 3-electrode system used to detect iron. Here, the platinum coil was used as a counter electrode (CE), the standard Ag/AgCl was used as a reference electrode (RE) and the g-C_3N_4 coated GC was used as a working electrode (WE). Figure 5-10(b) shows the obtained CVs over the potential range of -0.6 V to 0.8 V in the absence and presence of 2.5 mM of Fe^{2+} ions in the electrolyte solution. Here, the varied CV patterns indicate the occurrence of an electrochemical redox reaction. DPV patterns over the range of -0.2 V to 0.4 V, shown in Figure 5-9(c), were obtained in the absence and presence of Fe^{2+} ions in 0.1 M of PBS solution. The peak displayed in the anodic current at -0.09 V is in response to the oxidation of Fe ions, that causes the addition of evolved $2e^-$ free electrodes. This leads to the increase in the current level, which can be seen through the emergence of DPV peak for the analyte solution in comparison with the blank solution. The electrochemical redox mechanism can be explained easily using the following chemical reactions i.e., Fe to $Fe^{2+} + 2e^-$ and vice versa.

The electrochemical redox mechanism can be explained using the following anodic and cathodic reactions:

Anodic (oxidation) reaction:

$$Fe(s) \rightarrow Fe^{2+}(aq) + 2e^-$$

Cathodic (reduction) reaction:

$$Fe^{2+}(aq) + 2e^- \rightarrow Fe(s)$$

CONCENTRATION STUDY

For the concentration studies, both CV and DPV patterns of iron content in the electrolyte were obtained at different concentrations (from 0.9 mM to 5 mM). In Figure 5-10(d), the increase in the analyte concentration leads to an increase in oxidation peak in the forward scan with a slight shift from 0.05 V to -0.1 V. In the reverse scan, the increase in reduction peak is in the region over -0.29 V to -0.38 V. Figure 5-10(e) displays the DPV peak rising in anodic current over -0.06 V to -0.014 V to the increased iron concentration in the electrolyte solution. To find the linearity for the peak rise, the peak current value for each concentration in the DPV pattern was plotted against their respective concentration, as shown in Figure 5-10(f). It may be noted that there are two linear lines with the R^2 value of 0.9367 and 0.97233 over the concentration range of 1.0 to 1.5 mM and 2 to 5 mM, respectively. The linear equations for the above ranges were

$$Ip\ (\mu A) = 0.0612\ Conc\ Fe\text{^}(2+)\ (mM) - 0.8573 \quad (3)$$

$$\text{Ip}\ (\mu\text{A}) = 0.70\ \text{Conc Fe\^{}(2+)(mM)} - 0.5056 \quad (4)$$

In the lower concentration region of 1.0 mM to 1.5 mM, the hexagonal core-shell structure of g-C_3N_4 may have caused the absorption of oxidised Fe^{2+} ions over the sensing layer, which leads to the blockage of most incoming free electrons for diffusion. For the higher concentration region, even though the deposited Fe^{2+} ions block the current path for incoming ions, the oxidation of the higher concentration of Fe^{2+} ions over the g-C_3N_4 nanosheet leads to excessive free electron charges, leading to a sudden rise in the peak observed after the formation the current path for the driving free electrons [199].

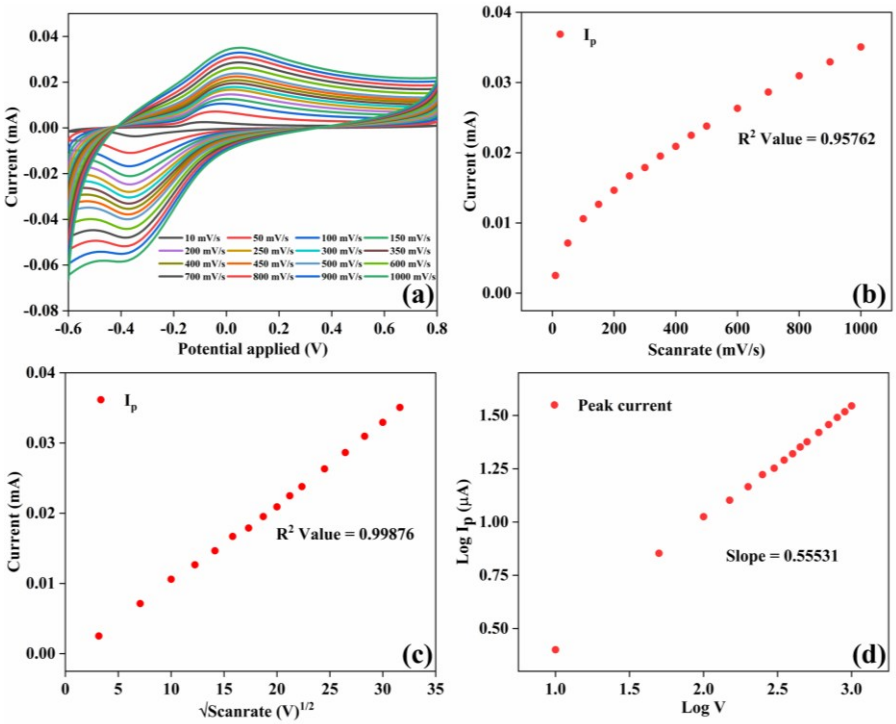

Figure 5-11: (a) CV response curves for g-C3N4 /GCE in 2.5 mM of Fe2+ ions in PBS with different scan rate of 10 to 1000 mV/s; (b) IP versus scan rate; (c) IP versus √scan rate; (d) log of IP versus Log of scan rate.

The accumulation study was conducted to investigate the electrochemical behaviour of the g-C_3N_4/GCE electrode toward Fe^{2+} ions by analysing the effect of scan rate on the cyclic voltammetry (CV) response. This study aims to elucidate the underlying detection mechanism—whether adsorption-controlled, diffusion-controlled, or a combination of both—by examining the relationship between peak current and scan rate. The CV patterns were obtained for different scan rates to study their detection mechanisms for the accumulation study. Figure 5-11(a) displays the CV patterns over the region of -0.6 V to 0.8 V with the scan speed of 1 mV/s to 1000 mV/s for detecting 1.5 mM Fe^{2+} ions in 0.1 M PBS electrolyte. The oxidation peak current value from the different scan rates was plotted against each other in Figure 5-11(b). The R^2 value for the plotted peaks is 0.95762, which shows a highly linear relationship between the scan speed and peak current. This confirms the occurrence of an absorption-controlled mechanism. Figure 5-11(c) displays higher linearity between the square root of scan speed and peak current with an R^2 value of 0.99876. This confirms the diffusion-controlled mechanism as well. From the scan speed studies, the mechanism occurring over the g-C_3N_4 layers was both adsorption-controlled and diffusion-controlled. However, at higher concentrations of iron analyte detection, a diffusion-controlled mechanism plays a significant role, confirmed by plotting Log V against Log Ip. Here the slope was found to be 0.55, which was closer to the ideal diffusion-controlled mechanism (0.5) [200].

REPEATABILITY

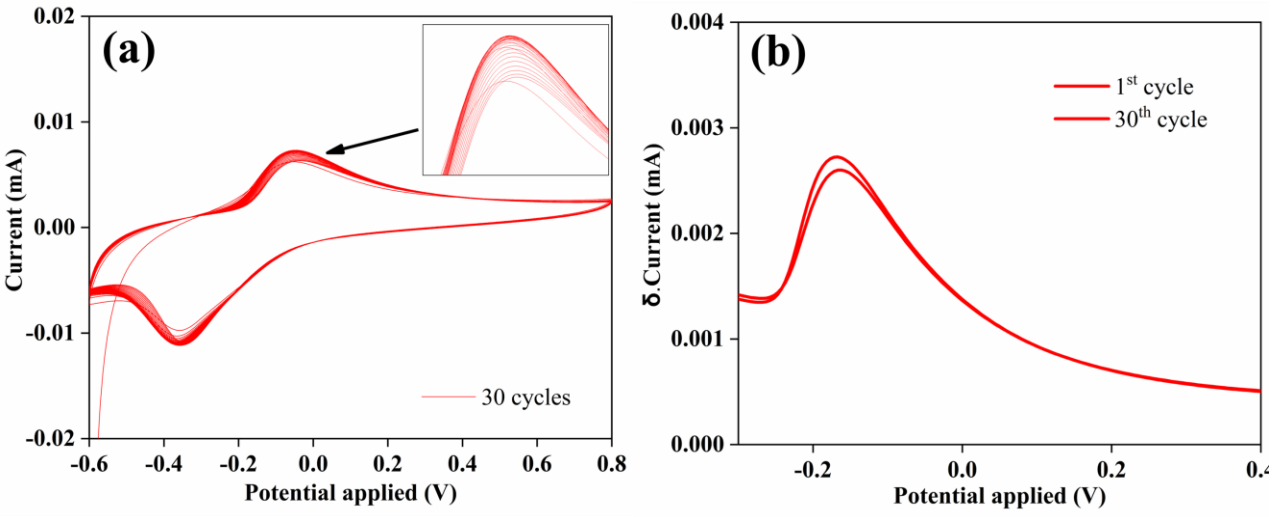

Figure 5-12: (a) CV response of 30 scans in 2.5 mM of Fe2+ ions in PBS 50mV/s; (b) DPV response for the 1st and 30th consecutive cycles.

For the repeatability studies, a continuous cycle of 30 CV scans was obtained, and the respective DPV patterns were obtained before and after scanning, as shown in Figure 5-12(a, b). From the repeatability study, it may be noted that a slight change in oxidation peak occurs for the initial scans. Later, these peaks converge to have a more reliable and accurate response.

5.3 Conclusion

The carbon-based printed sensors fabricated using commercial inks were found suitable for detecting Fe^{2+} and Fe^{3+} ions, as their results could be benchmarked against ICP-OES and demonstrated reproducibility. While silver-based sensors were also attempted, they proved inadequate due to instability and crumbling issues, leading the study to focus solely on the more promising carbon-based sensors made from commercial inks. The carbon-based screen-printed sensors fabricated on Mylar substrates using commercial inks proved to be a viable and robust within pH 2.5 – 6.5 range.

The carbon-based screen-printed sensors successfully demonstrated their viability for detecting and quantifying Fe^{2+} ions through cyclic voltammetry, exhibiting high linearity ($R^2 > 0.99$) in calibration curves spanning concentrations from 8 – 560 ppm, with an accuracy of around 85-90% for a 10 ppm blind test sample. The sensors proved mechanically and chemically robust, enduring hundreds of CV scans without performance degradation, crumbling or delamination. They are promising candidates for practical applications within their optimal detection range for Fe^{2+} of > 20 ppm. Similarly, the carbon-based screen-printed electrode demonstrated high linearity ($R^2 = 0.993$) and reliability in detecting Fe^{3+} ions in the range of 6.25 - 100 ppm through cyclic voltammetry, accurately quantifying a 10 ppm blind test sample with minimal error.

While the Fe^{2+} detection exhibited comparatively higher measurement errors, potentially due to weaker sensor response or uncertainties in the water content of the supplied salts, the study successfully validated the suitability of these robust carbon-based sensors for quantitative electrochemical analysis of both Fe^{2+} and Fe^{3+} species in aqueous solutions.

In summary, the 2D g-C_3N_4 nanomaterials-based sensor shows excellent response for detecting iron in water. The performance of the sensor is examined for iron content concentrations ranging from 0.9 mM to 5 mM using CV and DPV techniques. Along with the concentration study, the accumulation study (with a scan speed of 10 mV/s to 1000 mV/s in -0.6 V to 0.8 V region) and repeatability analysis (30 CV scans) are also carried out. The electrodes on rigid substrates can be replaced with flexible, eco-friendly, biodegradable materials for easy disposability and practical field applications. This will be the focus of our future work.

[6] Reusability of the printed sensor for the Differential pulsed anodic stripping voltammetry application

6.1 Introduction

The SPCE-based 3-electrode sensor detects zinc ions at lower and higher concentrations (i.e. ppm, ppb) using cyclic voltammetry and differential pulsed anodic stripping voltammetry techniques. The deposition, preconditioning, and postconditioning states were discussed in relation to detection in lower concentrations, and this is essential for achieving repeatable usage of the fabricated sensor. The issue concerning repeatable usage arises in anodic stripping due to not achieving complete stripping of deposited ions when approaching stripping-based detection. This causes varying voltammogram responses for the same concentration as the unstripped ions accumulate and provides a uniform response. Therefore, for the first section, the experiment's approach involved deposition, preconditioning, and the postconditioning stage was discussed, and their respective results were investigated.

In this chapter, the idea focuses on optimising techniques on the Anodic stripping voltammetry technique to find the reusability of the printed electrochemical sensor. The section is divided into two sections where: 1) the usage of SPCE-based sensors for the detection of zinc ions by DPASV method and the optimisation of precondition, deposition, and post-condition process while the detection of zinc ions in water; 2) The usage of SPCE based sensor for the detection of lead and cadmium ions and further using a mixture of commercial metal oxides, made from titanium oxide (TiO) and Magnesium oxide (MgO) for the detection of lead and cadmium in the lower range of ppb. Here, a simple comparison of DPV and DPASV methods is shown for the significance of the stripping method.

The main aims of this chapter are therefore to:

- Optimise the preconditioning, deposition, stripping, and post-conditioning steps in DPASV so that the same SPCE can be reused reliably.
- Demonstrate the detection of Zn^{2+}, Cd^{2+}, and Pb^{2+} using bare SPCEs and TiO_2–MgO modified SPCEs, and compare DPV with DPASV for low-concentration measurements.

The chapter is organised as follows:

- Section 6.2 – Materials and methods for sensor fabrication, reagents, and stripping protocols.
- Section 6.3 – Results and discussion for zinc detection and optimisation of reusability.
- Section 6.4 – Results and discussion for lead and cadmium detection using bare and TiO_2–MgO modified SPCEs, including DPV vs DPASV comparison.
- Section 6.5 – Conclusions.

6.2 Materials and methods

6.2.1 Sensor platform and fabrication

A screen-printed carbon electrode (SPCE) with a three-electrode layout was used as the base platform. The working and counter electrodes were printed using a commercial carbon paste (Sun Chemical), which was also self-modified for some experiments as described below. A commercially printed Ag/AgCl electrode (3.5 M KCl) served as the reference electrode.

For TiO_2–MgO modified electrodes, a 1:1 (w/w) mixture of commercial titanium oxide (TiO_2) and magnesium oxide (MgO) nanopowders was dispersed in an appropriate solvent (e.g. DMF) and thoroughly blended. A defined volume of this dispersion was drop-cast onto the SPCE working electrode and allowed to dry, forming a heterogeneous metal-oxide composite sensing layer.

6.2.2 Reagents and solutions

- **Zinc:** Stock solutions of Zn^{2+} were prepared by dissolving zinc nitrate hexahydrate (Sigma-Aldrich) in deionised (DI) water.
- **Cadmium:** Stock solutions of Cd^{2+} were prepared using cadmium chloride (Sigma-Aldrich).
- **Lead:** Stock solutions of Pb^{2+} were prepared using lead chloride (Sigma-Aldrich).
- **Supporting electrolyte:** 0.1 M phosphate buffer solution (PBS, pH ~ 7) was used as supporting electrolyte unless otherwise stated.

Typical working solutions were prepared by diluting the stock to the required concentration in 0.1 M PBS.

6.2.3 Practical stages in stripping voltammetry

In heavy metal detection, generally pulsed technique-assisted stripping voltammetry methods detection such as LSASV, DPASV, and SWASV involves two primary stages. The first stage is pre-concentration, where metal ions in the solution are electro-reduced (deposited) onto the working electrode's surface as zero-valent metal at a constant potential. In the second stage, a voltage sweep in the anode direction is applied to re-oxidize the zero-valent metal into its ionic form. This process allows the analyte deposited on the electrode to be stripped (dissolved) at a designated potential. This technique enables the specific detection of various metal ions by leveraging their distinct oxidation potentials. However, a hidden third stage, which the literature doesn't cover much, is called post-conditioning, and is used to ensure the reusability of the same sensor. In most printed sensors, the stripping process doesn't altogether remove the deposited metal analyte at the working electrode surface. Therefore, optimisation of pulsed technique-assisted stripping voltammetry methods should require an in-depth study on both the deposition and postcondition phases. Otherwise, the stripping results cause inaccurate results when reusing the same sensor.

STAGE 1: PRECONDITIONING OR DEPOSITION STAGE

For the deposition of HMIs, finding an optimised deposition potential and deposition time is necessary. The deposition potential of heavy metal ions is the specific voltage at which these ions are reduced and deposited onto an electrode during electrochemical analysis. This potential differs for various heavy metals and is critical

for techniques like Anodic Stripping Voltammetry (ASV). By accurately setting the deposition potential, selective and sensitive detection of individual metal ions can be achieved. In ASV, the deposition potential is adjusted to ensure that only the target metal ions are reduced and accumulated on the working electrode. This is done by selecting a potential where the metal ion of interest is reduced while avoiding interference from other ions. After deposition, the electrode potential increases to oxidise the metal back into its ionic form, allowing for its measurement and analysis. Different heavy metals exhibit unique deposition potentials due to their electrochemical properties, which are influenced by factors such as the electrolyte's composition, pH, and the electrode material. Proper control of the deposition potential is crucial for obtaining accurate and reliable results in electrochemical sensing. Usually, the potential shown for the half-reaction of a redox reaction gives an overall idea of the occurrence of a redox reaction and data gathered from the Pourbaix diagram for each PTE in water (attached in appendix)

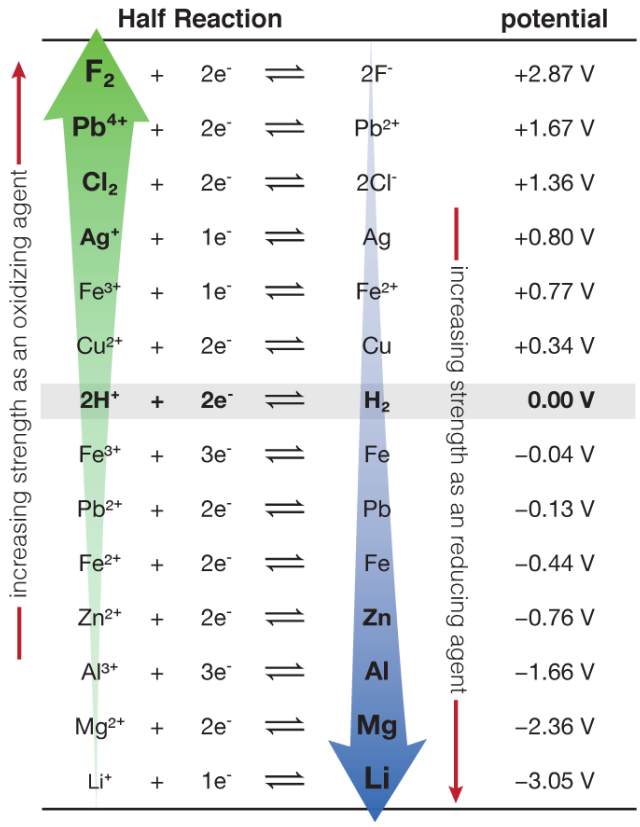

Figure 6-1: Oxidation potential, which is required for the half-reactions of heavy metal ions.

STAGE 2: STRIPPING OR DETECTION STAGE

The stripping potential gradually increases after metal ions are deposited onto the working electrode. The stripping potential is the voltage at which these ions are oxidised and removed from the electrode. Each metal ion has a distinct stripping potential due to its unique electrochemical characteristics. Therefore, when multiple metal ions analyte are deposited onto the electrode, individual heavy metals strip off from the electrode at a definite potential, leaving multiple occurrences of peaks at various potentials.

STAGE 3: POST-CONDITIONING OF THE SENSOR

In most cases of printed sensors, the deposited metals don't completely strip away from the working surface of the electrode. For the complete recovery of the sensors, it is crucial to determine the equilibrium criteria between the deposition and conditioning stages. A fine calibration will result in deposition and stripping techniques, heavy metal ions deposit more easily than other analytes. This is largely due to their stable deposition characteristics, low reduction potentials, high conductivity, and significant charge density. Heavy metal ions generally possess higher atomic masses and multiple positive charges, allowing them to conduct electricity more effectively, which enhances their reactivity in electrochemical methods like electroplating and anodic stripping voltammetry. Upon reduction, heavy metals typically form stable metallic deposits that adhere strongly to electrode surfaces, thanks to their cohesive and adhesive properties. This results in a consistent and reliable deposition, facilitating measurement and analysis. Heavy metal ions such as lead (Pb^{2+}), cadmium (Cd^{2+}), and zinc (Zn^{2+}) have relatively low reduction potentials, making them easier to reduce from their ionic to metallic states. When a slight negative potential is applied to the electrode, these ions readily undergo reduction and deposit onto the electrode as metal. Additionally, heavy metals show a high affinity for surfaces like carbon, gold, and platinum electrodes, which further promotes their reduction and deposition during electrochemical processes, making the procedure both efficient and dependable. In this Chapter, The SPCE-based EC sensor was used to detect Cadmium, Lead and Zinc ions in water through the DPASV method. The Unspoken issue in reusability of the sensor is discussed in detail with an investigation towards the hidden stages of DPASV methods such as preconditioning and postconditioning.

6.2.4 Methodology for zinc detection

A 3-electrode-based fabricated electrochemical sensor was used to detect zinc ions in water. The counter, working electrode, and screen-printed carbon electrode used the self-modified commercial carbon paste from sun chemicals. Ag/AgCl (3.5 M KCl) was the reference electrode. The analyte stock solution was prepared using zinc nitrate hexahydrate powder from Sigma. Electrochemical experiments such as cyclic voltammetry and differential pulsed voltammetry techniques were used.

For zinc detection, a bare SPCE was used as working and counter electrode, with Ag/AgCl as reference and 0.1 M PBS as supporting electrolyte. Initial tests employed CV and DPV to understand the redox before the haviour of Zn^{2+} and to determine suitable potential windows.

Subsequently, DPASV was applied to study zinc deposition and stripping:

- Deposition potential: typically around –1.3 to –1.4 V
- Deposition time: varied from 10 s to tens of minutes, depending on the experiment
- Stripping window: typically from the deposition potential up to 0 or +0.5 V
- Post-conditioning: positive potential (e.g. +1.1–1.3 V) for several minutes, with optional CV cycles

The effect of deposition potential, deposition time, and conditioning potential/time was investigated systematically to determine conditions that both give a measurable signal and allow sensor recovery.

6.2.5 Methodology for lead and cadmium detection

For the electrochemical sensor setup, a screen-printed carbon electrode was used as both a counter electrode and a working electrode. Ag/AgCl (3.5 M KOH) was the reference electrode. 0.1 M Phosphate buffered solution was used as the supporting electrolyte to maintain constant ionic strength (pH 7). A stock solution of 500 µM concentration was prepared for the analyte solution by dispersing cadmium chloride in DI water. Differential Pulsed Anodic stripping voltammetry (DPASV) was used to detect varying cadmium concentrations in 0.1 M PBS solution.

Bare SPCE

- Deposition potential: typically –1.3 to –2.0 V
- Deposition time: ~120 s (and longer for lead where required)
- Stripping window: from deposition potential to ~+0.5 V
- Post-conditioning: positive potential (around +1.3–1.4 V) for 3–5 min, plus CV cycles in blank PBS.

TiO_2–MgO modified SPCE

- Modification: drop-cast 1:1 TiO_2–MgO mixture on the SPCE working electrode.
- Deposition potential: –1.0 V
- Deposition time: 30 s
- Stripping window: –1.0 V to +0.8 V
- Analyte concentrations: 100 nM to 500 µM for Cd^{2+} and Pb^{2+}.

6.3. Results and Discussion: Zinc detection and reusability

6.3.1 Electrochemical detection of zinc (CV and DPV)

Based on the Preliminary results for the detection, Zinc ions are more straightforward to detect at higher concentrations. Here, for our understanding of the peak occurrence, cyclic voltammetry between -1 V and 1V was scanned at 50 mV/s for the varying concentration of Zinc ions from 39.06 uM to 5 uM (i.e. 2.55 ppm to 65.38 ppm) and displayed in figure 6-2. It was observed that there is multiple redox potential. When the forward scanned cycle occurs from -1 V to 1 V, Zn is oxidized to Zn^{+} and Zn^{2+} while losing $1e^{-}$ and $2e^{-}$ at approximately 0.4V and 0.8 V. In the reverse cycle, the oxidized zinc ions were reduced to zinc at -0.8 V, causing a clear peak between 2.5 ppm and 327 ppm.

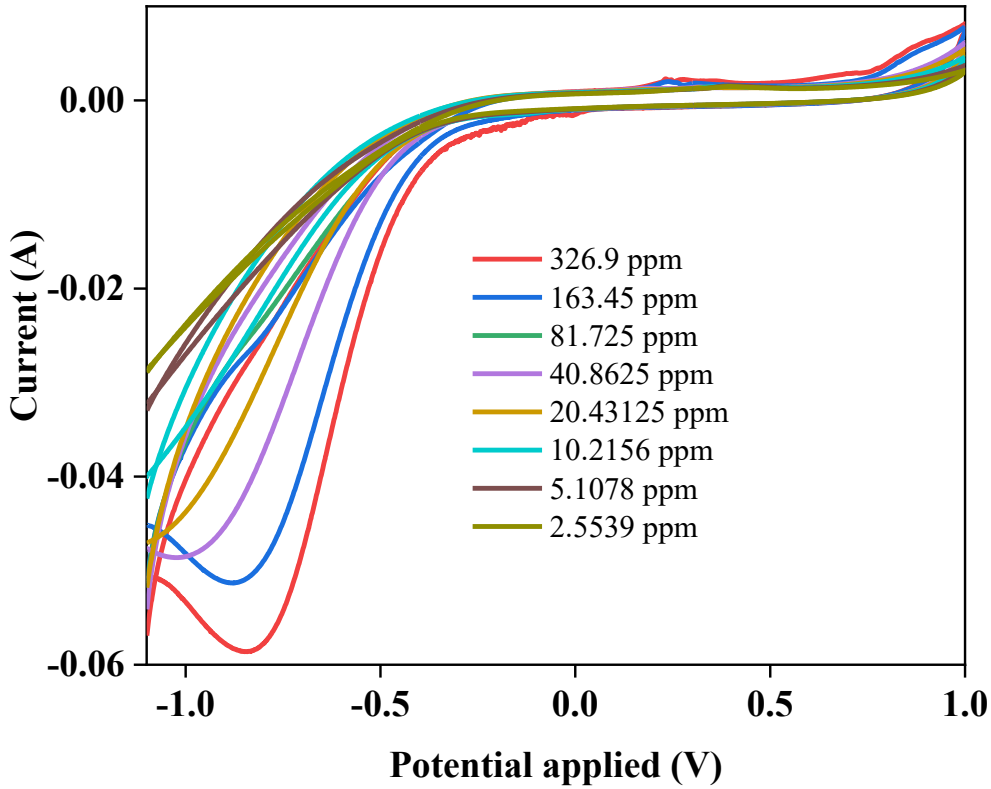

Figure 6-2: Cyclic voltammetry was used for the potential window between -1V and 1V for the varying concentrations.

Here, the Differential pulsed voltammetry method is used to gather responses for the varying concentrations of zinc between 1.2 ppm to 81.8 ppm. Initially, zinc is oxidized at 1V and when the reverse scan is applied, the oxidized zinc ion is reduced causing the peak due to reduced current occurring around -0.4V.

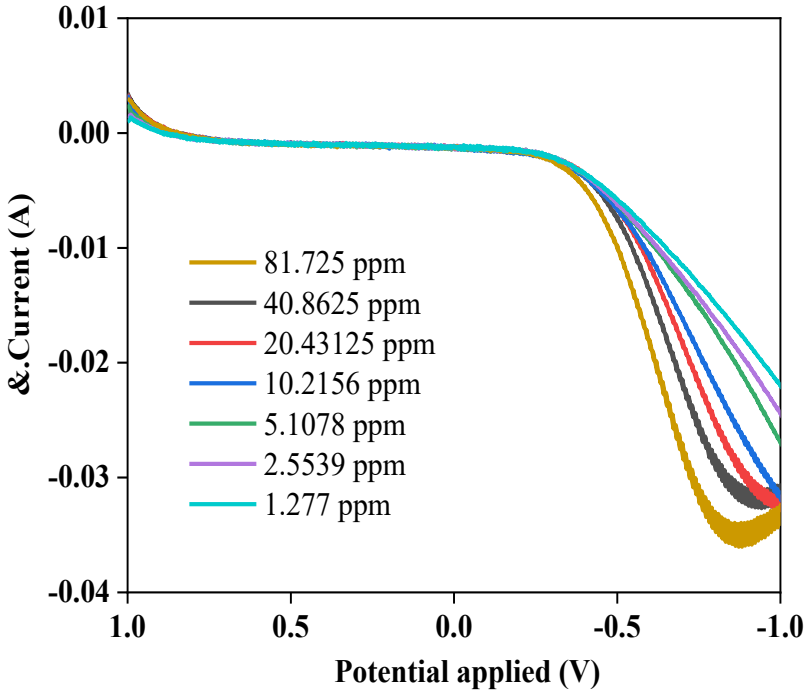

Figure 6-3 : DPV response is obtained for varying zinc concentrations between 1V to -1V.

The reduction peak appears between -0.5V to -1V, with the peak occurring at -0.85V. A slight peak shift occurs at lower concentrations from -0.8V to -1V. To understand the occurrence of peak shift, the potential window is extended to the negative side, which is displayed in Figure 6-3. Similarly, to understand the linearity, the peak current is plotted against the varying concentration in Figure 6-4. It is observed that there are two linear detection ranges with R-square values of 0.994 and 0.995 value.

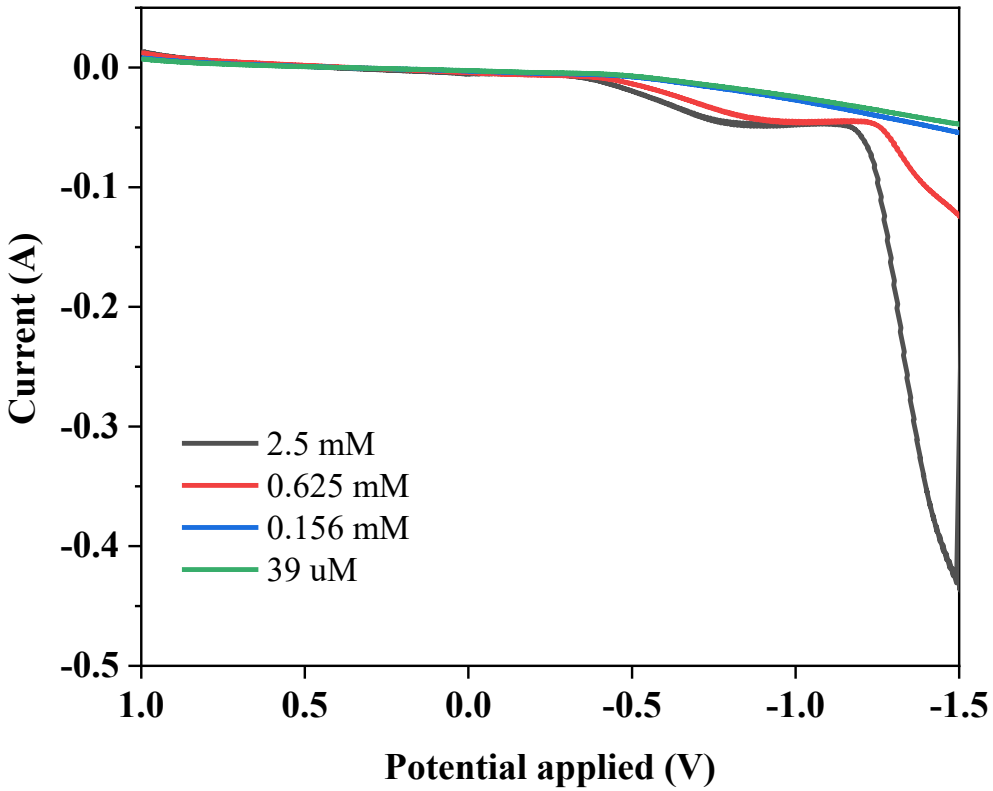

Figure 6-4: DPV response between 1 to -1.5V for zinc concentration (39 uM,156 uM,625 uM, and 2500 uM)

The two linear range occurrences in Figure 6-5 can be distinguished as lower concentration response and higher concentration response. The lower concentration response is more sloppy in nature due to the result of the available active surface area of the working electrode. At higher zinc concentrations, the slope decreases compared to the lower concentration range, which may be attributed to the deposition of oxidized zinc ions on the electrode surface, leading to surface blockage and a reduced current response.

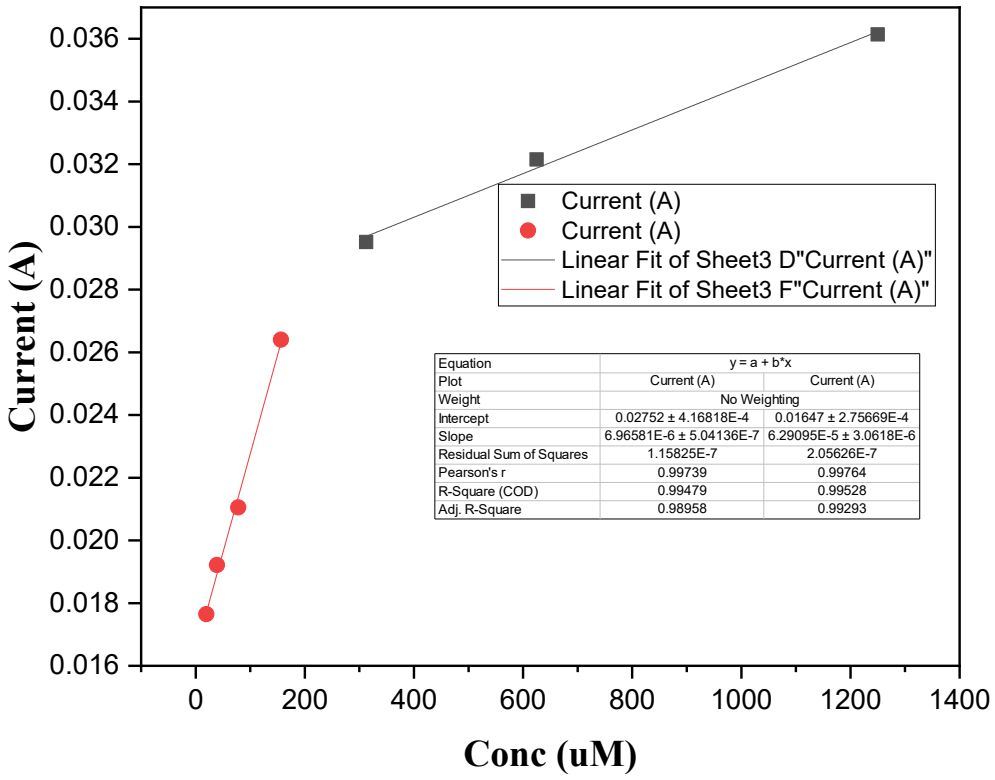

Figure 6-5: linear detection ~(varying concentration vs DPV peak response current)

6.3.2 Optimisation of DPASV parameters (deposition and conditioning stage)

This portion discusses optimizing deposition and stripping conditioning for sensor recovery. Let's divide the process into preconditioning, deposition and stripping, and postconditioning. The observation of such stages is visibly seen over the sensor, where the color of the working electrode changes from a dark grey to light grey and further to a black layer in Figure 6-6, indicating that the zinc has been deposited over the WE during the deposition potential and also the stripped off of zinc in the stripping stage and completely recovered sensor in the latter stage (ie postconditioning). To optimize such stages, parameters such as deposition potential, time of deposition, postconditioning potential and its respective time, number of CV cycles, and their potential windows account for the repeatability of a used sensor in the practical condition.

PRECONDITIONING OF THE SENSOR:

For this process, the freshly built electrodes should be conditioned to acquire reproductivity, provide a repeatable baseline, and avoid initial noisy signals. This also helps to see the uniformity of a batch-produced electrochemical sensor. Even though the printer produces the same design and thickness of the printed sensor, the uniformity can be distorted due to a few reasons, such as the cause of the difference in ink formulation as the composition of the required thinning agent varies from batch to batch as the electrode ink paste might be in a different stage of dried condition and even in the same batch, the composition of ink may vary due to inhomogeneous among the blended material. Another primary reason is human error, which makes it challenging to provide perfect wiring and insulation.

Therefore, sensor preconditioning is essential to identify sensors with similar behavior. This can be achieved through cyclic voltammetry and IR compensation processes. The dipping and cleaning of the printed sensor in

DI water is also recommended as it doesn't let the solvent dry out quicker, and thus, the moist electrode is tenacious to the bending process. The CV cycle is recommended for the operating process for a certain number of cycles to see if there isn't any discrepancy in the sensor's response curve.

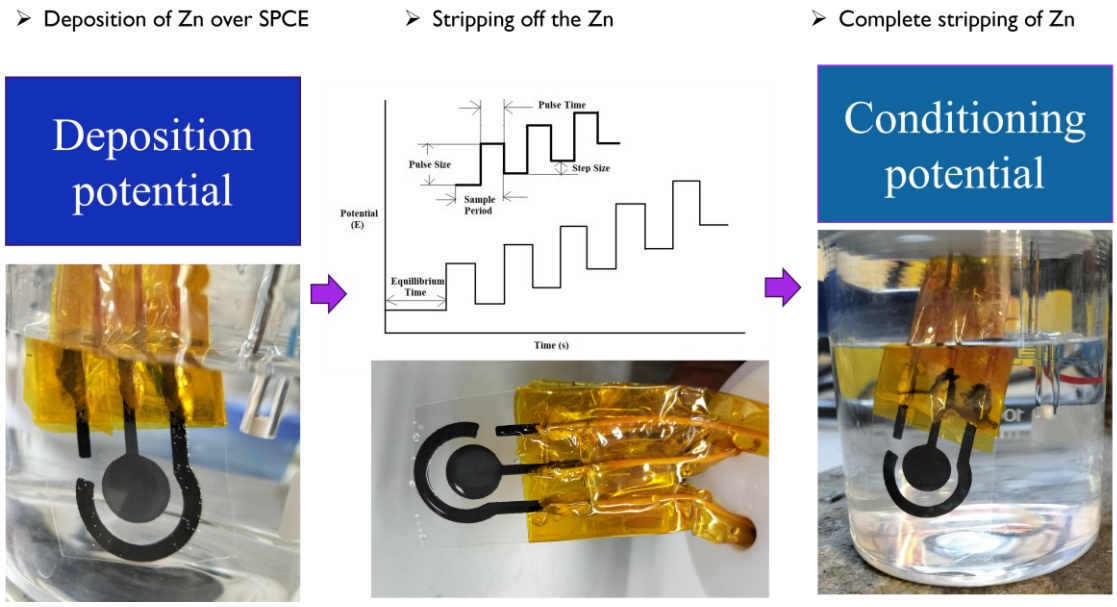

Figure 6-6: Parametric steps in the anodic stripping process.

Based on most of the work, the SPCE electrode needs an average of 50 cycles to show a similar response in the blank solution for both the CV and DPV response. However, for the silver electrode, this process is usually eliminated for my work as the switch in the current potential in the negative potential to positive potential, or vice versa, results in quicker darkening of the silver electrode. It is primarily due to the easier oxidation of the silver electrode. Thus, the based sensors are often used in my work.

QUALITATIVE DESCRIPTION OF IR DROP:

In electrochemical sensing, the IR drop refers to the voltage loss that happens when current passes through the solution's resistance. This phenomenon can lead to shifts in the measured potential and create artifacts, particularly in low-conductivity solutions or when high currents are applied.

Unlike the DPV methods, the deposition and further stripping of the deposited HMIs are easier to notice due to the surge in the peak observed. This is explained in detail in the upcoming section.

The tedious process is the postconditioning of the used sensor for reusability. Unlike the deposited reduced ions on the electrode surface. The affinity between these HMIs and the carbon-based surface causes an incomplete stripping of the ions. Several trials and observations for the deposition of zinc are shown. The significance of postconditioning, which leaves a clear pathway for continuous monitoring ions in field conditions, will be explained below. Here, for the concentration of 2.5 mM and 10 mM of zinc nitrate solution, several trial tests were done to optimize the sensor.

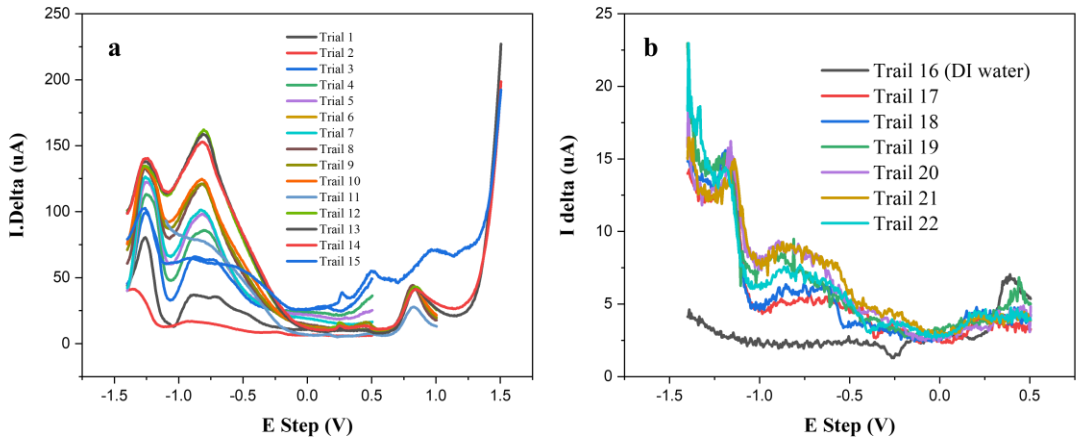

Figure 6-7: DPASV Trails for optimizing.

6.3.3 Systematic trials for zinc DPASV and post-conditioning

A series of trials (labelled here as Trials 1–22) was carried out to understand how deposition potential/time and conditioning potential/time affect zinc stripping and sensor recovery.

Trial 1: For the initial study, Ei is set to be -1.4 V for 2mins, and the DPV scan was set from -1.4V to 0.5 V. The setup is pulsed height pH is 50 mV, the pulse width is 50 ms, step height is 5 mV and step time is 500 ms. The conditioning potential was set to 0.5 V for 1 min. The CV for 5 cycles, ZIR compensation, and DPV studies are done here. Trial 2: The same setup is set for repeatability study. It is noted that the peak occurs at two potentials, which are around -1.3 V and -0.8 V. Here, ZIR and DPV studies are done without CV studies. Trial 3: For the third trial, Just the DPV study is done as a part of the trial study. It is noted that the peak shape for trial 3 is not the same as trials 1 & 2. Therefore, Just IR compensation and DPASV study are done for the rest of the testing. Trial 4: IR and DPASV are done with the same setup parameters to confirm this. The Peak shape returns similar to trials 1 & 2, which makes the peak more precise than just DPV results. Trial 5: It is noted that the peak height is increasing for the constantly rising for the same experimental setup. It is suspected that the zinc deposited at the deposition potential is not entirely stripped off from the sensor. It is also noted that the zinc deposited on the sensor is visually seen as a grey layer at the carbon electrode.

Trial 6: To confirm the above statement regarding the zinc ions that don't wholly strip off from the electrode, the same trail is repeated, and the peak height is seen to be increased. Trial 7: Therefore, the conditioning time was increased to 5 minutes. Trial 8: The setup is redone with increased conditioning potential at 1 V for 5 minutes. Trial 9: For this trial, it is seen that the same setup is used to see whether the peak height is still increasing. Also, the DPV studies were run till 1V. It is observed that the peak height is still the same and not increasing. Let's say that the deposition and conditioning are almost optimized. Trial 10: The same setup as trials 8 and 9 is repeated. The peak observed is quite the same in all three cases. Trial 11: In this study, Ei is set to be -1.4 V for 2mins, and the DPV scan was set from -1.1 V to 1 V.

Trial 12: By repeating, the peak height is further increased, showing that at higher deposition potential, less time is required to deposit. It is also noted that at the increased conditioning time, the DPASV is quite

repetitive, and these parameters can be seen as optimized setup values. Trial 13: The DPV technique is further run up to 1.5 V to strip off the deposited zinc ions completely. It is observed that the peak height is gradually lowering, indicating that the zinc accumulated at the surface of the electrode is starting to be ripped off, which allows the sensor to get closer to the baseline value. Trial 14: Repeating the experiment reduces the peak height, stating that the zinc ions have yet to be completely stripped off. Trial 15: In this trial, the conditioning time is 15 mins. The resulting peak observed is drastically reduced, which displays that the complete recovery of the sensor is made at higher positive potential and conditioning time. It is also noted that the grey scale on the sensor is entirely gone, stating that the deposited zinc is completely striped after this trial.

Trial 16: A new baseline is obtained for the DI water to check further whether the optimized parameters for the higher concentration of 2.5 mM. Trial 17: The deposition potential is set at -1.4 V for 10 sec to deposit zinc ions quickly. The detection or the stripping potential scan is scanned from -1.4 V to 0.5 V. The conditioning potential is set to be 1.1 V for 1 min. Trial 18: The same experiment is repeated. The conditioning time is set to be 5 mins. The potential increases to 1.1 V. Trial 19: The peak height at -0.8 V still increases. So the conditioning potential is increased to 1.2 V. Trail 20: here, the conditioning potential is increased to 1.3 V, and as for the increased voltage, the condition time is reduced to 10 seconds. Trail 21 & Trial 22: The experiment is repeated, and the reduced peak height suggests that the deposited zinc will be stripped entirely, and the recovery is possible at varying concentrations as well.

As a collective observation, the optimized parameters for achieving repeatability of the SPCE-based sensor to detect zinc ions in water by performing a DPASV method are tabulated in Table 6-1.

Table 6-1: Optimised parameter for the DPASV-based detection of zinc using SPCE-based results in lower concentration (i.e., ppm range).

Parameter	Optimized value
Preconditioning of fresh sensor	CV cycles: 40 ~ 50 cycles; IR compensation is recommended.
Deposition of zinc	Deposition potential: -1.3; Deposition time: 10 mins~30 mins.
Detection or Stripping	Stripping window: -1.3 V to 0 V.
Postconditioning for sensor recovery	Conditioning potential: 1.3 V, Conditioning time: 3 ~ 5 mins. CV cycles in the positive potential region are recommended for a few cycles.

6.3.4 Low-concentration zinc detection (1–20 ppm)

However, our aim was for the sensor to reliably detect lower concentrations, specifically in the range of 1–20 ppm, similar to the levels found in the water sample we collected from Welsch. We tried the same sensing parameter in the lower concentration of 1 ppm of zinc in DI water where the DPASV response is noisy, and it was hard to distinguish the detection peak and noisy signal. We tried with a buffer solution (0.1 M PBS) to see

if the lack of ions at lower concentrations the reason for the poor signal might be. While introducing the buffer solution, the DPASV response is less noisy, and to verify, the current rise (blunt peak) appears around approximately -0.1V, as shown in Figure 6-8. To ensure the validity of the deposition, the deposition time was increased from 1 min to 3 min and a further 9 mins. It is seen that the longer the deposition time, the slight blunt peak height gradually increases, ensuring the deposition's validity. It is also shown that the reverse DPASV responses from 1.3 V to 1.0 V as a postconditioning set have a similar baseline, which is also an indication of the optimized postconditioning parameters ensure the complete stripping of deposited analyst ions from the WE surface, and this way, the screen printed sensors can be easily repeatable.

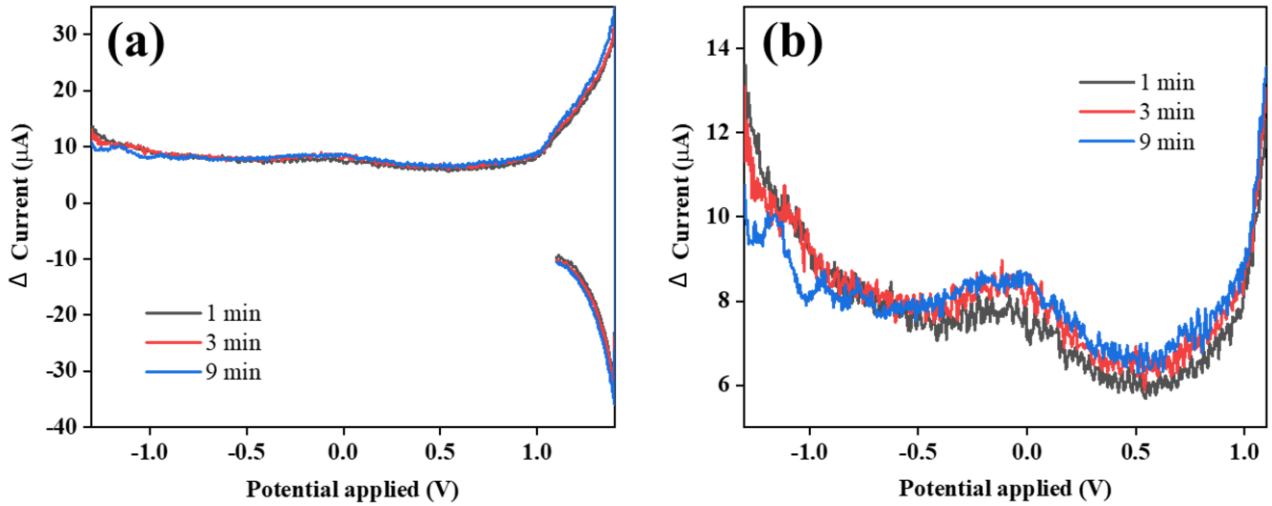

Figure 6-8: DPASV voltammograms response obtained for analyte concentrations of 5 ppm with varying deposition time (1,3,9 min), showing the change in peak current with concentration at the TiO–MgO modified SPCE.

After the optimized deposition time of 9 minutes and the different concentrations of zinc ions from 1 ppm to 20 ppm are tested, their respective DPASV response curves are plotted in Figures 6-9. The reverse DPASV response curves are slightly varying from each other, which indicates incomplete stripping. Therefore,

conditioning and further CV cycles are repeated to achieve a similar baseline as the postconditioning treatment. The detection limit is set as 5 ppm for the distinguishable peak shape.

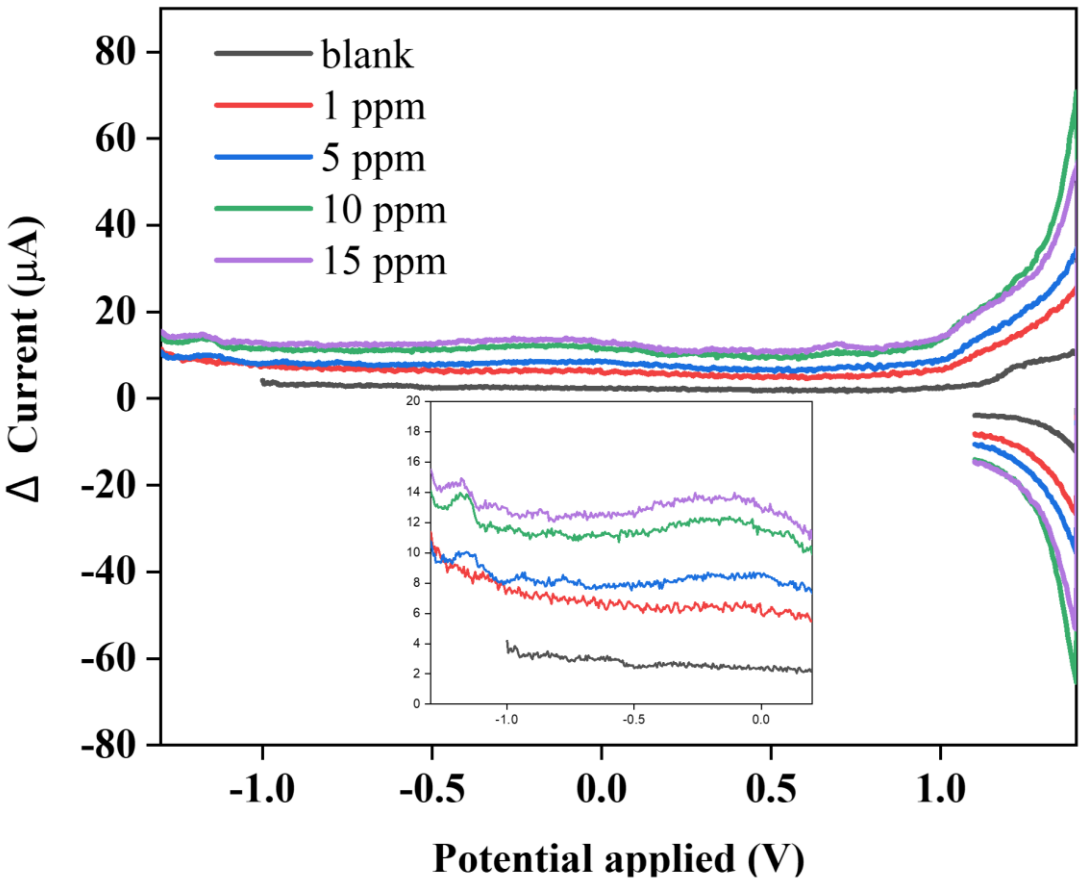

Figure 6-9: Calibration plot of DPASVpeak current versus analyte concentration (1–20 ppm) for the TiO–MgO modified SPCE, demonstrating the linear detection range and sensitivity of the sensor.

The higher Zinc ion concentration in water was detected using CV, and the DPASV method was optimized for detection in the lower concentration range. In conclusion, the DPASV response is observed from 5 ppm. To obtain clearer, more amplified, and more easily distinguishable peaks at lower analyte concentrations, future work will extend the present study by systematically applying square-wave anodic stripping voltammetry (SWASV) to optimise the detection conditions.

6.4 Results and discussion: lead and cadmium detection

6.4.1 Motivation and overview

Lead and cadmium are highly toxic metals and must be strictly monitored in environmental waters. Lead is carcinogenic and affects the central nervous system and kidneys, while cadmium exposure is associated with renal dysfunction, bone damage, and neurological effects. Both are widely used in industry (e.g. alloys, pigments, batteries, electroplating) and are common environmental pollutants.

Similar SPCE-based sensors were used for the stripping voltammetry-based detection of Lead and cadmium ions. Usually, The multiple heterogeneous sensing layer is avoided as it leads to a nonuniform coating layer with varying surface area properties, but however, I prepared a mixture of metal oxide nanoparticles of titanium

oxide and magnesium oxide to observe how a heterogenous nanomaterials.e TiO—MgO screen-printed carbon electrodes-based sensor will perform to similar space layer. Here, The DPASV technique detects lead and cadmium ions in the lower ppm to ppb concentration range. There is also a section imposing the DPASV technique over the DPV technique to show why the ASV technique is superior at the lower concentration of HMIs.

6.4.2 Bare SPCE: DPASV detection of cadmium

For the deposition of cadmium, the deposition potential is kept at -1.3 V for 120 seconds. The stripping is done by performing a differential pulsed voltammetry scan from the deposition potential, i.e., 1.3V, to 0.5V, displayed in Figure 6-10(a). The deposited cadmium at the surface of the electrode seems to be stripped at -0.8 V from 0.1 ppm to 5 ppm. Figure 6-10(b) shows the third cycle of respective cyclic voltammetry. It is seen that after ppm, the shape of the cyclic voltammetry can be easily used to detect higher concentrations. In contrast, DPV was used at lower concentrations, where the CV response does not seem distinguishable.

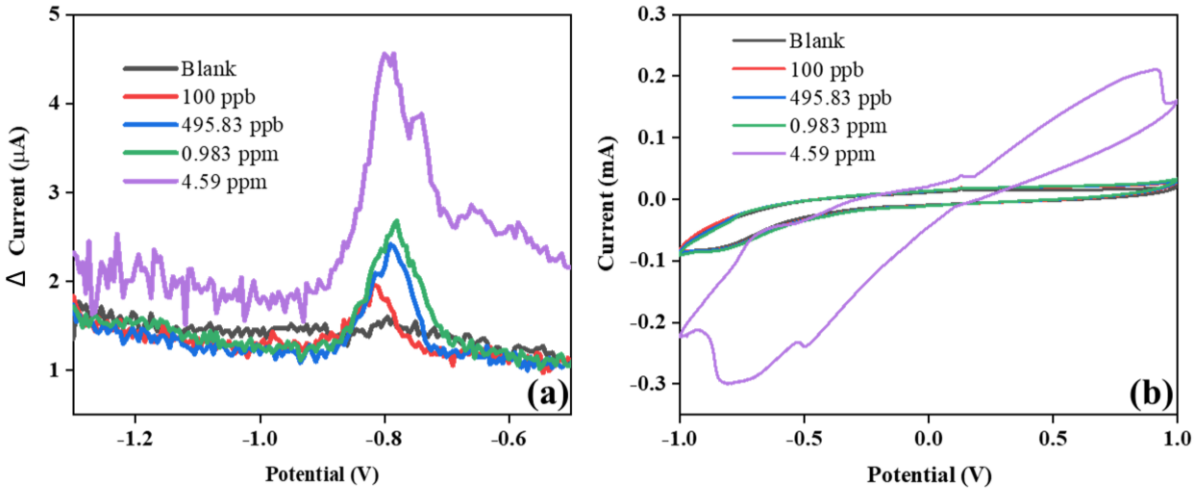

Figure 6-10: (a,b) DPASV and CV responses of varying concentrations of cadmium ions in water by using an SPCE-based sensor

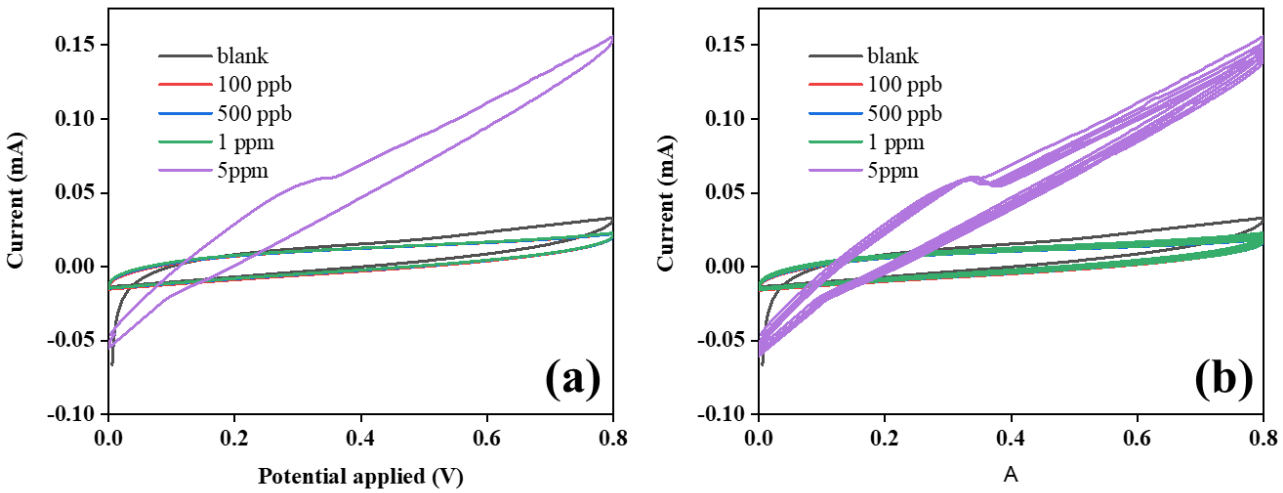

Figure 6-11: (a,b) 2nd cycle and 5 continuous postconditioning CV cycle.

Postconditioning CV cycles were run in a blank PBS solution after every DPASV step from 100 ppb to 5 ppm, shown in Figure 6-11(a, b). Here, for the detection of cadmium ions, the CV cycles were not similar to the baseline, which indicates that the deposited ions have not been completely stripped off from the surface of the working electrode. Therefore, a conditioning potential of 1.4 V is kept for 3 to 5 mins. This ensures the reuse of the printed sensor.

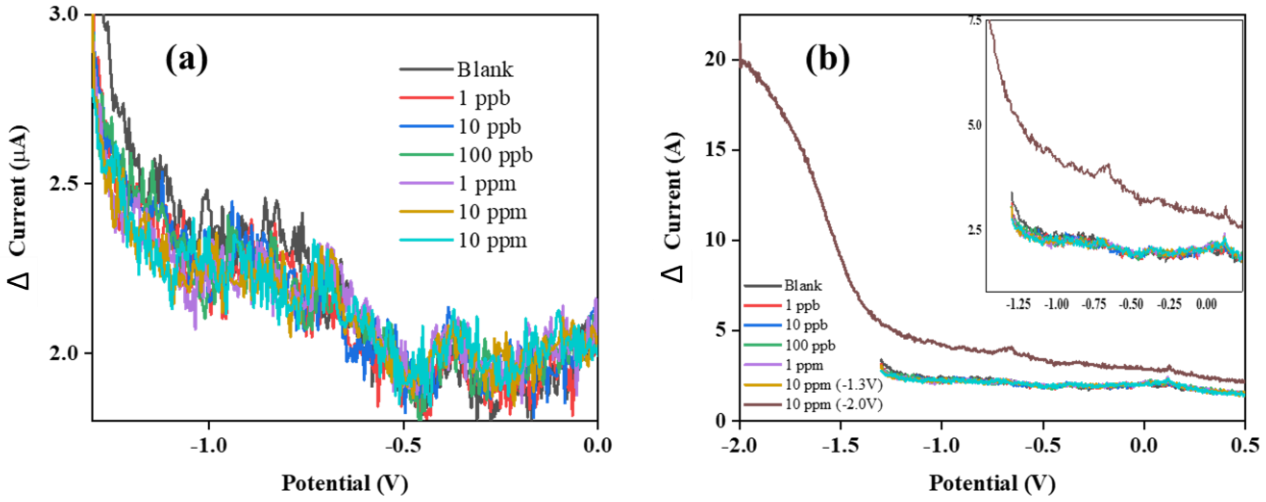

Figure 6-12:(a,b) DPASV response of SPCE-based electrochemical sensor for detecting lead ions in water.

Similar DPASV parameters, such as deposition potential as -1.3 V for the exact parameters for the anodic stripping voltammetry, were followed for the deposition time of 2 mins. However, the DPASV response for varying concentrations (i.e., 1 ppb to 10 ppm) shown in Figure 6-12(a) doesn't show a prominent peak. Therefore, the deposition potential is increased from -1.3 V to -2 V for the same deposition time (120 seconds), and it is observed that -0.67 V. This clearly shows that the deposition and stripping of lead are easier than cadmium. Therefore, a prominent peak isn't as clear as cadmium for the same DPASV setup. As Cadmium (Cd^{2+}) has a more negative reduction potential than lead (Pb^{2+}), An enormous amount of lead must be deposited

to achieve a prominent peak. So on the literature survey, it is observed that the optimised time for the deposition of lead is 5 to 30 mins.

However, cadmium and lead's reduction (or stripping peaks) appear at -0.8V and -0.67V, which indicates a separate peak similar to other literature articles. On observation, the zinc ion detection at lower concentrations failed as sufficient deposition wasn't achieved quickly. Therefore, I can focus on zinc after lead and cadmium-based work.

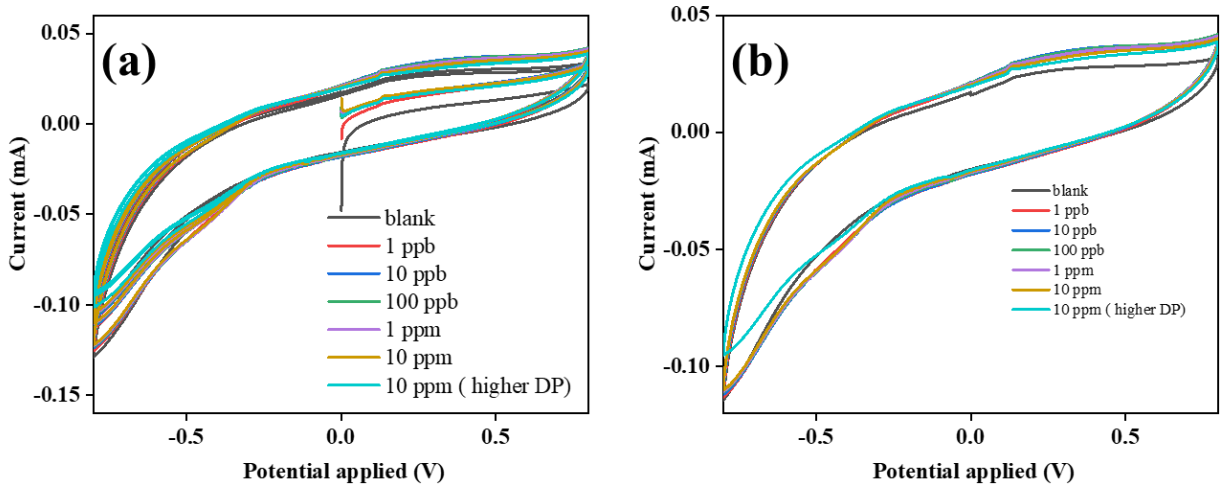

Figure 6-13:(a,b) preconditioned CV before DPASV detection method

Several CV cycles were run before DPASV-based testing for the above results, as shown in Figure 6-13(a). Most of the baselines of the 2nd CV cycle remain close to each other in Figure 6-13(b) except for the final redo run. In this case, the higher concentration of lead, 10 ppm, has been run several times, and more CV postconditioning is needed to remove the deposited lead ions. The immediate postconditioning CV cycles in Figure 6-14(a,b) afer the DPASV without changing the analyte spiked electrolyte shows that the shape of the CV curves doesn't have prominent peak heights indicating that the redox reaction isn't predominant in the positive potential window and the CV response on multiple consecutive cycles, showing that the stripping process doesn't leftover much of the depostited lead ions on the surface of the working electrode.

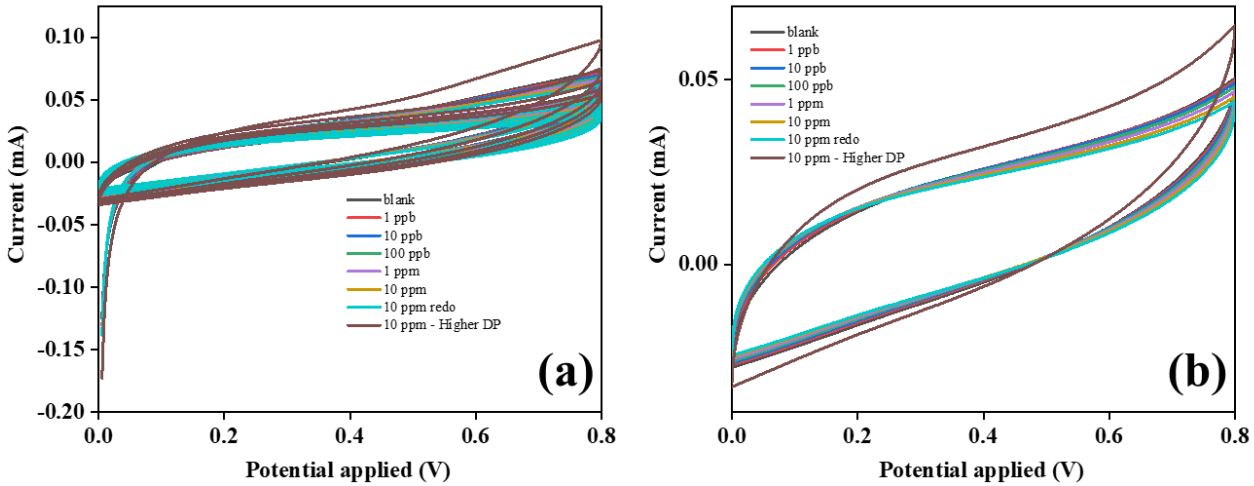

Figure 6-14: (a, b): postconditioning CV cycles after DPASV-based detection

6.4.4 TiO-MgO mixture modified SPCE-based electrochemical sensor

To perform anodic stripping voltammetry (ASV) for the detection of cadmium ions (Cd^{2+}) and lead ions (Pb^{2+}), mixtures of TiO_2 and MgO were thoroughly blended and then coated onto the working surface of the SPCE working electrode (WE). Because this coating is based on a heterogeneous mixture of metal oxides, small variations in the local composition and microstructure of the film are expected between electrodes. Such variations can lead to differences in the effective electrode surface area and active sites, which in turn may reduce batch-to-batch reproducibility of the sensor response.

Nevertheless, this TiO_2–MgO composite layer provides a useful model system for investigating how mixed metal-oxide nanomaterials in the sensing layer influence the stripping behaviour and overall analytical performance of the sensor.

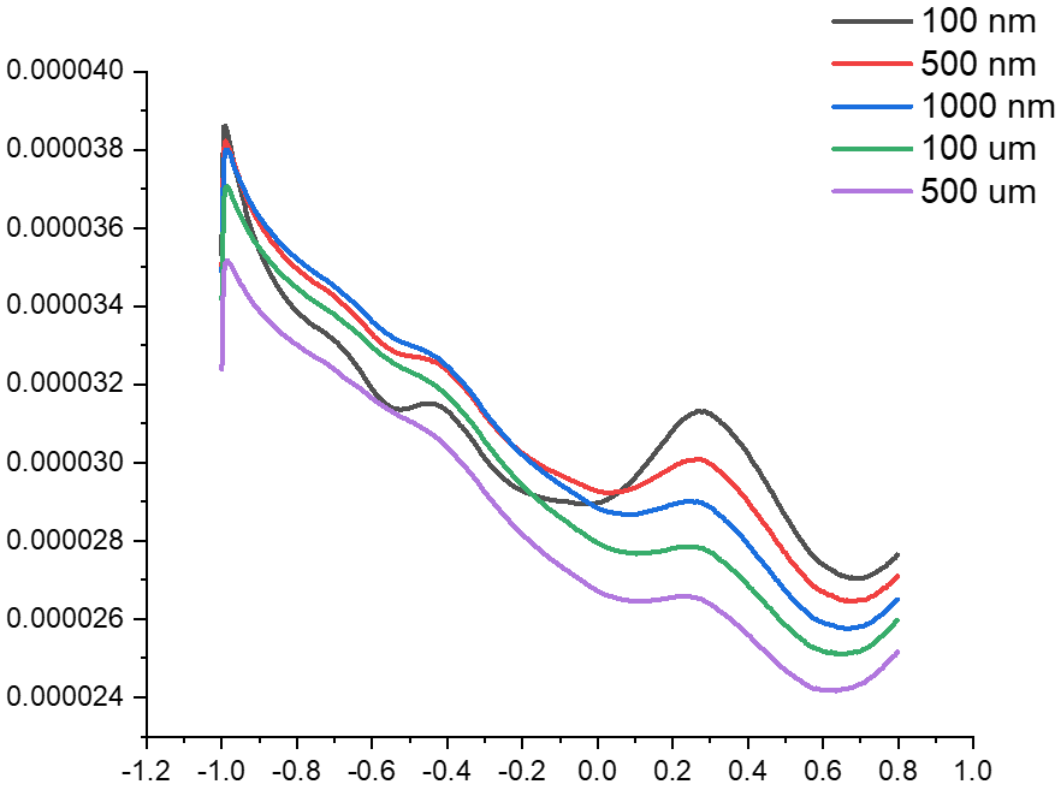

Figure 6-15: (a, b) DPASV response of Cd^{2+} ions in 0.1 M phosphate buffer solution.

For this, A bare screen-printed carbon electrode is modified with a nanomaterial mixture of titanium oxide (TiO) and magnesium oxide (MgO) in a 1:1 ratio to enhance its sensing capabilities. In this experiment, a solution of lead chloride at a concentration of 100 µM is introduced into a 0.1 M phosphate buffer solution to serve as the analyte. The initial electrochemical characterisation is performed using differential pulse voltammetry (DPV), scanning a potential range from -0.8 V to 0.8 V and displayed in Figure 6-15. However, no significant peaks are observed during this scan, indicating that no redox reactions occur on the electrode's surface under these conditions.

Anodic stripping voltammetry (ASV) is adopted as a more suitable method for detecting cadmium and lead ions, as shown in Figures 6-15 and 6-16, respectively. Firstly, Cadmium is deposited onto the modified working electrode by applying -1 V potential for 30 sensors, and their DPASV response is gathered for the varying concentrations from 100 nM to 500 µM of cadmium ions in 0.1 M PBS, as shown in Figure 6-10. Cadmium ions are pre-concentrated onto the electrode surface by applying a deposition potential of -1 V for 30 seconds. Following this deposition step, the DPV is re-run, now scanning from -1 V to 0.8 V. This approach allows for the electrochemical reduction and subsequent oxidation of lead, enabling its detection. The DPASV response from 100 nM, 500 nM and 1000 nM (i.e., 11 ppb, 56 ppb and 112 ppb) shows a DPASV peak at -0.8 V. These results show excellent sensitivity compared to the unmodified SPCE-based sensors. This might be

due to multiple reasons, such as the mixed nanomaterials' catalytic properties, the working electrode's better surface area, or particular affinity from these nanomaterials towards the analyte.

Similarly, a concentration study of lead ions was conducted under identical conditions, as displayed in Figure 6-17, with a deposition potential of -1 V and a deposition time of 30 seconds. The experiment involves preparing lead chloride solutions in varying concentrations, ranging from 100 nM to 500 µM, within a 0.1 M phosphate buffer solution. DPV response curves are collected across the potential range of -1 V to 0.8 V. In these curves, a clear and distinct peak is observed at -0.4 V for a lower concentration of 100 nM (20 ppb), but the modification of TiO -MgO doesn't help in obtaining a distinct peak after such concentration. In both cases of lead and cadmium detection, it is seen that the peak occurring on the baseline caused by probable redox of magnesium has been affected by the increasing concentration of both lead and cadmium art 0.2 V. This leaves the possibility of gathering information from both stripping-based peaks and peaks of the modified surface

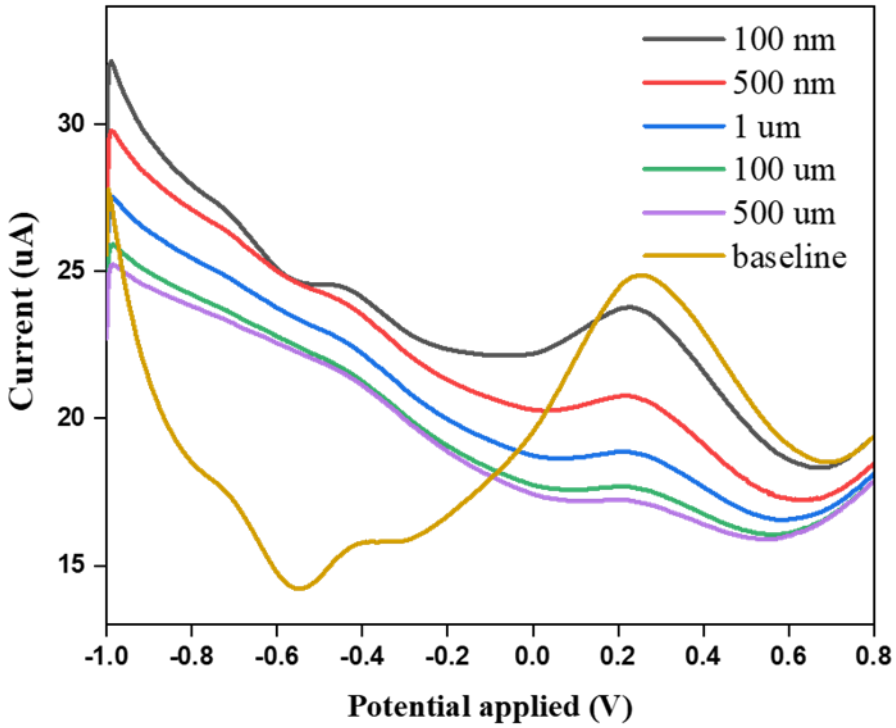

Figure 6-16:DPASV response of Pb2+ ions in 0.1 M phosphate buffer solution.

material, which can be tactically understood and further calibrated to detect in higher concentrations. Therefore, the data acquisition method can not only from the direct interaction between the analyte and the working electrode besides the intention of the proposed scanning technique but also from the indirect

interaction between the modifying material and the proposed electrochemical technique, which can be used for further investigation of the sensitivity of the targeted analyte.

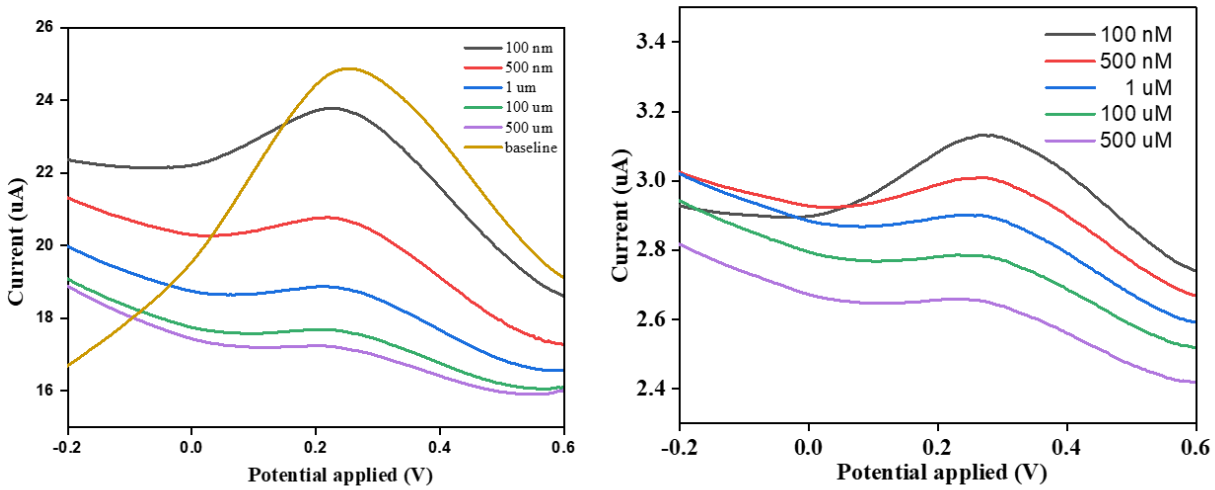

Figure 6-17: (a, b) Effect of lead and cadmium ion0 on Mg based peak respectively.

6.2.5 Comparison of DPV and DPASV for lead detection

A significant difference between DPV and stripping methods (DPASV) shows that the interaction between the regular pulsed technique and anodic stripping-assisted pulsed technique can be seen from the displayed plotted Figure 6-18. Here the X-axis and Y- Axis with were referred as A and B were potential applied (V) and differential current measures (A).

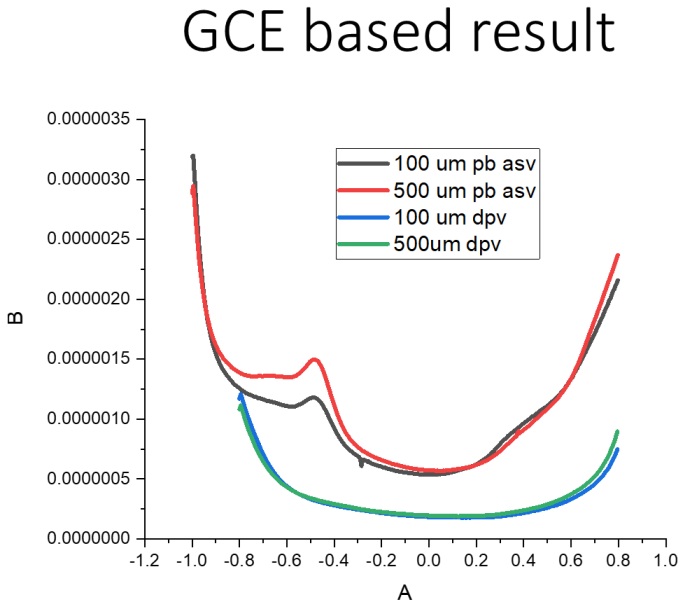

Figure 6-18: DPV and DPASV-based detection is done on lead ions.

For the setup, the concentration study is run for the same deposition potential of -1 V, and the deposition time is 30 seconds. From 100 nM to 500 µM concentration of lead chloride in 0.1 M phosphate buffer solution, the DPV and DPASV response curves were obtained from -1 V to 0.8 V. The peak is observed at 0.225 V. So, the deposition stage is skipped, which gives the idea that the lead hasn't been deposited in the DPV method, which leads to unidentifiable or lack of peak currents. So, obtaining a certain level of analyte deposited onto the working electrode is essential if there is a lack of prominent interaction between the sensing layer and the targeted analyte.

6.5 Conclusion

In conclusion, the hidden stages of the Anodic stripping voltammetry method, such as preconditioning and post-conditioning of the printed sensor, are discussed. Further, the optimisation of the deposition stage and the conditioning stage is crucial for the reusability of the fabricated sensor to achieve field application. Even while deposition is based on the affinity between the targeted analyte and the working electrode, some data can be gathered from an indirect approach between the sensing layer and the analyte (for example, lead and cadmium on magnesium reduction) can be utilised for acquiring sensor data and this is crucial in field application where unknown interfering agents are present. The reusability of printed SPCE-based sensors for heavy metal detection using differential pulse anodic stripping voltammetry has been investigated in detail.

- For zinc, the hidden stages of ASV—particularly preconditioning and post-conditioning—were shown to be critical for achieving repeatable use of the same sensor. Systematic optimisation of deposition potential/time and conditioning potential/time yielded conditions under which Zn^{2+} could be detected down to ~5 ppm while maintaining sensor reusability.
- For cadmium and lead, both bare SPCEs and TiO_2–MgO modified SPCEs were studied. The TiO_2–MgO composite significantly improved sensitivity for Cd^{2+} and Pb^{2+} in the low ppb range, though at the expense of some batch-to-batch uniformity. The work also highlighted that useful analytical information can be obtained not only from direct analyte peaks but also from indirect interactions between the analyte and the modifying layer (e.g. cadmium/lead influencing Mg-related peaks).

Overall, this chapter demonstrates that:

1. **Optimised deposition and post-conditioning steps are essential** for reusing printed sensors in stripping voltammetry, particularly in field applications where single-use disposability may not be economically feasible.
2. **Mixed metal-oxide sensing layers** such as TiO_2–MgO can significantly enhance sensitivity for trace heavy metals, while also introducing new features in the voltammograms that can potentially be exploited.
3. **Stripping-based techniques (DPASV, and in future SWASV)** provide clear advantages over standard DPV when dealing with low-concentration heavy metals and modest sensor–analyte affinity.

[7] Designing of readout equipment for field application.

This chapter focuses on the development of readout equipment for field-deployable electrochemical sensing of potentially toxic elements (PTEs) in water. First, g-C_3N_4 nanomaterials are used to detect Cobalt ions in water using square wave voltammetry, and readout equipment is built using Arduino for amperometry monitoring for the change of cobalt ions. Second, we use Zinc oxide nanomaterials for the possible detection of gold, silver, manganese, and cobalt ions in water. This chapter attempts to make a simple Arduino-based amperometric detection and PCB-based readout.

The chapter is structured as follows. Section 7.1 provides a brief overview of how a potentiostat operates, to motivate the design of custom readout electronics. Section 7.2 describes the materials and methods used for sensor development. Section 7.3 presents the electrochemical characterisation of the g-C_3N_4- and ZnO-modified sensors. Section 7.4 details the development and testing of the Arduino-based and PCB-based readout electronics. Finally, Section 7.5 summarises the main findings.

7.1 Operating principle of the potentiostat

Understanding the working mechanism of the readout potentiostat is crucial for its basic construction. For this, we adapted the discussion on practical potentiostat and readout design presented in a webinar by Pine Research Instrumentation. A potentiostat is an analytical instrument that regulates the working electrode's potential within a multi-electrode electrochemical cell. It comprises various internal circuits that enable it to perform this function by generating and measuring both potentials and currents. The potentiostat is connected to the electrodes in the electrochemical cell via external wires in a cell cable. In a standard three-electrode setup, this cable connects the working, counter (or auxiliary), and reference electrodes on one end and the potentiostat's cell cable connector on the other. The potentiostat's internal circuitry manages the applied signal to ensure accurate measurements and control. The fundamental electronic element of a potentiostat is the operational amplifier, commonly known as an op-amp. This component incorporates a feedback mechanism by routing a portion of the op-amp's output signal back into itself. This feedback loop allows the potentiostat to control the working electrode's potential precisely.

During the operation of a potentiostat, the user applies a voltage Vi to the electrochemical cell. The High Gain Operational Amplifier (Op-Amp) sends an output voltage Vo to the cell through the counter electrode (CTR). The counter electrode transmits current (iCTR) through the solution to the reference electrode (REF), the working electrode sensing (WRK_sense), and the working electrode drive (WRK_drive). It is important to remember that the inputs to the operational amplifier have high impedance, so no current flows through them. Thus, the only path for current flow is through the WRK_drive.

The electrometer measures the voltage difference between REF and WRK_sense. As current flows from the CTR to the WRK_drive, it causes a voltage drop across the solution, which is proportional to the solution's bulk resistance. This affects the potential at REF and WRK_sense. However, because reference electrodes are designed to maintain a stable potential, the potential at REF remains constant. Consequently, any variations in the measured potential are attributed to changes at WRK_sense. The voltage difference between REF and WRK_sense, known Vfeedback, is fed into a voltmeter (V) to measure this difference.

Figure 7-1: General layout of potentiostat for a 3-electrode system

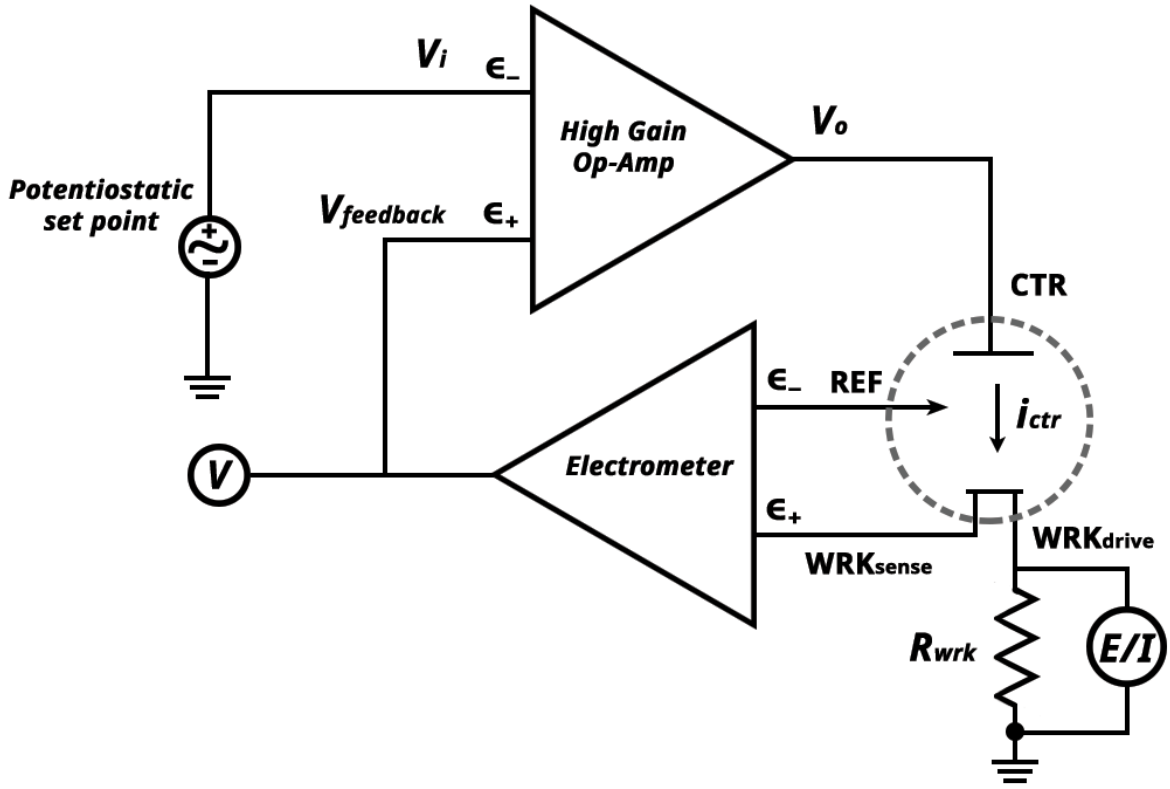

This voltage also enters the non-inverting (ϵ+) input of the High Gain Op-Amp. The Op-Amp amplifies the difference between ϵ+ and ϵ− . If Vfeedback deviates from Vi, the op-amp adjusts Vo until they match. It's important to note that in potentiostat design, the current at the working electrode is not measured directly. Instead, the voltage across a known resistor Rwrk , located between WRK_drive and ground, is measured. Using Ohm's Law, the current can be calculated as:

i=V/RwrkV

where i is the current, V is the voltage, and Rwrk is the known resistor between WRK_drive and ground. In summary, the current at the working electrode is determined by measuring the voltage across Rwrk using a voltmeter (E/I), the working electrode potential is measured by the electrometer (V), and the applied potential is set by the potentiostatic control. The feedback mechanism of the op-amp allows precise adjustment of the working electrode's potential relative to the reference electrode while simultaneously measuring the current, which is fundamental to voltammetric techniques.

7.2 Materials and methods for sensor development

7.2.1 g-C_3N_4 nanomaterial modified SPCE based electrochemical sensor for the detection of cobalt ions in water

Cobalt is a vital micronutrient for both animals and plants, serving as an essential component of the cofactor in vitamin B12 and other cobalamines. A deficiency in cobalt can lead to various health issues, including anaemia, stunted growth, and decreased appetite. Conversely, excessive intake of cobalt can be toxic, resulting in symptoms such as diarrhoea, gastrointestinal irritation, and vomiting. Moreover, exposure to cobalt has been linked to severe lung diseases. Given its widespread presence in oceans, freshwater systems, and the Earth's crust, detecting Co(II) ions is critical.

For the preliminary data, a g-C_3N_4 modified GCE-based conventional Electrochemical Sensor, i.e., platinum coil as counter electrode and Ag/AgCl as reference electrode, was used to check gC_3N_4 for detecting Cobalt ions. Cobalt chloride salt is used to prepare the stock solution.Cobalt chloride salt was used to prepare the stock solution. The g-C_3N_4 nanomaterial was dispersed by adding 20 mg of g-C_3N_4 to 1 mL of DMF, followed by ultrasonication, and 20 µL of this dispersion was drop-cast onto the GCE surface.

For the printed version of the sensor, the gC3N4 nanomaterial is coated over an SPCE-based sensor. Electrochemical techniques such as cyclic voltammetry, differential pulse voltammetry, and square wave voltammetry are compared for their speed and sensitivity in detecting cobalt ions in water.

7.2.2 ZnO-modified SPCE-based electrochemical sensor

Silver is extensively utilised across a variety of industries, including cosmetics, jewellery, catalysis, and electronics. Silver ions are toxic to certain bacteria, viruses, and algae, primarily because they can inhibit the activity of free thiol-containing proteases and thereby disrupt biological functions. However, excess silver ions in the human body also pose health risks. Due to the widespread industrial use of silver, silver-containing wastewater can exacerbate pollution in both water and soil. The World Health Organization (WHO) has established a safe limit for silver in drinking water of 0.05 ppm, and the threshold exposure limit for silver in water to protect fish and microorganisms is below 1.6 nmol L^{-1}.

Manganese is the third most abundant transition metal in the Earth’s crust and is an essential trace element for human health. It plays a key role in activating numerous enzymes involved in metabolic processes in humans, animals, and plants. Manganese is widely used in batteries, fertilisers, ceramics, and electrical coils. However, elevated manganese concentrations can lead to neurological and respiratory complications. Therefore, monitoring manganese levels in environmental resources is also important.

In this section, a commercially obtained ZnO nanomaterial is used for the possible detection of multiple PTE analytes (Mn, Co, Au, and Ag). Stock solutions of manganese, cobalt, gold, and silver ions were prepared from manganese acetate, cobalt chloride, gold nitrate, and silver chloride (Sigma Aldrich), respectively. For sensor fabrication, 20 mg of ZnO was dispersed in 1 mL of DMF using an ultrasonicator for 30 min. Then, 20 µL of

the ZnO dispersion was drop-cast onto the SPCE working electrode and allowed to dry. DPV scans were carried out at a scan rate of 20 mV s^{-1} in 0.1 M PBS for electrochemical measurements.

7.3 Electrochemical characterisation of the sensors

7.3.1 gC_3N_4 modified GCE-based electrochemical sensor for the detection of cobalt ions:

The preliminary testing for the conventional setup-based sensor, where the GCE is modified with 20 µL of g-C_3N_4 nanomaterial, which is dispersed as 20 mg in 1 ml of DMF solution, is tested with varying concentrations of blank, 100µM, and 500µM in 0.1M PBS solution (ie 5.893 ppm & 29.465 ppm). The differential pulsed voltammetry responses for the potential window of -0.3 V to 0.8 V have been obtained at the scan speed of 20 mV/s and displayed in Figure 7-2. In comparison to the blank solution, it is seen that the oxidation of cobalt ions from Co to Co^{2+} occurs in the range of +0.18V to +0.28V. This shows that the gC_3N_4 material is sensitive towards the detection of cobalt ions in water.

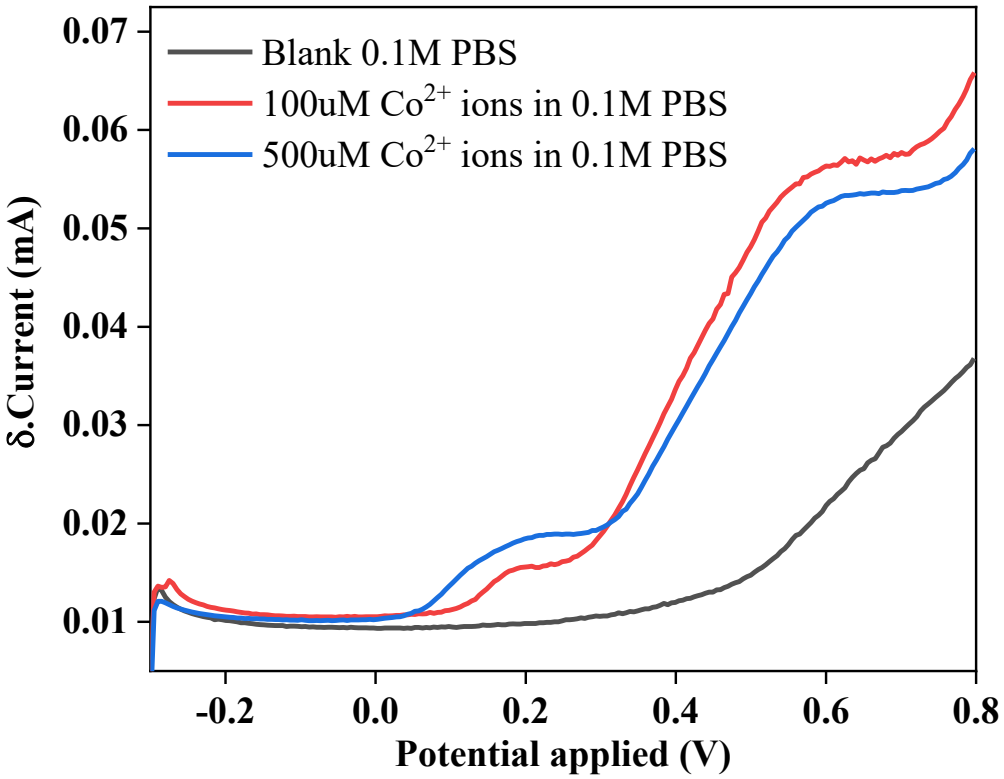

Figure 7-2:: Differential pulse voltammetry response for detecting 100, 500µM of cobalt ions in 0.1M PBS solution using gC3N4 modified Glassy carbon-based conventional electrochemical sensor with the platinum coil as CE and Ag/AgCl as reference electrode.

SPCE-BASED SENSOR: CONCENTRATION STUDY:

For the printed sensor, gC_3N_4 nanomaterial is coated over the SPCE electrode using the drop cast method. Cyclic voltammetry was used to scan for the varying cobalt ion concentration from 50 µM to 1000 µM, i.e. 2.95 ppm to 58.93 ppm in 0.1 M PBS. Figure 7-3(a) shows that the CV response shows a clear oxidation and reduction peak in the 0.6 V to 0.8 V and 0.2 V to 0.7 V, respectively. The change in the oxidation potential between the GCE and SPCE-based sensors is due to the change of reference electrode from the standard

Ag/AgCl electrode to the printed carbon electrode. Their DPV responses for the same concentration of cobalt ions obtained at the scan speed of 20 mV/s show a peak around the +0.5 V to 0.75 V range, and it is shown in Figure 7-3(b). The comparative performance of SPCE over GCE is visible as the peak current height of SPCE is almost five times higher than GCE for the same concentration of 500 µM cobalt. This is either due to the higher nonfaradaic current caused by the capacitive nature of the printed sensor or the greater affinity of the exposed screen printed carbon layer. The foremost is almost insignificant as the DPV-based technique is designed to reduce the background nonfaradaic current. In comparison to the CV-based response, DPV is still relevant and more sensitive in this case of detection, but the response time is around 2 to 3 mins for the set potential window.

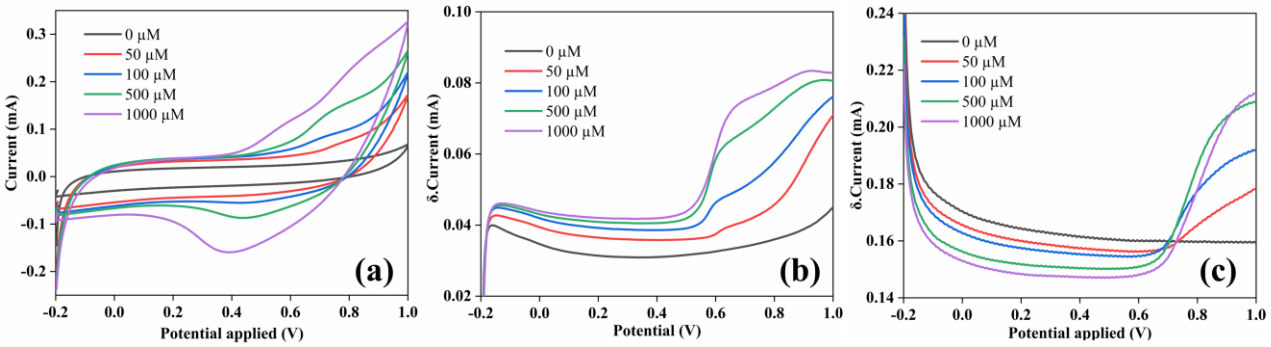

Figure 7-3:(a, b, c): CV, DPV, SWV response of cobalt ions in 0.1M phosphate buffer solutions for the varying concentration of cobalt ions from 50 µM to 1000 µM

Figure 7-3(c) shows the performance of the printed sensor under the squarewave voltammetry technique. For the same potential window between -0.2 V and 1 V., the scan speed is around 50 mV/s, and the response time was roughly under 45 seconds. The SQW response shows a high current change in the peak occurring at 0.75 V as the amplitude current is almost double the pulse in DPV, which leads to a high faradaic current, which implies a high signal-to-noise ratio. However, SQW is usually unsuited for this irreversible system as it usually runs a bidirectional pulse, allowing both oxidation and reduction to occur with the amplified pulse. This case shows less reliability in an irreversible system.

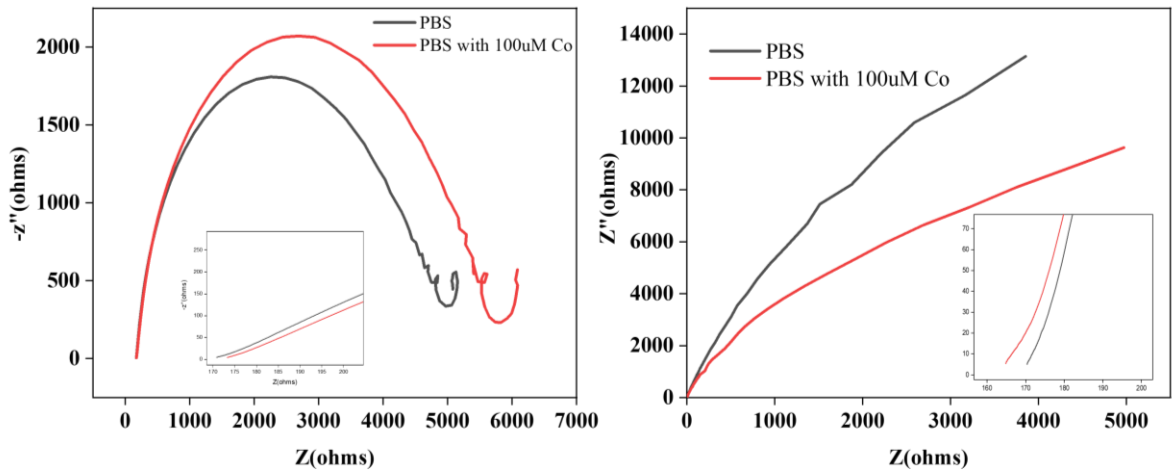

Figure 7-4:(a,b) Nyquist (EIS) response of gC3N4 modified GCE and SPCE-based sensors for the detection of Co^{2+} ions

EIS STUDY:

The EIS responses for the g-C_3N_4-modified GCE and SPCE sensors are given in Figure 7-4. Figure 7-4 shows Nyquist responses for the GCE and SPCE-based gC_3N_4 modified electrochemical sensor. For the GCE-based sensor in Figure 7-4(a), it is observed that there is a large semicircle that implies that there is a high charge transfer resistance between the interfaces of the electrode and the electrolyte layer, along with the double-layer capacitance. In the presence of the cobalt ions, it is seen that the magnitude of the semicircle increases further, and this shows that the electrode transfer is reduced further due to the increase in charge transfer resistance. This happens as the oxidised cobalt ions deposit over the surface of the electrode and hinder or insulate the electrode transfer during the redox reaction. There is a small tail at the end, which shows that there are fewer mass transport phenomena in the electroactive species.

Figure 7-4(b) shows no semicircle, which implies insignificant charge transfer resistance. The sloppy curve results from Warburg impedance, representing the diffusion control. This indicates that the electroactive species' mass transport occurs at the electrodes' surface due to the electrochemical process (in this case, diffusion due to redox reaction).

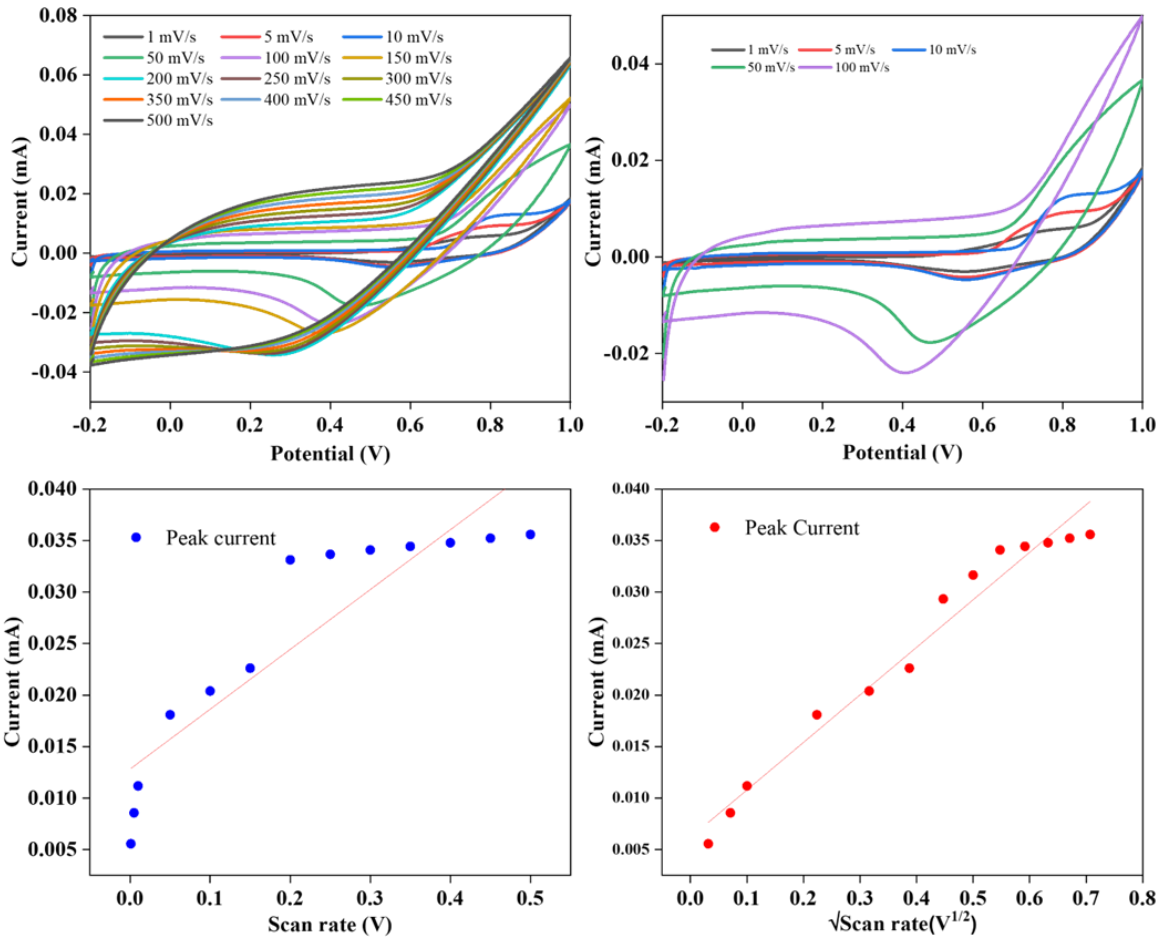

Figure 7-5: (a,b) effect of scan rate study for the present iof 100 µM cobalt concentration from 1 mV/s to 500 mV/s, (c) Scan rate vs Peak current height observed in CV cycles, (d) √Scan rate vs Peak current height.

THE EFFECT OF SCAN RATE:

Figure 7-5(a) shows the effect of scan rate for the CV cycles to detect the concentration of 100 µM of cobalt ions in 0.1 M PBS while varying the speed of the scanning voltammetry from 1 mV/s tro 500 mV/s. Figure 7-5(b) displays he possible scan speed to distinguish the redox peak, which is 1 mV/s to 100 mV/s; increasing the scan speed leads to the not recognisable of the redox current as the scan might skip the working potential for the occurrence of the redox reaction. The scan rate is plotted against their corresponding peak current height in Figure 7-5(c), which shows that the slope obtained is poorly linear and doesn't cover them significantly. This typically means that the detection mechanism isn't predominantly due to the diffusion of cobalt ions over the surface area of the working electrode. Figure 7-5(d) shows that the plotted graph between the square root of the scan rate vs their respective peak current has a high linearity, and their slope covers the significant plot points. This is due to the detection phenomena over the sensing layer being driven by an adsorption-based mechanism, which correlates well with the EIS result where the gC3N4 modified SPCE has more mass transfer of the electroactive species in the sensing system.

7.3.2 Possible detection of PTEs using ZnO-modified SPCE sensor

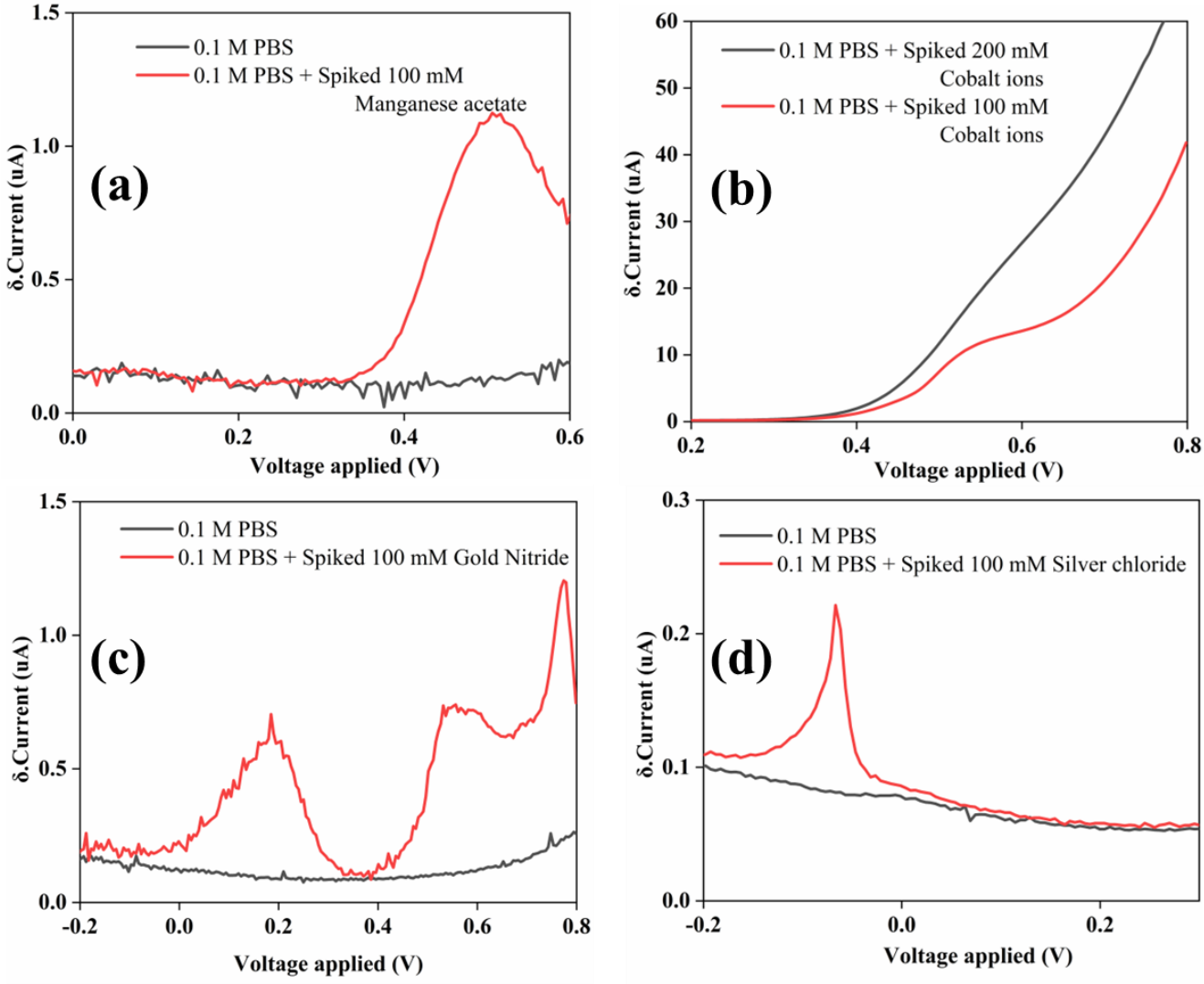

Figure 7-6:(a,b,c,d): DPV response for the spiked PTE ions in water using ZnO modified SPCE based EC sensor.

Here, the DPV response for the concentration of 100 mM individually spiked analytes of manganese, cobalt, Gold and silver in 0.1 M PBS solution was displayed in Figure 7-9(a,b,c & d) accordingly. The ZnO-modified SPCE-based EC sensor has been analysed before with other HMI salts formed from Chloride, acetate and nitrate salts. Theu tends to show a plain DPV response. However, the DPV has multiple peak current spikes in this case due to multiple redox-based electrochemical reactions. This suggests that the DPV response might arise from our targeted analytes. Since the ASV technique is not adapted here, the ZnO-modified electrode surface might have other interactions with the targeted analytes. In Figure 7-9(a), the reduction potential observed around +0.55 V, might be due to the half-reaction of manganese species

$$MnO^2 + 4H^+ + 2e^- \rightleftharpoons Mn^{2+} + 2H^2O: E° \approx +0.59\,V(SHE) \quad (5)$$

For Figure 7-9(b), the cobalt ion is reducing from Co to Co^{2+}, similar to the previous working potential of +0.58 V. Figure 7-9(c), even though the DPV responses show multiple peaks at 0.2 V, 0.58 V and +0.78 V.

The Other peaks at 0.2 V and 0.58 V might be due to the formation of intermediate gold hydroxide components in water. The sharp peak occurs at 0.78 V, which might be the half-reaction of gold species to metallic gold.

$$Au(I) + e^{-} \rightleftharpoons Au(s); E° \approx +0.8\,V\ (SHE) \quad (6)$$

Figure 7-9(d) shows the sharp peak in the DPV response due to the easier deposition of silver ions over the ZnO-modified working electrode surface. This can effectively be used for the detection of silver ions in water.

7.4 Readout electronics development and testing

7.4.1 Arduino-based readout for field deployment

For the readout application, a simple Arduino-based readout was designed to concentrate copper ions from 0.1 mM to 100 mM; the results are shown in Figure 7-6(a). Figure 7-6(b) shows the circuit layout of the sensing-based readout system. The readout circuitry works by applying a potential difference between the counter electrode and working electrode via the digital-to-analogue (DAC) pin of the Arduino microcontroller and measuring the current passing between the working electrode and the reference electrode of the sensor, using operational amplifiers to enhance the signal strength and minimise the electrical noise of the circuit. The readout circuit was implemented on a printed circuit board (PCB), shown in Figure 7-6(c), to minimise the noise and enhance the instrument's overall electrical stability. Upon testing, it was determined that the circuit needs further improvement for high-sensitivity detection.

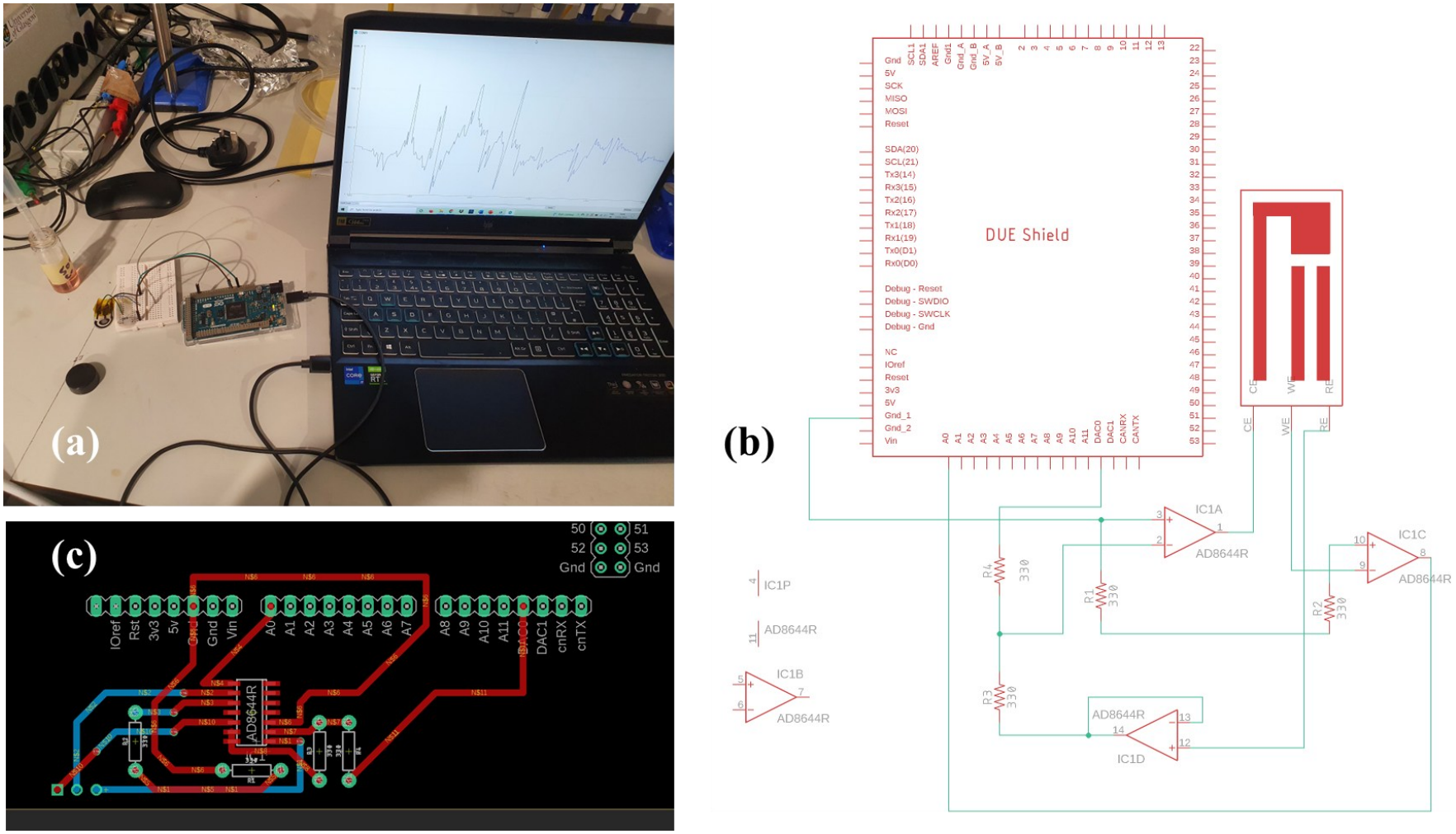

Figure 7-7:: (a) Arduino-based Readout as sensing equipment for chronoamperometric application in detecting Cobalt ions in water; (b) circuit schematic for the readout equipment; (c) PVB layout.

Demonstration: To a blank solution of 0.1 M PBS where the readout-based sensor is dipped, the varying concentration of cobalt ions from 100 µM to 100 mM (i.e. 5.89 ppm, 58.93 ppm, 2946.5 ppm, 5893 ppm) is added once the baseline is reached, and the response is plotted in Figure 7-7. Here the response is measured in resistance(ohms) and later can be converted to current. For a quicker response, the working potential of 0.7 V was constantly applied in a 3-electrode system to perform the chronoamperometry technique and see the live monitoring of cobalt ions in water. It is seen that the sensor is dipping in a blank solution of 100uM of cobalt ions, and the sensor takes around 120 seconds to reach a similar baseline. When the same sensor system was under constant varying concentrations, the current fluctuated significantly for two reasons. 1) the deposited cobalt isn't completely stripping off, and 2) the Arduino system fails due to the requirement of the current measuring system in microamps, whereas the resolution isn't sufficient.

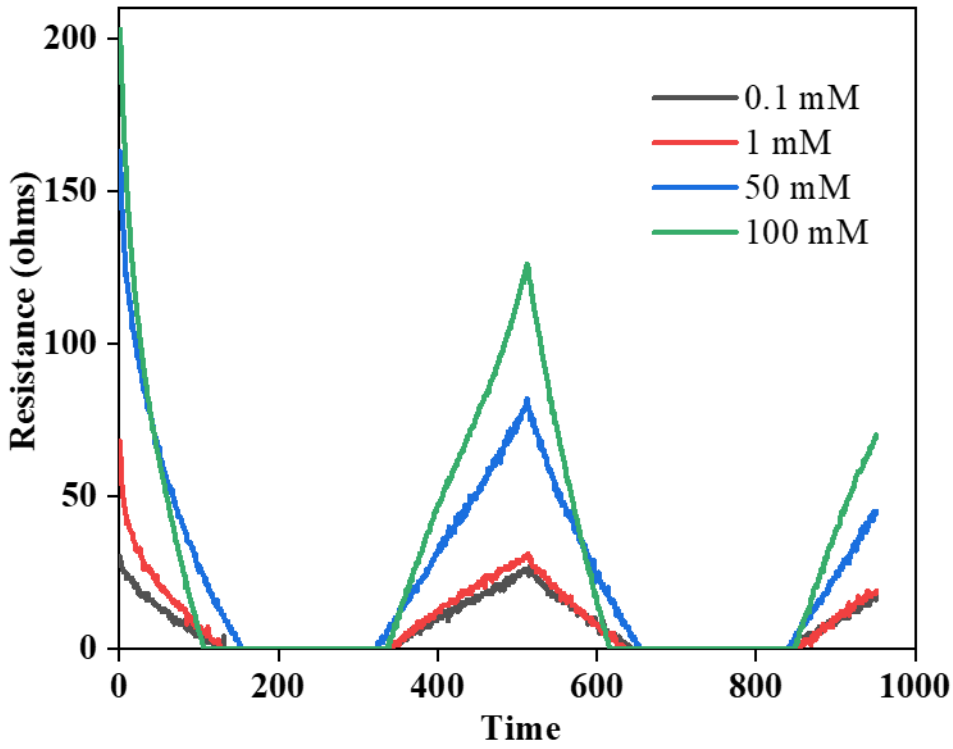

Figure 7-8: The results from the Arduino-based readout for the varying cobalt concentrations of 0.1 mM, 1 mM, 50 mM and 100 mM.

The same sensor system is consequently dipped in multiple analyte concentrations of cobalt ions, and it is noticed that the response displayed in Figure 7-8(a,b) of such chronoamperometric technique takes a lot of time to return to the initial baseline. This might happen due to the constant accumulation of the oxidised cobalt ions on the surface of the gC_3N_4-modified SPCE-based electrochemical sensor system.

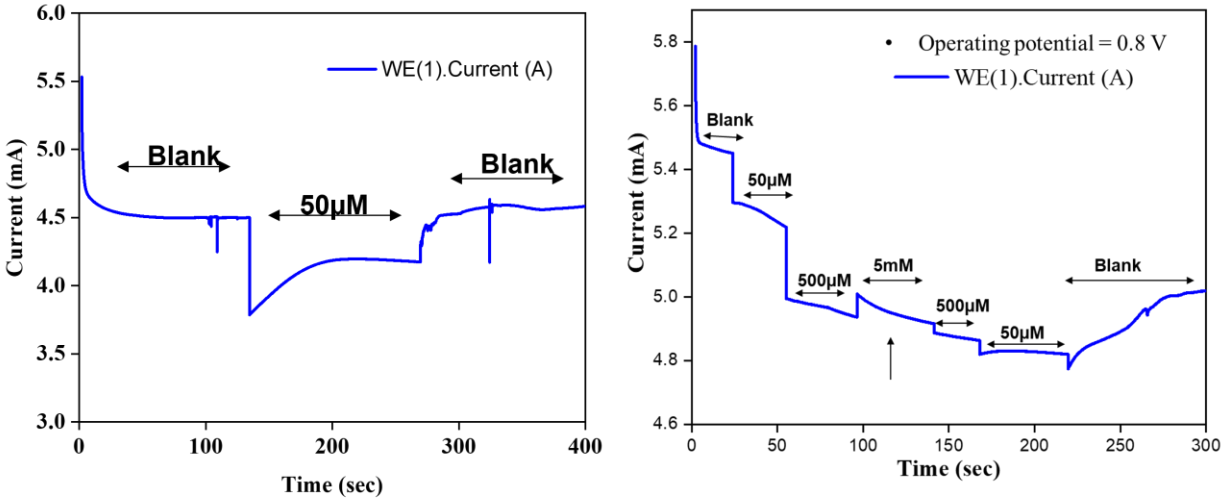

Figure 7-9: (a, b) chronoamperometric response of cobalt ions while varying concentration for continuous monitoring.

As the current resolution isn't good enough, a PCB is made using OP-Amps to amplify the current change. The design is based on a feedback OP-amps circuit similar to the usual potentiostat setup.

7.4.2 PCB-based readout equipment for field deployments

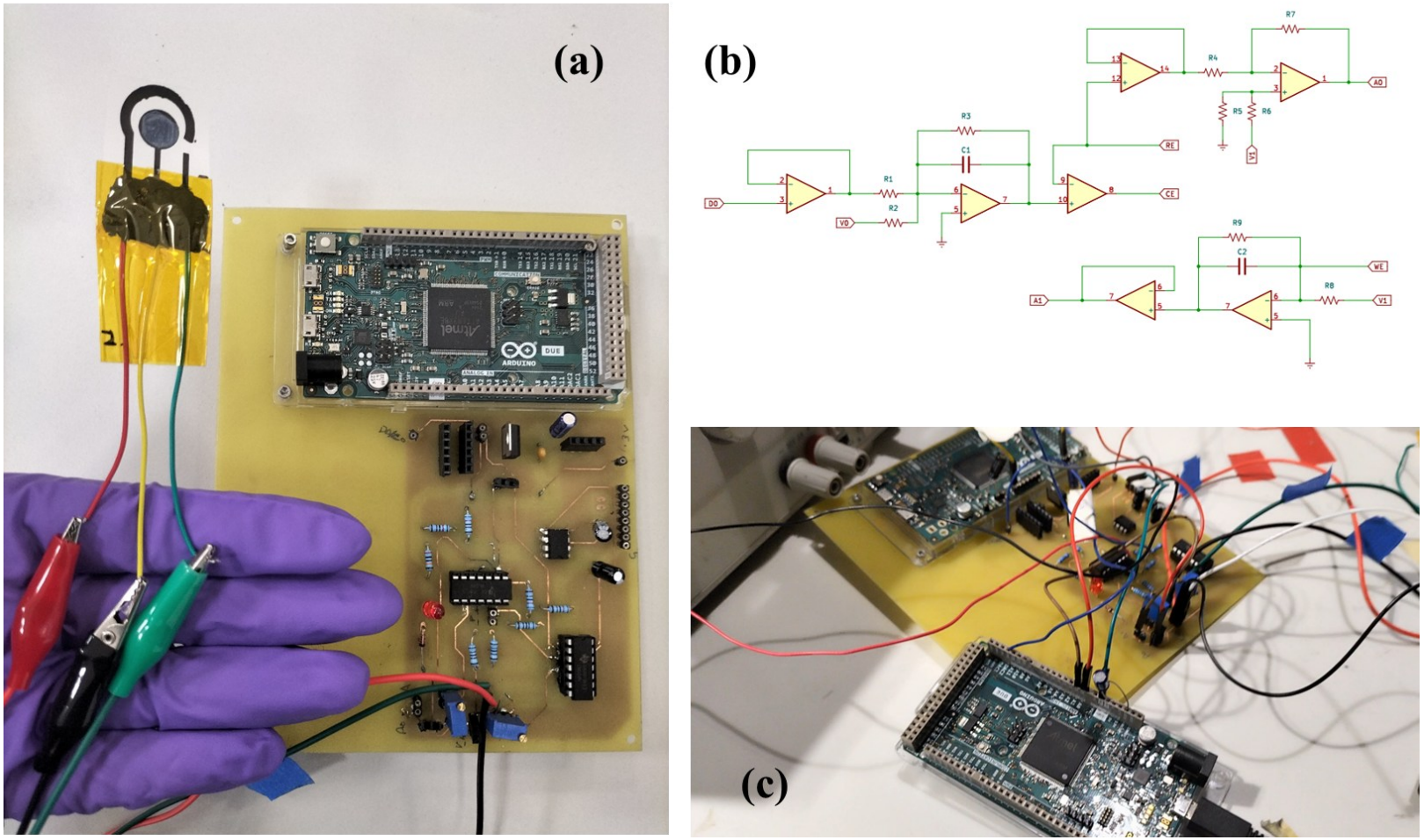

Figure 7-10: (a,c) Photographs of self built PCB based electrochemical detction; (b) Circuit schematics

To overcome the limitations of the Arduino-only system, a dedicated PCB-based readout circuit was designed using op-amps to amplify the current change. The design is based on a feedback op-amp circuit similar to that of a conventional potentiostat.

The final readout circuit, shown in Figure 7-10, comprises a series of unity-gain amplifiers (buffers) and active low-pass filters that ultimately improve the potentiostat circuit's overall performance and electrical stability. By employing a buffer circuit at every stage of the readout, the electrical impedance of the sensor would not play a significant role in the performance of the circuit, and the potential difference between the counter electrode and the reference electrode could be used as feedback which maintains the constant potential of the working electrode. The readout circuit was implemented on a PCB following circuit design and testing, as shown in Figure 7-10(b).

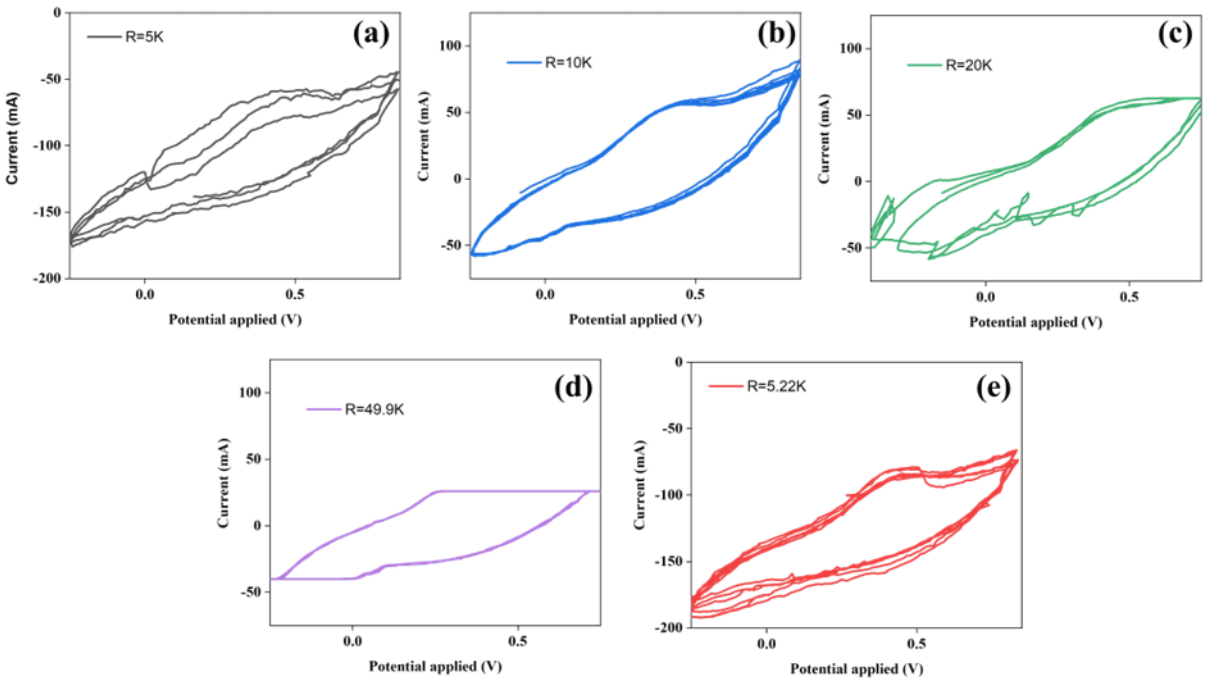

Figure 7-11:(a,b,c,d,e) Optimising the resistors for the current measurement unit.

The readout circuit resistors are optimised to achieve a proper CV-based measurement similar to the auto lab potentiostat, as shown in Figure 7-11 (a,b,c,d,e). Once the readout circuit is built, its scan rate between 10, 20, 30, and 50 mV/s is adjusted to get similar CV shapes, and a 20 mV scan is selected as the suitable scan speed. The optimising scan speed is 20 mV/s for the builtin readout equipment.

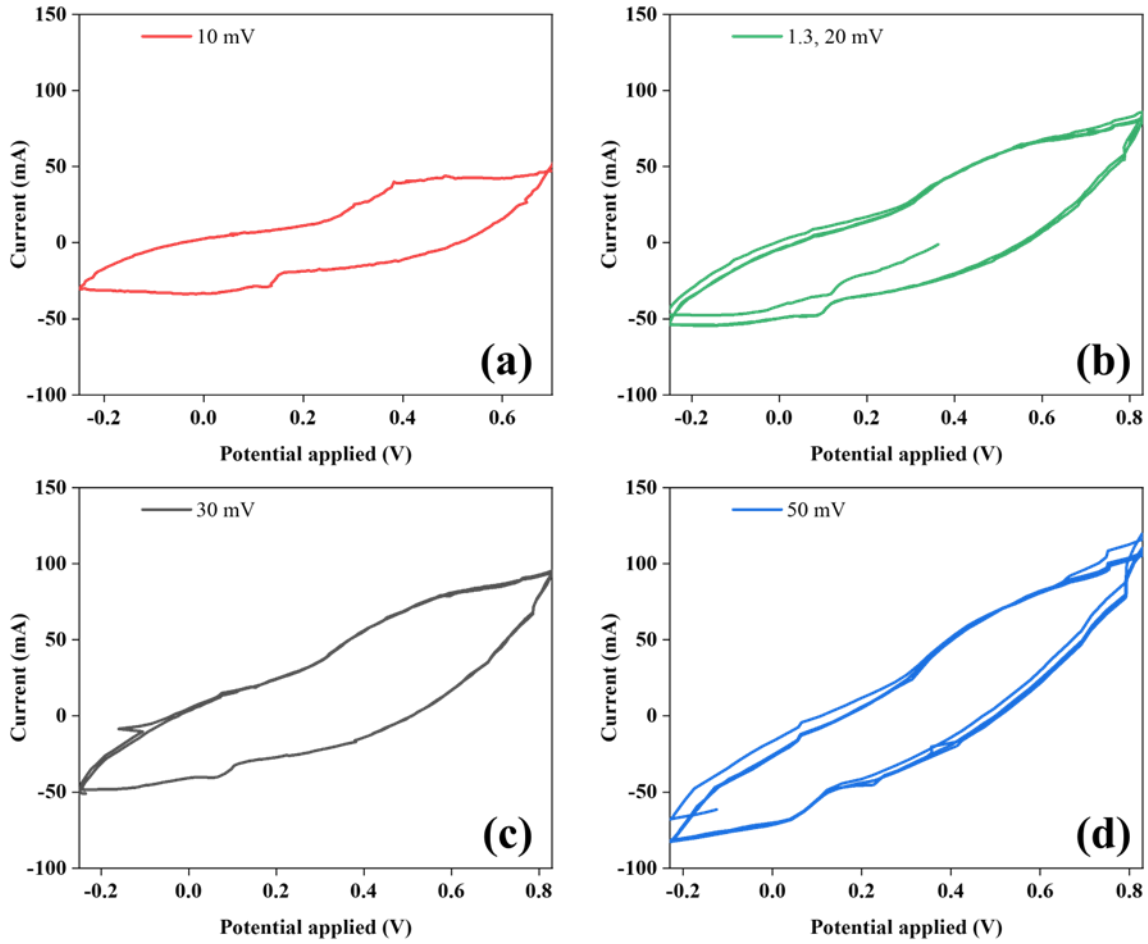

Figure 7-12: (a,b,c&d) CV response for blank 0.1 M blank PBS solution with varying scan speed of 10, 20, 30 and 50 mV/s.

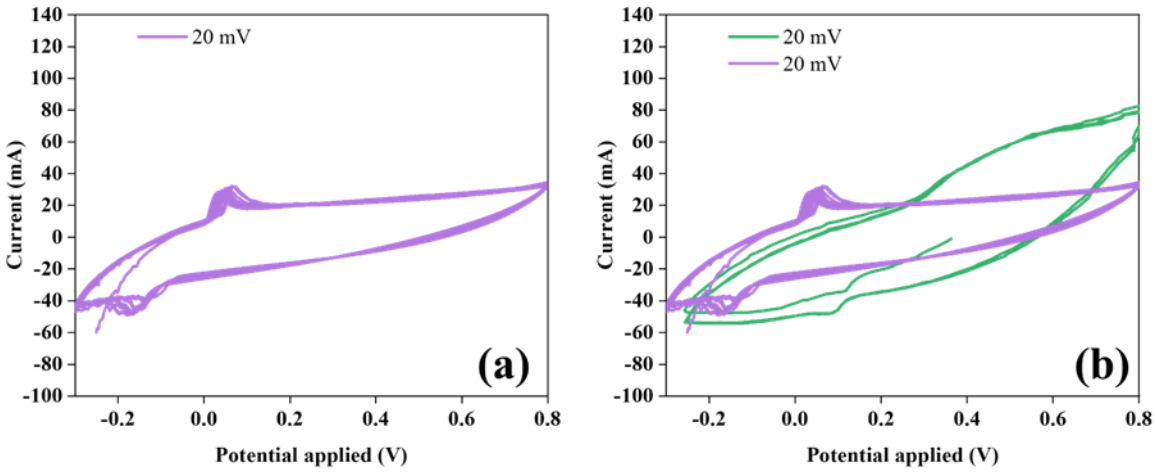

Figure 7-13:(a, b): The CV response for adding 100 mM Manganese ions in 0.1 M PBS solution is compared to Blank 0.1 M PBS.

Figure 7-13 shows the CV response for adding 100 mM manganese ions to 0.1 M PBS, compared to the CV cycle obtained for the blank 0.1 M PBS. The redox peak reaction is seen at 0.1V and -0.18 V. However, the readout built has much to improvise for field application. This work is currently ongoing for future work.

7.5 Conclusion

In this chapter, two different nanomaterial-modified SPCE-based electrochemical sensors and associated readout systems were designed and evaluated for the detection of metal ions in water.

First, a g-C_3N_4-modified SPCE-based sensor was developed for Co(II) detection. The limit of detection for cobalt was approximately 3 ppm, and the performance of CV, DPV, and SWV techniques was compared in terms of response time and sensitivity. EIS and scan-rate studies indicated that the detection mechanism is largely adsorption-controlled at the g-C_3N_4-modified SPCE.

Second, a ZnO-modified SPCE-based sensor was fabricated and investigated for the possible detection of Mn, Co, Au, and Ag ions. DPV measurements showed multiple peak responses, which were rationalised in terms of the corresponding redox processes. The ZnO-modified sensor demonstrated particularly strong responses for silver ions.

In parallel, two readout platforms were developed and tested: a simple Arduino-based chronoamperometric readout and a more advanced PCB-based potentiostat-like circuit. While both systems successfully recorded electrochemical signals, the PCB-based design provided better control and higher potential for further optimisation towards field-deployable, low-cost readout equipment.

[8] General Conclusion

As a concluding chapter, this section summarises the main findings of the work, provides an overview of the results presented in each chapter, and outlines future perspectives for the development of electrochemical sensor systems.

8.1 Main findings :

- **MoS_2-modified GCE and SPCE sensors for copper and ascorbic acid (AA):** Display of MoS_2 nanomaterial-modified GCE and SPCE-based electrochemical system for detecting copper and AA ions in water. The optimisation of thickness required for the screen-printed electrodes was demonstrated with the help of the DPV technique, where the elimination of the generated noise is avoided for a clean baseline. The significance of utilising the capacitance behaviour of SPCE due to the non-faradic current generation is that it is used for the fine detection of Flexible SPCE over the conventional GCE-based rigid electrode system.
- **g-C_3N_4-based sensors for iron detection:** The sensor based on 2D g-C_3N_4 nanomaterials demonstrates an impressive ability to detect iron in water. Its performance is assessed across iron concentration levels from 0.9 mM to 5 mM using cyclic voltammetry (CV) and differential pulse voltammetry (DPV) techniques. In addition to the concentration analysis, an accumulation study is conducted with a scan speed ranging from 10 mV/s to 1000 mV/s within the -0.6 V to 0.8 V range, along with a repeatability assessment involving 30 CV scans. Moreover, the electrodes built on rigid substrates can be substituted with flexible, environmentally friendly, and biodegradable materials to enhance disposability and facilitate practical applications in the field. Therefore, g-C_3N_4-based SPSE and SPCE were used to detect Ferrous and Ferric ions in water.
- **ASV-based detection of Zn, Cd, and Pb using SPCE:** The pretreatment and posttreatment for the ASV-based technique are investigated using SPCE for the detection of Zinc ions. The Cadmium and lead ions were also detected using both unmodified and TiO-MgO-modified electrodes. Here some non-conventional data acquirement method is discussed for further sensor characterisation.
- **g-C_3N_4-modified SPCE for cobalt detection and EIS analysis:** G-C_3N_4 modified SPCE-based EC sensors are also used to detect cobalt ions in water using multiple electrochemical techniques, such as Cv, DPV, and SWV. An EIS study helps understand the sensing mechanism for the detection of cobalt using a carbonaceous electrode as a working electrode.

8.2 Summary of the observation and performance

Chapter 3: Screen printing is a widely used technique for fabricating printed sensors and electronics. The performance of these devices can be influenced by various printing parameters, such as the thickness of the printed layer, the length and pressure applied during the printing process, and more. Although sensor design and the inks used for printing sensitive layers have been extensively studied, the critical impact of printing parameters has received less attention.

This paper explores how the thickness of printed sensors affects their electrochemical sensing properties. Carbon ink was employed to print sensors with a three-electrode geometry, and the working electrode was modified with MoS_2 to detect ascorbic acid. The thickness of the sensitive layers ranged from approximately 4 µm to 120 µm, depending on the number of printed ink layers, which varied from 1 to 5, 10, and 20. Cyclic voltammetry, differential pulse voltammetry, and impedance spectroscopy were used to evaluate electrochemical performance. It was observed that the peak current, corresponding to the oxidation of ascorbic acid at 0.04 V, increased with the electrode thickness and the number of printed layers. Higher current values and lower series resistance were noted for the 10- and 20-layer configurations, suggesting the optimal printed thickness for sensors designed for low-power operation and easy interfacing with readout electronics. With the help of AA detection using MoS2 modified SPCE electrode, it is seen that the rigid structure of the sensing layer, featuring small nanopores, offers a larger surface area, which improves the diffusion of analyte ions across the catalytic surface. The molecular dynamics study supported the experimental findings and provided insights into the molecular interactions occurring on the catalytic surface.

Chapter 4: This study presents a systematic approach for the fabrication of thick film electrodes using the screen-printing technique. The screen-printed carbon electrodes undergo modification with 2-dimensional MoS2 nanoparticles dispersed in a DMF solution. Electrochemical impedance studies conducted on both the conventional GCE-based electrochemical sensor and the modified screen-printed carbon electrodes provide insights into their capacitive and diffusion behaviours. Notably, the SPCE-based sensors exhibit superior electrochemical performance compared to the GCE-based sensor. While the modified GCE demonstrates better diffusion-controlled phenomena, the capacitive behaviour observed in SPCE contributes to achieving higher sensitivity in detecting copper ions in water. Interference studies reveal that the presence of ferrous ions could impact the detection of copper. With a detected range from 5 µM to 5 mM and a LOD of 5.43 µM, this sensor is well-suited for copper ion detection in water resources. Furthermore, the flexible form factor and cost-effective fabrication make these sensors an appealing alternative to the currently expensive, rigid sensors commonly employed for field testing.

Chapter 5: This study introduces an electrochemical sensor based on a 2-dimensional (2D) graphitic carbon nitride (g-C_3N_4) modified glassy carbon electrode (GCE) for the detection of Fe^{2+} ions in water. The 2D g-C_3N_4 nanomaterial was synthesised by dispersing and ultrasonication, then modifying the GCE surface using the drop-casting method. The structural and morphological properties of the g-C_3N_4 were characterised using X-ray diffraction (XRD) and scanning electron microscopy (SEM). The sensor's performance was evaluated for various iron concentrations (ranging from 0.9 mM to 5 mM) in the electrolyte using cyclic voltammetry (CV) and differential pulse voltammetry (DPV). The results demonstrated excellent sensitivity to the target ions. An accumulation study (with scan rates from 10 mV/s to 1000 mV/s in the -0.6 V to 0.5 V range) and a repeatability test (30 CV scans) were performed. Based on these findings, the 2D g-C_3N_4 modified sensor is a promising tool for the electrochemical detection of Fe^{2+} ions in water, with the potential for a wide range of applications.

Chapter 6: Here, an SPCE-based EC sensor detects zinc, lead, and cadmium ions in water using the pulse-assisted anodic stripping voltammetry method. This includes optimising the deposition and condition stage for the printed sensor's reusability. The sensor's pretreatment and posttreatment validate its reusable nature. TiO-MgO-based nanomaterial was used to make a heterogeneous mixture, which improved the sensitivity of the SPCE-based working electrode, which was caused by the better surface area due to the properties of the assisted nanomaterial material. The LoD of SPCE using the DPASV technique for the detection of Zinc,Cadmium, and Lead is 5ppm, 4.59 ppm and 10 ppm, respectively. TiO-MgO-based nanomaterial modified SPCE shows LoD for Cadmium and Lead is around 11 ppb and 20 ppb.

Chapter 7: In this session, the two potentiostat-based readout equipment were built, and their performance was demonstrated for the detection of the cobalt and manganese ions in water. Firstly, the g-C_3N_4 modified SPCE-based EC sensor is also demonstrated with varying electrochemical techniques for a simple comparison. Secondly, for the detection of Mn ions in water, a powerful low-cost PCB readout is built using OP-AMPS for better amplification of the measuring current.

8.3 Future perspective:

Novel materials:

Detecting heavy metals in solid matrices or suspended particulates will require further development of sample pretreatment methods. Challenges such as poor stability, limited reproducibility, and unsatisfactory performance in complex real-world matrices must also be addressed. The potential toxicity of interfacial materials, such as quantum dots, should be carefully considered before applying them to natural water samples.

Future work should focus on designing and developing innovative nanomaterials with tailored sizes and shapes that provide optimal electrochemically active sites. Appropriately designed bi- or trimetallic nanostructures could enhance specificity while improving stability. New surface modification and functionalisation techniques are also needed to enable robust attachment of functional molecules, thereby improving selectivity towards specific heavy metal ions. Sensitivity and selectivity can be further improved by creating novel substrate materials with large surface area, high chemical and mechanical stability, and good conductivity. Finally, disposable test strips with integrated electrodes could be developed for household water quality testing, in a similar manner to disposable blood glucose sensors

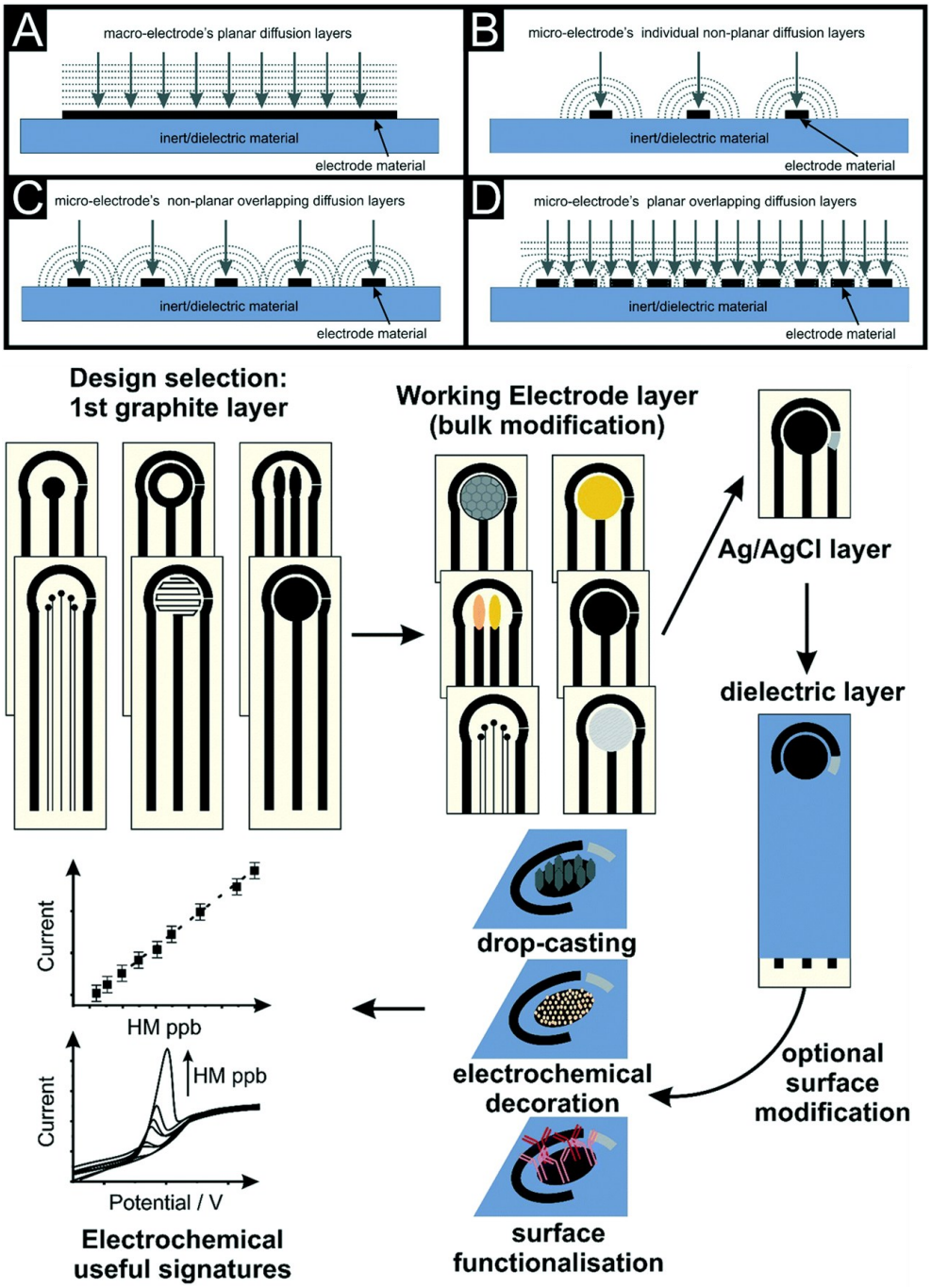

Figure 8-1: literature regarding the design of EC sensors.

Novel electrode designs:

The design and geometry of the electrode strongly affect its electrochemical performance. As reported in the literature, transitioning from macro-electrodes to micro-electrodes alters the diffusion regime for electron transfer, changing from planar diffusion to more radial diffusion and shifting from non-overlapping to overlapping diffusion layers. These changes can increase current densities, reduce ohmic losses, and improve the ratio of faradaic to capacitive currents.

Micro-electrode array sensors typically exhibit lower LODs and higher sensitivity than single macro-electrodes of the same total geometrical area, especially when individual micro-electrodes are arranged in parallel. In such configurations, radial diffusion dominates, improving mass transport and resulting in a larger effective diffusion area. Moreover, using different surface modifications on each working electrode within an array allows for simultaneous detection of multiple analytes, which is both time- and cost-effective in critical situations. For example, Rusling and co-workers demonstrated improved performance in microfluidic immunosensors by immobilising different antibodies on each working electrode of an array. Similar strategies could be applied to screen-printed electrode platforms to enable the simultaneous detection of several heavy metal ions.

Portable potentiostats for field deployment:

Portable potentiostats have become increasingly accessible as compact, low-cost devices suitable for in situ, online, and point-of-care analyses. The adoption of open-source hardware and software has given electrochemists access to affordable circuits, microcontrollers, and code. Recent work has focused on miniaturising potentiostat systems and enhancing their portability. For example, some groups have developed implantable, dynamically configurable potentiostats for remote monitoring, while others have created open-source, battery-powered, Bluetooth-enabled potentiostats capable of covering the potential ranges required for most aqueous electrochemical analyses.

Future research should prioritise the development of portable, high-throughput devices such as multichannel paper-based chips and universal probes capable of simultaneously detecting multiple heavy metal ions. There is also a growing need for nanosensors that can both remove and analyse heavy metal ions. As technology advances, the number of nanosensors designed for heavy metal detection is expected to increase substantially, with important applications in environmental monitoring, food safety, and disease diagnosis.

Appendix

1. Sensor Characterisation - MoS_2 modified SPCE based sensor for the detection of AA:

1.1 Electrochemical Impedance Spectroscopy (EIS)

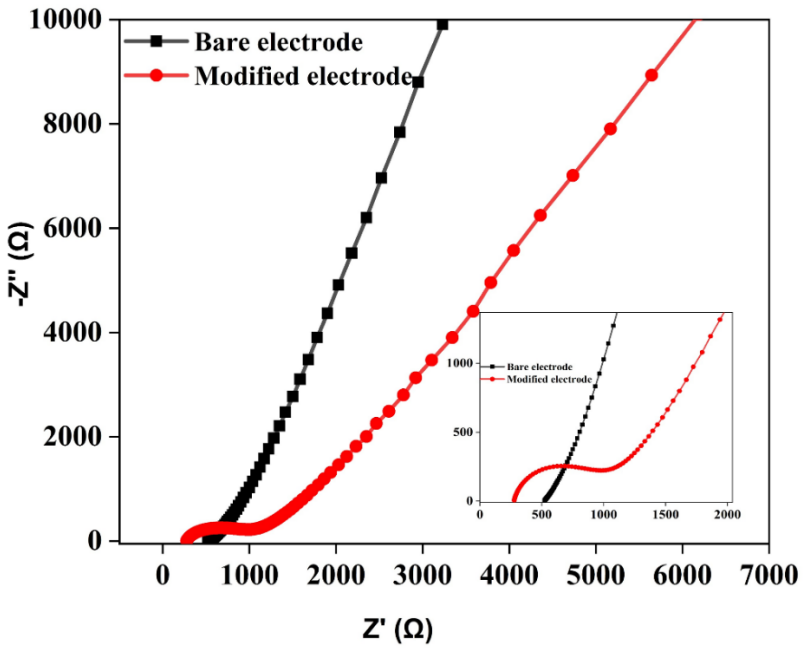

Figure 1. Nyquist plot of bare and MoS2 modified SPCE.

The EIS measurements were carried out to understand the charge transfer characteristics and the electron transfer process. The impedance response of the bare and modified electrode is illustrated in Figure 1 as a Nyquist plot. The real and the imaginary values of impedance are plotted across X and Y axes, respectively. The complex phase plot is divided into three distinguishable sections, (1) a high-frequency zone where the semicircles are formed; (2) the medium frequency zone where details about charge transport and ion diffusion are explained; finally, (3) the low-frequency zone where a linear line parallel to the Y-axis provides insights about the internal capacitance developed. The Nyquist plot for the bare electrode displays a straight line but it is not vertical across the three defined zones. Since the bare electrode is a carbon/graphene composition, the results are on expected lines. The absence of semicircle at the high frequency zone is due to the low charge transfer resistance and high conductivity observed. In the case of MoS_2 modified working electrode, the presence of MoS_2 lowers the series resistance (Rs) compared to the bare electrode, which leads to improved electrode-electrolyte interaction. The intercept at the real impedance axes provides an approximate measure of Rs, which was estimated to be 0.519 kΩ and 0.275 kΩ for the bare electrode and modified electrode, respectively. The presence of the characteristic semicircle in the case of the modified electrode is explained by the double layer formation. Finally, in the low frequency region a Warburg impedance is introduced, which is the characteristic of the diffusion process. The Bode plots for both electrodes are given in Figure 2 (a). The

phase angle for bare and modified electrodes at low frequency region is observed to be -76 º and -59 º, respectively. The bare electrode displayed a closer value to an ideal capacitor (-90 º).

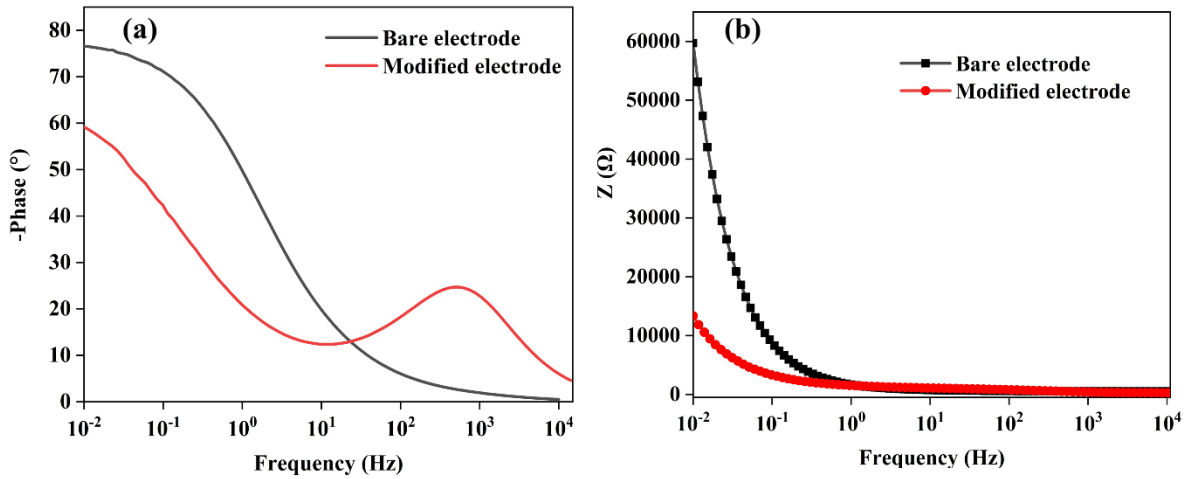

Figure 2. (a) Bode plot and (b) variation of impedance values across various frequencies.

1.2. Electrochemical detection and performance of the fabricated sensor

1.2.1. Electrochemical detection of ascorbic acid using CV, DPV

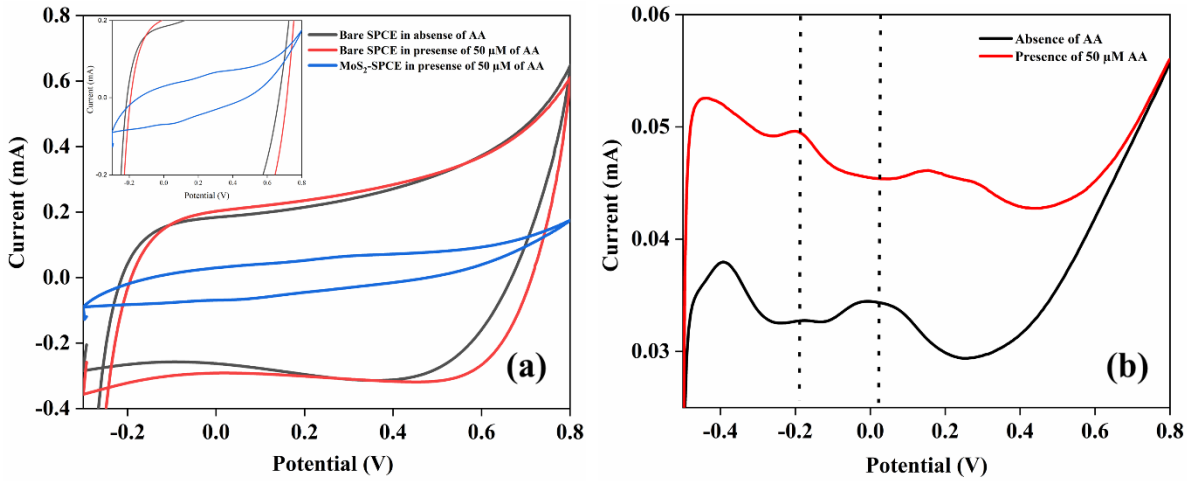

Figure 3. (a) CV profile of bare SPCE in the presence and absence of 50 mM AA and the modified SPCE in the presence of 50 mM AA, (b) DPV profile of modified SPCE in the presence and absence of 50 mM AA.

The electrochemical studies for the bare and MoS_2 modified SPCE, which involves cyclic voltammetry (CV), and differential pulsed voltammetry (DPV), were carried out in PBS solution of 0.1 M at pH 7. The cyclic voltammograms at the scan rate of 100 mV/s for the potential window of -0.3 to 0.8 V are displayed in Figure 3 (a). The figure shows the response of bare SPCE in the absence (black) and presence of 50 mM AA (red) in PBS and the MoS_2 modified SPCE for the 50 mM AA (blue) in PBS. The bare electrode is composed of carbon and graphene mixture and hence the CV profile displays a rectangular form. The modification of the electrode with MoS_2 is observed by the change in the shape of the curve and smaller area enclosed. Moreover, the

presence of an electrochemical oxidation peak is observed around 0.3V in the CV profile of the modified SPCE. It is attributed to the oxidation of AA by MoS_2 nanomaterial, and it appears to be a reversible process as there occurs a reduction peak around -0.1 to 0V. The inset of the graph provides a clearer view of the peaks. Figure 3 (b) displays the DPV curves of modified SPCE in the presence and absence and 50 mM of AA in the electrolyte solution and the oxidation and reduction peaks appear at around 0.2V and -0.2V. The addition of AA results in a shift of the oxidation peak towards the right, i.e., from 0.0 to 0.08 V. This shift in the peaks could be clearly observed and hence the detection process is evident.

1.2.2. Concentration studies

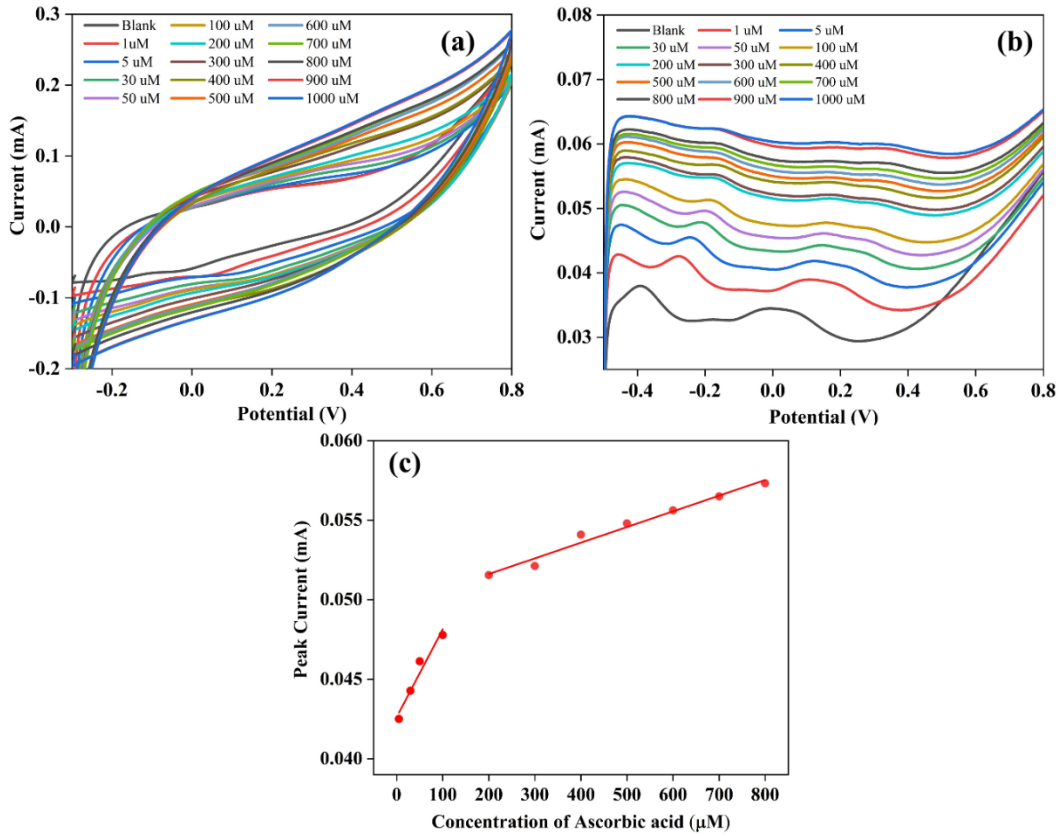

Figure 4. (a) CV measurements; (b) DPV measurements in the absence and presence of various concentrations of AA, within the range of 1-1000 mM and (c) Peak current (Ip) vs AA concentration.

The oxidation of molybdate ions in various oxidation states with the increase in the AA concentration is evident in the positive shift of the cathodic current. Figure 3 (a) provides the cyclic voltammogram at different concentrations (1-1000 mM) of AA scanned at a rate of 50 mV/s. The DPV profiles of the same is illustrated in Figure 3 (b), which also shows the shift in the peaks with the increase in the concentration. The change in the peak current and the shifts become more convoluted at higher concentrations (1-100 mM), while they are significantly observed at lower values (200-1000 mM). However, the shift in the peak displayed a linear function within the logarithmic of the AA concentration of 1 to 100 mM, and 200-1000 mM as displayed in Figure 3(c).

The linear calibration values for both ranges are provided in the linear regression equation as given below. For 1-100 mM,

$$Ip\ (mA) = 6E - 05 * Conc.AA\ (\mu M) + 0.0426\ ;\ R^2 = 0.9467 \quad (7)$$

The sensitivity (slope) of the second linear range increased with the increase in AA concentration, due to the enhanced electrocatalytic ability. The limit of detection (LOD) is estimated to be 30 mM using the 3σ/m criterion where σ is the standard deviation of the intercept and m is the slope of the calibration plot. Further details of the values calculated is provided in Table 1 of the supporting information.

For 200-1000 mM

$$\text{Ip (mA)} = 1\text{E} - 05 * \text{Conc. AA (µM)} + 0.0496 \quad (R^2 = 0.9788) \quad (8)$$

Further details of the values calculated are provided in Table 2 of the supporting information.

Table 1. Analytical parameters for AA detection using MoS_2 modified SPCE.

Parameter	
Linear dynamic range (µM)	1-100
Linear regression	y = 6E-05x + 0.0426
Correlation Coefficient	0.9462
SD of intercept	0.000925224
LOD (µM)	30

Table 2. Analytical parameters for AA detection using MoS_2 modified SPCE

Parameter	
Linear dynamic range (µM)	200-1000
Linear regression	y = 1E-05x + 0.0496
Correlation Coefficient	0.9788
Adj. R-square value	0.99945

1.2.3. Effect of scan rate

The influence of scan rate in the electrochemical detection of 50 mM AA at the surface of MoS_2 modified carbon layer was investigated using cyclic voltammetry method, in the range of 10 to 700 mV/s as shown in Figure 4 (a). In Figure 4 (b), the peak current (Ip) is not directly proportional to the scan rate (v), and this supports the idea that the mechanism is not predominantly a surface-controlled process. It is observed that, there is a linear relationship between the peak current values and the square root of scan rate. The values of the anodic peak current increased with the increase in the scan rate. Based on Cottrell's equation, this confirms that the diffusion-controlled process plays the major role. There is a slight shift in the anodic peak current towards the right with the increase in scan rate, which may be due to the irreversibility of the oxidation process. Using the slope value from the plot between peak current and square root of scan rate (Figure 4 (c)), the diffusion coefficient was calculated to be $1.2262*10^{-3}$ cm^2/s from the Randles–Sevcik equation for the scan speed 100 mV/s at 7.5 pH for 100uM of AA.[21]

$$\mathrm{Ip} = 2.69 * 10^5 \mathrm{n}^{\frac{3}{2}} \mathrm{AD}^{\frac{1}{2}} \mathrm{Co}\, \mathrm{v}^{\frac{1}{2}} \quad (9)$$

Where *Ip* is the anodic peak current, *A* is the Surface area of the modified region, C_o is the concentration of electroactive species, $D^{1/2}$ is Diffusion coefficient, $v^{1/2}$ is the square root of scan rate and *n* is the number of electrons transferred.

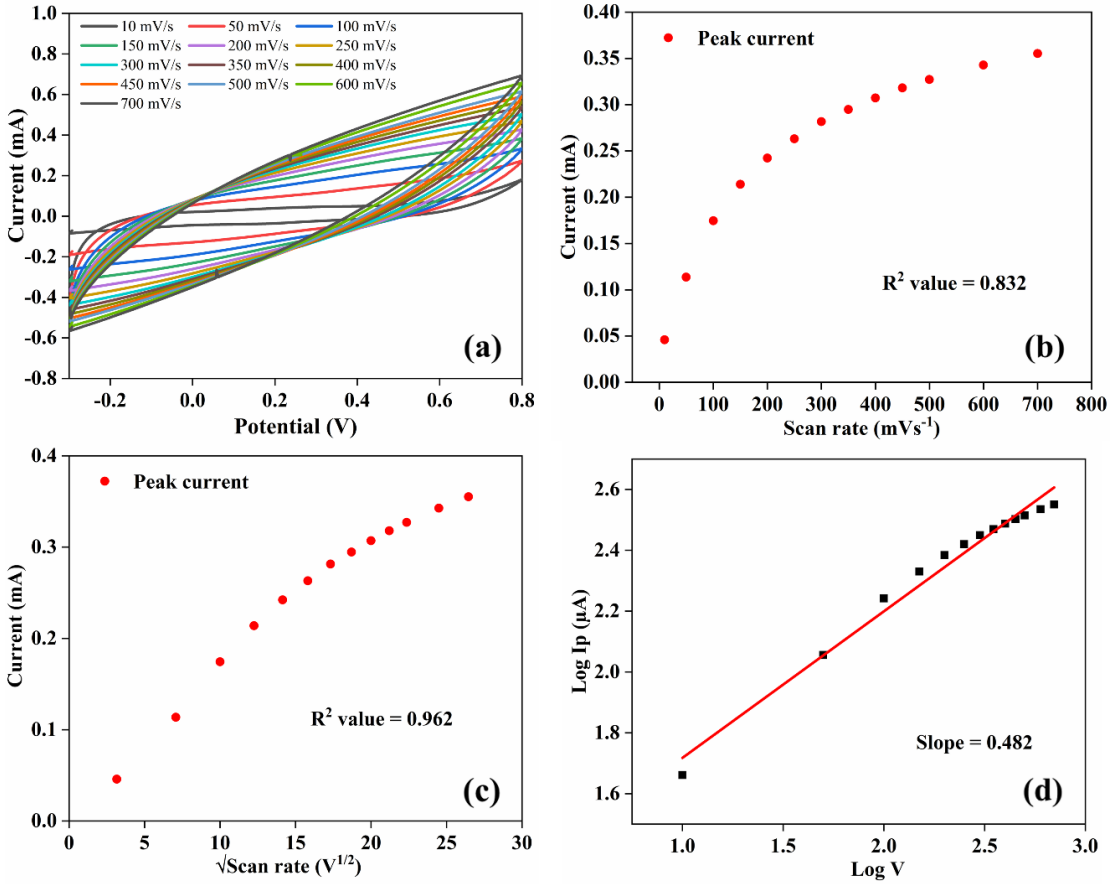

Figure 4. (a) CV scans at different scan rate; (b) Peak current (Ip) vs Scan rate; (c) Peak current (Ip) vs √Scan rate; (d) Log of Ip vs Log of scan rate

From Figure 4 (d), the slope value for the plotted graph between the logarithm of oxidation peak current and the logarithm of scan rate is 0.48 (Equation 4). This value is much closer to 0.5, which is the theoretical value for an ideal diffusion-controlled process. This helps us understand that the detection of AA is a result of diffusion from the bulk solution towards the modified electrode surface.

$$\text{Log Ip} = 0.48\ \text{LogV} + 1.23 \qquad (10)$$

1.2.4. Repeatability study

To examine the repeatability of the screen-printed sensor, the MoS_2-modified SPCE was subjected to a cyclic voltammetry experiment for a continuous 30 cycles (Figure 5 (a)) at a scan rate of 50 mV/s. A 50 mM AA solution was used as the preferred concentration. After the completion of 30 CV scans, the obtained cyclic voltammetry pattern for each cycle were found to be similar with a small standard deviation of 4.263 % in the anodic peak current values (Figure 5 (b)). The change in the peak current of the first cycle to the rest of the successive cycles was noticeable and is likely due to the need for initial preconditioning of the screen-printed electrodes. From the bar diagram displayed in Figure 5 (c), the first cycle shows the smallest peak current value compared to the rest of the CV scans. This shows the appreciable repeatability observed in the sensor performance.

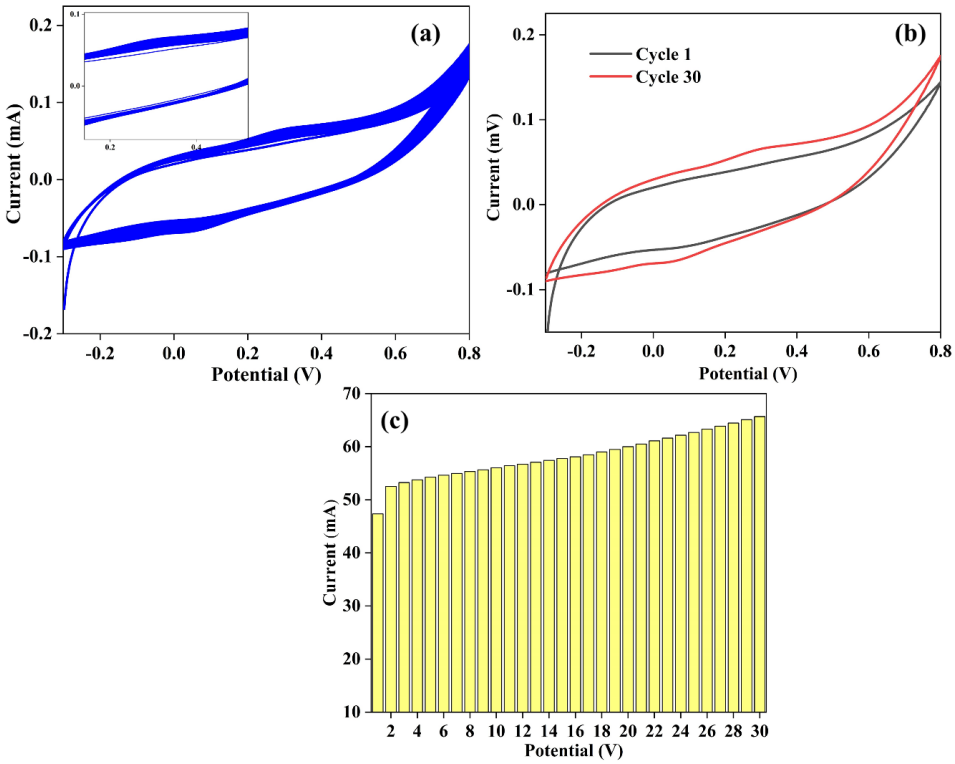

Figure 5. (a) CV of 30 successive cyclic run taken at 50 mV/s scan rate; (b) CV of the first and the thirtieth CV scans; (c) Peak current (Ip) values plotted against 30 successive cycles

2. **Design of the working electrode adapted from**:

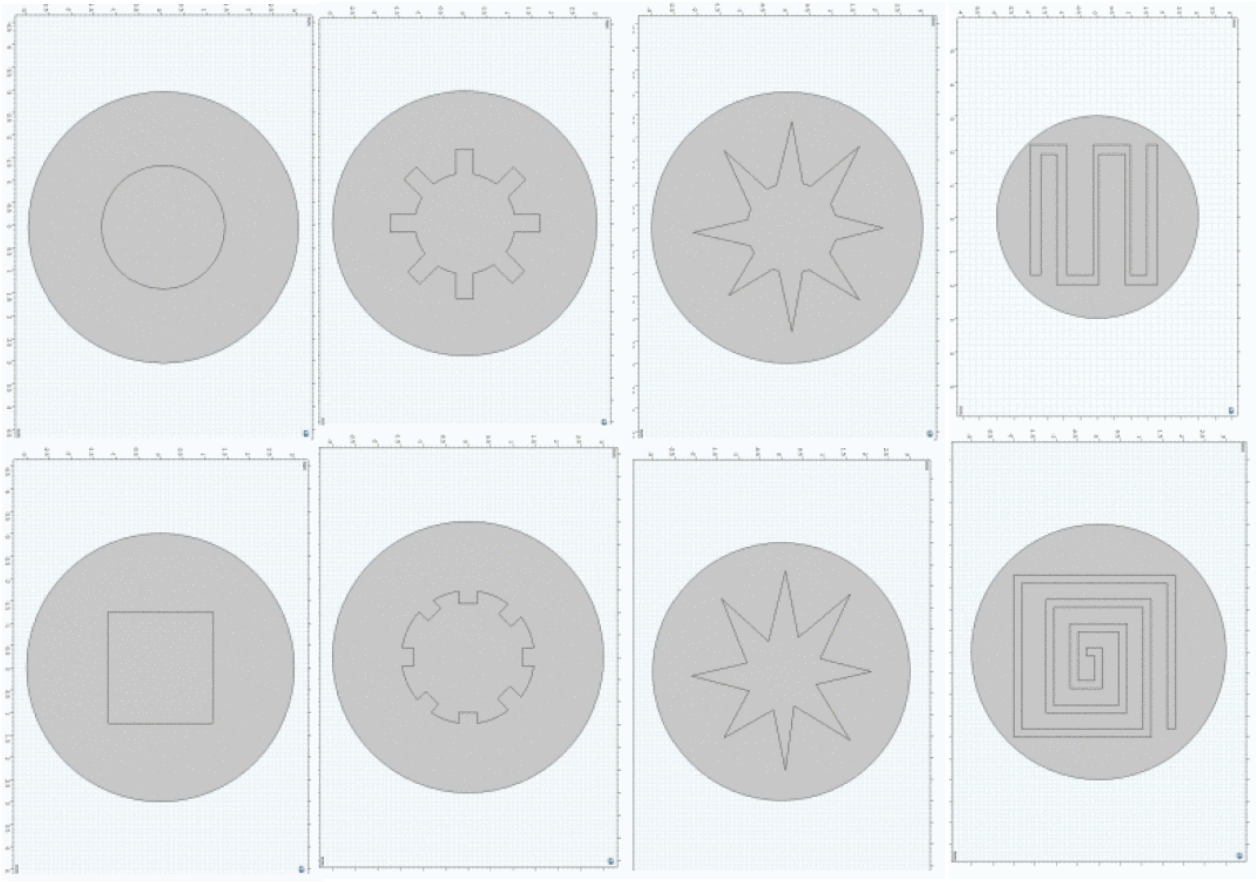

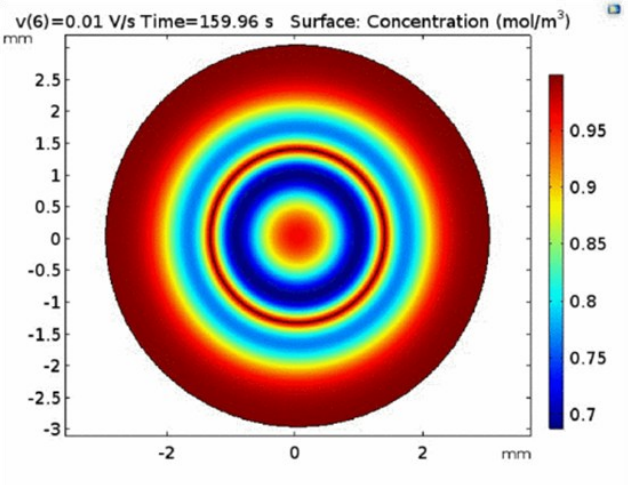
v(6)=0.01 V/s Time=159.96 s Surface: Concentration (mol/m3)
mm
mm

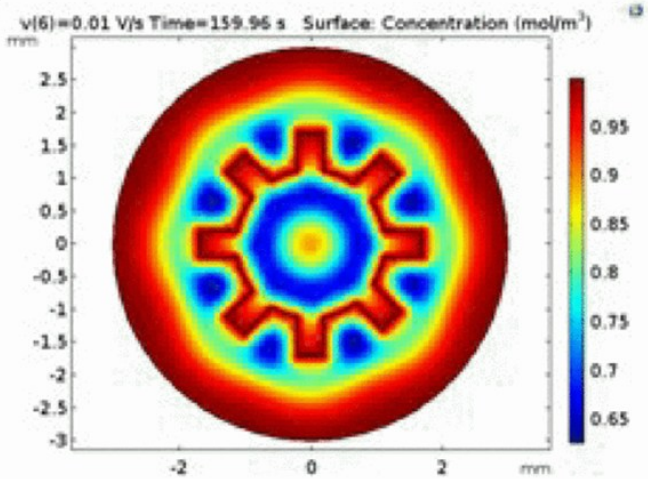
v(6)=0.01 V/s Time=159.96 s Surface: Concentration (mol/m3)
mm
mm

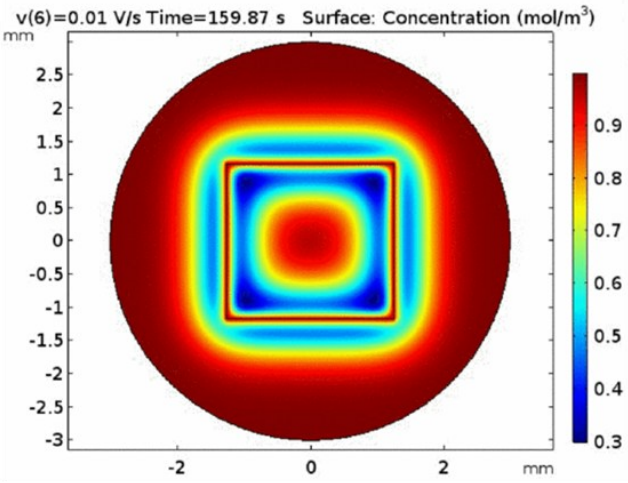
v(6)=0.01 V/s Time=159.87 s Surface: Concentration (mol/m3)
mm
mm

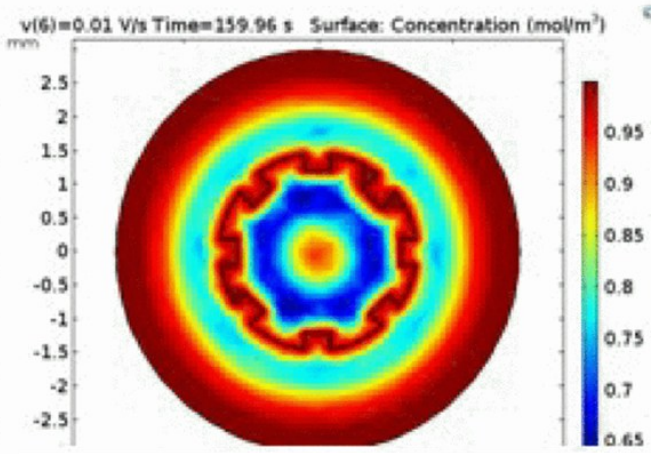
v(6)=0.01 V/s Time=159.96 s Surface: Concentration (mol/m3)
mm

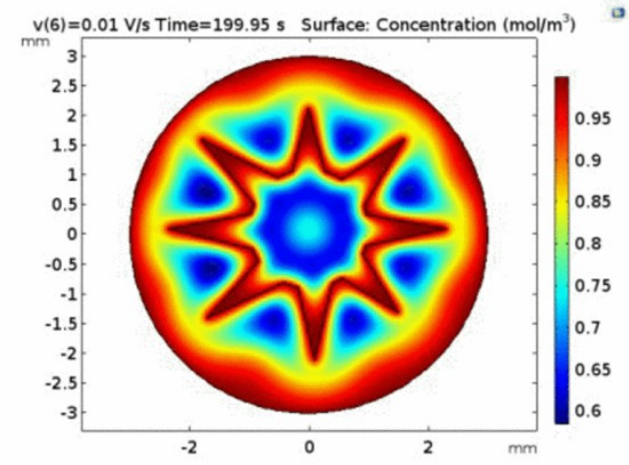
v(6)=0.01 V/s Time=199.95 s Surface: Concentration (mol/m3)
mm
mm

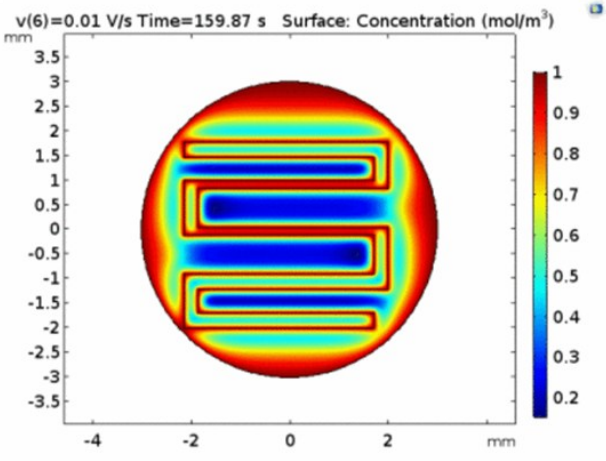
v(6)=0.01 V/s Time=159.87 s Surface: Concentration (mol/m3)
mm
mm

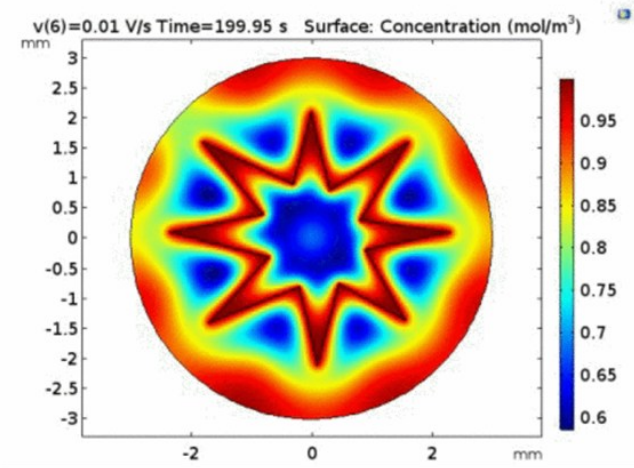
v(6)=0.01 V/s Time=199.95 s Surface: Concentration (mol/m3)
mm
mm

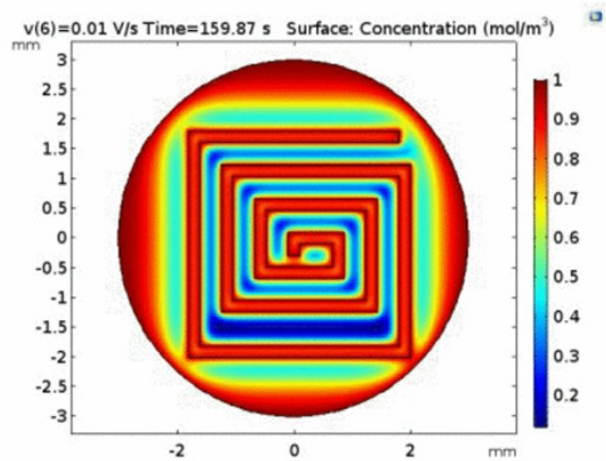
v(6)=0.01 V/s Time=159.87 s Surface: Concentration (mol/m3)
mm
mm

References:

1. Bansod, B., et al., *A review on various electrochemical techniques for heavy metal ions detection with different sensing platforms.* Biosens Bioelectron, 2017. **94**: p. 443-455.
2. Mohajan, H., *Third industrial revolution brings global development.* 2021.
3. Sinha, K., J. Ghosh, and P.C. Sil, *New pesticides: a cutting-edge view of contributions from nanotechnology for the development of sustainable agricultural pest control*, in *New pesticides and soil sensors*. 2017, Elsevier. p. 47-79.
4. Braun, E. and S. MacDonald, *Revolution in miniature: The history and impact of semiconductor electronics*. 1982: Cambridge University Press.
5. Singh, A., et al., *An approach towards different techniques for detection of heavy metal ions and their removal from waste water.* Journal of Environmental Chemical Engineering, 2024: p. 113032.
6. Malik, L.A., et al., *Detection and removal of heavy metal ions: a review.* Environmental Chemistry Letters, 2019. **17**: p. 1495-1521.
7. Moore, J.W. and S. Ramamoorthy, *Heavy metals in natural waters: applied monitoring and impact assessment*. 2012: Springer Science & Business Media.
8. Moore, J.W., et al., *Impact of heavy metals in natural waters.* Heavy Metals in Natural Waters: Applied Monitoring and Impact Assessment, 1984: p. 205-233.
9. Hoekstra, R., P. Blondeau, and F.J. Andrade, *Distributed electrochemical sensors: recent advances and barriers to market adoption.* Analytical and Bioanalytical Chemistry, 2018. **410**(17): p. 4077-4089.
10. Hanrahan, G., D.G. Patil, and J. Wang, *Electrochemical sensors for environmental monitoring: design, development and applications.* Journal of environmental monitoring, 2004. **6**(8): p. 657-664.
11. Noviana, E., et al., *Electrochemical paper-based devices: Sensing approaches and progress toward practical applications.* Lab on a Chip, 2020. **20**(1): p. 9-34.
12. Singh, S., J. Wang, and S. Cinti, *An overview on recent progress in screen-printed electroanalytical (bio) sensors.* ECS Sensors Plus, 2022. **1**(2): p. 023401.
13. Kurup, P., et al., *A review of technologies for characterization of heavy metal contaminants.* Indian Geotechnical Journal, 2017. **47**: p. 421-436.
14. Wing Fen, Y. and W. Mahmood Mat Yunus, *Surface plasmon resonance spectroscopy as an alternative for sensing heavy metal ions: A review.* Sensor Review, 2013. **33**(4): p. 305-314.
15. Prestel, H., A. Gahr, and R. Niessner, *Detection of heavy metals in water by fluorescence spectroscopy: On the way to a suitable sensor system.* Fresenius' journal of analytical chemistry, 2000. **368**: p. 182-191.
16. Rasheed, T., et al., *Fluorescent sensor based models for the detection of environmentally-related toxic heavy metals.* Science of the Total Environment, 2018. **615**: p. 476-485.
17. Oehme, I. and O.S. Wolfbeis, *Optical sensors for determination of heavy metal ions.* Microchimica Acta, 1997. **126**: p. 177-192.
18. Fen, Y.W. and W.M.M. Yunus, *Characterization of the optical properties of heavy metal ions using surface plasmon resonance technique.* Opt. Photonics J, 2011. **1**(03): p. 116-123.
19. Jain, R., et al., *Advances in imaging-assisted sensing techniques for heavy metals in water: Trends, challenges, and opportunities.* TrAC Trends in Analytical Chemistry, 2020. **123**: p. 115758.
20. Sadak, O., *Chemical sensing of heavy metals in water*, in *Advanced Sensor Technology*. 2023, Elsevier. p. 565-591.
21. Wang, J., et al., *Remote electrochemical sensor for trace metal contaminants.* Analytical Chemistry, 1995. **67**(8): p. 1481-1485.

22. Neethipathi, D.K., et al. *MoS 2 modified screen printed carbon electrode based flexible sensor for detection of Copper*. in *2022 IEEE International Conference on Flexible and Printable Sensors and Systems (FLEPS)*. 2022. IEEE.
23. Saha, A., et al., *A new paradigm of reliable sensing with field-deployed electrochemical sensors integrating data redundancy and source credibility.* Scientific Reports, 2023. **13**(1): p. 3101.
24. Alam, M.A., A. Saha, and M. Fratus, *Reliable sensing with unreliable sensors: Rethinking the theoretical foundation of field-deployed wearable/implantable/environmental sensors.* Innovation and Emerging Technologies, 2022. **9**: p. 2240003.
25. Saha, A., et al., *Temperature self-calibration of always-on, field-deployed ion-selective electrodes based on differential voltage measurement.* ACS sensors, 2022. **7**(9): p. 2661-2670.
26. Choudhari, U., et al., *Screen-printed electrochemical sensors for environmental monitoring of heavy metal ion detection.* Reviews in Chemical Engineering, 2023. **39**(7): p. 1227-1268.
27. Ganguly, P., et al. *Influence of Thickness of Screen Printed Carbon Electrodes on Electrochemical Sensing*. in *2022 IEEE International Conference on Flexible and Printable Sensors and Systems (FLEPS)*. 2022.
28. Ambaye, A.D., et al., *Recent developments in nanotechnology-based printing electrode systems for electrochemical sensors.* Talanta, 2021. **225**: p. 121951.
29. Cagnani, G.R., et al., *Fully-printed electrochemical sensors made with flexible screen-printed electrodes modified by roll-to-roll slot-die coating.* Biosensors and Bioelectronics, 2020. **165**: p. 112428.
30. Stefano, J.S., et al., *Electrochemical (bio) sensors enabled by fused deposition modeling-based 3D printing: A guide to selecting designs, printing parameters, and post-treatment protocols*. 2022, ACS Publications.
31. Pradela‐Filho, L.A., et al., *Controlling the inkjet printing process for electrochemical (bio) sensors.* Advanced Materials Technologies, 2023. **8**(8): p. 2201729.
32. Gholamalizadeh, N., et al., *Stencil printing of a highly conductive graphene ink toward flexible electrochemical biosensors for glucose monitoring.* Progress in Organic Coatings, 2022. **172**: p. 107083.
33. Bounegru, A.V. and C. Apetrei, *Carbonaceous nanomaterials employed in the development of electrochemical sensors based on screen-printing technique—A review.* Catalysts, 2020. **10**(6): p. 680.
34. Beitollahi, H., et al., *Applications of electrochemical sensors and biosensors based on modified screen-printed electrodes: a review.* Analytical Methods, 2020. **12**(12): p. 1547-1560.
35. Popoola, O.A., et al., *Development of a baseline-temperature correction methodology for electrochemical sensors and its implications for long-term stability.* Atmospheric environment, 2016. **147**: p. 330-343.
36. Torres-Rivero, K., A. Florido, and J. Bastos-Arrieta, *Recent trends in the improvement of the electrochemical response of screen-printed electrodes by their modification with shaped metal nanoparticles.* Sensors, 2021. **21**(8): p. 2596.
37. Ferrari, A.G.-M., S.J. Rowley-Neale, and C.E. Banks, *Screen-printed electrodes: Transitioning the laboratory in-to-the field.* Talanta Open, 2021. **3**: p. 100032.
38. Silva, R.M., et al., *Carbon nanomaterials-based screen-printed electrodes for sensing applications.* Biosensors, 2023. **13**(4): p. 453.
39. Kant, T., et al., *Design and development of conductive nanomaterials for electrochemical sensors: a modern approach.* Materials Today Chemistry, 2022. **24**: p. 100769.
40. Jyothi, N.R., *Heavy metal sources and their effects on human health.* Heavy metals-their environmental impacts and mitigation, 2020: p. 1-12.
41. Ahmed, J., A. Thakur, and A. Goyal, *Industrial wastewater and its toxic effects.* 2021.
42. Munir, N., et al., *Heavy metal contamination of natural foods is a serious health issue: A review.* Sustainability, 2021. **14**(1): p. 161.

43. Singh, A., et al., *Heavy metal contamination of water and their toxic effect on living organisms*, in *The toxicity of environmental pollutants*. 2022, IntechOpen.
44. Shahjahan, M., et al., *Effects of heavy metals on fish physiology - A review.* Chemosphere, 2022. **300**: p. 134519.
45. Kumar, A., et al., *Lead toxicity: health hazards, influence on food chain, and sustainable remediation approaches.* International journal of environmental research and public health, 2020. **17**(7): p. 2179.
46. Wu, D., et al., *Detection techniques for lead ions in water: a review.* Molecules, 2023. **28**(8): p. 3601.
47. Sani, A.H. and M. Amanabo, *Lead: A concise review of its toxicity, mechanism and health effect.* GSC Biological and Pharmaceutical Sciences, 2021. **15**(1): p. 055-062.
48. Punia, P., et al., *Recent advances in detection and removal of heavy metals from contaminated water.* ChemBioEng reviews, 2022. **9**(4): p. 351-369.
49. Schoofs, H., J. Schmit, and L. Rink, *Zinc toxicity: understanding the limits.* Molecules, 2024. **29**(13): p. 3130.
50. Obasi, P.N. and B.B. Akudinobi, *Potential health risk and levels of heavy metals in water resources of lead–zinc mining communities of Abakaliki, southeast Nigeria.* Applied Water Science, 2020. **10**(7): p. 1-23.
51. Papanikolaou, G. and K. Pantopoulos, *Iron metabolism and toxicity.* Toxicology and applied pharmacology, 2005. **202**(2): p. 199-211.
52. Yuen, H.-W. and W. Becker, *Iron toxicity*, in *StatPearls [Internet]*. 2023, StatPearls Publishing.
53. Flemming, C.A. and J.T. Trevors, *Copper toxicity and chemistry in the environment: a review.* Water, Air, and Soil Pollution, 1989. **44**(1): p. 143-158.
54. Stern, B.R., *Essentiality and toxicity in copper health risk assessment: overview, update and regulatory considerations.* Journal of Toxicology and Environmental Health, Part A, 2010. **73**(2-3): p. 114-127.
55. Royer, A. and T. Sharman, *Copper toxicity.* 2020.
56. Genchi, G., et al., *The effects of cadmium toxicity.* International journal of environmental research and public health, 2020. **17**(11): p. 3782.
57. Sharma, H., N. Rawal, and B.B. Mathew, *The characteristics, toxicity and effects of cadmium.* International journal of nanotechnology and nanoscience, 2015. **3**(10): p. 1-9.
58. Rahimzadeh, M.R., et al., *Cadmium toxicity and treatment: An update.* Caspian journal of internal medicine, 2017. **8**(3): p. 135.
59. Leyssens, L., et al., *Cobalt toxicity in humans—A review of the potential sources and systemic health effects.* Toxicology, 2017. **387**: p. 43-56.
60. Blust, R., *Cobalt*, in *Fish physiology*. 2011, Elsevier. p. 291-326.
61. Best, S.L. and P.J. Sadler, *Gold drugs: mechanism of action and toxicity.* Gold bulletin, 1996. **29**: p. 87-93.
62. Lansdown, A.B., *GOLD: human exposure and update on toxic risks.* Critical reviews in toxicology, 2018. **48**(7): p. 596-614.
63. Organization, W.H., *Silver in drinking water: Background document for development of WHO Guidelines for Drinking-water Quality*. 2021, World Health Organization.
64. Wood, C.M., *Silver*, in *Fish physiology*. 2011, Elsevier. p. 1-65.
65. Adjovu, G.E., et al., *Measurement of total dissolved solids and total suspended solids in water systems: A review of the issues, conventional, and remote sensing techniques.* Remote Sensing, 2023. **15**(14): p. 3534.
66. Mukherjee, S., et al., *Sensory development for heavy metal detection: A review on translation from conventional analysis to field-portable sensor.* Trends in Food Science & Technology, 2021. **109**: p. 674-689.
67. Ning, Y., et al., *Recent progress in optical current sensing techniques.* Review of Scientific Instruments, 1995. **66**(5): p. 3097-3111.

68. O'rourke, S. and N. Holden, *Optical sensing and chemometric analysis of soil organic carbon–a cost effective alternative to conventional laboratory methods?* Soil Use and Management, 2011. **27**(2): p. 143-155.
69. Gumpu, M.B., et al., *A review on detection of heavy metal ions in water–an electrochemical approach.* Sensors and actuators B: chemical, 2015. **213**: p. 515-533.
70. Jin, M., et al., *Review of the distribution and detection methods of heavy metals in the environment.* Analytical methods, 2020. **12**(48): p. 5747-5766.
71. Liu, X., et al., *Recent advances in nanomaterial-enabled screen-printed electrochemical sensors for heavy metal detection.* TrAC Trends in Analytical Chemistry, 2019. **115**: p. 187-202.
72. Simões, F.R. and M.G. Xavier, *Electrochemical sensors.* Nanoscience and its Applications, 2017. **1**: p. 155-178.
73. Scozzari, A., *Electrochemical sensing methods: a brief review.* Algal Toxins: Nature, Occurrence, Effect and Detection, 2008: p. 335-351.
74. Kell, D.B., et al. *Non-Faradaic electrochemical sensors: principles and practice*. in *Analytical proceedings*. 1991. Royal Society of Chemistry.
75. Kumar, N., A. Arora, and A. Krishnan, *Complementary AC Voltammetry—A Method for Simultaneous Measurement of Faradaic and Nonfaradaic Currents in an Electrochemically Reversible System.* IEEE Sensors Journal, 2020. **20**(22): p. 13196-13203.
76. Baranwal, J., et al., *Electrochemical sensors and their applications: A review.* Chemosensors, 2022. **10**(9): p. 363.
77. Bakker, E. and M. Telting-Diaz, *Electrochemical sensors.* Analytical chemistry, 2002. **74**(12): p. 2781-2800.
78. Lisak, G., *Reliable environmental trace heavy metal analysis with potentiometric ion sensors-reality or a distant dream.* Environmental Pollution, 2021. **289**: p. 117882.
79. Jagner, D., *Instrumental approach to potentiometric stripping analysis of some heavy metals.* Analytical Chemistry, 1978. **50**(13): p. 1924-1929.
80. Baracu, A.M. and L.A.D. Gugoasa, *Recent advances in microfabrication, design and applications of amperometric sensors and biosensors.* Journal of The Electrochemical Society, 2021. **168**(3): p. 037503.
81. Seddon, B., Y. Shao, and H. Girault, *Printed microelectrode array and amperometric sensor for environmental monitoring.* Electrochimica acta, 1994. **39**(16): p. 2377-2386.
82. Kokkinos, C. and A. Economou, *Recent advances in voltammetric, amperometric and ion-selective (bio) sensors fabricated by microengineering manufacturing approaches.* Current Opinion in Electrochemistry, 2020. **23**: p. 21-25.
83. Copeland, T. and R. Skogerboe, *Anodic stripping voltammetry.* Analytical Chemistry, 1974. **46**(14): p. 1257A-1268a.
84. Ruić, I., *Theory of pulse polarography and related chronoamperometric and chronocoulometric techniques: I. Influence of mass transport regime and heterogeneous kinetics on current-potential curves.* Journal of Electroanalytical Chemistry and Interfacial Electrochemistry, 1977. **75**(1): p. 25-44.
85. Chang, B.-Y. and S.-M. Park, *Electrochemical impedance spectroscopy.* Annual Review of Analytical Chemistry, 2010. **3**(1): p. 207-229.
86. Wang, S., et al., *Electrochemical impedance spectroscopy.* Nature Reviews Methods Primers, 2021. **1**(1): p. 41.
87. Lee, S., et al., *A sensitive electrochemical sensor using an iron oxide/graphene composite for the simultaneous detection of heavy metal ions.* Talanta, 2016. **160**: p. 528-536.
88. Fall, B., et al., *Synthesis of highly sensitive rGO@CNT@Fe2O3/polypyrrole nanocomposite for the electrochemical detection of Pb2+.* Materials Today Communications, 2021. **26**: p. 102005.

89. Fan, H.-L., et al., *Continuous preparation of Fe3O4 nanoparticles through Impinging Stream-Rotating Packed Bed reactor and their electrochemistry detection toward heavy metal ions.* Journal of Alloys and Compounds, 2016. **671**: p. 354-359.
90. Yang, H., et al., *Sensitive and selective detection of Ag+ in aqueous solutions using Fe3O4@Au nanoparticles as smart electrochemical nanosensors.* Talanta, 2013. **116**: p. 548-53.
91. Sun, Y.-F., et al., *Selective detection toward Cd2+ using Fe3O4/RGO nanoparticle modified glassy carbon electrode.* Journal of Electroanalytical Chemistry, 2014. **714-715**: p. 97-102.
92. Sun, Y., et al., *Controlled synthesis various shapes Fe3O4 decorated reduced graphene oxide applied in the electrochemical detection.* Journal of Alloys and Compounds, 2015. **638**: p. 182-187.
93. Xiong, S., et al., *Electrochemical Detection of Pb(II) by Glassy Carbon Electrode Modified with Amine-Functionalized Magnetite Nanoparticles.* Analytical Letters, 2013. **46**(6): p. 912-922.
94. Song, Q., et al., *Bifunctional polydopamine@Fe3O4 core–shell nanoparticles for electrochemical determination of lead(II) and cadmium(II).* Analytica Chimica Acta, 2013. **787**: p. 64-70.
95. Deshmukh, S., et al., *Terephthalic acid capped iron oxide nanoparticles for sensitive electrochemical detection of heavy metal ions in water.* Journal of Electroanalytical Chemistry, 2017. **788**: p. 91-98.
96. Baghayeri, M., et al., *A simple approach for simultaneous detection of cadmium(II) and lead(II) based on glutathione coated magnetic nanoparticles as a highly selective electrochemical probe.* Sensors and Actuators B: Chemical, 2018. **273**: p. 1442-1450.
97. Zhou, S.-F., X.-J. Han, and Y.-Q. Liu, *SWASV performance toward heavy metal ions based on a high-activity and simple magnetic chitosan sensing nanomaterials.* Journal of Alloys and Compounds, 2016. **684**: p. 1-7.
98. Filik, H. and A.A. Avan, *Dextran modified magnetic nanoparticles based solid phase extraction coupled with linear sweep voltammetry for the speciation of Cr(VI) and Cr(III) in tea, coffee, and mineral water samples.* Food Chemistry, 2019. **292**: p. 151-159.
99. Han, X.-J., et al., *Mesoporous MnFe2O4 nanocrystal clusters for electrochemistry detection of lead by stripping voltammetry.* Journal of Electroanalytical Chemistry, 2015. **755**: p. 203-209.
100. Zhou, S.-F., et al., *Enhanced electrochemical performance for sensing Pb(II) based on graphene oxide incorporated mesoporous MnFe2O4 nanocomposites.* Journal of Alloys and Compounds, 2018. **747**: p. 447-454.
101. Jin, C., et al., *Functionalized hollow MnFe 2 O 4 nanospheres: design, applications and mechanism for efficient adsorption of heavy metal ions.* New Journal of Chemistry, 2019. **43**(15): p. 5879-5889.
102. He, Y., et al., *Synthesis of bismuth nanoparticle-loaded cobalt ferrite for electrochemical detection of heavy metal ions.* RSC Advances, 2020. **10**(46): p. 27697-27705.
103. Yamuna, A., et al., *Highly selective simultaneous electrochemical detection of trace level of heavy metals in water samples based on the single-crystalline Co3O4 nanocubes modified electrode.* Journal of Electroanalytical Chemistry, 2021. **887**: p. 115159.
104. Yu, X.-Y., et al., *Facet-dependent electrochemical properties of Co3O4 nanocrystals toward heavy metal ions.* Scientific Reports, 2013. **3**(1): p. 2886.
105. Ndlovu, T., et al., *Electroanalysis of copper as a heavy metal pollutant in water using cobalt oxide modified exfoliated graphite electrode.* Physics and Chemistry of the Earth, Parts A/B/C, 2012. **50-52**: p. 127-131.
106. Karthik, R. and S. Thambidurai, *Synthesis of cobalt doped ZnO/reduced graphene oxide nanorods as active material for heavy metal ions sensor and antibacterial activity.* Journal of Alloys and Compounds, 2017. **715**: p. 254-265.

107. Liao, J., et al., *Electrochemical and density functional theory investigation on the differential behaviors of core-ring structured NiCo2O4 nanoplatelets toward heavy metal ions.* Analytica Chimica Acta, 2018. **1022**: p. 37-44.
108. Jin, Z., et al., *Tin Oxide Crystals Exposed by Low-Energy {110} Facets for Enhanced Electrochemical Heavy Metal Ions Sensing: X-ray Absorption Fine Structure Experimental Combined with Density-Functional Theory Evidence.* Analytical Chemistry, 2017. **89**(4): p. 2613-2621.
109. Bhanjana, G., et al., *Sno2 quantum dots as novel platform for electrochemical sensing of cadmium.* Electrochimica Acta, 2015. **169**: p. 97-102.
110. Wei, Y., et al., *SnO2/Reduced Graphene Oxide Nanocomposite for the Simultaneous Electrochemical Detection of Cadmium(II), Lead(II), Copper(II), and Mercury(II): An Interesting Favorable Mutual Interference.* The Journal of Physical Chemistry C, 2012. **116**(1): p. 1034-1041.
111. Cui, X., et al., *Fabrication of thiazole derivatives functionalized graphene decorated with fluorine, chlorine and iodine@SnO2 nanoparticles for highly sensitive detection of heavy metal ions.* Colloids and Surfaces A: Physicochemical and Engineering Aspects, 2018. **546**: p. 153-162.
112. Memon, A.F., et al., *An improved electrochemical sensor based on triton X-100 functionalized SnO2 nanoparticles for ultrasensitive determination of cadmium.* Chemosphere, 2022. **300**: p. 134634.
113. Yang, M., et al., *Sensitivity and selectivity sensing cadmium(II) using amination functionalized porous SnO2 nanowire bundles-room temperature ionic liquid nanocomposite: Combined efficient cation capture with control experimental conditions.* Sensors and Actuators B: Chemical, 2017. **240**: p. 887-894.
114. Xie, Y.-L., et al., *Graphene/CeO2 hybrid materials for the simultaneous electrochemical detection of cadmium(II), lead(II), copper(II), and mercury(II).* Journal of Electroanalytical Chemistry, 2015. **757**: p. 235-242.
115. Li, Y., et al., *An ionic liquid supported CeO(2) nanoparticles-carbon nanotubes composite-enhanced electrochemical DNA-based sensor for the detection of Pb(2).* J Pharm Anal, 2011. **1**(4): p. 258-263.
116. Mourya, A., B. Mazumdar, and S.K. Sinha, *Application of CeO2-MWCNTs nanocomposite for heavy metal ion detection in aqueous solutions by electrochemical technique.* Cleaner Materials, 2021. **2**: p. 100021.
117. Huang, W., et al., *Morphology-controlled electrochemical sensing of environmental Cd2+ and Pb2+ ions on expanded graphite supported CeO2 nanomaterials.* Analytica Chimica Acta, 2020. **1126**: p. 63-71.
118. Singh, S., et al., *Cerium oxide-catalyzed chemical vapor deposition grown carbon nanofibers for electrochemical detection of Pb(II) and Cu(II).* Journal of Environmental Chemical Engineering, 2019. **7**(4): p. 103250.
119. Cui, K.-P., et al., *New strategy for fabricating Cd(II) sensing electrochemical interface based on enhanced adsorption followed by redox processes: Ferro-cerium oxide nanocomposite as an example.* Journal of Alloys and Compounds, 2020. **829**: p. 154551.
120. Zhao, N., H. Lian, and Y. Yu, *In situ electrochemical deposition of a bismuth/cerium dioxide/reduced graphene oxide nanofilm for enhanced Pb2+ sensing performance.* New Journal of Chemistry, 2022. **46**(34): p. 16603-16611.
121. Zhao, N., et al., *Determination of heavy metals in water using an FTO electrode modified with CeO2/rGO nanoribbons prepared by an electrochemical method.* RSC Advances, 2022. **12**(34): p. 21851-21858.
122. Saranya, J., et al., *Microwave Thermally Assisted Porous Structured Cerium Oxide/Zinc Oxide Design: Fabrication, Electrochemical Activity Towards Pb Ions, Anticancer Assessment in HeLa and VERO Cell Lines.* Journal of Inorganic and Organometallic Polymers and Materials, 2021. **31**(3): p. 1279-1292.

123. Yukird, J., et al., *ZnO@ graphene nanocomposite modified electrode for sensitive and simultaneous detection of Cd (II) and Pb (II).* Synthetic Metals, 2018. **245**: p. 251-259.
124. Lu, Y.-Y., et al., *Preparation of Zinc Oxide-Graphene Composite Modified Electrodes for Detection of Trace Pb(II).* Chinese Journal of Analytical Chemistry, 2015. **43**(9): p. 1395-1401.
125. Nagaraju, G., et al., *Electrochemical heavy metal detection, photocatalytic, photoluminescence, biodiesel production and antibacterial activities of Ag–ZnO nanomaterial.* Materials Research Bulletin, 2017. **94**: p. 54-63.
126. Oliveira, V.H.B., et al., *A sensitive electrochemical sensor for Pb2+ ions based on ZnO nanofibers functionalized by L-cysteine.* Journal of Molecular Liquids, 2020. **309**: p. 113041.
127. Bhanjana, G., et al., *Zinc Oxide Quantum Dots as Efficient Electron Mediator for Ultrasensitive and Selective Electrochemical Sensing of Mercury.* Electrochimica Acta, 2015. **178**: p. 361-367.
128. Moutcine, A., et al., *Preparation, characterization and simultaneous electrochemical detection toward Cd (II) and Hg(II) of a phosphate/zinc oxide modified carbon paste electrode.* Inorganic Chemistry Communications, 2020. **116**: p. 107911.
129. Padmalaya, G., et al., *A Facile Synthesis of Cellulose Acetate Functionalized Zinc Oxide Nanocomposite for Electrochemical Sensing of Cadmium ions.* Journal of Inorganic and Organometallic Polymers and Materials, 2019. **29**(3): p. 989-999.
130. Malik, L.A., et al., *Zinc oxide-decorated multiwalled carbon nanotubes: a selective electrochemical sensor for the detection of Pb(II) ion in aqueous media.* Journal of Materials Science: Materials in Electronics, 2022. **33**(9): p. 6178-6189.
131. Liu, W., *Preparation of a zinc oxide-reduced graphene oxide nanocomposite for the determination of cadmium (II), lead (II), copper (II), and mercury (II) in water.* Int. J. Electrochem. Sci, 2017. **12**: p. 5392-5403.
132. Hamid, H.A., et al., *Sensitive detection of Pb ions by square wave anodic stripping voltammetry by using iron oxide nanoparticles decorated zinc oxide nanorods modified electrode.* Materials Chemistry and Physics, 2021. **273**: p. 125148.
133. Bhanjana, G., et al., *Zinc oxide nanopillars as an electrocatalyst for direct redox sensing of cadmium.* Journal of Industrial and Engineering Chemistry, 2017. **53**: p. 192-200.
134. Zhang, X., et al., *Studies on fabrication and application of arsenic electrochemical sensors based on titanium dioxide nanoparticle modified gold strip electrodes.* Analytical Methods, 2016. **8**(5): p. 1162-1169.
135. Kang, M., et al., *Highly selective and sensitive reversible sensor for Cu (II) detection based on hollow TiO2 spheres modified by fluorescein hydrozine-3,6-diacetic acid.* Electrochimica Acta, 2015. **161**: p. 186-194.
136. Nguyen, P.K.Q. and S.K. Lunsford, *Electrochemical response of carbon paste electrode modified with mixture of titanium dioxide/zirconium dioxide in the detection of heavy metals: Lead and cadmium.* Talanta, 2012. **101**: p. 110-121.
137. Ramezani, S., M. Ghobadi, and B.N. Bideh, *Voltammetric monitoring of Cd (II) by nano-TiO2 modified carbon paste electrode sensitized using 1,2-bis-[o-aminophenyl thio] ethane as a new ion receptor.* Sensors and Actuators B: Chemical, 2014. **192**: p. 648-657.
138. Narouei, F.H., K.A. Kirk, and S. Andreescu, *Electrochemical Quantification of Lead Adsorption on TiO2 Nanoparticles.* Electroanalysis, 2021. **33**(1): p. 188-196.
139. Yu, Z., et al., *PEDOT-type conducting polymers/black TiO2 composites for electrochemical determination of Cd2+ and Pb2+.* Journal of The Electrochemical Society, 2020. **167**(6): p. 067514.
140. Wei, Y., et al., *Stripping voltammetry study of ultra-trace toxic metal ions on highly selectively adsorptive porous magnesium oxide nanoflowers.* Analyst, 2012. **137**(9): p. 2183-2191.
141. Krishnan, S., et al., *Aminotetrazole-Functionalized SiO2 Coated MgO Nanoparticle Composites for Removal of Acid Fuchsin Dye and Detection of Heavy Metal Ions.* ACS Applied Nano Materials, 2020. **3**(11): p. 11203-11216.

142. Xu, R.-X., et al., *Non-conductive nanomaterial enhanced electrochemical response in stripping voltammetry: The use of nanostructured magnesium silicate hollow spheres for heavy metal ions detection.* Analytica Chimica Acta, 2013. **790**: p. 31-38.
143. Buica, G.-O., et al., *Zr/ZrO2 nanotube electrode for detection of heavy metal ions.* Electrochemistry Communications, 2020. **110**: p. 106614.
144. Dölle, K., *Original Research Article Paper for Screen Printing Applications–A Paper Development Study.* Journal of Engineering Research and Reports, 2021. **21**(9): p. 45-63.
145. Tsuen-hsuin, T., *History of printing.* Digital printing, 1986. **1981**(3D).
146. Kishore, N., *Different Textile Printing Techniques-Hand Block Printing, Screen Printing, And Digital Printing.* Webology, 2022. **19**(2).
147. Wang, J., et al., *Performance of screen-printed carbon electrodes fabricated from different carbon inks.* Electrochimica Acta, 1998. **43**(23): p. 3459-3465.
148. Wahyuni, W.T., et al., *A brief review on fabrication of screen-printed carbon electrode: materials and techniques.* Indonesian Journal of Chemical Research, 2021. **8**(3): p. 210-218.
149. Morrin, A., A.J. Killard, and M.R. Smyth, *Electrochemical characterization of commercial and home-made screen-printed carbon electrodes.* Analytical letters, 2003. **36**(9): p. 2021-2039.
150. Sharp, D. and R. Burkitt, *Carbon materials for analytical electrochemistry: printed carbon materials and composites.* Materials Technology, 2015. **30**(sup7): p. B155-B162.
151. Anderson, J.L. and N. Winograd, *Film electrodes*, in *Laboratory Techniques in Electroanalytical Chemistry, Revised and Expanded*. 2018, CRC Press. p. 333-365.
152. Ru, C., et al., *A review of non-contact micro-and nano-printing technologies.* Journal of Micromechanics and Microengineering, 2014. **24**(5): p. 053001.
153. Khan, S., L. Lorenzelli, and R.S. Dahiya, *Technologies for printing sensors and electronics over large flexible substrates: A review.* IEEE Sensors Journal, 2014. **15**(6): p. 3164-3185.
154. Voskuhl, J., J. Brinkmann, and P. Jonkheijm, *Advances in contact printing technologies of carbohydrate, peptide and protein arrays.* Current opinion in chemical biology, 2014. **18**: p. 1-7.
155. Hengsteler, J., et al., *Bringing electrochemical three-dimensional printing to the nanoscale.* Nano letters, 2021. **21**(21): p. 9093-9101.
156. Banks, C.E., C.W. Foster, and R.O. Kadara, *Screen-printing electrochemical architectures*. 2015: Springer.
157. Sardini, E., M. Serpelloni, and S. Tonello, *Printed electrochemical biosensors: Opportunities and metrological challenges.* Biosensors, 2020. **10**(11): p. 166.
158. Fanjul-Bolado, P., et al., *Electrochemical characterization of screen-printed and conventional carbon paste electrodes.* Electrochimica Acta, 2008. **53**(10): p. 3635-3642.
159. Maddipatla, D., et al. *Development of a printed impedance based electrochemical sensor on paper substrate*. in *2016 IEEE SENSORS*. 2016. IEEE.
160. Windmiller, J.R. and J. Wang, *Wearable electrochemical sensors and biosensors: a review.* Electroanalysis, 2013. **25**(1): p. 29-46.
161. Sinha, A., A.K. Stavrakis, and G.M. Stojanović, *Textile-based electrochemical sensors and their applications.* Talanta, 2022. **244**: p. 123425.
162. Manjakkal, L., D. Shakthivel, and R. Dahiya, *Flexible Printed Reference Electrodes for Electrochemical Applications.* Advanced Materials Technologies, 2018. **3**(12): p. 1800252.
163. Ives, D.J. and G.J. Janz, *Reference electrodes*. Vol. 92. 1961: Academic Press, New York.
164. Uludag, Y., Z. Olcer, and M.S. Sagiroglu, *Design and characterisation of a thin-film electrode array with shared reference/counter electrodes for electrochemical detection.* Biosensors and Bioelectronics, 2014. **57**: p. 85-90.
165. Krejci, J., et al., *Effective surface area of electrochemical sensors.* Journal of the Electrochemical Society, 2014. **161**(6): p. B147.

166. Dai, X., S. Wu, and S. Li, *Progress on electrochemical sensors for the determination of heavy metal ions from contaminated water.* Journal of the Chinese Advanced Materials Society, 2018. **6**(2): p. 91-111.
167. Song, H., et al., *Carbon nanomaterials-based electrochemical sensors for heavy metal detection.* Critical Reviews in Analytical Chemistry, 2024. **54**(7): p. 1987-2006.
168. Li, B., et al., *Recent advance of nanomaterials modified electrochemical sensors in the detection of heavy metal ions in food and water.* Food Chemistry, 2023: p. 138213.
169. Jeerapan, I. and S. Poorahong, *Flexible and stretchable electrochemical sensing systems: materials, energy sources, and integrations.* Journal of The Electrochemical Society, 2020. **167**(3): p. 037573.
170. de Araujo Andreotti, I.A., et al., *Disposable and flexible electrochemical sensor made by recyclable material and low cost conductive ink.* Journal of Electroanalytical Chemistry, 2019. **840**: p. 109-116.
171. Minot, E.D., et al., *Carbon nanotube biosensors: The critical role of the reference electrode.* Applied Physics Letters, 2007. **91**(9).
172. Kahlert, H., *Reference electrodes.* Electroanalytical methods: guide to experiments and applications, 2010: p. 291-308.
173. Cook, J.B., et al., *Suppression of Electrochemically Driven Phase Transitions in Nanostructured MoS2 Pseudocapacitors Probed Using Operando X-ray Diffraction.* ACS Nano, 2019. **13**(2): p. 1223-1231.
174. Hof, F., et al., *Conductive inks of graphitic nanoparticles from a sustainable carbon feedstock.* Carbon, 2017. **111**: p. 142-149.
175. Wang, C., A.J. Appleby, and F.E. Little, *Charge–discharge stability of graphite anodes for lithium-ion batteries.* Journal of Electroanalytical Chemistry, 2001. **497**(1): p. 33-46.
176. Tatara, R., et al., *The effect of electrode-electrolyte interface on the electrochemical impedance spectra for positive electrode in Li-ion battery.* Journal of The Electrochemical Society, 2019. **166**(3): p. A5090-A5098.
177. Nahir, T.M., *Impedance Spectroscopy: Theory, Experiment, and Applications, Edited by Evgenij Barsoukov (Texas Instruments Inc.) and J. Ross Macdonald (University of North Carolina, Chapel Hill). John Wiley & Sons, Inc.: Hoboken, NJ. 2005. xvii+ 596 pp. $125.00. ISBN 0471-64749-7*. 2005, ACS Publications.
178. Bharathi, S.J., S.H. Thilagar, and V. Jayasurya. *Design and Modeling of Electrochemical Sensor for Determining ION Concentration*. in *2019 IEEE 1st International Conference on Energy, Systems and Information Processing (ICESIP)*. 2019.
179. Shojaei Baghini, M., et al., *Ultra-thin ISFET-based sensing systems.* Electrochemical Science Advances, 2022. **2**(6): p. e2100202.
180. Shojaei Baghini, M., A. Vilouras, and R. Dahiya, *Ultra-Thin Chips With ISFET Array for Continuous Monitoring of Body Fluids Ph.* IEEE Trans Biomed Circuits Syst, 2021. **15**(6): p. 1174-1185.
181. Vilouras, A., et al., *Ultrathin ion-sensitive field-effect transistor chips with bending-induced performance enhancement.* ACS applied electronic materials, 2020. **2**(8): p. 2601-2610.
182. Hosseini, E.S., et al., *Biodegradable materials for sustainable health monitoring devices.* ACS applied bio materials, 2020. **4**(1): p. 163-194.
183. Khan, S., et al., *Flexible Pressure Sensors Based on Screen-Printed P(VDF-TrFE) and P(VDF-TrFE)/MWCNTs.* IEEE Transactions on Semiconductor Manufacturing, 2015. **28**(4): p. 486-493.
184. Pu, W., et al., *Effects of copper mining on heavy metal contamination in a rice agrosystem in the Xiaojiang River Basin, southwest China.* Acta Geochimica, 2019. **38**(5): p. 753-773.
185. Manjakkal, L., et al., *Connected sensors, innovative sensor deployment, and intelligent data analysis for online water quality monitoring.* IEEE Internet of Things Journal, 2021. **8**(18): p. 13805-13824.

186. Bernalte, E., et al., *Rapid and on-site simultaneous electrochemical detection of copper, lead and mercury in the Amazon river.* Sensors and Actuators B: Chemical, 2020. **307**: p. 127620.
187. Kaur, I., et al., *Ultra-sensitive electrochemical sensors based on self-assembled chelating dithiol on gold electrode for trace level detection of copper(II) ions.* Sensors and Actuators B: Chemical, 2020. **312**: p. 127935.
188. Frag, E.Y., M.E.B. Mohamed, and E.M. Fahim, *Application of carbon sensors for potentiometric determination of copper(II) in water and biological fluids of Wilson disease patients. Studying the surface reaction using SEM, EDX, IR and DFT.* Biosensors and Bioelectronics, 2018. **118**: p. 122-128.
189. Adhikari, H., et al., *Facile hydrothermal synthesis of molybdenum disulfide (MoS2) as advanced electrodes for super capacitors applications.* MRS Advances, 2016. **1**(45): p. 3089-3097.
190. Ejaz, A., J.H. Han, and R. Dahiya, *Influence of solvent molecular geometry on the growth of nanostructures.* Journal of colloid and interface science, 2020. **570**: p. 322-331.
191. Pullanchiyodan, A., L. Manjakkal, and R. Dahiya, *Metal coated fabric based asymmetric supercapacitor for wearable applications.* IEEE Sensors Journal, 2021. **21**(23): p. 26208-26214.
192. Thomaz, D.V., et al., *Predictive modelling to study the electrochemical behaviour of PdO, TiO2 and perovskite-type LaFeO3 modified carbon paste electrodes.* Traektoriâ Nauki= Path of Science, 2019. **5**(4): p. 4001-4007.
193. Mathis, T.S., et al., *Energy Storage Data Reporting in Perspective—Guidelines for Interpreting the Performance of Electrochemical Energy Storage Systems.* Advanced Energy Materials, 2019. **9**(39): p. 1902007.
194. Rahman, M.S. and G.A. Gagnon, *Bench-scale evaluation of drinking water treatment parameters on iron particles and water quality.* Water research, 2014. **48**: p. 137-147.
195. Aliyana, A.K., et al., *Disposable pH Sensor on Paper Using Screen-Printed Graphene-Carbon Ink Modified Zinc Oxide Nanoparticles.* IEEE Sensors Journal, 2022.
196. Dervin, S., P. Ganguly, and R.S. Dahiya, *Disposable Electrochemical Sensor Using Graphene Oxide–Chitosan Modified Carbon-Based Electrodes for the Detection of Tyrosine.* IEEE Sensors Journal, 2021. **21**(23): p. 26226-26233.
197. Beniwal, A., et al., *Screen-printed graphene-carbon ink based disposable humidity sensor with wireless communication.* Sensors and Actuators B: Chemical, 2022: p. 132731.
198. Khandelwal, G. and R. Dahiya, *Self‐powered active sensing based on triboelectric generators.* Advanced Materials, 2022. **34**(33): p. 2200724.
199. Nguyen Van, M., et al., *Fe-Doped g-C3N4: High-Performance Photocatalysts in Rhodamine B Decomposition.* Polymers, 2020. **12**(9): p. 1963.
200. Neethipathi, D.K., et al. *MoS2 modified screen printed carbon electrode based flexible sensor for detection of Copper*. in *2022 IEEE International Conference on Flexible and Printable Sensors and Systems (FLEPS)*. 2022.

203. https://pineresearch.com/support-article/eis-basics/